

This item was submitted to [Loughborough's Research Repository](#) by the author.
Items in Figshare are protected by copyright, with all rights reserved, unless otherwise indicated.

Effects of high intensity, large-scale free-stream turbulence on combustor effusion cooling

PLEASE CITE THE PUBLISHED VERSION

PUBLISHER

Loughborough University

LICENCE

CC BY-NC-ND 4.0

REPOSITORY RECORD

Martin, Damian. 2014. "Effects of High Intensity, Large-scale Free-stream Turbulence on Combustor Effusion Cooling". figshare. <https://hdl.handle.net/2134/14725>.

This item was submitted to Loughborough University as a PhD thesis by the author and is made available in the Institutional Repository (<https://dspace.lboro.ac.uk/>) under the following Creative Commons Licence conditions.



For the full text of this licence, please go to:
<http://creativecommons.org/licenses/by-nc-nd/2.5/>

Effects of high intensity, large-scale free-stream
turbulence on combustor effusion cooling

Damian Martin

A Thesis submitted for the degree of Doctor of Philosophy

Department of Aeronautical and Automotive Engineering
Loughborough University

18/12/2013

© 2013, Damian Martin

Abstract

Full-coverage or effusion cooling is commonly used in the thermal management of gas turbine combustion systems. The combustor environment is characterised by highly turbulent free-stream conditions and relatively large turbulent length scales. This turbulent flow field is predominantly created by the upstream fuel injector for lean burn systems. In rich burn systems the turbulent flow field is augmented further by the addition of dilution ports. The available evidence suggests that large energetic eddies interact strongly with the injected coolant fluid and may have a significant impact on the film-cooling performance. The desire to create compact low-emission combustion systems with improved specific fuel consumption, has given rise to a desire to reduce the quantity of air used in wall cooling, and has led to the need for improved cooling correlations and validated computational methods. In order to establish a greater understanding of effusion cooling under conditions of very high free-stream turbulence, a new laboratory test facility has been created that is capable of simulating representative combustor flow conditions, and that allows for a systematic investigation of cooling performance over a range of free-stream turbulence conditions (up to 25% intensity, integral length scale-to-coolant hole diameter ratios of 26) and coolant to mainstream

density ratios ($\frac{\rho_c}{\rho_\infty} \approx 2$).

This thesis describes this new test facility, including the method for generating combustor relevant flow conditions. The hot side film cooling performance of cylindrical and fanned hole effusion has been evaluated in terms of adiabatic film-cooling effectiveness and normalised heat transfer coefficient (HTC) and heat flux reduction (HFR). Infrared thermography was employed to produce spatial resolved surface temperature distributions of the effusion surface. The analysis of this data is supported by fluid temperature field measurements. The interpretation of the data has established the impact of turbulence intensity, integral length scale and density ratio on the mixing processes between free-stream and coolant flows. Elevated levels of free-stream turbulence increase the rate of mixing and degrade the cooling effectiveness at low blowing ratios whereas at high blowing ratios, where the coolant detaches from the surface, a modest increase has been observed under certain conditions; this is due to the turbulent transport of the detached coolant fluid back towards the wall.

For angled cylindrical hole injection the impact of density ratio as an independent parameter was found to be relatively weak. Adiabatic effectiveness data gathered at DR's of 1 - 1.4 scaled reasonable well when plotted against momentum flux ratio. This suggests data collected at low DR's can be scaled to engine representative DR's. The investigation of shaped cooling holes found fanned effusion has the potential to dramatically improve film effectiveness. The diffusion of the flow through a fanned exit prevented jet

detachment at blowing ratios up to 5, increasing spatially averaged effectiveness by 89%.

Contents

1	Introduction	1
1.1	Historical overview	2
1.2	Gas Turbine cooling	4
1.3	Theory of heat transfer over a flat plate	9
1.4	Film cooling parameters	12
1.5	Research focus and thesis outline	14
1.6	Publications	15
2	Literature survey	16
2.1	Introduction	17
2.2	Film cooling	20
2.3	Turbulence generation	37
2.4	Summary	44
3	Experimental apparatus and techniques	46
3.1	Experimental test facilities	47
3.2	Main tunnel design and construction	54
3.3	Experimental models	73

3.4	Summary	78
4	Measurement techniques and instrumentation	102
4.1	Test Matrix	103
4.2	IR camera measurements	106
4.3	Coolant film mixing	110
4.3.1	Data reduction	110
5	Measurement uncertainty	121
5.1	Measurement uncertainty	122
5.1.1	Surface temperature measurements	122
5.2	Flow parameters	128
6	Investigation of plain hole effusion subjected to highly turbulent free-stream conditions	134
6.1	Adiabatic effectiveness	135
6.1.1	Free-stream turbulence effects	135
6.1.2	Free-stream turbulence length scale	139
6.1.3	Flow field temperature measurements	141
6.1.4	Density ratio	143
6.2	Normalised Heat Transfer Coefficient	144
6.3	Summary	147
7	Investigation of shaped film cooling effusion arrays	169
7.1	Fanned shaped cooling	170
7.1.1	Modified fan design	176
7.2	Summary	180

8	Conclusions	193
8.1	Experimental test facility	194
8.2	Cylindrical hole effusion subjected to highly turbulent free- stream conditions	195
8.3	Fanned hole effusion	197
8.4	Summary	197
8.5	Outlook and future work	201
A	Appendix	214
A.1	Flow Nozzle	214
A.2	Rig drawings	217
A.3	Conduction Loss	236
A.4	Pressure Loss	240
A.5	Misalignment	245
A.6	Uncertainty Calculations	248
A.7	ASME GT2012-68863	252

List of Figures

1.1	Sketch from John Barbers Patent	3
1.2	Rolls Royce Trent XWB	3
1.3	Simple gas turbine cycle	5
1.4	Pressure ratio trend for civil aero engines	6
1.5	Effusion holes and liner temperature distribution	8
1.6	Velocity and temperature gradient over a flat plate	9
1.7	Film cooling parameters	13
2.1	Sketch of CRVP	18
2.2	spanwise effectiveness variable blowing ratio	21
2.3	effectiveness for different blowing and density ratios	23
2.4	Effusion holes and liner temperature distribution	24
2.5	Definition of inclination and flow orientation angle	26
2.6	Variation of HFR with momentum flux (I)	28
2.7	Various hole shape definitions	29
2.8	length scale	32
2.9	Variation of coolant pdf	34
2.10	Multi row superposition predictions	35

2.11	Grid generated turbulence	38
2.12	Schematic of turbulence generator design and a close-up of the jet hole geometry	40
2.13	Schematic of wind test section with cross flow jets	43
3.1	Wind tunnel schematic	80
3.2	Schematic of dual and single skin architecture at a 3% liner pressure drop	80
3.3	Conventional closed circuit wind tunnel schematic	81
3.4	Turbulent intensity measurements from a lean burn combustor at 25% tile distance	81
3.5	Turbulent length scale measurements from a lean burn com- bustor at 25% tile distance	82
3.6	Photograph of tunnel return circuit	82
3.7	construction of the right hand sub assembly	83
3.8	Photograph of test section	84
3.9	Tunnel warm up cycle	84
3.10	Bell mouth inlet arrangement	85
3.11	Sectional view of test section	85
3.12	Assembled multi diameter turbulence plate	86
3.13	Thermocouple and coldwire comparison	86
3.14	coldwire measurements with turbulence generation	87
3.15	Hotwire setup	88
3.16	Predicted jet trajectory for $\phi 13$ injection at $V_r 21$	88
3.17	Center line profile at various VR	89

3.18	Center line profile at various VR	90
3.19	Hotwire traverse profile	91
3.20	Hotwire traverse profile	92
3.21	Hotwire traverse profile	93
3.22	Hotwire traverse profile	94
3.23	Photography and schematic of turbo expander system	95
3.24	IHI RB85 turbine performance and similar sized Garret turbo	96
3.25	A diagram that illustrates the coolant feed plenum construction	96
3.26	Array test plate	97
3.27	Effusion hole array pattern for fanned effusion tests	97
3.28	Datum fan definition	98
3.29	Plain hole definition	98
3.30	Modified fan definition	99
3.31	Laser drilled designs	99
3.32	Photographs of the insert assembly and the finished foil bonded test plate	100
3.33	Test plate with bonded heating foil	100
3.34	Effusion array mounted in test section with heater foil and reference thermocouples	101
4.1	Testing campaign for chapter 6	104
4.2	Testing campaign for chapter 7	106
4.3	IR calibration set-up	116
4.4	Isothermal calibration plate construction	116
4.5	typical pixel calibration curve	117

4.6	Assembled fine wire thermocouple mounted to ceramic tube	117
4.7	Typical surface temperature map from IR camera	118
4.8	Typical data set and line fit used for adiabatic effectiveness and heat transfer coefficient	118
4.9	Comparison of measurement techniques at Br 2.5 Dr \approx 1.1, Tu 25%	119
4.10	Schematic of test rig instrumentation locations	119
4.11	Rig monitor virtual instrument	120
5.1	A contour plot of the difference between measured wall surface temperature and modelled adiabatic wall temperature.	126
5.2	Typical pressure transducer calibration plot	129
5.3	Schematic of orifice plate configuration for coolant mass flow measurement	130
6.1	Adiabatic test plate loaded into test section	150
6.2	Spanwise averaged adiabatic effectiveness	151
6.3	Surface adiabatic effectiveness, DR 1.4, BR 0.3 - 0.7, Tu 10 -25%	152
6.4	Surface adiabatic effectiveness, DR 1.4, BR 0.8 - 1.2, Tu 10 -25%	153
6.5	Surface adiabatic effectiveness, DR 1.4, BR 1.3 - 1.5, Tu 10 -25%	154
6.6	Surface adiabatic effectiveness for fixed DR 1.4 and free-stream turbulence Tu16%	155
6.7	Spanwise averaged adiabatic effectiveness	156

6.8	Measured span-wise gas temperature and surface effectiveness, DR 1.0.65, BR 0.4, Tu 10%	157
6.9	Measured span-wise gas temperature and surface effectiveness, DR 1.0.65, BR 0.4, Tu 25%	158
6.10	Measured span-wise gas temperature and surface effectiveness, DR 1.0.65, BR 1.3, Tu 10%	159
6.11	Measured span-wise gas temperature and surface effectiveness, DR 1.0.65, BR 1.3, Tu 25%	160
6.12	Streamwise temperature traverse (rows 2-4), DR 1.065, BR 1.3, Tu=10%	161
6.13	Streamwise temperature traverse (rows 2-4), DR 1.065, BR 1.3, Tu=25%	161
6.14	Average Surface effectiveness against velocity ratio, Vr	162
6.15	Average Surface effectiveness against blowing ratio, BR	162
6.16	Average Surface effectiveness against momentum flux ratio, I .	163
6.17	Average heat transfer with coolant on, DR 1.1, BR 1.5, Tu 25%	163
6.18	Average heat transfer with coolant off at free-stream Tu 25% .	164
6.19	normalised h/h_o plot at DR 1.1, BR 1.5, Tu 25%	164
6.20	Normalised heat transfer coefficient, DR 1.1, BR 0.3 - 1.5, Tu 10 - 25%	165
6.21	Surface adiabatic effectiveness, DR 1.1, BR 0.3 - 1.5, Tu 10 - 25%	166
6.22	Span average h/h_o , DR 1.0.65, BR 0.3 and 1.5 at Tu 10 - 25%	167
6.23	Span-average effectiveness, DR 1.0.65, BR 0.3 and 1.5 at Tu 10 - 25%	167

6.24	Span-average heat flux reduction, $\phi = 0.8$, DR 1.0.65, BR 0.3 and 1.5 at Tu 10 - 25%	168
7.1	Measured spanwise gas temperature and surface effectiveness, Dr 1.065, Br 2.5, Tu 10%	183
7.2	Measured spanwise gas temperature and surface effectiveness, Dr 1.065, Br 2.5, Tu 25%	184
7.3	Measured spanwise gas temperature and surface effectiveness, Dr 1.065, Br 5, Tu 10%	185
7.4	Measured spanwise gas temperature and surface effectiveness, Dr 1.065, Br 5, Tu 25%	186
7.5	Normalised HTC, Dr 1.065, Br 2.5	187
7.6	Normalised htc, Dr 1.065, Br 5	188
7.7	Span averaged effectiveness of fanned and plain hole effusion .	189
7.8	Span-averaged HFR of fanned and plain hole effusion, $\phi = 0.8$	189
7.9	Film effectiveness of datum plain cylinder, datum fan and modified fan, Br 5, Tu25 %	190
7.10	Normalised htc of datum plain cylinder, datum fan and mod- ified fan, Br 5, Tu25%	191
7.11	Span-averaged effectiveness of datum fan, modified fanned and plain hole effusion, Tu 25%	192
7.12	Span-averaged HFR of datum fan, modified fanned and plain hole effusion, $\phi = 0.8$, Tu 25%	192

List of Tables

3.1	Rig scaling summary * based on combustion conditions of Pratt & Whitney JT9D [1]	54
5.1	Rohacell material properties	124
5.2	Summary of surface measurement error	128
5.3	Flow parameter uncertainties	130
5.4	Hot-wire measurement uncertainties	133
6.1	Spatially averaged adiabatic effectiveness at high and low tur- bulence intensity (masked effusion holes).	139
7.1	Spatially averaged effectiveness at high and low turbulence (masked effusion holes).	173
7.2	Spatially average normalised HTC and HFR at high and low turbulence intensity (masked effusion holes).	176
7.3	Spatially average effectiveness, normalised HTC and HFR at high and low turbulence not including holes.	179

Acknowledgements

It was a great privilege for me to be able to study at Loughborough University within the UTC and I would like to thank Dr. Steven Thorpe who provided the opportunity. The work presented in this thesis would not have been possible without the help of a number of people whom I would like to thank.

I would like to thank my supervisors Dr. Steven Thorpe and Dr. Paul Denman for their support, guidance and encouragement. Special thanks are extended to Neil Thorley for his help with the construction of the wind tunnel facility. Whenever I was in a bind with machining work or last minute modifications, he always came through for me.

I would like to acknowledge the Engineering and Physical Science Research Council (EPSRC) and Rolls-Royce Plc for providing funding for the research.

On a personal level I would like to thank Dani for her love, support and encouragement. I know without a doubt that I would not have achieved many of my successes without you.

Nomenclature

D	Effusion hole diameter
d	Rod diameter
\dot{m}	Mass flow rate, kg/s
DR	Coolant to free-stream density ratio, (ρ_c/ρ_∞)
BR	Coolant to free-stream blowing ratio, $(\rho U)_c/(\rho U)_\infty$
I	Coolant to free-stream momentum ratio, BR^2/DR
VR	Coolant to free-stream velocity ratio, U_c/U_∞
ΛL	Integral length scale
P	Spanwise effusion hole spacing, mm
Re_j	Coolant Reynolds number
S	Streamwise effusion hole spacing, mm
T	Temperature, K
P	Pressure, Pa
Tu	Turbulence intensity, %
Λ_x	Grid generated turbulent length scale
U	Velocity, m/s
X	Streamwise coordinates, mm
Y	Vertical coordinates, mm

Z	Spanwise coordinates, mm
L	Cooling hole length
Lf	Cooling hole fan length
A	Area
α	Coolant hole angle, deg
φ	Coolant hole fan angle
β	Coolant compound angle, deg
ρ	Density, kg/m^3
η	Film cooling effectiveness
h	Heat transfer coefficient
q	Surface heat flux
ε	Emissivity
η_T	Thermal efficiency
γ	Ratio of specific heats
θ	Normalised gas temperature $\frac{T_\infty - T_{xy}}{T_\infty - T_c}$
ϕ	Dimensionless wall temperature $\frac{T_\infty - T_w}{T_\infty - T_c}$
Θ	Heat flux reduction

Subscripts

aw	Adiabatic wall
rad	Radiative
avg	Average

w	Wall
∞, g	Freestream
c	Coolant
xy	Local position
j	Coolant jet
f	Film
o	No film

Acronyms

CRVP	Counter rotating vortex pair
HTC	Heat transfer coefficient
HFR	Heat flux reduction
pdf	Probability density function
PR	Pressure ratio

Chapter 1

Introduction

Effusion cooling schemes are used extensively in the thermal management of gas turbine combustor liners. The basic function of an effusion scheme is to deliver cool combustor bypass flow through an array of effusion holes. This cool air then creates a protective film on the combustor liner. In the design of such a system, it would be important to understand the impact of; free-stream turbulence conditions, integral length scale, coolant to mainstream density ratios and blowing ratio (ie. wall/system pressure drop). The following chapter provides an overview of film cooling in the context of gas turbines.

1.1 Historical overview

The history of the gas turbine can be traced back to Hero of Alexandria who in the first century AD demonstrated a device he named the Aeolipile. This device was the first example of a steam reaction turbine and consisted of a rotational ball driven with steam propulsion. While the device had no real practical use it demonstrated the ability to generate thrust by accelerating hot gas through a nozzle. The first foundation for the modern gas turbine is credited to the English coal master and inventor John Barber who took out a patent in 1791 (patent no. 1833 Obtaining and Applying Motive Power, & c. A Method of Rising Inflammable Air for the Purposes of Procuring Motion, and Facilitating Metallurgical Operations). The machine contained all of the major components associated with a gas turbine engine, Fig 1.1 shows the sketch from Barbers patent. The principle of the design was to deliver compressed air and fuel from reciprocating gas compressor into a combustion chamber. The resulting hot gases were then passed through a nozzle onto a turbine wheel. While the design concept was sound, materials of the day were inadequate for construction and operation. It wasn't until the 20th century that engineers were able to fully realise this concept into something useful. The application of gas turbines for propulsion began in the 1930's with the first patent for a turbojet engine being submitted in January 1930 by Frank Whittle. The first succesful test of the engine was performed in April 1937. Independently, Hans von Ohain had started similar work in Germany 1935. Ohain and Ernst Heinkel worked together to produce the first jet plane, Heinkel He 178. The experimental plane flew on the 27th of August 1939

powered by the He.S3B with a maximum thrust of 1,000lbs. From these pioneering gas turbine engines, thrust levels have increased dramatically. Today, civil gas turbines such as the Rolls Royce Trent XWB (See Fig 1.2) produce thrust levels in excess of 72,000lbs with turbine inlet temperatures approaching 2000K.

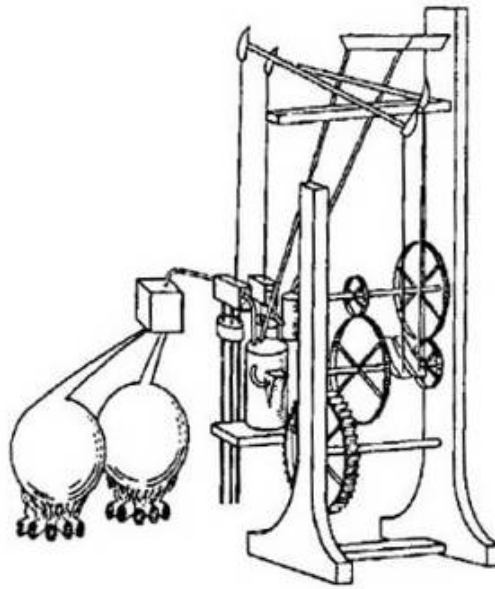


Figure 1.1: Sketch from John Barbers Patent

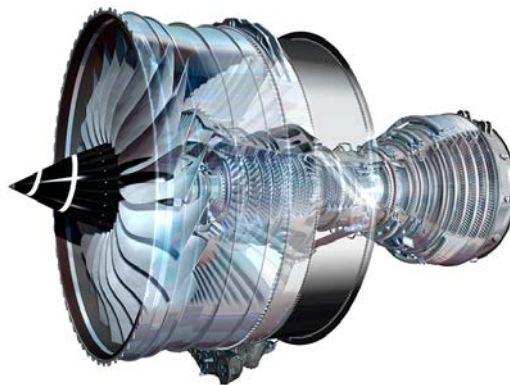


Figure 1.2: Rolls Royce Trent XWB

1.2 Gas Turbine cooling

In its most fundamental form the gas turbine can be best described by the Brayton cycle. The Brayton power cycle represents the ideal turbine power cycle see Fig 1.3. It is composed of four processes: isentropic compression, constant-pressure heat addition, isentropic expansion and constant-pressure heat rejection. In the ideal cycle, there are no pressure losses in the combustion chamber and exhausting ducts. The working fluid is considered calorically perfect gas. For this ideal cycle the thermal efficiency and net work can be calculated as a function of the pressure ratio and temperature ratio:

$$\eta_T = 1 - \frac{T_4 - T_1}{T_3 - T_2} = 1 - \left(\frac{1}{PR} \right)^{(\gamma-1)/\gamma} \quad (1.1)$$

The efficiency of the cycle depends only on the pressure ratio and the type of gas. The highest temperature in the cycle occurs at the end of the combustion process (T_3), and it is limited by the maximum temperature the turbine blades can withstand. This temperature also limits the pressure ratio that can be used in the cycle. Therefore, the trend over the years is to develop engines with increasing OPR as shown in Figure 1.4. This relentless drive towards increased OPR's inevitably leads to high turbine entry temperatures (TET's). In modern gas turbines, temperatures of 2000K+ can be present at the first set of nozzle guide vanes, with flame temperatures in the combustion chamber significantly higher. The temperatures in these regions are well in excess of the material melting points used to construct the turbines and combustion chambers. Therefore, turbine blades, vanes, discs and combustor liners all require some form of cooling.

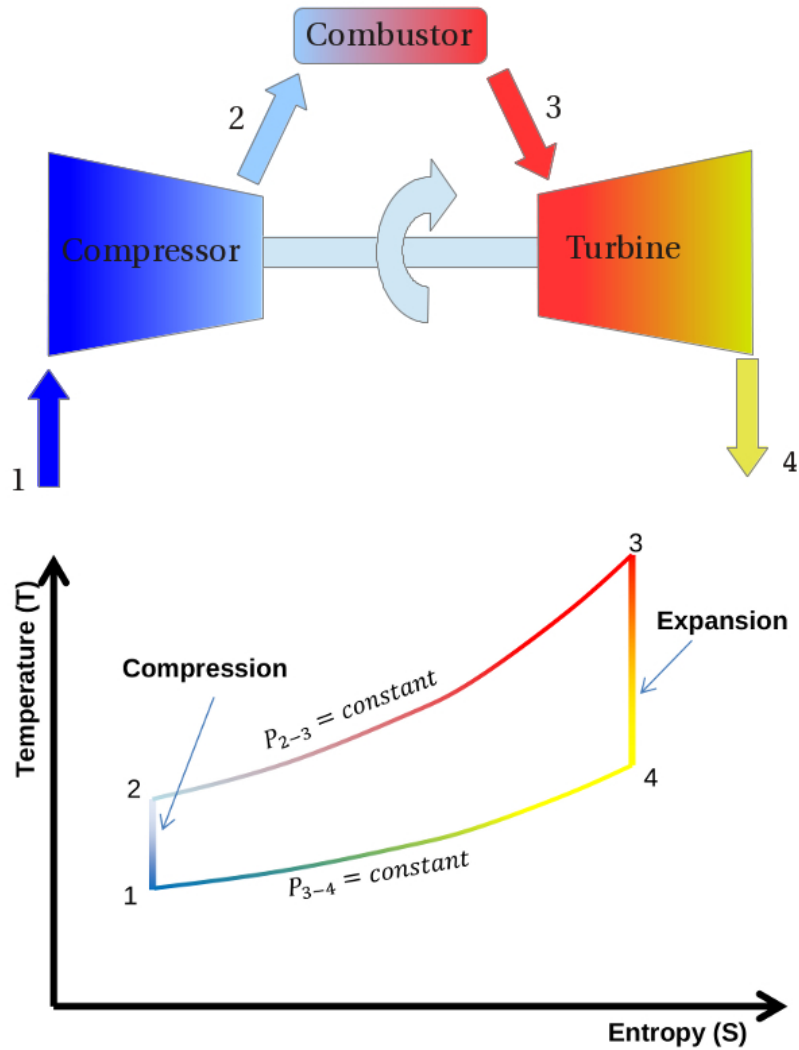


Figure 1.3: Simple gas turbine cycle

The coolant comes in the form of compressed air from the compressor stage of the engine. Since this extraction of air plays no part in the thermodynamic cycle, it results in a reduction in the cycle efficiency. Even with this reduced efficiency, the historical trends in turbofan engine design have continually pushed for increases in turbine entry temperature, overall pressure ratio and bypass ratio in order to improve both the thermal and propulsive

efficiencies. Coolant requirements in the combustion liner have been squeezed further as engine designers continue to develop lean burn combustor technology, which reduces the amount of available coolant, as a greater fraction of engine core air is passed through the injector. The primary advantage of this type of system is reduced flame temperatures and hot spots which can significantly reduce the amount of NO_x formation. These design trends have the potential to drastically reduce the product life of combustor liners without carefully designed cooling schemes. Early cooling schemes utilised slots to generate a cool film of air on the liner surface. More recent designs use effusion cooling schemes which allow for a greater control of wall temperature and utilise coolant more efficiently.

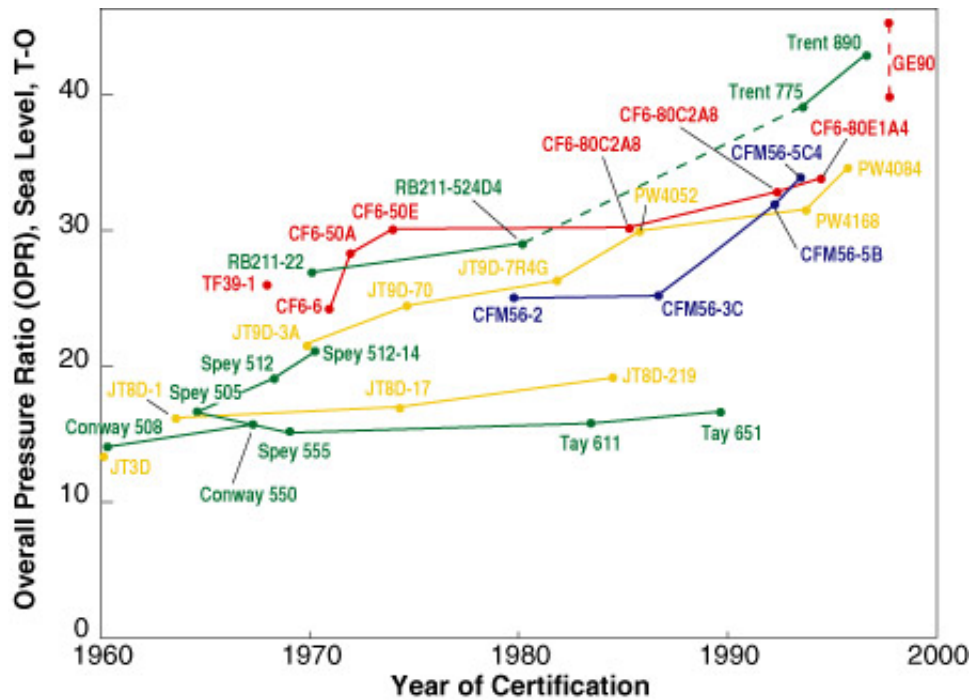
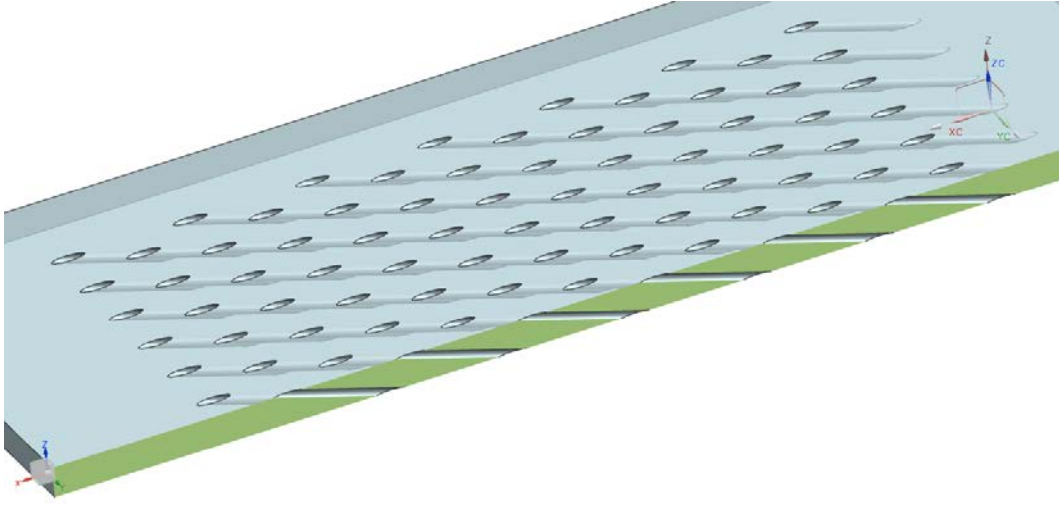
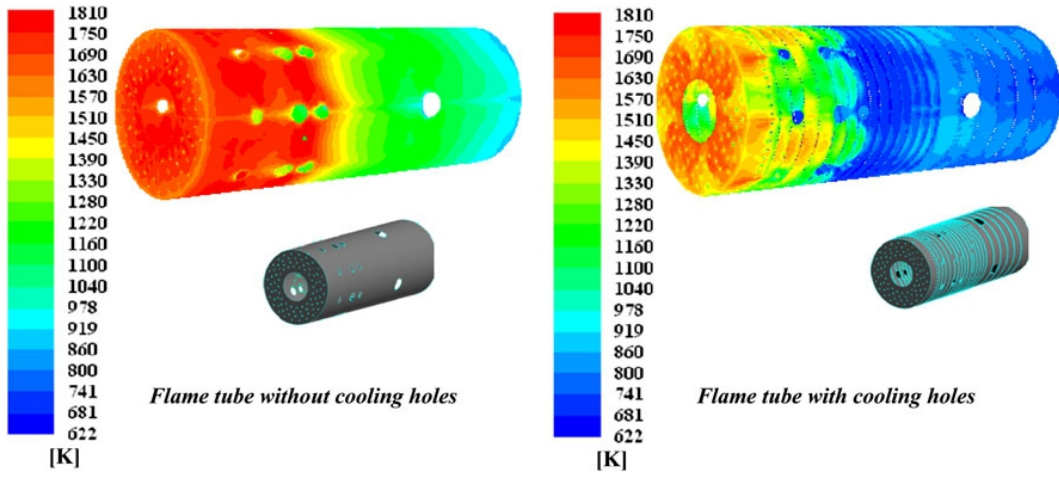


Figure 1.4: Pressure ratio trend for civil aero engines [2]

Typical effusion cooling schemes use multiple patterns of small diameter holes ($\phi 0.7\text{mm}$ engine scale) which are laser drilled through the liner wall at shallow angles (of the order 20°). An example of this type of effusion array is shown in Fig 1.5(a). The effusion array generates a layer of cooling flow on the combustor liner to isolate the component from the hot gases, therefore it is desirable to have high mass flow with little mixing. There is also a significant cooling effect from the holes themselves as heat is removed by the passage of coolant inside the holes [3]. In general terms all cooling schemes have a negative impact on specific fuel consumption (sfc) as cooling air does not contribute to the thermodynamic cycle. Effusion cooling also requires thicker liner walls when compared with traditional slot cooling to cope with the buckling load created by the pressure differential across the liner wall. This increase is typically around 20% [4]. An example of effusion cooling applied to an industrial combustor liner is shown in Figure 1.5(b). The behavior of film cooling arrangements is complicated by the particular free-stream conditions that are usually present, namely highly turbulent swirling flows, and the presence of relatively large diameter dilution jets. In general, for a particular wall geometry, the film-cooling situation can be characterised by the coolant and free-stream flow conditions: velocity ratio, density ratio, Reynolds number and turbulence level. An understanding of these parameters enables cooling strategies to be tailored to specific regions in the combustor liner.



(a)



(b)

Figure 1.5: (a) Typical plain hole angled effusion array; (b) Wall temperature distribution with and without effusion cooling

1.3 Theory of heat transfer over a flat plate

Heat transfer by convection is the mode of energy transfer between a solid surface and the adjacent liquid or gas and it involves the combined effects of conduction and fluid motion [5]. For a simple case of boundary layer flow over a flat surface, velocity and temperature distribution would be similar to Figure 1.6.

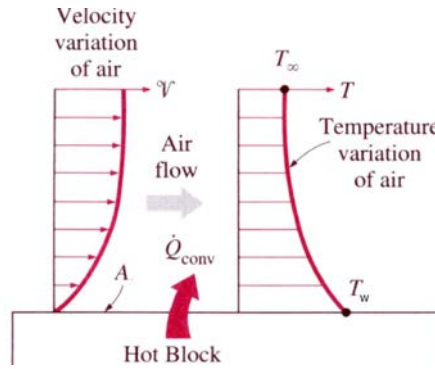


Figure 1.6: Velocity and temperature gradient over a flat plate [5]

The rate of convective heat transfer is observed to be proportional to the temperature difference and is expressed by Newton's law of cooling.

$$q = hA(T_\infty - T_w) \quad (1.2)$$

Where h is the convective heat transfer coefficient, A is the surface area, T_w is the surface temperature and T_∞ is the main-stream temperature. The convective heat transfer coefficient (HTC) is a parameter which depends on all of the variables influencing convection. This includes surface geometry, nature of fluid motion, fluid properties and fluid velocity. In terms of film cooling, the free stream temperature is rarely used in the definition of

heat transfer coefficient because film cooling involves two fluid temperatures, coolant and free stream. Downstream of the injection the two flows mix. Therefore, if T_∞ is used then the heat transfer coefficient will be some function of the flow field and the temperature of the coolant. To ensure the heat transfer coefficient is independent of coolant and freestream temperature, the adiabatic wall temperature is used, as this temperature represents the fluid temperature immediately above the surface for an adiabatic surface (zero heat flux). Therefore this temperature includes any mixing effects between the coolant and the free stream. By using the adiabatic wall temperature different cooling schemes become more comparable. Therefore the heat flux q_f is more usually represented by adopting an equivalent equation given by [6].

$$q_f = h_f(T_{aw} - T_w) \quad (1.3)$$

The adiabatic wall temperature represents the driving temperature potential for heat transfer, and is often presented in a normalised form called the adiabatic effectiveness.

$$\eta_{aw} = \frac{T_\infty - T_{aw}}{T_\infty - T_c} \quad (1.4)$$

Where T_∞ is the free-stream gas temperature, T_c is the coolant delivery temperature and T_{aw} is the adiabatic wall temperature. For areas close to the vicinity of the injection location, η_{aw} would be close to unity ($T_{aw} \approx T_c$). Further downstream, η_{aw} will approach zero ($T_{aw} \approx T_\infty$), where the boundary layer recovers to its undisturbed condition.

By considering the equations 1.3 and 1.4, it is clear that a reduction in T_{aw} relative to T_∞ will reduce heat flux to the wall. However, as mentioned earlier the heat transfer coefficient is sensitive to the nature of the fluid motion. This implies that the introduction of the film is likely to disturb the near wall flow which would cause an increase in the heat transfer to the wall, and hence is detrimental to the cooling performance. Therefore, a more comprehensive way of describing the film cooling performance is by the heat flux reduction (HFR). The HFR was first identified by [7].

$$HFR = 1 - \frac{q_f}{q_o} \quad (1.5)$$

The best cooling is achieved at large values of HFR, indicating maximum reduction of the heat flux into the film cooled wall q_f compared to that without a cooling film q_o . Combining equations 1.3 - 1.4 gives

$$HFR = 1 - \frac{h_f}{h_o} \left(1 - \frac{\eta_{aw}}{\phi}\right) \quad (1.6)$$

ϕ is a non-dimensional temperature defined as:

$$\phi = \frac{T_\infty - T_w}{T_\infty - T_c} \quad (1.7)$$

The heat flux reduction includes the adiabatic effectiveness and accounts for the changes in heat transfer coefficient as result of the disturbance caused by coolant injection. This provides a more complete description of the film cooling process.

In conclusion, there are three main parameters of major interest to designers of film cooled surfaces. The adiabatic wall temperatures T_{aw} represented in normalised form by η_{aw} , the surface heat transfer coefficient h_f and the combined influence of HTC augmentation and film coverage captured by the HFR parameter. This data enables the ultimate goal of predicting metal temperatures to be realised.

1.4 Film cooling parameters

The prediction of the film cooling performance is complicated by the many factors that affect the film cooling effectiveness as shown in Fig 1.7. These parameters are not necessarily independent from one and other, therefore each combination can potentially change the film cooling performance. This requires a large number of operating conditions to be explored, hence the inherent difficulty in predicting film cooling performance. Systematic studies of the many film cooling parameters have given some insight into their influence. However, further work is required to produce quantitative information of individual and combined effects across a range of conditions, especially those typical of combustor liner applications. In any one film cooling investigation the number of parameters varied is usually restricted, due to time and cost limitations.

A review of the available literature describing parameters which have a significant influence on the film cooling performance is given in the following chapter.

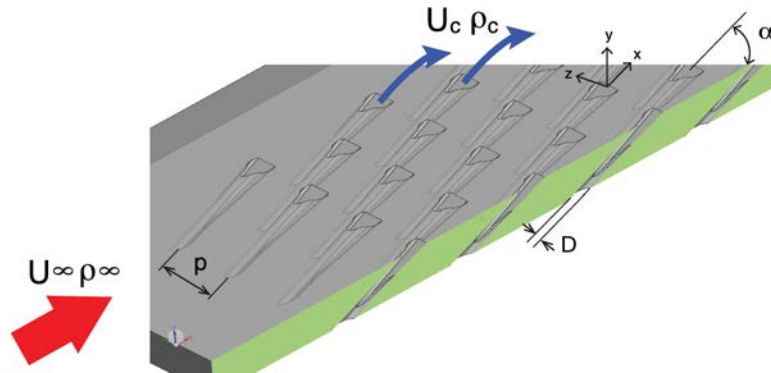


Figure 1.7: Film cooling parameters

Flow conditions

- Blowing ratio, $BR = (U\rho)_c / (U\rho)_\infty$
- Momentum ratio, $I = (U^2\rho)_c / (U^2\rho)_\infty$
- Density ratio, $DR = \rho_c / \rho_\infty$
- Main stream Reynolds number, $Re_{\infty D}$
- Jet Reynolds, Re_{jD}
- Free stream turbulence intensity & length scale, $Tu, \Delta L$

Geometric

- Hole inclination, α
- Pitch and row spacing, $p/d, s/d$
- hole shape, (fanned, slotted etc)
- compound angle, β

1.5 Research focus and thesis outline

In order to reduce emissions and cooling flow requirements the development of improved cooling schemes are required. For this to be possible all of the properties affecting film cooling must be understood. Whilst much research has been performed on film cooling, there is a distinct short fall in the understanding of the interaction between the cooling film and the main combustor flow. In particular the impact of combustor generated turbulence and flow structures is not well characterised. Therefore, the initial objective of this research is to investigate the effects of high levels of free-stream turbulence up to 25% and turbulence length scale at representative flow conditions found in low-emission gas turbine combustors. In addition to the evaluation of film cooling effectiveness and normalised heat transfer coefficient, any mechanisms driving the changes in film cooling performance are to be identified.

As well as producing this fundamental knowledge, the work will also produce valuable data for the development and validation of computational codes, and the improvement of design tools in the gas turbine industry. The individual objectives of this research are as follows: Design and build a new wind tunnel facility which is capable of supplying a scaled film cooled test section at engine representative flow conditions. Understand the response of cooling films to the unsteady flow features typically found in modern gas turbine combustors. Investigate the effect of free-stream flow parameters on cooling-film behaviour under controlled conditions, including large scale energetic flow-structures and high turbulence intensity. To understand the

impact of density ratio as an independent parameter, in particularly the appropriate scaling parameter for low density ratio tests.

Investigate the use of shaped cooling holes for combustor liner applications. In particular the development of a reduced cost diffusing design which can be manufactured using conventional laser/percussion drilling technology.

1.6 Publications

The results of the adiabatic film effectiveness measurements have been so far presented in [8] at the 2012 ASME turbo exposition held in Copenhagen.

The shaped cooling hole research has been presented in the following technical reports: [9], [10].

Chapter 2

Literature survey

A review of relevant experimental work is given in this chapter. First of all, details of the common non-dimensional parameters used and their relevance to film cooling performance. This is then followed by a review of turbulence generation techniques employed to manipulate the freestream flow conditions.

2.1 Introduction

Film cooling represents one of the few technologies that has made a significant contribution to the increase in cycle temperatures and efficiencies of today's modern gas turbine engines. Over the last five decades, film cooling investigations have been performed by a broad spectrum of researchers to understand the fundamental physics of film cooling, and to improve the state of the art. Early work was mainly focused on injection through continuous slots. A survey of this early work is given by Goldstein [6]. In general the cooling film generated by a two-dimensional slot represents the ideal case as the coolant is distributed evenly across the slot width. However, due to the many competing factors (eg. high thermal and mechanical stress, weight, cost, fabrication, efficiency) the sole use of slot cooling in gas turbines is impractical. Therefore, the majority of research for the past 30 years has mainly been directed at three dimensional injection through discrete holes.

Despite the limitations of slot cooling, it is in all cases the goal of discrete geometry film cooling to approximate the formation of an ideal tangential slot injection, which creates a continuous layer of film over the surface. There is a considerable amount of experimental data in the literature on film cooling with injection through discrete holes. It is important, however, to understand the mixing process between the mainstream and the injectant, since this is highly three-dimensional unlike the mixing of a 2D slot generated films. Discrete film cooling in its most simple form can be described by the fundamental jet in a cross flow. The flow field created by the jet cross flow

interaction is very complex. An early study by [11] classified the interaction region into four types of coherent structures. Fig 2.1 shows the structures in a sketch. In the study smoke streaklines were used to visualise these structures in the near field of the jet.

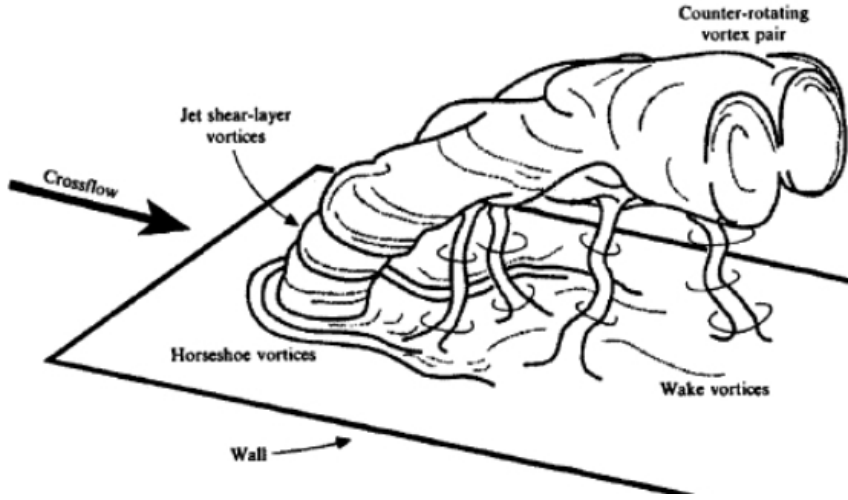


Figure 2.1: Sketch of vortical structures found in a transverse-jet near field [11]

The four main structures are identified as i) Jet shear layer vortices which produce Kelvin-Helmholtz instabilities, ii) Horseshoe vortices caused by the adverse pressure gradient upstream of the jet, iii) Kidney vortices or counter-rotating vortex pair, iv) Wake vortices generated by the cross flow boundary layer. By far the most dominant flow structures are the kidney vortices. There are many hypotheses behind the formation of counter-rotating vortex pair (CRVP). [12] suggested that the formation of the CRVP begins inside the hole by vortices grouping together. A CFD study by [13] managed to simulate CRVP with both a single vortex and a pair of vortices, which suggests the hole vortices are not the sole creation mechanism. Other studies

suggest that the roll up of jet shear layer creates the vortices. Irrespective of the mechanism which creates CRVP the fact remains; the complex interaction between coolant jet and freestream has a great influence on the film cooling effectiveness and heat transfer coefficient. Therefore, variables which directly affect this mixing process such as the cooling hole geometry and free-stream flow conditions can have a profound impact on the film cooling performance. Generally most film cooling studies focus on the surface effectiveness and heat transfer coefficients downstream of a single row of effusion holes. These types of experiments are generally performed under moderate turbulence conditions $< 10\%$, which are representative of the cooling situation on a high pressure turbine blade or nozzle guide vane. In the combustor environment flow conditions are substantially more chaotic as the upstream injector atomises the fuel by imposing a turbulent flow field. The presence of the highly turbulent free-stream rapidly breaks down the cooling film. This requires the cooling film to be constantly regenerated through multiple cooling rows. Therefore, most of the recent experimental research on combustor film cooling is concerned with multi hole arrays, as is the case in the current work. Following is a brief discussion of the investigations that are pertinent to the present experimental work, with an emphasis on the influence of the freestream turbulence intensity and discrete hole arrays.

2.2 Film cooling

Blowing ratio

The blowing ratio scales the thermal transport capacity of the coolant because the convective transport is proportional to $C_p \rho U_c$ [14] blowing ratio is defined as:

$$Br = \frac{(\rho U_c)}{(\rho U_\infty)} \quad (2.1)$$

The blowing ratio gives an indication of the quantity of film cooling fluid being used relative to the cross flow. The blowing ratio in the combustor liner is set by the pressure drop across the liner wall, typical civil applications use a double skin architecture whereby most of the available pressure drop is utilized by the cold side impingement process. The remaining pressure then drives the effusion holes. The pressure drop across the liner wall is typically $\frac{\Delta P}{P} = 3\%$ however, local variations in the static pressure can vary considerable due to the flow field generated by the injector as shown by [15]. Therefore it is important to understand the performance of cooling arrangements across a range of blowing conditions. Typical blowing ratios found in combustor liners range from $Br=1$ to $Br=4$. For a simple angle hole case, low blowing ratios will generally yield good film effectiveness in the near jet region as the jet spreads across the wall surface immediately after exiting the holes. However, the coolant mass flow is diluted rapidly by the hot gas flow and therefore a rapid decay of effectiveness follows downstream of the maximum [16].

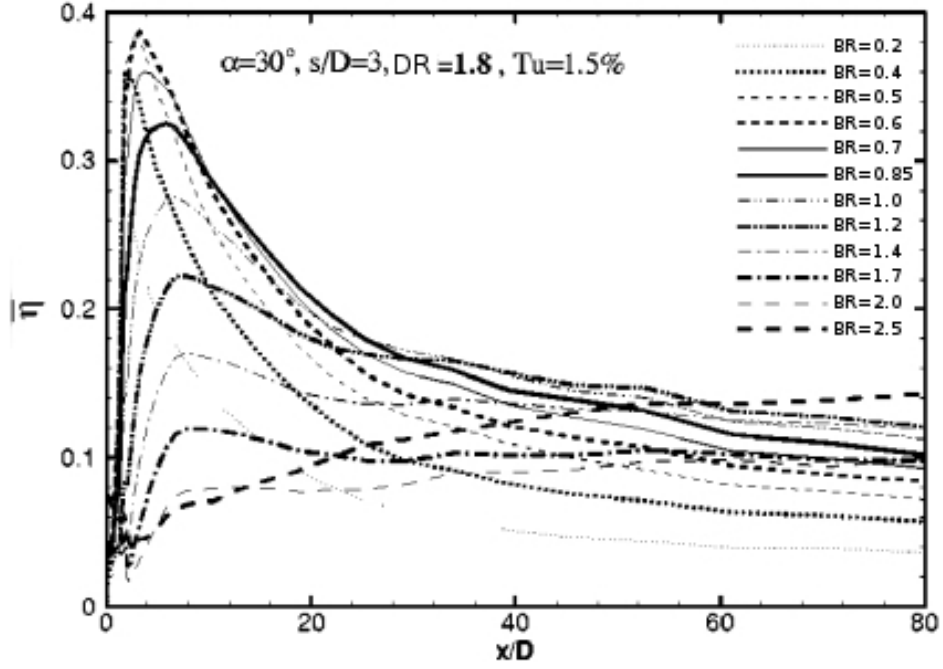


Figure 2.2: Film effectiveness distribution in the streamwise direction at different blowing ratios [16]

Fig 2.2 shows this rapid decrease in effectiveness in the streamwise direction at low blowing ratios. The plot also shows the consequence of a high blowing ratio. At blowing ratios above $Br=0.6$ the effectiveness begins to decrease immediately downstream of the hole due to jet lift off. For the blowing ratio $Br=1.7$ a secondary peak can be found at $x/D=25$ which corresponds to the re-attachment of the jet to the surface. The distributions of effectiveness are typical of a single jet in a cross flow. For blowing ratios above $Br=1.7$ the interaction between neighbouring jets begins to dominate the flow regime. Optimizing the blowing rate of a cooling scheme is critical because blowing rates that are too high eject large portions of the coolant into the free-stream, whereas low blowing rates provide insufficient coolant

coverage. The optimum blowing rate depends primarily on the injection angle and hole shape. Studies by [17] , [18] and [19] all showed general conclusions that the optimum blowing ratio for cylindrical holes is around 0.5 in the near hole region.

Density ratio

The density ratio is simply the ratio of the cooling jet and free-stream flow density.

$$Dr = \frac{\rho_c}{\rho_\infty} \quad (2.2)$$

In terms of combustor liner cooling this ratio can be anything up to DR=3 as the cooling flow supplied from the HP compressor is at a much lower temperature than the combustion products. This density ratio range is difficult to simulate under experimental conditions. Therefore, understanding the effects of DR on film cooling performance is crucial if it is to be scaled to engine designs. In an early study by [20] density ratios ranging from 0.75 to 4.17 were studied at different blowing ratios ranging from 0.2 to 2.0. Fig 2.3 has been reproduced from this study.

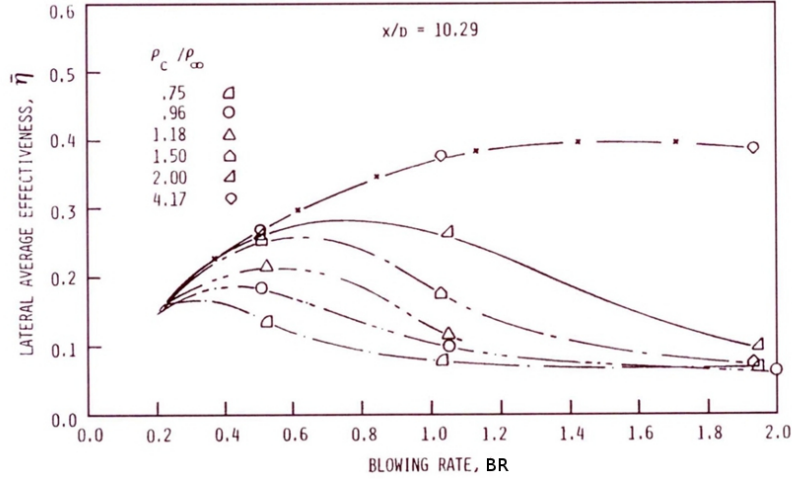
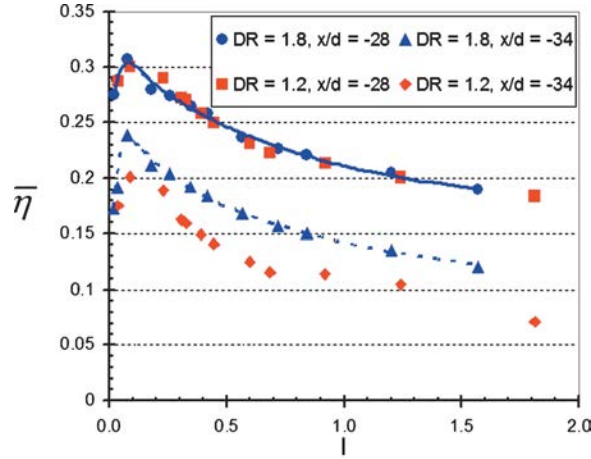


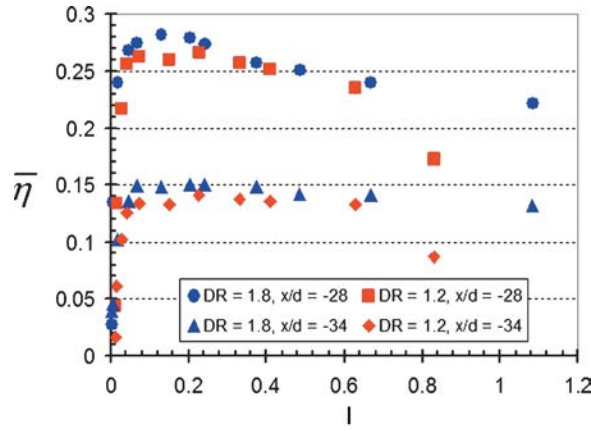
Figure 2.3: Effect of blowing ratio on laterally averaged film effectiveness for different coolant density ratios [20]

The geometry in this study consisted of a single row of simple angle holes inclined at 35° to the stream-wise direction. Improved film effectiveness was reported for higher DR coolant jets operating at the same BR. This was attributed to the lower density coolant jets having higher momentum ratios for a given BR, hence, a tendency of coolant jet to separate from the surface. For higher density ratios the coolant remains much closer to the test surface, which increases the cooling effectiveness. A similar study by [21] found adiabatic effectiveness scaled well with blowing ratio while the coolant jet was attached. For cases where the jet begins transition to a detached state no consistent scaling was found. Another study by [22] investigated the film effectiveness on the pressure side of a vane. The cooling film was generated by a row of compound angle holes inclined at 35° to surface and 45° to mainstream flow. Coolant density ratios of 1.2-1.8, turbulent intensities of

0.5-20% and blowing ratios of $Br=0.2-2.5$ were tested. The results indicated, film effectiveness at high and low turbulence levels was most similar when plotted against momentum flux ratio. Fig 2.4 is reproduced from this study.



(a)



(b)

Figure 2.4: Comparisons of laterally averaged film effectiveness for different DRs on the pressure side of the vane for (a) $Tu = 0.5\%$ and (b) $Tu = 20\%$ [22]

Momentum flux

The momentum flux ratio is essentially a velocity weighted blowing ratio and is defined as follows:

$$I = \frac{Br^2}{Dr} = \frac{(\rho U^2)_c}{(\rho U^2)_\infty} \quad (2.3)$$

Jet detachment is primarily a function of momentum flux ratio. Therefore, at moderate to high blowing ratios ($Br > 0.5$) where the coolant jet begins transition to a detached state, momentum flux is the most appropriate for scaling centerline effectiveness at different density ratios [21].

Injection angle

This represents the angle of the jet relative to the cross flow stream. The injection angle has a significant effect on film cooling performance. Cooling holes are typically angled at 20-35 deg to the surface, with the intention to promote attached cooling jets. For increasing injection angles the normal component of the jet momentum increases. This produces a coolant jet which is susceptible to jet detachment, resulting in a reduction of film effectiveness. [23] investigated a single row of cooling holes with injection angles of 35 and 55 deg. For the 55 deg holes a reduction in film effectiveness of 10% and 30% for momentum flux ratios of $I=0.16$ and 0.63 respectively. This reduction in effectiveness can be considered conservative, as the effective porosity was not matched in this study. The increased turning of the coolant flow required by the shallow angled 20 degree hole, will result in a lower discharge coefficient. Therefore, not only is the 55 deg hole producing reduced film effectiveness, it

also passes more coolant for a given pressure drop. Studies by [24], [16] have reported similar trends in effectiveness reduction by using shallow angled injection. The injection angle is not restricted to the stream-wise direction, studies by [7] [25] [13] and others have also considered the case where some spanwise angle is also introduced to form a compound angle. Fig 2.5 below shows a typical compound angle setup.

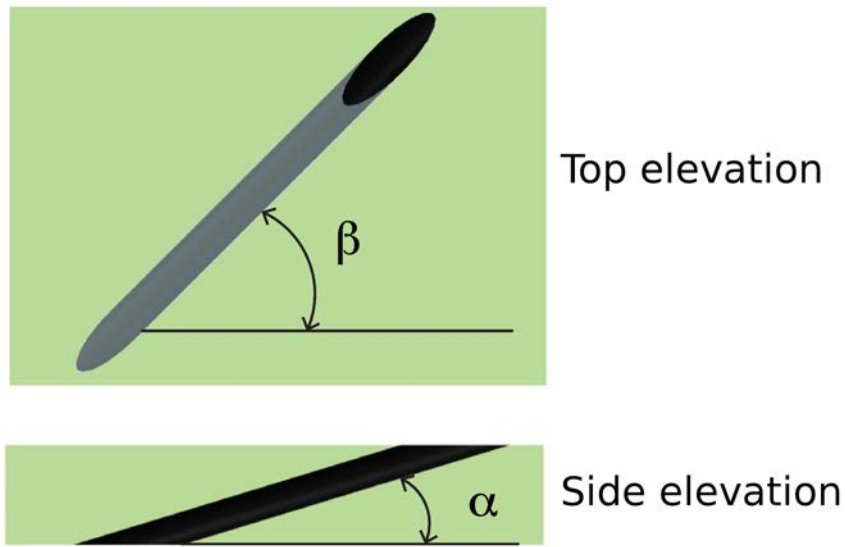


Figure 2.5: Definition of inclination and flow orientation angle

The primary purpose of using compound angled jets is to promote the spreading of the film coolant in the spanwise direction. A study by [25] used PIV to investigate the flow structure of compound angled film cooling. In this study it was shown that the CRVP becomes highly asymmetrical with one of the vortex structures merging into the boundary layer. This then causes the boundary layer to pile-up on one side at the expense of the other causing thinning. This thinning actually reduces the local effectiveness, but

when global effectiveness is considered the additional spreading of the jet caused a net increase in the film effectiveness. Apart from additional manufacturing complexity there are also some aerodynamic penalties which are incurred by using compound angled holes. Increasing angles of inclination or orientation results in increased losses at the hole entry, which decreases the discharge coefficient [26]. The surface heat transfer coefficient is also increased due to the stronger interaction with the mainstream. Therefore studies which have investigated compound injection have also considered the heat flux reduction (HFR) in order to quantify the counteracting effects. A study by [7] measured the normalised heat transfer coefficient $\frac{h_f}{h_o}$ and the resulting heat flux reduction for 0 and 60 deg compound angles. Results indicated a 15% increase in heat transfer coefficient with a 60-deg compound angle. Comparisons of the HFR shown in Fig 2.6 produced similar values for both compound angles, indicating that the improved effectiveness is negated by the augmented heat transfer coefficient. This highlights the importance of knowing both adiabatic effectiveness and heat transfer coefficient for evaluating film performance.

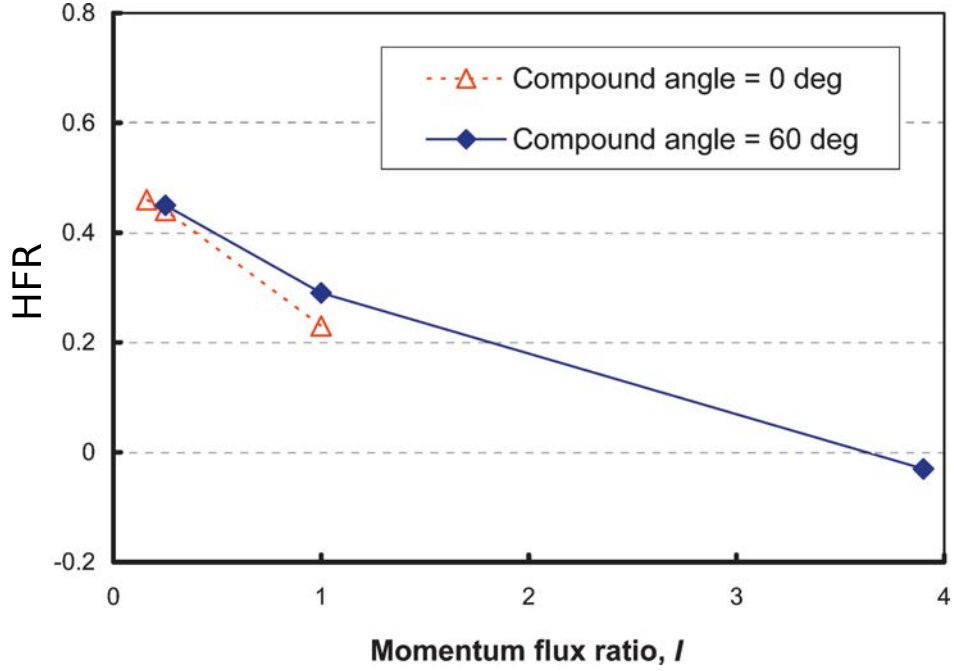


Figure 2.6: Variation of HFR with momentum flux (I) [7]

Hole exit shape

This parameter represents one of the primary advancements in discrete film cooling technology in recent years. The use of shaped holes was first applied to military engines and then commercial engines. An extensive review of previous work on shaped film cooling holes is given by [27]. By shaping the hole with a diffusing type exit it is possible to increase the spread of coolant in the lateral direction. The spreading of the jet also reduces the jet momentum which allows the coolant to remain attached to the surface at typical blowing ratios found in gas turbines (i.e. $1.0 \leq BR \leq 4$). Studies by [28] and [29] have shown that increasing blowing ratio improves the film effectiveness. The diffusing section is often confined to the last 20-50%

of the wall thickness to maintain sensible stress concentration factors. By shaping the exit hole it is possible to expand the exit area by a factor of 2-3 in comparison with a plain circular jet. Two typical examples of fan shapes used on for cooling turbine blades surfaces are shown in Figure 2.7 below.

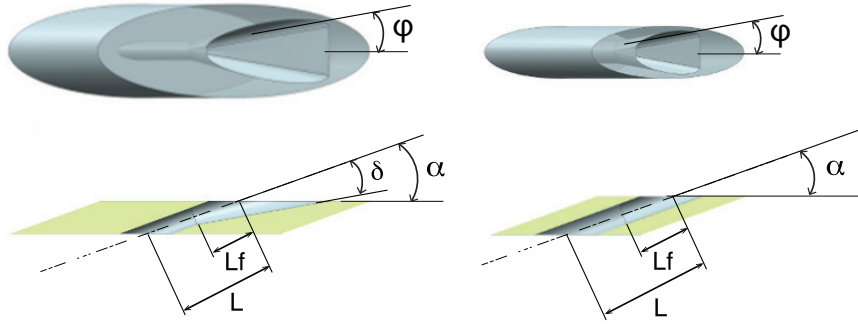


Figure 2.7: Various hole shape definitions [27]

A study by [30] compared laid-back fan shaped holes with cylindrical cooling holes on vane end walls. It was shown that the area averaged film effectiveness of the fan shaped arrangement was able to improve the film effectiveness by 75%. Another benefit was reduced sensitivity to turbulence intensity with an increase in Tu 1.2% to 8.9% resulting in 6% reduction in effectiveness. In a similar study by [28] laid-back compound angled fanned holes were compared with simple cylindrical holes. This study also reported an increase in film cooling effectiveness of around 45% at blowing ratios of $Br \approx 4$. This improvement was a result of reduced jet penetration into the cross flow, increased coolant diffusion (spreading), lower velocity gradients because of increased exit area and greater injectant concentration near the coverage surface. However, while shaped holes provide improved performance

over standard cylindrical holes, the fan shaped holes are approximately four to eight times more expensive to manufacture. This makes the use of fanned effusion unattractive for combustor liner applications because the large arrays of cooling holes would add significant cost to the liner component.

Free stream turbulence and length scale

The introduction of turbulence into a flow generates eddies of many different length scales. Most of the kinetic energy of turbulent flow is captured in large scale structures. The influence of these structures, in particular the larger length scales, is not well understood. However, evidence of the impact of small scale structures on film cooling was investigated in early studies by [31], [32] and [33]. Various turbulence generating grids were used to investigate the effects of both turbulence intensity and length scale on angled cylindrical film cooling holes. The free-stream turbulence intensity ranged from 0.3-20.6% with length scales of $\frac{\Lambda_x}{D}=0.06-0.33$. It was found increasing turbulence intensity improved centreline effectiveness at higher blowing ratios. This was due to enhanced mixing of the coolant and mainstream air, which resulted in a smaller penetration of the jets into the hot gas flow. This trend has been reported by numerous other studies [18], [34] and [35], which also found significant increases in lateral effectiveness as the jet spread out. It was also reported that for low turbulence intensity the larger length scales produced a more uniform distribution of effectiveness in the lateral direction. It was argued that larger scale structures reduced the effect of the counter-rotating vortex.

A study by [36] investigated the effects of free-stream turbulence on heat transfer coefficient and heat flux reduction. At elevated free-stream turbulence levels up to $Tu=18\%$, similar distributions of normalised HTC h_f/h_0 were observed when varying the free-stream turbulence. This indicates mainstream turbulence has little effect on the mechanisms responsible for the increase in heat transfer rate associated with film cooling. Other notable studies include those of [37] and [38] which have used a combination of laboratory-based combustor simulators and passive grids to generate a range of turbulence intensities and length scales. These studies considered the heat transfer characteristics of a nozzle guide vane in response to high freestream turbulence. In all of the test cases reported, elevated turbulence levels led to augmented heat transfer. The turbulent length scale was varied by using grids for small scale turbulence ($Tu=7.6\%$, $\frac{\Lambda_x}{D} \approx 1.29$) and a combustor for large scale turbulence ($Tu=8.8\%$, $\frac{\Lambda_x}{D} \approx 3.3$). The results indicated an earlier transition to turbulent flow and increased heat transfer at smaller scales.

A more recent study by [39] investigated the effects of turbulence intensity ranging from $Tu=3.6-11\%$ and length scales of $\frac{\Lambda_x}{D}=2.1-3.5$ on angled shaped film cooling holes. This study found that the gains in effectiveness at high blowing ratios and free-stream turbulence levels observed for cylindrical holes, does not exist for fan-shaped holes. This is because the lateral spread of the coolant is already enhanced, therefore there is no potential to improve coolant spreading by the action of increased turbulence. Consequently elevated free stream turbulence can only result in reduced film cooling ef-

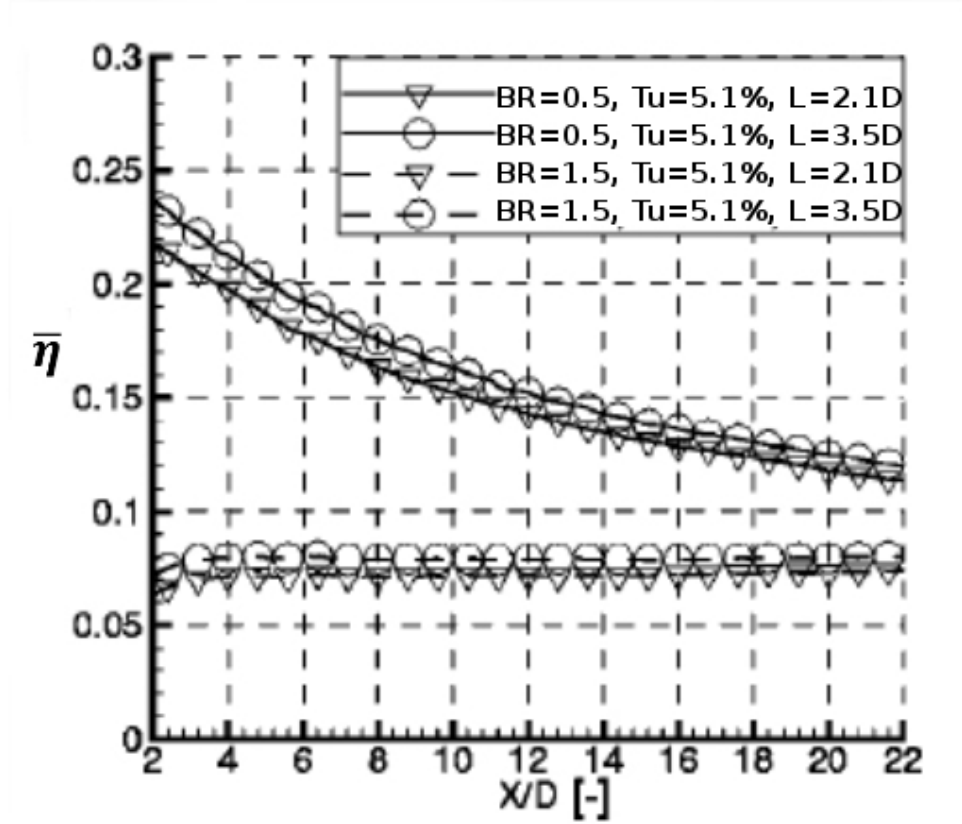
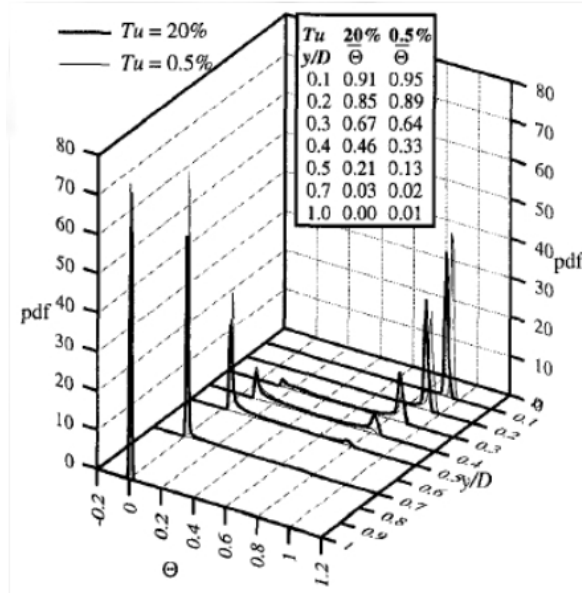


Figure 2.8: Laterally average film effectiveness [39]

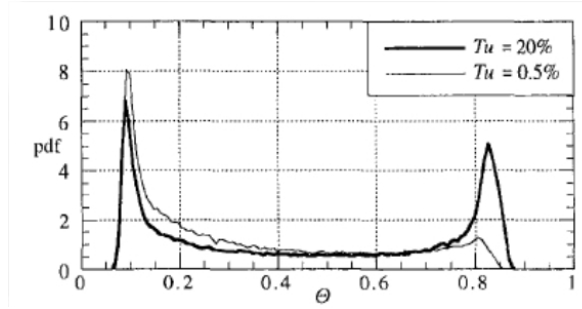
effectiveness for all blowing ratios. Additional tests were performed with a constant intensity of 5.1% and length scales of $\frac{\Lambda_x}{D}=2.1-3.5$. Similar results to the earlier study by [31] and [32] were produced with increases in length scales improving the lateral film effectiveness. It has been observed that the length scale effect was small in comparison to changes in turbulence intensity. This is shown in Fig 2.8 reproduced from the study.

A more detailed analysis of the jet interaction with the mainstream was conducted by [35], who investigated the physical mechanisms which cause

the rapid dispersion of cooling films at high and low free stream turbulence levels. The report suggested for low free stream turbulence (0.5%), turbulent mixing and dispersion of the coolant are primarily driven by large scale turbulent structures. These are generated by large shear layers between the mainstream and the coolant jet. For the higher free stream turbulence case (20%), the shear layer generated by the turbulence is quickly superseded by large-scale turbulent structures from the free stream, which were typically $\frac{\Lambda_x}{D}=6$. The free-stream fluid then penetrates through the core of the coolant jet, all the way to the wall. Consequently the turbulent mixing becomes more complicated. This was shown in the non-Gaussian pdf (probability density function) distributions of temperature. The pdf gives an insight into the nature of the turbulent transport by indicating the fraction of time it takes a fluid of a certain temperature to pass through a point in the flow. Fig 2.9 shows that the high-turbulence case contains intermingling of distinct elements of both the free stream and the coolant jet. The sharp peak at $\Theta \approx 0$ indicates a very narrow range for Θ which is essentially the steady mainstream temperature. Figure 2.9(b), indicates colder near wall temperatures for $Tu=20\%$ and it is suggested that this is a direct result of turbulence ejecting coolant fluid away from the wall. Whilst the turbulence intensities in this study are relatively low (20%), it reveals that the process of coolant dispersion differs greatly between high and low free-stream turbulence levels.



(a)



(b)

Figure 2.9: Variation of pdf

(a) on the jet centreline X/D ; (b) detail plot at $y/D=0.4$ [35]

Effusion array cooling

The current cooling schemes used in combustor effusion designs are usually based around staggered arrays of very shallow injection holes. In comparison

to single-row discrete hole film-cooling the reported work on effusion arrays is somewhat sparse. Attempts have been made to extrapolate single row data to the multi-row case with limited success. An early study of effusion arrays by [40] evaluated the surface effectiveness at low blowing rates of 0.15-0.5. They found that the laterally averaged effectiveness for the first 3 rows could be accurately predicted, by applying the Sellers Super Position model [41] to single row data. Downstream of the 3rd row, superposition tended to over predict effectiveness. A similar result was reported in a more recent study by [42] which considered short normal effusion holes. Fig. 2.10 has been reproduced from this study.

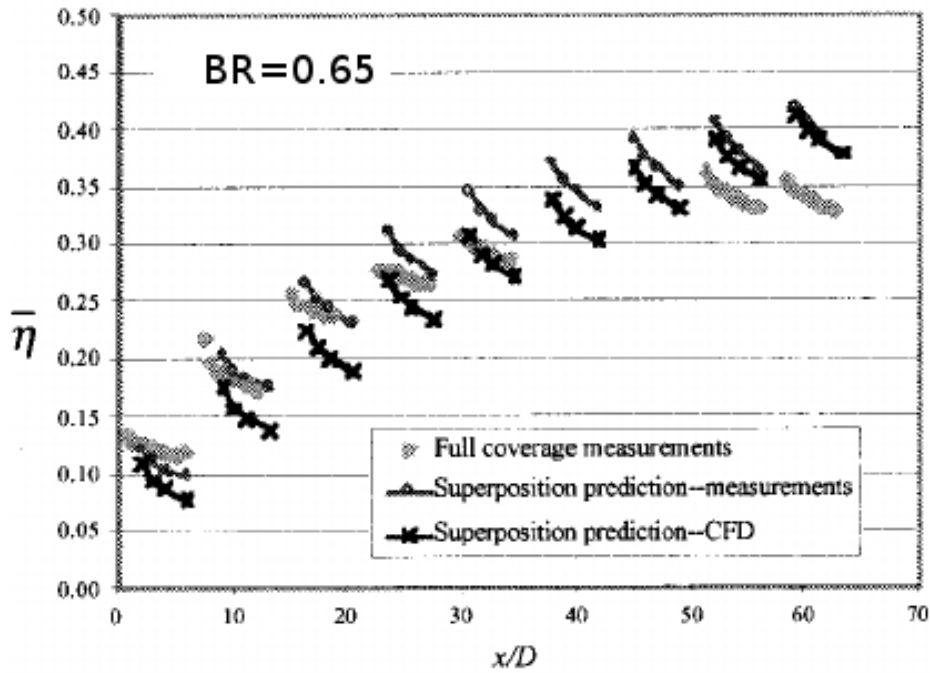


Figure 2.10: Superposition predictions using experimental and CFD single row baselines. Low mainstream turbulence, $Tu = 0.005$ [42]

It was argued that the superposition model does not include the row-to-row interactions which limit adiabatic effectiveness. Consequently the asymptotic behaviour shown in the experimental data is not shown in the superposition model. Further evidence of the impact row-to-row interaction has on film development has been demonstrated by [43] in which a 4 row effusion array is investigated with a very low injection angle of 17 deg. Adiabatic effectiveness measurements were made over a blowing ratio range of 0.5-4. Their results indicated significantly different flow patterns depending on cooling jet blowing ratio.

The studies that have considered the cooling performance of combustor-relevant effusion cooling, have done so without directly addressing the issue of high free-stream turbulence. For example, a parametric study by [3] measured the temperature distributions of effusion cooled arrays across a range of blowing ratios, density ratios, hole spacing and inclination angle for a nominal freestream turbulence $Tu=1\%$. A study by [15] has considered the aerodynamics of an angled effusion array consisting of 972 holes in the presence of a fuel injector induced flow field. Interchangeable injectors allowed the swirl angle to be varied. The work of [44] presented detailed velocity profiles and adiabatic effectiveness measurements of an effusion array operated over a range of blowing ratios at $Tu=10\%$. More recently, the work of [45] and [46] have considered a combustor representative geometry that includes slot-style starter films and dilution ports. Note that in general these studies have not directly isolated the impact of free-stream turbulence on effusion cooling as an independent parameter.

2.3 Turbulence generation

A key component of this experiment is the design of a turbulence generator capable of producing a range of turbulence intensities and length scales. There are a number of different methods that have been used by previous studies. These can be categorised into jets in cross flow, passive and active grids. A brief review of the techniques are covered in the following section.

Passive grids

Passive grids represent one of the simplest methods of turbulence generation. The turbulence is generated by a relatively coarse grid with solidities of typically 0.3-0.4, which is placed normal to a uniform upstream flow. The effect of the grid on the flow can be considered in separate components, a manipulation effect and a wake effect. The manipulation effect consists of a process where the spectrum of the turbulence is altered, which reduces or increases the scale of the upstream turbulent eddies relative to the grid dimensions. The wake effect consists of another process which contributes turbulent energy to the downstream flow field. This energy, however, is of relatively high frequency and as a result, tends to decrease the scale of the upstream turbulent eddies [47]. The turbulent energy generated by this method decays downstream from the grid as the turbulent energy is transferred from large eddies into small eddies by the process of vortex stretching. While the turbulent energy decreases, the eddy scales increase in size with downstream distance. An approximation of the turbulence energy distribution can be calculated by using the following correlations developed by Baines and Peterson

[48].

$$T_\mu = C \left(\frac{x}{d} \right)^n, \Lambda_x = A.d \left(\frac{x}{d} \right)^m \quad (2.4)$$

Where T_μ is the streamwise component of the turbulence intensity, x is the streamwise distance from the grid and d represents the rod diameter or bar width. The constants C , and A are dependent on grid geometry and Reynolds number. The exponent n is typically $-5/7$ and m ranges between 0.5 and 0.56 according to published data. Fig. 2.11 shows plots of grid generated turbulence distribution using a curve fit based on the formula above.

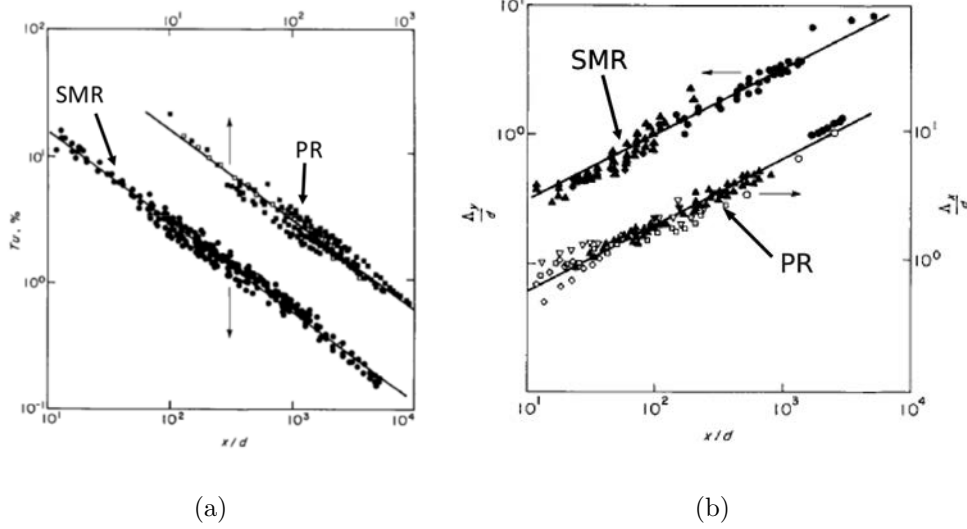


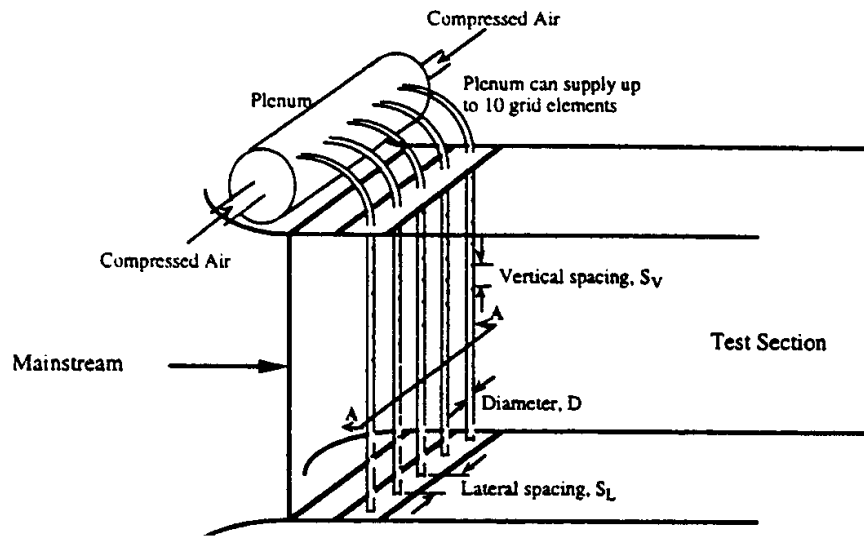
Figure 2.11: Streamwise turbulence intensity decay of
(a) square mesh rods (SMR) and parallel rods (PR); (b) Integral scale
growth downstream of grids [47]

Figure 2.11 shows the corresponding dispersion in length scale as the flow progresses downstream. For the purpose of experimentation, turbulence conditions can be varied to a degree by placing the grid in different

upstream locations. Generally using grids alone to generate turbulence intensities $>10\%$ is difficult in a low speed wind tunnel. However, passive grids can be used to generate higher levels of turbulence by using a high pressure blow down rig. An early study by [49] used perforated plates to generate turbulence levels of up to 45% . A recent study by [50] used this arrangement to generate turbulence intensities of 16% using a passive square mesh turbulence grid. The length scale was reported as $\frac{\Lambda_x}{P}=0.26$ based on a turbine vane pitch of 83mm . Both intensity and length scale showed good uniformity in the spanwise direction with variations of 2% and 0.6% respectively.

Active grids

Active grids use hollow bars or rods with evenly spaced holes. The rods are then supplied by air which is injected into the mainstream flow to enhance turbulence generation. An early study using active grids can be found in [51], who used parallel bars with holes, which could inject jets in either the upstream or downstream direction relative to the main flow. It was shown in this study that a weak up stream injection could actually reduce turbulence in comparison to a passive grid. However, increasing the mass flux of the injection above 5.5% results in increased turbulence as the additional shear created by the jets becomes significant. At the maximum flux injection rate of 8% a turbulence level of $Tu=6\%$ was produced. In a similar study by [52] turbulence intensities of $Tu=20\%$ with integral length scales of $\frac{\Lambda_x}{D}=8$ were generated, using an array of vertical rods with diameters of $\phi 38\text{mm}$ spaced 85mm apart.



Detail of Section A-A

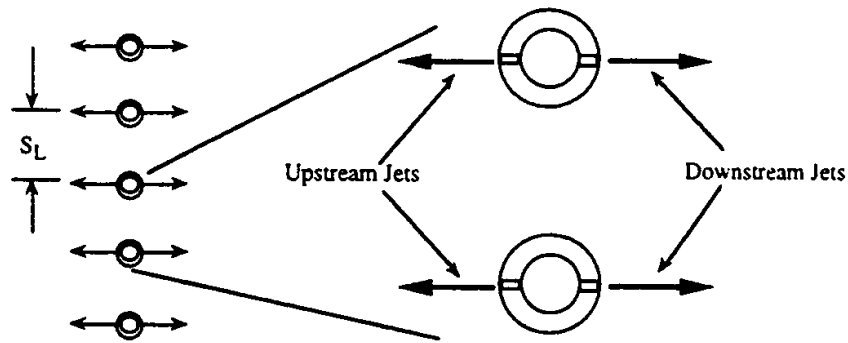


Figure 2.12: Schematic of turbulence generator design and a close-up of the jet hole geometry [33]

As with the passive grid arrangement, early blown grids still had very limited control over the turbulent length scale. The first study to introduce length scale control over blown grids was [33]. In this apparatus hollow bars with adjustable lateral spacing were adopted to provide control over the length scale. A schematic of the turbulence generator is shown in Fig. 2.12.

During the development of this generator it was found that the momentum flux added by the jets caused non-uniformities in the mean flow greater than $\pm 10\%$. The uniformity was improved by injecting flow simultaneously upstream and downstream. By injecting the flow downstream the wake area behind the bars was filled which improved flow uniformity. The ability to adjust the lateral spacing proved a very effective method of controlling length scale. A length scale range of $0.4 < \frac{\Lambda_x}{P} < 0.64$ (based on a turbine vane pitch of 85mm) at a turbulence intensity of $Tu=20\%$ and a mean flow uniformity of $<6\%$ was created. Analysis also showed that the generation of very large length scales is limited by the rod spacing-to-diameter ratio $\frac{S}{d}$ with $\frac{S}{d} > 15.9$ resulting in poor uniformity. Therefore larger length scales must be attained in a similar method as the passive grid by placing the test section further downstream.

As a method of turbulence generation, active grids with adjustable pitch spacing allow both length scale and turbulence intensity to be varied independently. A potential drawback of this system is the need for a high pressure delivery system. Moreover, for transient heat transfer problems it would be difficult to match free stream and jet temperatures.

Jets in cross flow

This technique works by placing a series of jets normal to the mainstream flow. The amount of turbulence created depends on the jet-to-mainstream velocity ratio and Reynolds number. As the Reynolds number increases,

a higher jet-to-mainstream velocity ratio is required to generate the same level of turbulence. This technique was pioneered by [53], who used this method to generate Tu levels from 5 to 25%. A study by [54] also used this method to generate turbulence intensities of up to 20% with length scales of $\frac{\Lambda_x}{D}=7.7$ at 1.2m downstream of the jets. Spanwise and vertical velocity was uniform within $\pm 4\%$ and $\pm 5\%$ respectively, while RMS velocities were uniform within $\pm 9\%$. Fig. 2.13 shows a schematic of the test section. This generator also includes a splitter plate, which is required to prevent the jets interacting with each other and creating a non-uniform bulge in the velocity field downstream. Further improvement of the velocity uniformity were made by [42], which involved placing a full length cylinder at the end of the splitter plate. Turbulence levels up to 20% were achieved with length scales of $\frac{\Lambda_x}{D}=3.9-5.9$. One advantage of this method is that it is relatively simple to construct and supply air at the same temperature can be drawn from downstream locations. Turbulence decay rates are generally less than grid generated turbulences, especially at lower turbulence levels $T_u < 10\%$. However, length scale cannot be independently adjusted without physically changing the jet hole spacing.

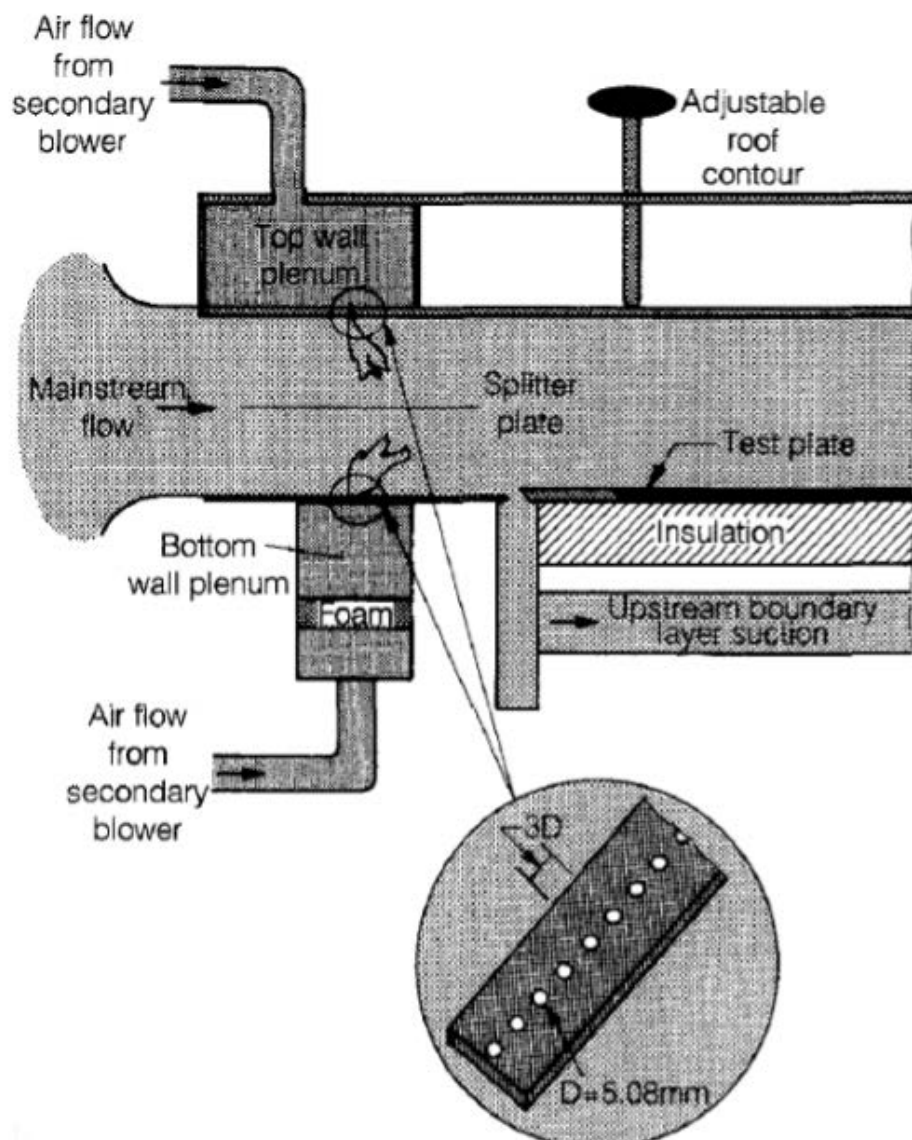


Figure 2.13: Schematic of wind test section with cross flow jets [54]

2.4 Summary

The research detailed in the proceeding sections has broadly covered the main parameters that affect film cooling performance. While general conclusions drawn from single row studies can be applied to multi-hole arrays, an area which is lacking is the performance of effusion arrays under high freestream turbulence. Some research has been performed into the effects of freestream turbulence and it is generally acknowledged that freestream turbulence reduces the cooling performance. However, the vast majority of work in this area has been conducted at intensity levels of up to the mid-teens percent, which is considered typical of combustor exit / turbine inlet conditions, usually with just a single row of cooling holes. While this gives a useful insight into the influence of freestream turbulence, more work is required to establish the performance of cooling arrays at combustor representative conditions. In addition, the characteristic length-scale of the free-stream turbulence has rarely been considered as an independent parameter. Moreover, those cases that have addressed this, have generally considered relatively small turbulent scales. In addition, the review of turbulence generation systems highlights the difficulties of producing a uniform, highly turbulent flow field. There is also no clear method of independently controlling the turbulent length scale. Therefore, the development of a suitable turbulence generation system will be a key feature of any new test facility used to study the physics of engine representative film cooling schemes.

The mode in which the coolant jet operates (attached or detached) has

a significant influence on the film cooling performance. To some extent the influence of all film cooling variables can be distilled into the impact they have on the jet mode. The most effective method demonstrated by a broad spectrum of researchers, is to apply some diffusion before the hole exit plane. Using current manufacturing methods many of the shaped cooling holes investigated can only be created by expensive laser ablation techniques. This limits their use to turbine applications where the high mechanical and thermal stresses justify the additional expense. Many of the studies in this area compare different hole designs without consideration of the effective porosity. This makes the direct comparison of cooling schemes difficult, as each cooling scheme will pass a different amount of coolant for the same pressure drop. Therefore, the development of a diffusing cooling scheme, which can be made more cheaply with similar performance to a porosity matched turbine based fan is required. This would potentially offer significant improvements over plain hole effusion without a disproportionate increase in manufacturing costs.

Chapter 3

Experimental apparatus and techniques

In this chapter the test facility and effusion test plate designs are discussed in detail. A re-circulating wind tunnel capable of generating combustor relevant flow conditions was built and commissioned. A turbulence generation system was developed, which was capable of generating turbulent free-stream levels measured within a typical aero combustor. The coolant to mainstream density ratio was created by imposing a temperature difference between the free-stream and coolant flow. The coolant flow temperature was reduced by a turbo expander system based around an automotive turbo charger. Large scale effusion test plates have been constructed for the investigation of plain and fanned hole effusion.

3.1 Experimental test facilities

In the modern combustor environment temperatures may peak at over 2000°C , which is considerably higher than the melting points of the materials the combustor liner is manufactured from. In fact, for the nickel or cobalt based alloys in common use, a rapid decrease in mechanical strength occurs as temperatures exceed 1100K [4]. In addition to the mechanical requirements, the cooling scheme must also be efficient, for the reasons mentioned in chapter 1. Therefore, the designer requires detailed knowledge of how cooling schemes perform in the combustion environment. The primary measure of film cooling performance is the film effectiveness η , as this has a dominating effect on the resulting heat flux reduction [14]. Early studies have shown that results obtained from simple flat plate models can be applied to real engine designs with only slight corrections [55]. It is this type of information therefore, that is required by the designer to predict metal temperatures and service life.

The behaviour of a film cooling arrangement is complicated by the particular free-stream conditions that are usually present. Namely, highly turbulent swirling flows and the presence of relatively large diameter dilution jets. In general, for a particular wall geometry, the film cooling situation can be characterised by the coolant and free-stream flow conditions: velocity ratio, density ratio, Reynolds number and turbulence level. Each of these factors is not necessarily independent of the other. For example an increase in free-stream turbulence can in some cases increase the film coverage depending on blowing ratio as reported by [31, 32]. Therefore, any combination of these

factors can potentially change the film cooling performance. Hence, the inherent difficulty in accurately predicting film cooling performance. In order to establish a fundamental understanding of the many variables that affect film cooling performance and avoid generating data which is very specific to a particular scheme, experimental tests are required that isolate the effects of different variables. Much of the previous literature reflects this with test facilities providing some degree of independent control of the main flow properties.

In general the test facilities fall into two main categories: steady state and transient, with each type offering advantages/disadvantages depending on the intended measurement techniques and required data. The steady state type require relatively powerful fans to drive the main flow, while a typical blow down facility can be run with a relatively small compressor and receiver tank setup. The main advantage of transient facilities such as [50] with respect to heat transfer measurements is, the ability to adjust temperatures of both solids and fluids, without taking serious account of conduction errors in the short duration test. For steady state test facilities, such as those used by [42], [25] and [30], much longer measurement times are possible. This is necessary for application of more detailed flow field measurement techniques such as temperature traverse and particle image velocimetry (PIV).

There are two main sub components of the test facility which have a major impact on the appearance, capability and cost of a film cooling test rig: free-stream turbulence generation and density ratio. The free-stream turbulence

level is often not fully realised, mainly because of the difficulty in generating sufficiently high levels ($>20\%$). This parameter holds particular importance in combustor liner cooling as turbulence levels are high throughout this engine component. Moreover, the free-stream turbulence and coolant mass flux are the two coolant/mainstream variables which dominate the cooling performance [14]. There are numerous approaches to generating turbulent free-stream conditions as identified in chapter 2, with the method often determined by the facility type and the intended turbulence level. Some studies also include free-stream swirl, with work by [56] and [57] using laboratory based combustor simulators. In the engine environment, the density ratio between the coolant and mainstream flow varies throughout the combustion chamber, with localised near wall regions as low as 1.4. Further away from the liner wall, ratios of up to 3 occur in civil engine applications. To cover these conditions experimentally in a lab environment is very difficult because even at large scale factors (>10), large temperature differences are required to generate engine representative density ratios (at atmospheric conditions). Previous studies have used foreign gases [58], [20] or a combination of heating and cooling [22].

Facility Overview

A schematic of the test facility is shown in Fig. 3.1. Essentially the facility is a recirculating wind-tunnel driven by a radial fan. As flow is circulated around the tunnel, an in-line 50kW electrical flow heater is used to set a variety of free stream temperatures up to 100°C . In order to generate engine representative

turbulence properties, a 'jets in cross flow' turbulence generator is employed. The effusion coolant holes are fed via a turbo expander system which is capable of lowering the coolant delivery temperature by 40°C below ambient conditions. Flow conditions are continuously monitored and recorded by a bespoke data acquisition system. These features allow for the systematic experimentation into the effects of free-stream turbulence conditions, blowing ratio and density ratio on effusion cooling performance. The test-section of this facility is equipped with instrumentation that permits the measurement of: adiabatic wall cooling effectiveness (spatially resolved), spatially resolved measurements of local flow temperature (coolant/free-stream mixture fraction), flow velocity/turbulence parameters and non dimensional heat transfer coefficient. The following sections cover in detail the design decisions made during the development of the test facility.

Rig scaling

To establish an appropriate experimental scale, a balance between cost and what is experimentally important must be drawn. As indicated at the start of this chapter, the designer requires detailed performance data at 'representative flow conditions'. From the review of previous research covered in chapter 2. It is apparent that there are a large number of parameters involved. However, from a rig scaling point of view, the main parameters to consider are the coolant delivery conditions: blowing ratio (BR), Reynolds number (Re), density ratio (DR) and the free-stream turbulence intensity (Tu) and Length scale (Λ_x). These parameters set the flow requirements of

the main tunnel circuit and the coolant delivery system. With this information the wind tunnel can be sized and specified in detail.

The flow rate through the cooling holes is a strong function of the combustion system pressure drop. This system pressure drop consists of two main sources, pressure drop in the diffuser and the pressure drop across the liner wall. Under burning conditions, this pressure loss would be augmented by the fundamental loss due to combustion, which is relatively small ($\sim 1\%$ of the cold loss). Hence, the cold pressure loss is often quoted and can be measured with reasonable accuracy from cold flow tests. The values are normally given as a percentage of the compressor exit total pressure, with typical values ranging from 2.5 to 8 % [4]. In terms of coolant blowing rate (BR), the liner architecture plays a significant role. Fig. 3.2 shows a typical arrangement of dual and single skin architecture. For dual skin liners which employ impingement effusion configurations (such as the European Gas Turbine (EGT) G30 DLN combustor and the Rolls Royce Environmentally Friendly Concept Engine (EFE)), blowing ratios in the lower range of 0 - 2 would be expected, since a large fraction ($\sim 50\%$) of the pressure drop would be used in the cold side impingement cooling process. For single skin arrangements, where the entire liner pressure drop is used to drive the effusion holes, much higher blowing ratios of the order 5 - 9 would be expected. Recent examples of single skin focused studies can be found in [59], [60] and [61].

The bulk axial velocity through the combustion chamber for both types of architecture typically falls within 30-60m/s [4]. At engine scale, cooling holes are of the order ϕ 0.7mm and applying the engine cycle conditions of a Pratt & Whitney JT9D [1] as an example, the free-stream Reynolds number is in the range $Re_D = 3100 - 6200$. The coolant hole Reynolds number would be of the order $Re_j = 30 \times 10^3$, depending on the blowing ratio being considered. These Reynolds numbers provide guidance on the flow rates required of the facility to generate data which can be matched to engine operating conditions.

The mixing processes in the combustion zone are of high importance, especially in the primary zone where good mixing is essential for efficient combustion. Civil combustors typically use hydrocarbon based liquid fuels which are atomised by the fuel injectors to deliver a fuel spray into the primary zone. The air speed at which combustion can occur is limited by the flame speed. For turbulent flames formed from hydrocarbon fuels, this speed is limited to about 5-8m/s and is reduced further to 0.3 m/s for the laminar case. To stabilize the flame and prevent extinction, a recirculation zone is set up by swirling flow around the fuel spray. This process also generates the high levels of turbulence required to increase the flame speed.

There are very few studies which describe the turbulence intensity and length scale of the flow field inside real combustors. Therefore preliminary turbulence measurements were performed on an isothermal 1:1 scale fully annular test facility. The annular test facility simulates the flow through a

full scale combustor under isothermal conditions. The test rig consists of a 1.5 stage axial flow compressor which delivers engine representative profiles of pressure, velocity and swirl angle to a set of full scale outlet guide vane (OGV). A fully featured lean burn combustor is located in the test section downstream together with a complete set of injectors. The injectors set up representative combustor flow conditions under non-combusting isothermal conditions. The combustor has a number of traverse locations which provide access for hotwire probes. To establish characteristic turbulence properties in close proximity to the tile wall, a hotwire traverse was performed. Fig. 3.4 and 3.5 show typical data for turbulence intensity and length scale at 25% tile length. Typical length scales were of the order $\Lambda_x \approx 37D$ with turbulence intensities $>25\%$.

With the main flow parameters and appropriate range identified, the rig scale factor could be decided upon. The selection of a rig scale factor is however, far more general than the effusion plate scale factor. The rig scale defines the testing envelope of effusion plate scales that can be studied in the facility. A rig scale factor of 12 was selected and is based on the corresponding Reynolds numbers of free-stream and cooling jets. At a scale factor of 12, the cooling hole diameters are of the order ϕ 8.5mm. At the free-stream Reynolds range of $Re_D = 3100 - 6200$, the required tunnel velocity range is 5.4-10.8 m/s. Jet Reynolds numbers of $Re_{ej} = 20 \times 10^3$ would be reached at cooling jet velocities as low as 37 m/s for a BR=7. Even at this modest scale factor, the test section height required, based on the combustor height-to-film hole diameter ratio of a typical combustor, is 1.4m. However, to adopt

	Engine	Rig (SF12)
U_∞	30-60m/s	5.4-10.8m/s
Re_∞	3100-6200	3100-6200
Tu_∞	> 25%	\approx 25%
$\Delta L/D$	5-37D	\approx 20D
T_∞^*	\approx 1600K	373K
T_c^*	\approx 800K	250
DR	3 (local 1.4)	\leq 1.5
$Re_j \times 10^3$	\leq 30	\leq 20
BR	0.3-7	\leq 7
<i>Effusion hole ϕ</i>	0.7mm	8.5mm
<i>Combustor Height</i>	200mm (annulus)	650x550mm (cross section)

Table 3.1: Rig scaling summary * based on combustion conditions of Pratt & Whitney JT9D [1]

a test section of this size was not considered since hotwire measurements taken from the lean burn combustor experiments indicated length scales of $\frac{\Delta L}{D} \approx 37D$, since this equates to $\sim 314\text{mm}$, a smaller test section would not prevent turbulent scales of this length being produced. A summary of the final test section dimensions and flow requirements are given in Table 3.1.

3.2 Main tunnel design and construction

Unlike many other film cooling test facilities which have adapted existing wind tunnels, this design allows for a bespoke facility to match the requirements of the test section. In regard to achieving the objectives set for the current research, and after evaluation of the appropriate flow conditions required by the test facility, a closed circuit wind tunnel layout was selected for the following reasons:

i) For tests involving density ratio, a portion of the density ratio change can be created by gradual heat addition into the free-stream circuit, rather than the step change required by a comparable open circuit design. This also allows temperatures to be maintained over long test periods without excessive electrical use. Thus, the required power from the heater can be significantly reduced.

ii) A recirculating design is preferable for flow measurements such as temperature traverse measurements. Temperature traverse data is typically gathered from single point measurements (thermocouples etc), which requires significant run times to acquire data of sufficient density to accurately describe the temperature of the coolant layer.

iii) Steady state conditions are more attainable, as temperatures can be allowed to stabilise over longer time periods.

iv) Isolating the inlet of an open circuit tunnel from its outlet can be difficult. The inlet flow can be affected by the tunnel exit conditions. Particularly when density ratio tests are performed.

Wind tunnel design lies somewhere between an art and a science, with occasional excursions into propitiatory magic [62]. Over the past few decades, wind tunnel design rules have become established which may be used to set appropriate diffusion rates, screen blockage ratios and contraction ratios with a reasonable level of confidence in the resulting flow conditions. The con-

ventional layout of a closed circuit wind tunnel is shown in Fig. 3.3. The main components consist of the test section, diffuser, wide angle diffuser, settling chamber, contraction and fan. While the test section shape is totally dependent on the requirements of the experiment, the length or minimum length is fixed by the settling distance required to achieve homogeneous flow. Typically test sections have length-to-diameter ratios of 2 or more [63]. Designed correctly, the diffusing sections of the tunnel allow static pressure to be recovered which reduces the total pressure rise required from the drive fan.

In the example shown in Fig. 3.3, the diffusion is split into two parts by the tunnel. The diffusion angle is usually within the range of $2\text{-}3.5^\circ$, with the smaller angle being more desirable. Higher angles are avoided, since flow separation can occur which causes unsteady pressure recovery and total pressure loss. This can lead to vibrations, oscillating fan loading and surging through the test section. The purpose of the wide angle diffuser is to rapidly increase the cross sectional area to reduce flow velocity so that conditioning techniques can be applied without significant pressure loss. Wide angle diffusers can be designed using charts developed by [64] which define the diffuser in terms of four parameters: area ratio, diffuser angle, number of screens and total loss coefficients. Typical properties are angles of 45° with area ratios 2-4. The wide angle diffuser is then followed by a settling chamber, containing honeycomb sections which are used to align the flow axially before the screens. Once aligned, a number of screens are used to improve flow uniformity by imparting a controlled pressure drop. The flow resistance of a wire screen is approximately proportional to the square of its speed.

Therefore the flow velocity becomes more uniform upon passing through the screen. The length of the settling chamber is constrained by the number of screens. Generally a combination of spacing equivalent to about 0.2 of the settling chamber diameter performs adequately [64]. Finally the air is passed through a contraction, that serves two main purposes; It increases the mean velocity and reduces both mean and fluctuating velocity variations to a smaller fraction of the average velocity. Typical area ratios range from 7-12.

This type of design is fundamentally aimed at producing low turbulence flows with minimal circuit pressure loss. This produces a highly flexible facility which can be adapted to perform a whole range of experimental studies. Whilst it is attractive to build a facility of this type, the inclusion of all these features is not possible or necessary for the current design. Indeed, for this experiment the laboratory space available was limited to 9.5m x 3m, which restricts the amount of diffusion possible as diffusion angles are limited by flow separation criteria cited earlier. This inevitably led to a high pressure loss design. The constraint of pressure loss is set by the available pressure rise from the fan. Axial fans have efficiencies of order 90% and are suited to low pressure high volume applications (high specific speed duties). Centrifugal fans are more suited to supply lower flows at high pressures (low specific speed duties) and are able to operate over a much wider range of flow conditions because the whole blade span operates at nominally the same lift coefficient. Therefore a combination of a centrifugal fan and high pressure loss closed circuit design provides a solution to lab space restrictions.

Without the emphasis on pressure recovery, flow through the tunnel can be diffused much more abruptly. For this facility the flow is directed around the tunnel circuit by two large plenums. These plenums act as both dump diffusers and settling chambers and remove the need for turning vanes. Generally, larger plenums give the flow more space to settle out and become uniform, both aerodynamically and thermally. Therefore the plenum size was dictated by the available laboratory and was therefore made as large as possible.

All of the main tunnel sections were constructed with rectangular cross sections as this allowed the tunnel components to be fabricated from sheet aluminium. For this wind tunnel, the presence of background turbulence in the test section is not of prime importance, provided the turbulence and velocity profiles are uniform. Therefore turbulence reducing features such as high ratio contractions were not considered necessary. A simple bell mouth arrangement was adopted as shown in Fig. 3.10 with a set of screens located downstream which are spaced on the design rules outlined in [63]. The total test section length is 3.4 m which allows a test plate to be located 1.35m downstream of the final flow control screen (equivalent length-to-diameter ratio 160). Downstream of the test section, an air vent serves to: prevent the tunnel from becoming pressurised as cooling air is introduced into the system via the test plate.

The air flow is then passed into a meter box which enables the mass flow to be calculated via a nozzle and diffuser arrangement. The nozzle dimensions

were tuned to match the differential pressure transducer range and intended flow rates. A sizeable pressure drop is required across the nozzle for accurate mass flow measurement and the diffuser allows some pressure recovery to be achieved. The diffuser has been designed based on the method described in [65]. Details of the nozzle and diffuser design can be found in Appendix A.1.

To provide structural support to the fabricated aluminium plenum sections, aluminium Flex link™ extruded bars are used. This structural system allowed the whole support structure to be assembled from a range of standard components. The principal advantage of this system is that no welding was required and adjustments could easily be made to cope with manufacturing tolerances and design adjustments. Fig. 3.7 shows an early stage of construction of the right hand sub assembly which consists of the drive fan and heater arrangement. During the commissioning phase of the tunnel, pressure transducers were placed in each feed plenum to ensure pressure differentials to ambient were within safe limits. In addition to the experimental requirements, maintenance features such as access panels are also located on the large feed plenums and meter box to allow periodic cleaning during operation. Full detail drawings of wind tunnel components are presented in Appendix A.2.

Heater and drive fan

For the purpose of controlling free-stream density and maintaining fixed operating temperatures, a large 50kW duct heater was selected which is capable

of increasing air temperatures up to 100°C. The power rating of the heater was selected based on approximate conduction losses outlined in Appendix A.3. The heater power is supplied via two 80amp SCR power controllers which are signalled by an Omega™ CNi8 Series PID controller. Feedback is provided by a K-type thermocouple located downstream of the heater unit. This system is capable of maintaining a stable free-stream temperature over a wide range of coolant blowing ratios with free stream temperatures within $\pm 0.5^\circ\text{C}$ in the test section.

The exterior of the tunnel is fully insulated with 50mm of high temperature insulation boards to minimise thermal temperature gradients and heat loss. Photographs of the insulated return circuit and test section are shown in Figs. 3.6 and 3.8. Typically the tunnel requires a run time of 1 hour to reach thermal equilibrium. Fig. 3.9 shows a typical temperature time history in the test section and coolant feed system during the warm up phase. Inevitably, the fabricated aluminium structure experiences thermal expansion during hot tests, therefore three high temperature silicone expansion joints were used to split the tunnel at various locations to cope with the thermal expansion of the rig. An estimation of the misalignment was also made to ensure expansion joints could cope with component tolerances, details are given in Appendix A.5. The expansion joints also serve a secondary purpose as a vibration suppressor, damping the vibrations created by the radial fans. The support structure was also assembled to allow thermal movement of tunnel components by having the minimum number of hard fixing points, particularly on long continuous sections.

The decision to use dump diffusion requires careful selection of a drive fan. In order to select an appropriate drive fan, an estimation of circuit pressure loss was calculated, details of which are shown in Appendix A.4. In order to meet the drive tunnel/test requirements, a high temperature 37kW radial fan was commissioned which is capable of producing a 6kPa pressure rise at a 100°C working temperature. The main drive fan was fitted with an encoder and controlled via a WEG inverter which was interlocked to the heater control system to prevent heater operation at zero flow conditions.

Turbulence generator

One of the main requirements of this test facility was to create highly turbulent free-stream conditions at engine representative values. As indicated in chapter 2, there are a number of different methods which have been employed in earlier studies. These can be categorised into jets in cross flow, passive and active grids. The high free-stream turbulence levels ($> 25\%$) measured in the isothermal annular test rig, make the use of passive grids unsuitable, as generating turbulence intensities $> 10\%$ is difficult in low speed flows. The most promising means of generating such high levels of turbulence is by adopting the jets in cross flow turbulence generator. Indeed, this technique has already been used successfully by Bogard et al [54] to generate turbulence intensities from 5 to 25%. Therefore, this approach has been adopted and developed for this test facility.

The components of the turbulence generator are shown in Fig. 3.11. The supply of air to the turbulence generator is provided by a secondary centrifugal fan which draws air from the upper section of the feed-plenum via internal ducting to prevent distortion of the inlet profile to the test section. The fan then provides a sufficient pressure rise (up to 13kPa) and mass flow rates up to 0.5kg/s to allow the injection of this fluid back into the working section upstream of the effusion plate, through rows of normal jets on both the top and bottom surfaces of the channel. At high velocity ratios, there was a significant rise in air flow temperature due to the compression from the bypass fan. In order to offset the temperature rise generated by the fan, high emissivity pipe work was used to duct the air around the outside of the tunnel to the feed plenums which drive the normal jets (see Fig. 3.11). This minimised the temperature differential between injected and mainstream flows to a maximum of 10°C.

Hot wire measurements

In order to characterise the free-stream turbulence conditions, a constant temperature (CTA) system was used. A CTA operates on the basis of convective heat transfer from a heated sensor (wire) to the surrounding fluid. The convective heat transfer depends on both the properties of the ambient fluid (density, viscosity, conductivity etc.) and the parameters of the flow (velocity vector, fluid temperature, pressure etc.). As the gas flows over the

wire, convection takes place cooling the wire. The system maintains a constant wire temperature (i.e. constant resistance) by varying the electrical energy ($\frac{E^2}{R}$). The voltage across the sensor wire can be related to the flow velocity using the following power law:

$$E^2 = A + BV^n \quad (3.1)$$

Where E is the voltage across the wire, A, B and n are calibration constants and V is the flow velocity. The calibration constants are calculated by placing the hot-wire in a uniform nozzle flow. The flow can then be cycled through a specified range of velocities allowing the relationship between voltage and velocity to be established. A more detailed description of the hot-wire calibration process and signal analysis can be found in [66].

As indicated in this section, the convective heat transfer of the hot-wire forms the basis of the measurement technique. Therefore, factors that affect this mechanism, may act as source of error and reduce the accuracy of the velocity measurement. A side effect of this type of turbulence generator adopted here was the potential to impose temperature fluctuations within the free-stream, caused by the temperature difference between the cross flow jets and the free-stream. Temperature variations in hot-wire measurements can impose significant measurement errors, as the heat transfer is directly proportional to the temperature difference between the sensor and the fluid. The error in measured velocity is approximately 2% per 1°C change in temperature. Therefore, before the main development of the turbulence

generator could take place, evaluation of the temperature fluctuations in the free-stream at the test section location was carried out. In order to assess these fluctuations, a 5 micron Dantec 1D hot-wire was operated as the cold wire in constant current mode. The probe was driven by a constant current bridge together with a high gain (x100) signal amplifier. The current driving the cold wire was typically 0.7ma, which was sufficiently low to minimise the ohmic heating effect. The analogue signal from the amplifier was then split into DC and AC components, then filtered and digitized using a National Instruments SCXI 1305 card. The AC signal was then converted into a fluctuating resistance. The relationship between wire resistance and temperature can be approximated via the linear relationship:

$$T = \frac{R}{\alpha \times R_{20}} \quad (3.2)$$

Where α represents the temperature coefficient of resistance and R_{20} the resistance of the wire at 20°C. Data was sampled at 1kHz for 20 seconds with a cut off frequency of 500Hz. In order to verify the performance of the cold wire, the probe stem was fixed with a fine wire thermocouple in a 'piggy back' arrangement so that a comparison of both signal responses could be made. Fig. 3.13 shows the raw signal from the fine wire thermocouple with a heavily filtered coldwire signal for a single traverse point. There is good agreement between the thermocouple and cold wire signal with a slight phase shift caused by the different locations of the probes. Cold wire temperature traverses at several test section locations were then performed with and without the turbulence generator. A typical result is shown in Fig. 3.14. Only

a slight increase in temperature variation was observed with fluctuations of around $\pm 1^\circ\text{C}$ for both cases. This suggests that the test section location is sufficiently far down stream of the turbulence generator so that the temperature difference between the turbulence jets and the free-stream flow has mixed out.

With the uniformity of the main stream flow temperature confirmed, the same 5 micron Dantec 1D probe was then operated in the CTA mode as a hot-wire. Figure 3.15 shows a schematic of the digital measurement system used to process the hot-wire measurements. The measurement system consists of a Dantec Dynamics 1D hotwire, a constant temperature anemometer (CTA) and a National instruments SCXI 1305/1600 A/D converter. In this system the wire forms one part of a bridge circuit and is heated by an electrical current. The balance of the bridge is maintained by controlling the current to the wire so that the resistance and the temperature are constant. The measured bridge voltage, E (which represents the heat transfer rate) is passed through a low-pass filter and a signal conditioning unit before conversion in the A/D card. The combination of the sensor's low thermal inertia and the high gain of the servo loop amplifier gives a very fast response to fluctuations in the flow. Data was sampled at 30kHz with a cut off frequency of 15kHz, All data points were sampled for 10 seconds. The sampled data was then used to establish the time-mean flow velocity and turbulence statistics. The length scale of the turbulent flow field used in this thesis is based on the streamwise integral length scale Λ_x . The streamwise integral length scale is representative of the largest eddies in flow and is determined by invoking

Taylor’s hypothesis of frozen turbulence which gives:

$$\Lambda_x = \overline{U} \cdot T \quad (3.3)$$

Where \overline{U} is the mean flow velocity and (T) is the integral time scale calculated from the autocorrelation of the fluctuating velocity time signal.

In order to provide a flow profile the hot-wire probe was mounted onto a 2-D traverse system, which enabled the hot-wire to be traversed across the start of the test section area. Turbulence profiles were created by traversing the hot-wire in 5mm increments in the X and Y direction. The measurements provide essential information for the turbulence generator development detailed below.

Jets in cross flow development

One of the main difficulties in the development of the turbulence generator is the control over the flow uniformity in terms of intensity, length scale and mean velocity. Studies by [67], [68] and [69] have generated high levels of turbulence but at the expense of flow uniformity. Creating a profile which is uniformly unsteady at the required unsteadiness and length scale presents a challenge. A turbulence generator with a highly non-uniform profile will eventually become uniform over a sufficient distance downstream of the turbulence generator. However, this is accompanied by a decay in turbulence intensity as the turbulent energy is transferred from the large eddies into

small eddies by the process of vortex stretching. While the turbulent energy decreases, the integral length scale increase in size with downstream distance. Therefore, the ideal turbulence generator is one which achieves an homogeneous flow field at the test plate location with the required length scale and turbulence intensity.

Unlike grid generated turbulence, jets in cross flow designs have many more variables which make the establishment of design rules more difficult. The jets in cross flow method relies on the interaction between the free-stream flow and cross flow jets to increase the free-stream turbulence intensity. The turbulence levels generated from this interaction are a strong function of the velocity ratio between the free-stream and cross flow jets. Generally speaking, increasing the velocity ratio increases free-stream turbulence levels. The seminal work conducted by Bogard et al [54] found a velocity ratio of 17 was required to generate turbulence intensities of 20%. The major problem with this approach is the imbalance of the flow distribution created by injecting air towards the central region of the mainstream flow. This makes this method prone to poor spatial uniformity in the free-stream flow profile (usually seen as a central peak in mean velocity). The uniformity of the profile can be greatly improved by placing a full span splitter plate between the opposing row of jets as shown by [54]. This then isolates the opposing jets from each other and prevents any jet interaction. Therefore as shown in Fig. 3.11 a splitter plate was incorporated into the design at the start of the development. The test section dimension and turbulence generator location have been fixed by the requirements of the scaling factor used for the exper-

iment, therefore the turbulence generator design must operate within these limitations. As suggested earlier, the mainstream unsteadiness is related to the velocity ratio. However there is also the jet trajectory to consider as high velocity small diameter jets will have significantly less momentum than a larger jet at the same velocity ratio. The scaling of jet trajectories of a circular jet in crossflow has been studied for many years and correlations describing the trajectory as function of velocity ratio and diameter have been established. Pratte and Baines [70] describe the jet trajectory using the following power-law formulation:

$$\frac{y}{rd} = A \left(\frac{x}{rd} \right)^B \quad (3.4)$$

where $A=2.05$ and $B=0.28$

This equation provided a useful starting point for the development of a turbulence plate configuration for this test facility. An initial hole diameter of 13mm was selected with a 3D pitch spacing as this produced a similar jet trajectory as the design used by [54]. With the fan operating at full capacity (13kPa), velocity ratios up to 27 could be produced. The estimated jet trajectory for this cross flow jet in relation to the central splitter plate is shown in Fig. 3.16. This design was then manufactured and tested in the turbulence generator. The traversing hot-wire system was used to establish the flow profile at the start of the test section. The resulting centre line mean velocity and turbulence intensity are shown across a range of jet velocity ra-

tios in Fig. 3.17. The data shows a significant bulge in the mean velocity profile which increases with velocity ratio. The bulge is likely to be a result of the concentration of mass flux towards the center of the cross section as predicted by the jet trajectory correlation. The non uniform mean velocity also creates a non uniform turbulence intensity profile as the fluctuations remain consistent. The impact of the mass flux distribution was reduced by placing a 6inch full span cylinder at the end of the splitter plate (see Fig. 3.11), which has been shown to reduce the distance required to reach a spatial uniform profile [71]. The aim of the cylinder is to increase mixing and reduce the channel length required to reach a uniform profile. Fig. 3.18 shows the resulting profile with the full span cylinder in place. Clearly there was an improvement in the uniformity of the profile but a significant variation in mean properties was still present. Based on these initial test runs, a new pair of turbulence plates was created with a jet-hole design, which combined a secondary set of smaller diameter holes. The purpose of the smaller diameter holes was to even out the mass flux distribution from the turbulence generator plate. The final turbulence generator design consisted of two rows of holes: row 1 consisted of ϕ 8 mm while row 2 consisted of ϕ 12 mm (pitch spacing to diameter ratio of 6.5 and 4.3 respectively), a photography of installed plate is shown in Fig. 3.12. Fig. 3.19, 3.20 and 3.21 show the resulting spatial profiles for $Tu=10\%$ upto $Tu=25\%$ at the start of the test plate. The profile was created by traversing the hotwire in 5mm increments, the turbulence properties of each measurement point were calculated from 10 seconds of data. Fig. 3.19 represents the baseline condition with the turbulence generator turned off and the span-wise cylinder removed. For the

elevated turbulence case ($Tu=25\%$), a span-wise cylinder was still required to improve the uniformity of the free stream profile. The introduction of the cylinder also significantly reduced the turbulent length scale from $\frac{AL}{D}$ 26 to 13 (based on a cooling hole ϕ 8.5mm) due to the temporary reduction in the cross-sectional area. At the intermediate turbulence case ($Tu=16\%$), it was possible to generate the same profile both with and without the span-wise cylinder. This allowed near identical mean velocity and turbulence intensity profiles to be generated with significantly different length scales. A comparison of the different profiles is presented in Fig. 3.22. These mainstream turbulence conditions were then used for the effusion plate testing campaign.

Turbo expander

The density ratio between the coolant and mainstream flow varies throughout the combustion chamber with localised near wall regions as low as 1.4. Further away from the liner walls, ratios of up to 3 occur in civil engine applications. To cover these conditions experimentally in a lab environment is very difficult because even at large scale factors (>10) large temperature differences are required to generate engine representative density ratios (at atmospheric conditions). For this study a modest density ratio of 1.4 was achieved by a combination of cooling and heating. This value is at the low end of the expected density ratio range to be seen in combustor applications. However, the intention here is to diagnose the impact of density ratio as an independent parameter over a sensible range of values. As suggested earlier, the elevated free-stream temperatures are created by virtue of the recircu-

lating heated design of the wind tunnel. The cold coolant is generated by a turbo expander system based around an automotive IHI RB85 turbo-charger see Fig. 3.23. The turbine of the turbo charger is supplied with dry compressed air (-40°C dew point) at ambient temperature from a large external compressed air facility. The compressed air is then expanded through the turbine of the turbo charger. The compressor of the turbo charger is driven by the turbine and absorbs the enthalpy and contributes to the reduction in temperature at the turbine exit. In order for the turbo charger to be operated outside of its intended application, an oil lubrication system was constructed to deliver pressurised oil to the turbo charger bearings. Due to the rotational speeds and energy absorbed by the compressor, an oil cooler was also required on the oil return feed to reduce oil temperatures to acceptable levels.

For a given turbine inlet pressure, a resulting exit temperature will be achieved based on the polytropic efficiency of the turbine. As there was no performance data available for the turbine, part of the commissioning phase involved characterising the turbine performance. This was achieved by cycling the turbine through a range of inlet pressures, while recording mass flow through an orifice plate and inlet/exit temperatures using sheathed k-type thermocouples. Each test condition was maintained until thermal equilibrium was achieved. This data enabled the normalised mass flow rate (corrected to SLS) to be calculated and plotted against pressure ratio, see Fig. 3.24. This provided vital information on the mass flow and pressure values required for a given exit temperature (coolant delivery temperature). This allowed the infrastructure of the turbo expander system to be appro-

priately sized. Based on preliminary turbo tests, a pneumatically controlled Shubert Salzer valve was selected to regulate the flow through the turbo. This was connected inline with an orifice meter which provided feedback to the valve controller. Using this control system it was possible to maintain a fixed turbine inlet pressure as the external receiver tank pressure varied. As can be noted from the performance map (Fig. 3.24), high density ratio tests for all but the highest blowing ratio cases would result in excessive coolant flow. Therefore a bypass valve is located on the turbine exit to control the final flow rate to the effusion feed plenum. The bypass flow is dumped to atmosphere through a series of noise attenuators. This allows the turbo expander to operate at the required pressure ratio for the target coolant temperature with independent control of the coolant flow rate. To accommodate situations requiring high mass flow and temperature, a waste-gate can be operated on the turbine which allows flow to bypass the turbine reducing the temperature drop. This also acts as fine tune for the coolant delivery temperature. This feature is particularly useful as atmospheric conditions can vary the receiver tank air temperature.

Downstream of the bypass valve there is a second orifice meter plate designed to ISO 5167 standards which measures the final mass flow delivered to the effusion test plate. In order to preserve the cold temperatures created by the expander, high quality insulation is applied to all pipe work downstream of the turbine exit. The cold air is then fed into the insulated plenum located beneath the effusion plate through a 2 inch perforated pipe. The perforated pipe prevents flow from jetting into the coolant plenum. The plenum also

contains control screens and an air filter to capture any oil that may have contaminated the air within the turbo-charger. The coolant temperature is measured in the feed plenum using a sheathed K-type thermocouple. These details are shown in Fig. 3.25. This system is capable of producing stable temperatures of -20°C for extended periods of time as required for time average tests. A brief summary of the wind tunnel capabilities are presented below.

Wind tunnel summary

- Blowing ratio 0.2-7
- Jet Reynolds up to 20,000
- Turbulence intensity 10-25%
- Length scale 150-300mm at $Tu=16\%$
- Density ratio 1-1.5
- Steady state measurements of nondimensional heat transfer and adiabatic effectiveness
- Test plate scale factors 10-22

3.3 Experimental models

For all test plate configurations the plate is mounted into an insulated plenum which consists of a system of flow control screens and air filters. The coolant

flow enters the lower half of the plenum through a perforated pipe which distributes the air laterally from the centreline of the plenum. The coolant flow is then passed through two sets of 50% blockage screens before passing through an oil filter. This presents the effusion array with an oil free homogeneous flow field, insulation is applied both internally and externally to maintain coolant delivery temperature. The plenum is instrumented with three k-type encapsulated thermocouples to monitor coolant delivery temperatures. A schematic of the test section is shown in Fig. 3.25. The test plate is fitted with inserts, which allow the test plate to be clamped onto a silicone sealing ring. This creates an airtight seal between the test plate and mainstream flow, ensuring all coolant is passed through the effusion array. A total of four effusion arrays were constructed for the testing campaign. The majority of the experimental tests were performed on the plain hole effusion array. The remaining three test plate designs were constructed for the investigation of fanned effusion. Details of the construction of each test plate are described below.

Plain hole effusion array (Test plate 1)

The test plate consisted of an array of cylindrical effusion holes with dimensions given in Fig. 3.26. The pitch spacing and length-to-hole diameter were selected to represent scaled engine geometry. The cylindrical effusion holes were inclined at 20° and arranged into a staggered array. The span-wise pitch to diameter ratio was 8, while the stream-wise pitch to diameter ratio was 7.5. A nominal inclination angle of 20° was selected as this angle approaches

the maximum angle possible using conventional laser drilling technology. The plate was manufactured from a closed cell rigid foam (Rohacell™) which has a low thermal conductivity (0.029 W/mK) and remains dimensionally stable across a wide temperature range. This test plate formed the basis of the experimental testing campaign.

Fanned effusion (Test plate 2 and 3)

For the investigation of fanned effusion the existing test section was extended further to accommodate additional cooling rows. This was deemed necessary as the results from the plain hole effusion tests revealed that more rows would be required to reach asymptotic behaviour, particularly at the higher blowing rates required by fanned effusion. The geometry of the baseline fanned effusion hole was derived from CAD models supplied by Rolls Royce before scaling by a factor of 15. The span-wise and stream-wise pitch to diameter ratio is 6.67 and the hole inclination angle is 17° as shown in Fig. 3.28. The thickness of the plate is such that the length-to-diameter ratio is approximately 10. Initial cold flow tests of the fanned and plain hole effusion test plates produced CDs of 0.72 and 0.65 respectively. This information enabled the effective porosities to be matched by using the following equation:

$$Effective\ porosity = \frac{CD \times Area_{hole} \times No_{holes}}{Measurement\ Area} \quad (3.5)$$

To account for the difference in CDs, the diameter of the plain cylindrical hole was increased from 9 to 9.7mm, while maintaining the same absolute

geometric hole spacing and inclination angles. This created two test plates with the same effective porosity (1.9%), enabling a true comparison of the two cooling schemes for a given flow rate. Both test plates were manufactured from Rohacell™ foam. The fanned effusion geometry proved difficult to machine in-situ, therefore, a full set of thin wall laser sintered glass filled polyimide rapid prototyped inserts were created. These were then bonded into the Rohacell™ base plate as shown in Fig. 3.32. The inserts did not have the same low thermal properties of Rohacell™, however by using thin walled inserts the impact on the usable measurement area was minimised.

Reduced cost fan (Test plate 4)

A manufacturable version of the baseline fan was developed by considering the possible fan shapes which can be created by conventional laser drilling. An approximation of the fan design can be created by laser drilling at angles in a similar plane to the inclined metering hole. The break out area of the fan is set by the laser crossover point and drilling angle. Fig. 3.31 shows a range of hole definitions which can be created by varying these parameters. Fan design 2 was selected as the test case, as this design contained a well-defined metering length and a more gradual diffusion of the central hole. The main metering hole angle was inclined at 22°, the fan shape was created by two further drilled holes at the maximum laser drilling angle of 20°. This created a slightly laid back fan with an even break out on to the test surface. The reduced turning of the flow produced the highest CD of 0.78, resulting in a metering hole diameter of 8.5mm. The simplicity of this design enabled the

fan to be directly machined into the Rohacell™ test plate. These test plates were then used as a base and modified to suit the measurement technique being applied as detailed in the following sections:

Heater foil test plate (HTC & effectiveness)

For moderate density ratio tests the upper surface of the test plate had a thin heater film bonded to the surface, see Fig. 3.33 and 3.32. The heater-film was 0.05mm thick and was made from constantan resistance alloy (Cu55/Ni45) that has a low temperature coefficient of electrical resistance. The foil was laser cut to match the effusion array pattern. Recessed copper bus bars were placed across the leading and trailing edge of the test plate. This enabled a smooth transition of foil from the bus bar to the test plate base. The bus bars were electrically connected to the heater foil by silver loaded epoxy. 10cm long studs were located at each end of the bus bars, which allowed external electrical connections to be made. The exposed surface of the foil was coated with a high emissivity black paint in order to aid infrared based thermographic measurements of wall temperatures. Three thin foil surface thermocouple were located at various free stream locations to provide reference temperatures for the IR camera. As is explained in a later section, both HTC and effectiveness data can be gleamed from the foil test plate alone. However, the limitations of the epoxy bond between the foil and the test surface restricts the free-stream temperature and ultimately the density ratio possible.

Adiabatic test plate (effectiveness only)

For tests involving high density ratio the RohacellTM base plate was prepared for direct surface temperature measurement. The surface was prepared in a similar way to the foil with a combination of high emissivity paint and reference thermocouples. The low thermal conductivity provides a near adiabatic surface for the calculation of adiabatic effectiveness. With the test plate in this configuration, only the adiabatic film effectiveness is measured. However, without the limitations of the foil bond this test plate is capable of running at the higher density ratios.

3.4 Summary

A new high turbulence test facility has been constructed for the purpose of investigating the hot-side performance of combustor effusion arrays. The test facility has been designed with the specific aim of isolating the effects of different variables effecting film cooling performance.

- A closed circuit wind tunnel has been designed, built and commissioned. A high pressure loss design was adopted to produce a compact wind tunnel, which maximises the working test section length.
- The fully insulated circuit consisted of a 50kW inline heater which enabled hot gas temperatures of up to 100°C.

- Hotwire traverse data of a fully featured lean burn combustor was used to establish representative flow conditions inside the combustion chamber. This data was then used to guide the scaling of the experiment, in particular the bulk free-stream turbulence properties.
- A turbulence generator has been designed and built, which is capable of producing highly turbulent free-stream conditions with independent control over length scale. Unlike previous work, the design of this turbulence generator has been developed with the specific aim of producing representative combustor turbulent free-stream intensity and length scales.
- For the simulation of engine density ratios, a turbo expander system was designed and built to deliver stable coolant flows across a range of temperatures. The system is capable of producing temperatures of -20°C for extended periods of time.
- Large scale (SF 12) effusion test plates have been constructed from an insulating closed cell rigid foam RohacellTM which produces a near adiabatic surface for direct film effectiveness measurements.
- A set of the three porosity matched effusion test plates have been designed at the same effective porosity allowing direct comparison of film performance.
- For the purpose of normalised heat transfer measurements a ohmic heater foil system was developed to vary the surface wall temperature during film cooled tests.

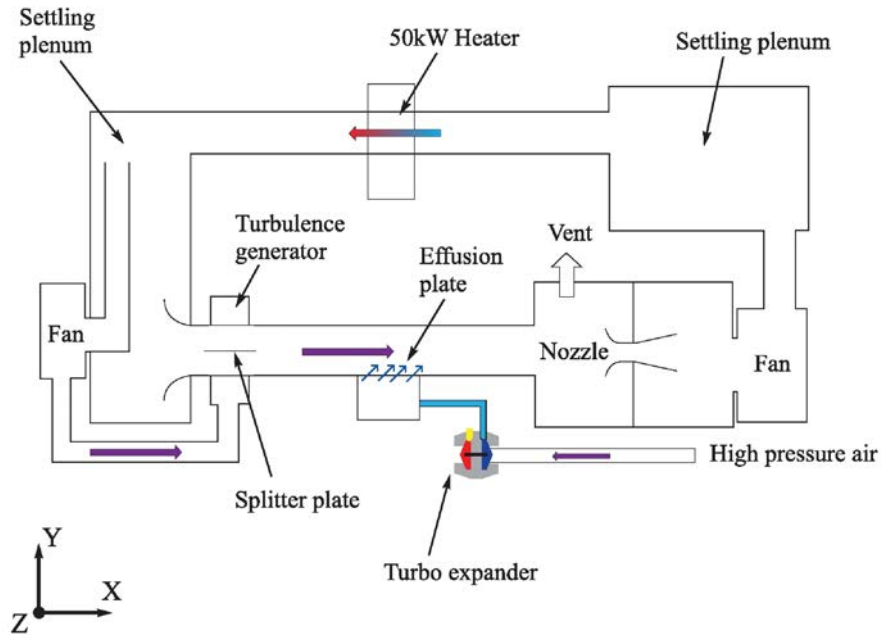


Figure 3.1: Wind tunnel schematic

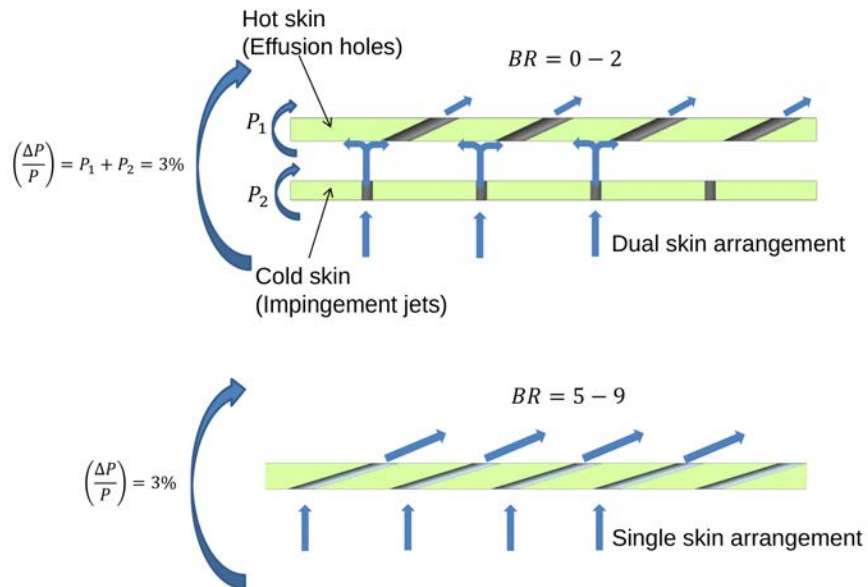


Figure 3.2: Schematic of dual and single skin architecture at a 3% liner pressure drop

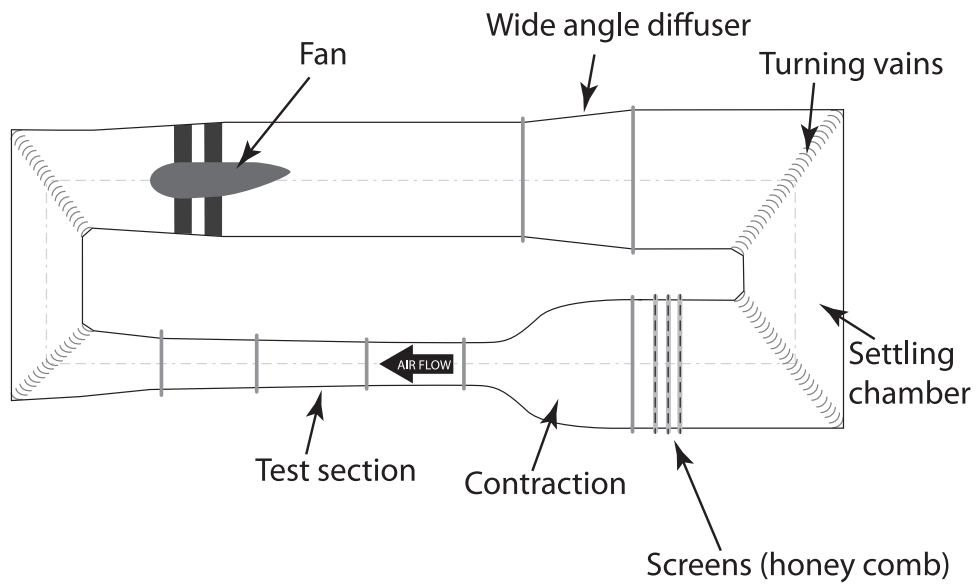


Figure 3.3: Conventional closed circuit wind tunnel schematic

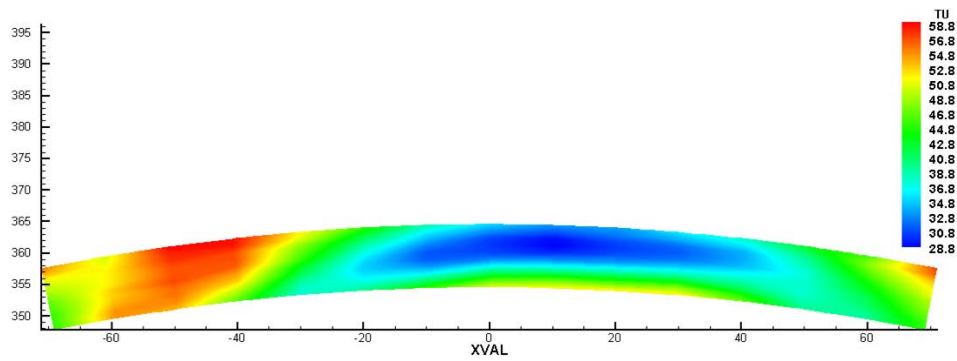


Figure 3.4: Turbulent intensity measurements from a lean burn combustor at 25% tile distance

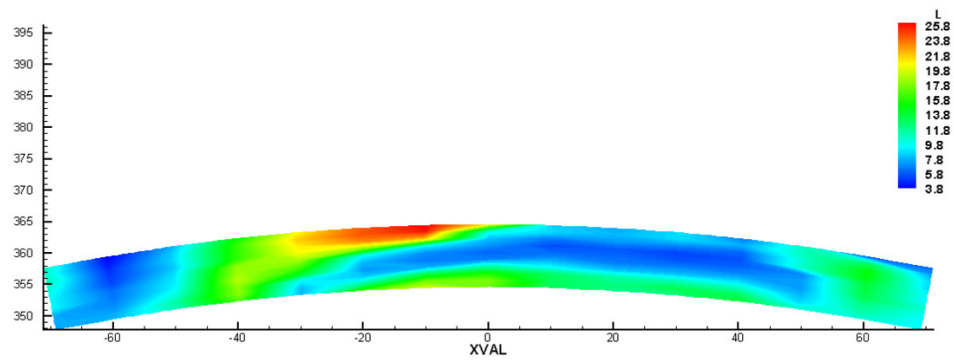


Figure 3.5: Turbulent length scale measurements from a lean burn combustor at 25% tile distance

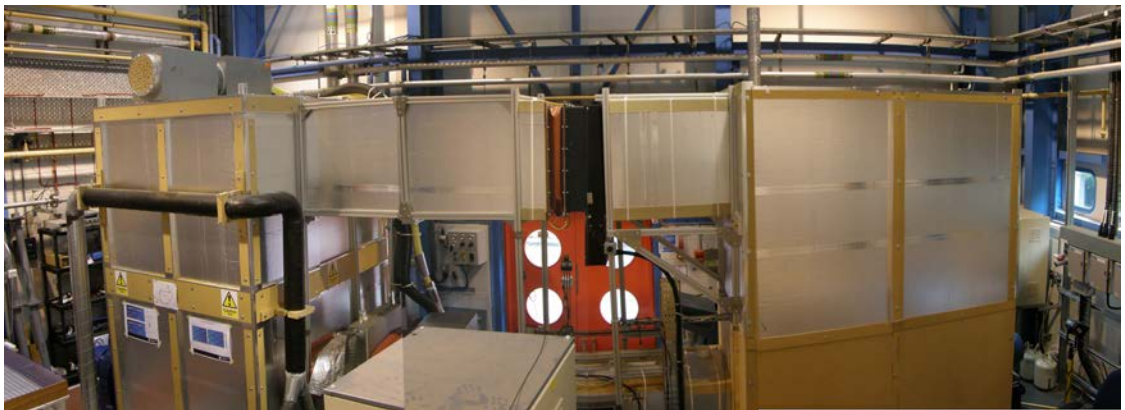


Figure 3.6: Photograph of tunnel return circuit



Figure 3.7: Construction of the right hand sub assembly

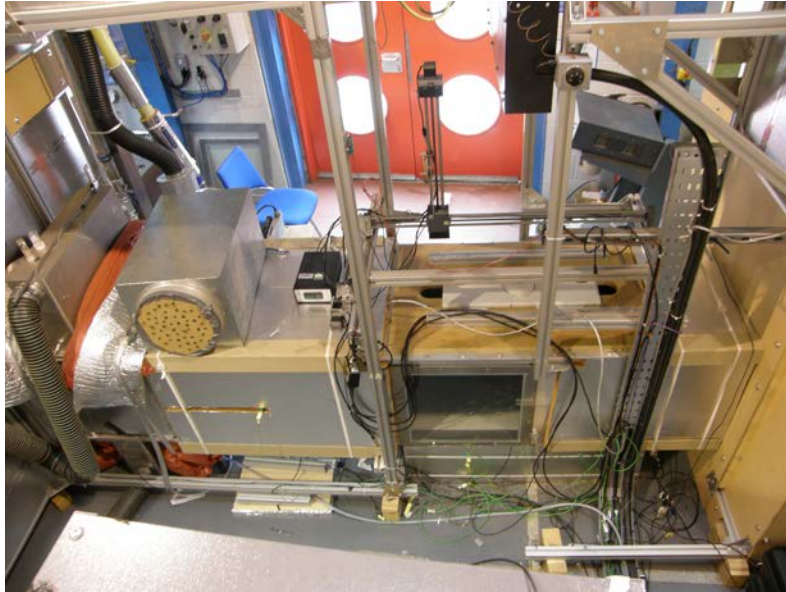


Figure 3.8: Photograph of test section

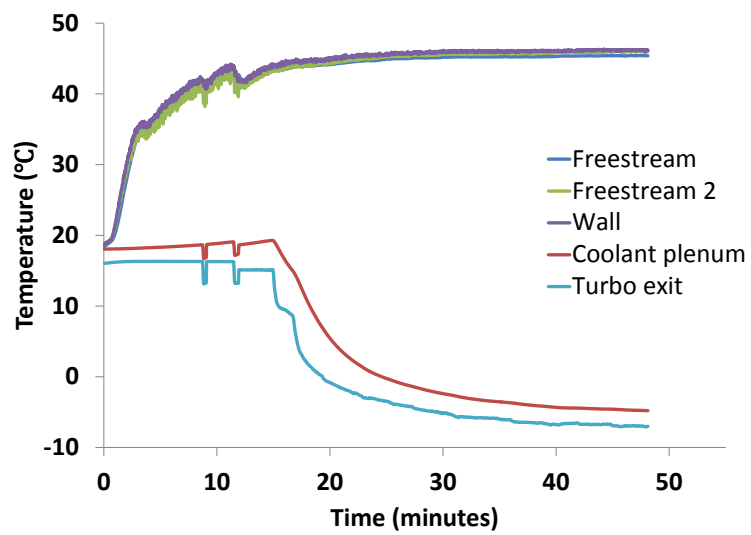


Figure 3.9: Tunnel warm up cycle



Figure 3.10: Bell mouth inlet arrangement

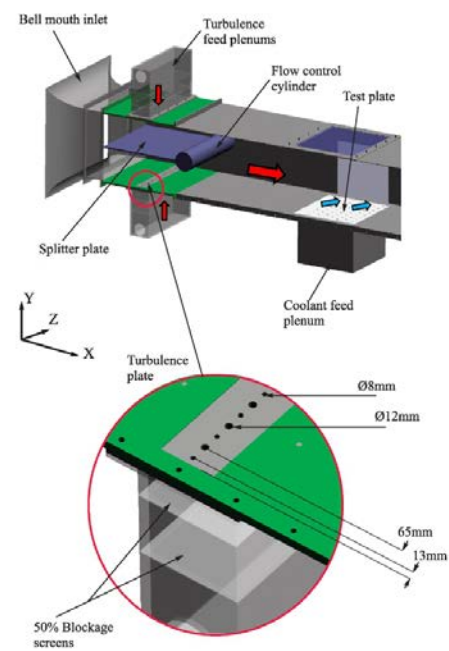


Figure 3.11: Sectional view of test section



Figure 3.12: Assembled multi diameter turbulence plate

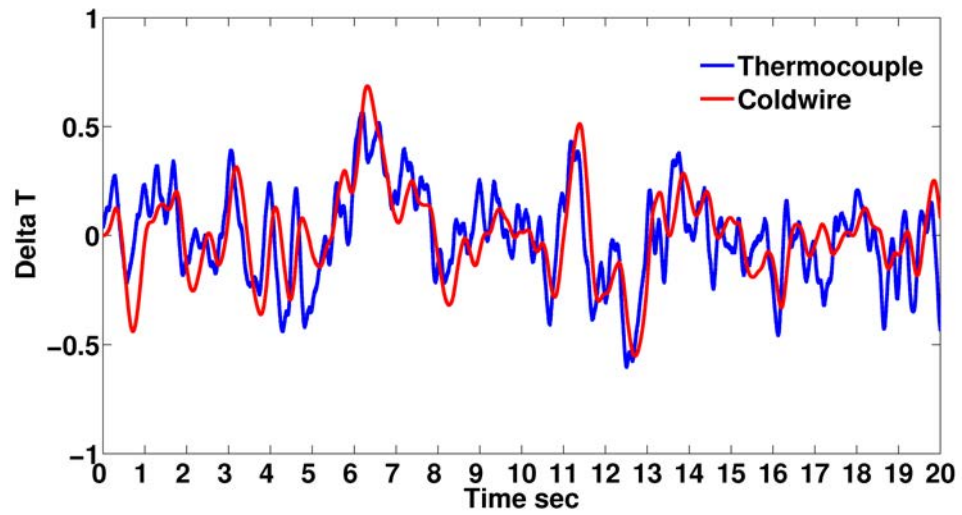
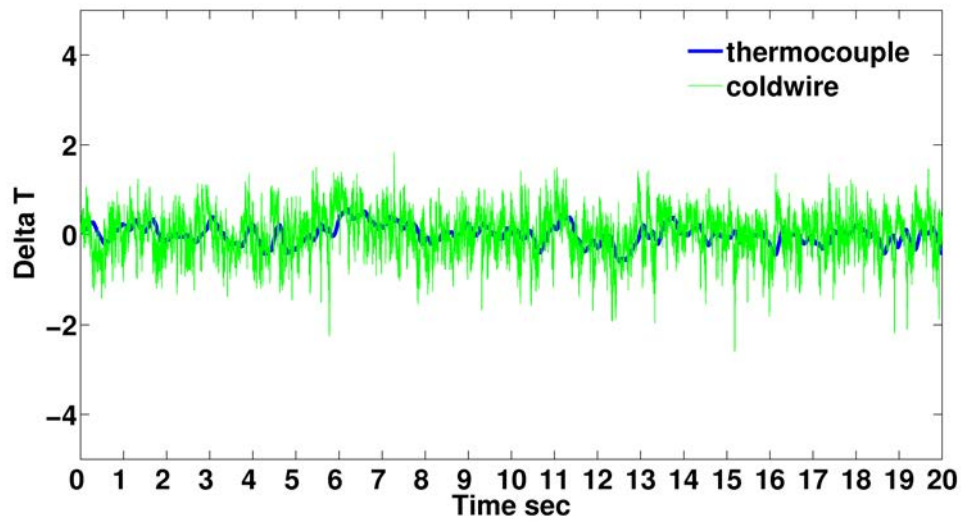
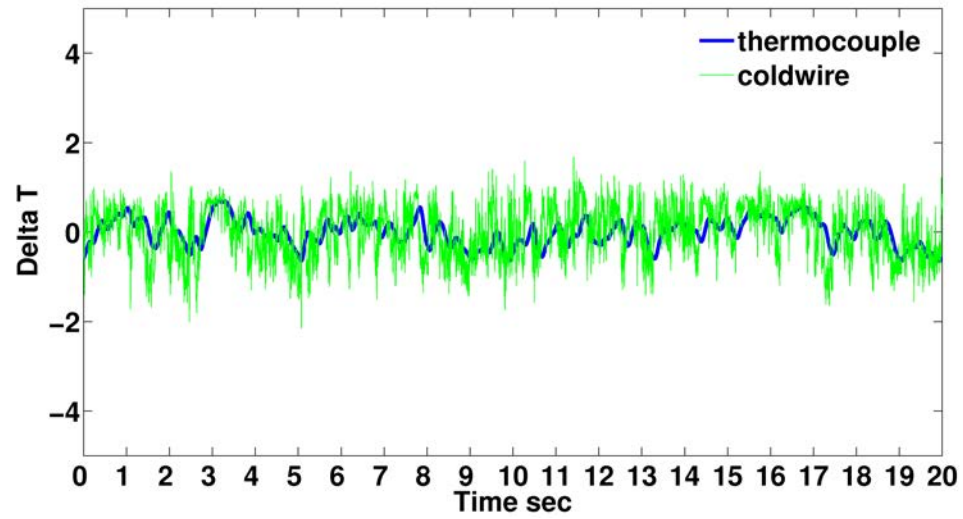


Figure 3.13: Raw thermocouple and filtered coldwire signal



(a)



(b)

Figure 3.14: Temperature variation with (a) Turbulence on; (b) Turbulence off

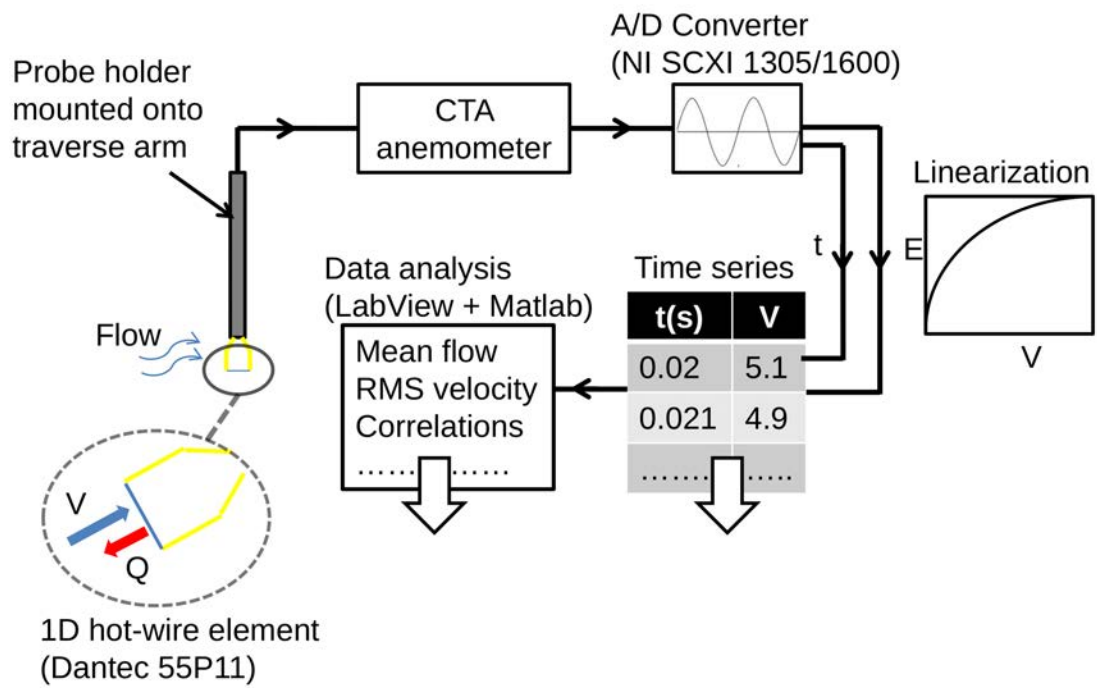


Figure 3.15: Hotwire setup

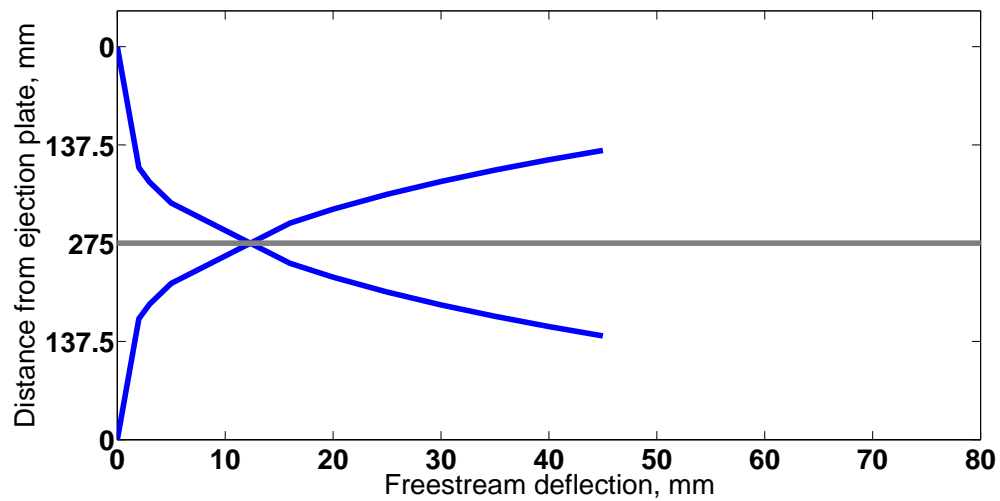
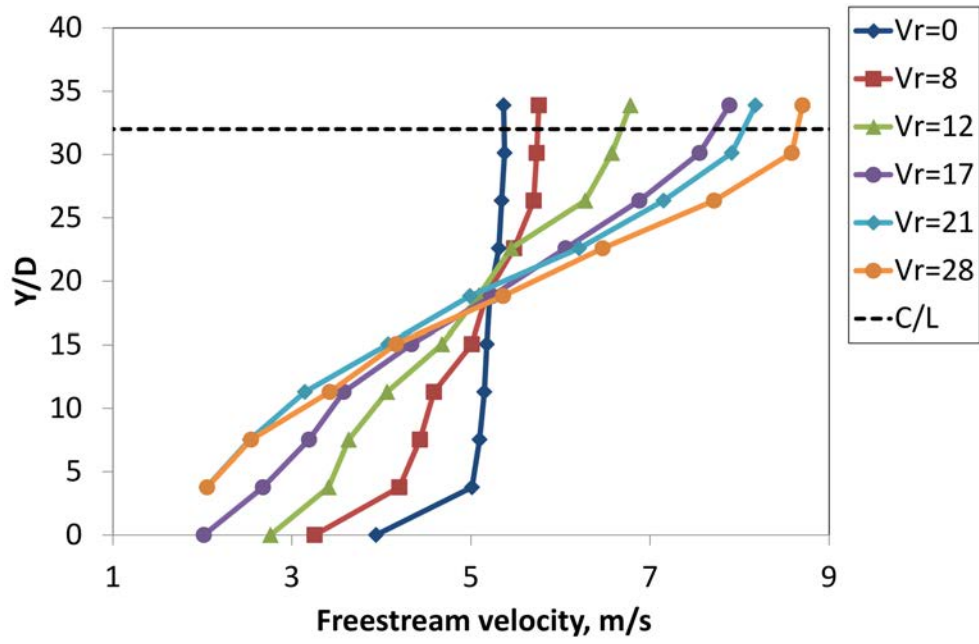
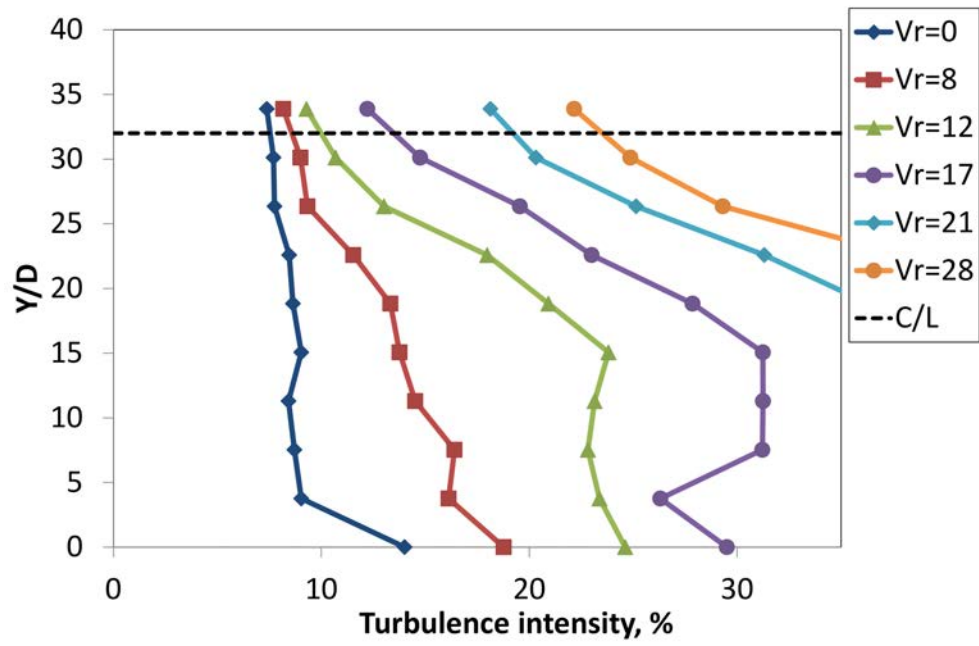


Figure 3.16: Predicted jet trajectory from a single row of $\phi 13$ holes at $V_r 21$

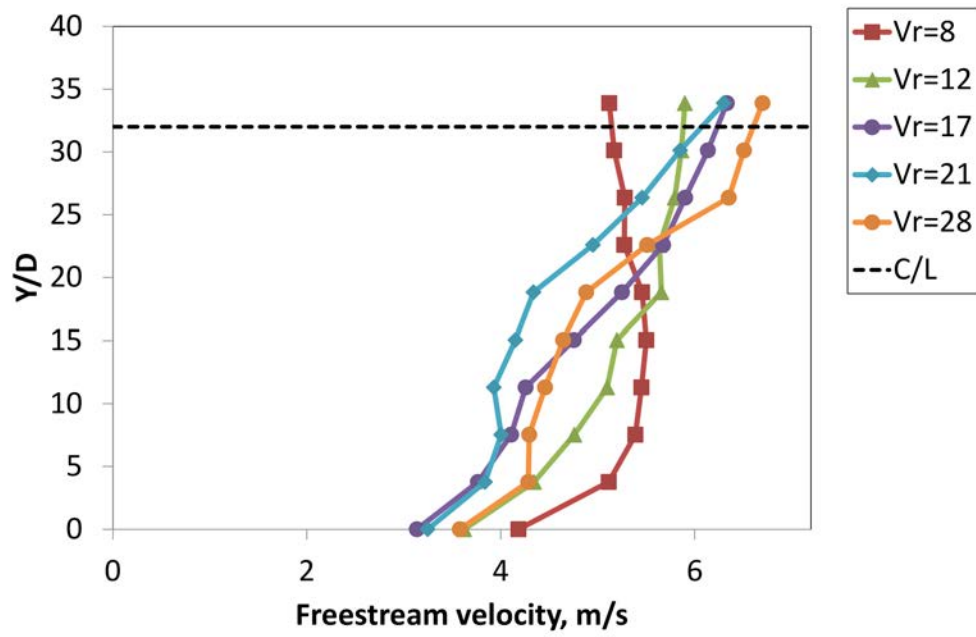


(a)

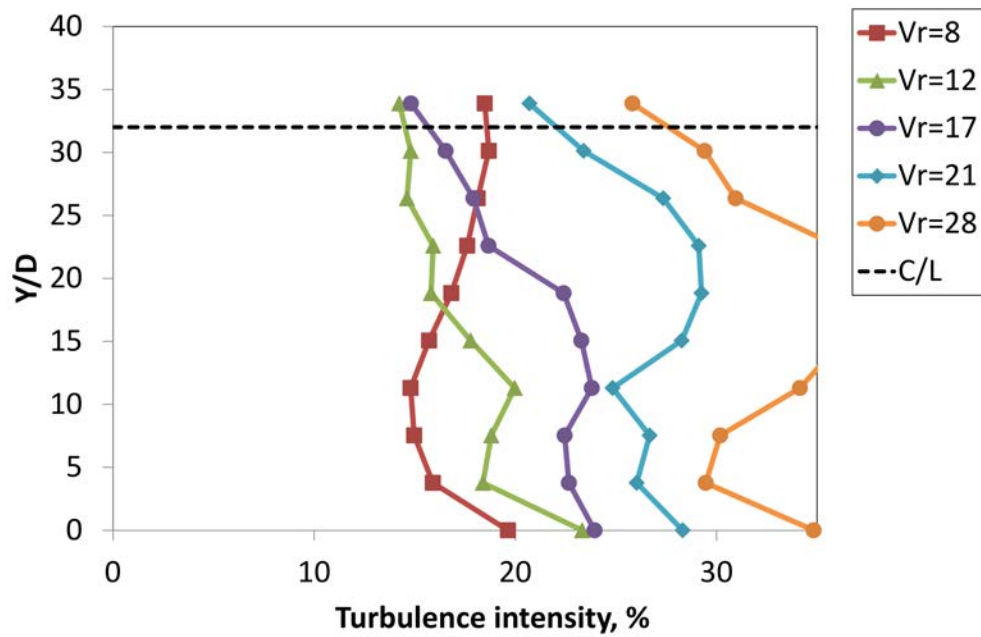


(b)

Figure 3.17: Hotwire center line traverse for ϕ 13mm jet plate without spanwise cylinder (a) Mean Velocity; (b) Turbulence intensity

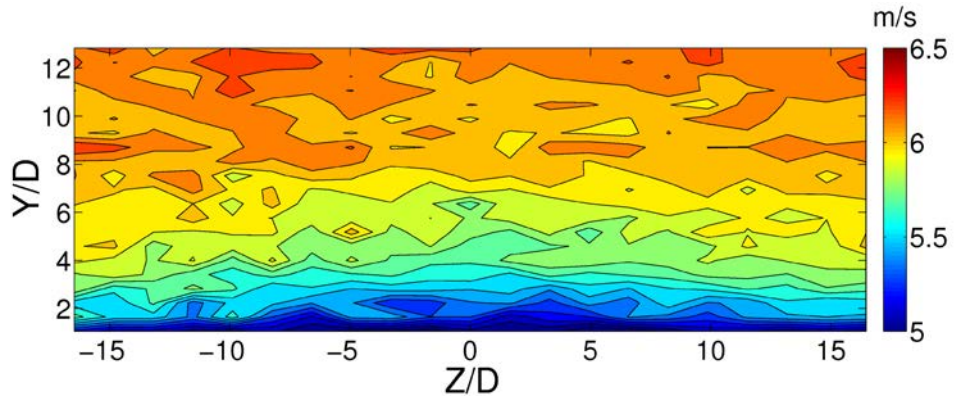


(a)

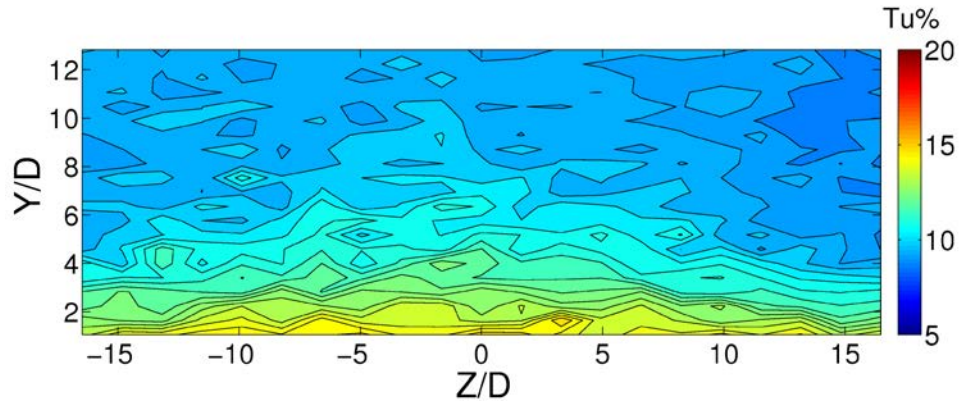


(b)

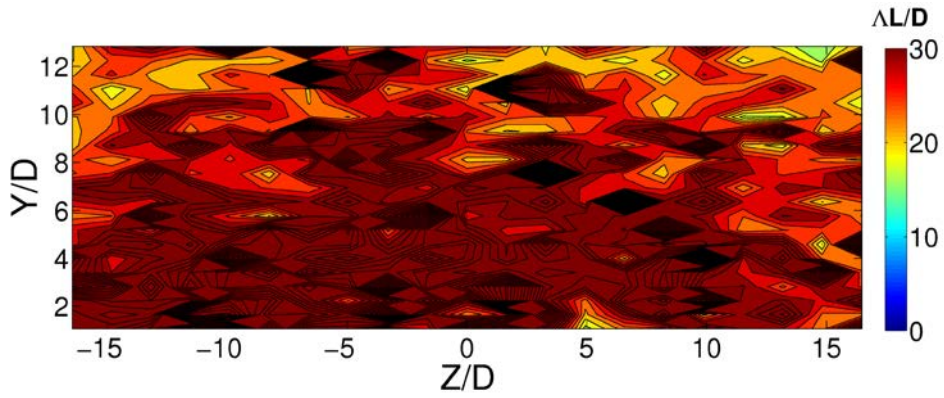
Figure 3.18: Hotwire center line traverse for ϕ 13mm jet plate with span-wise cylinder (a) Mean Velocity; (b) Turbulence intensity



(a)

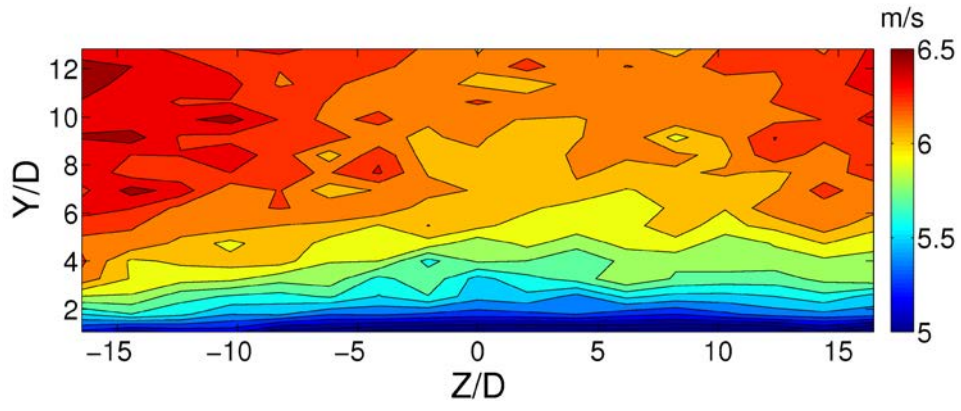


(b)

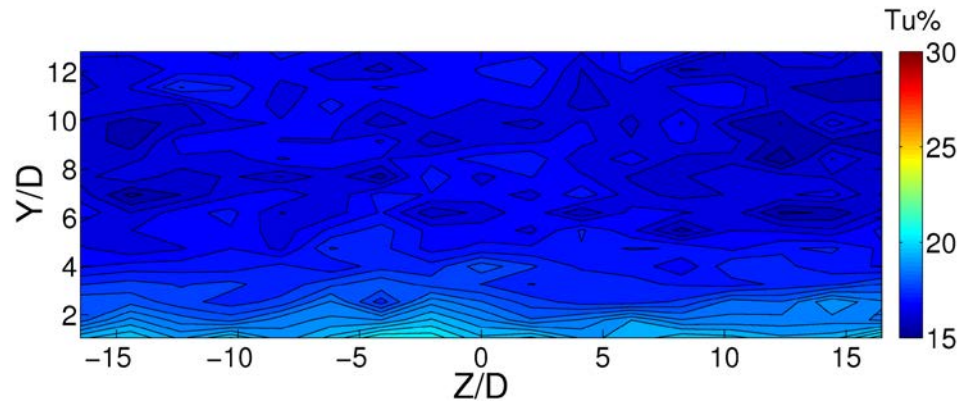


(c)

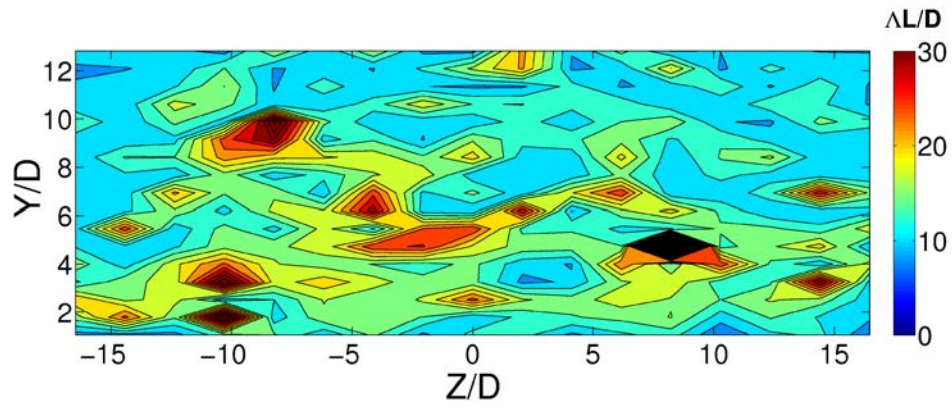
Figure 3.19: Hotwire traverse measurements for $Tu=10\%$ profile (a) U_∞ velocity; (b) Turbulence intensity; (c) Turbulence length scale



(a)

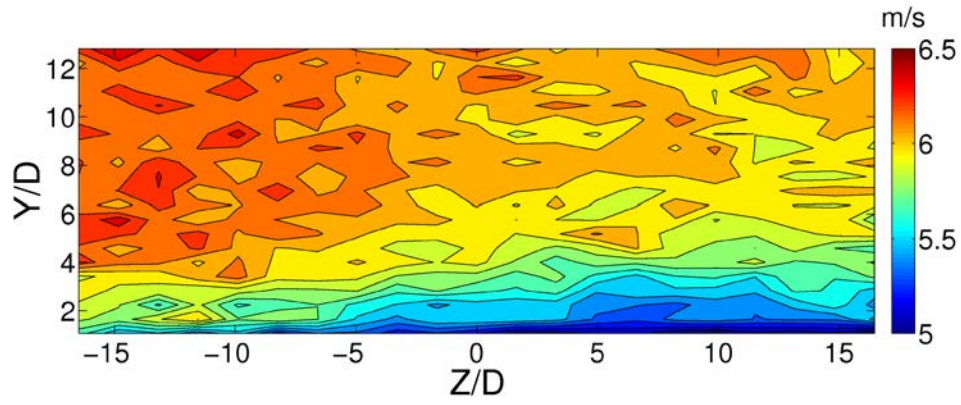


(b)

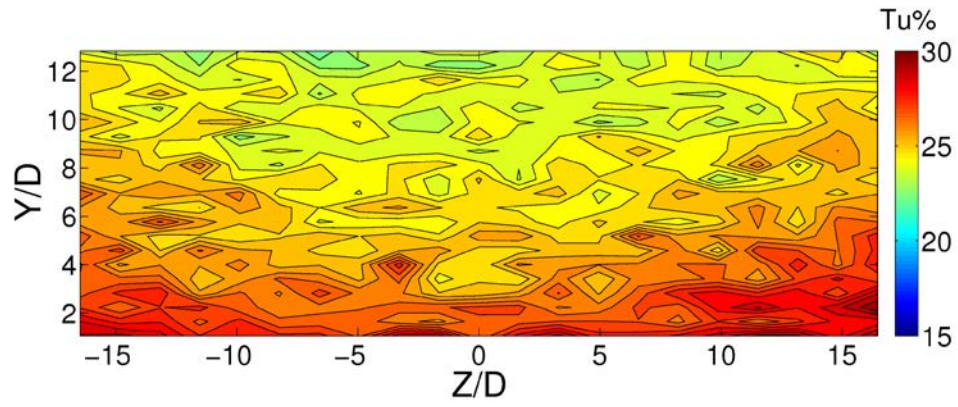


(c)

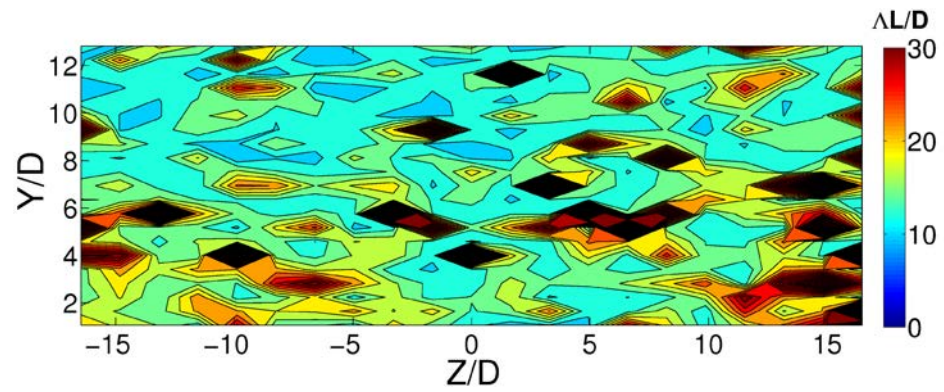
Figure 3.20: Hotwire traverse measurements for $Tu=16\%$ profile (a) U_∞ velocity; (b) Turbulence intensity; (c) Turbulence length scale



(a)

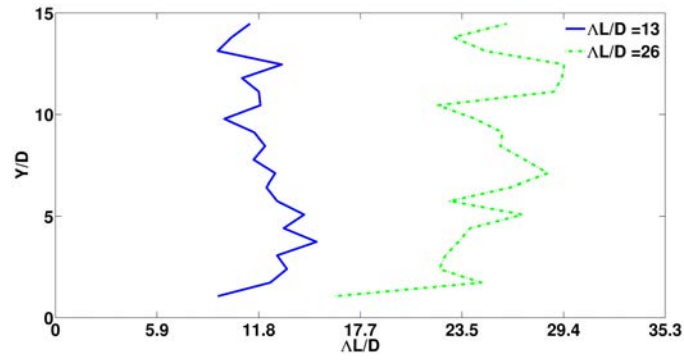


(b)

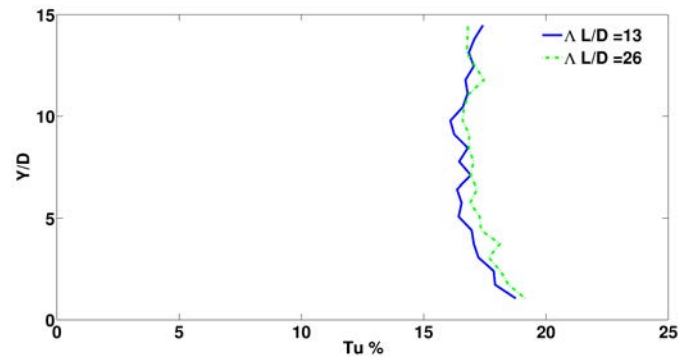


(c)

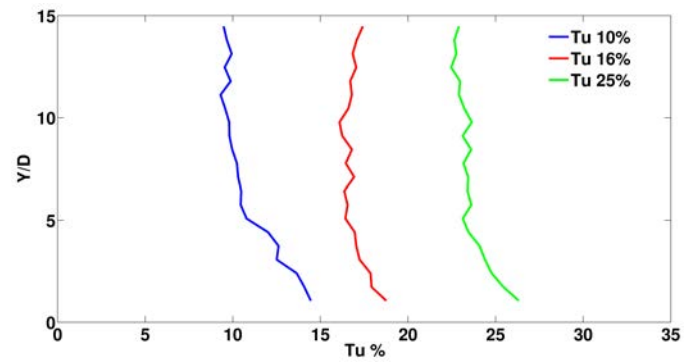
Figure 3.21: Hotwire traverse measurements for $Tu=25\%$ profile (a) U_∞ velocity; (b) Turbulence intensity; (c) Turbulence length scale



(a)



(b)



(c)

Figure 3.22: Span-average hot-wire measurements (a) Length scale variation at $Tu=16\%$; (b) Turbulence intensity with length scale variation; (c) Turbulence intensity

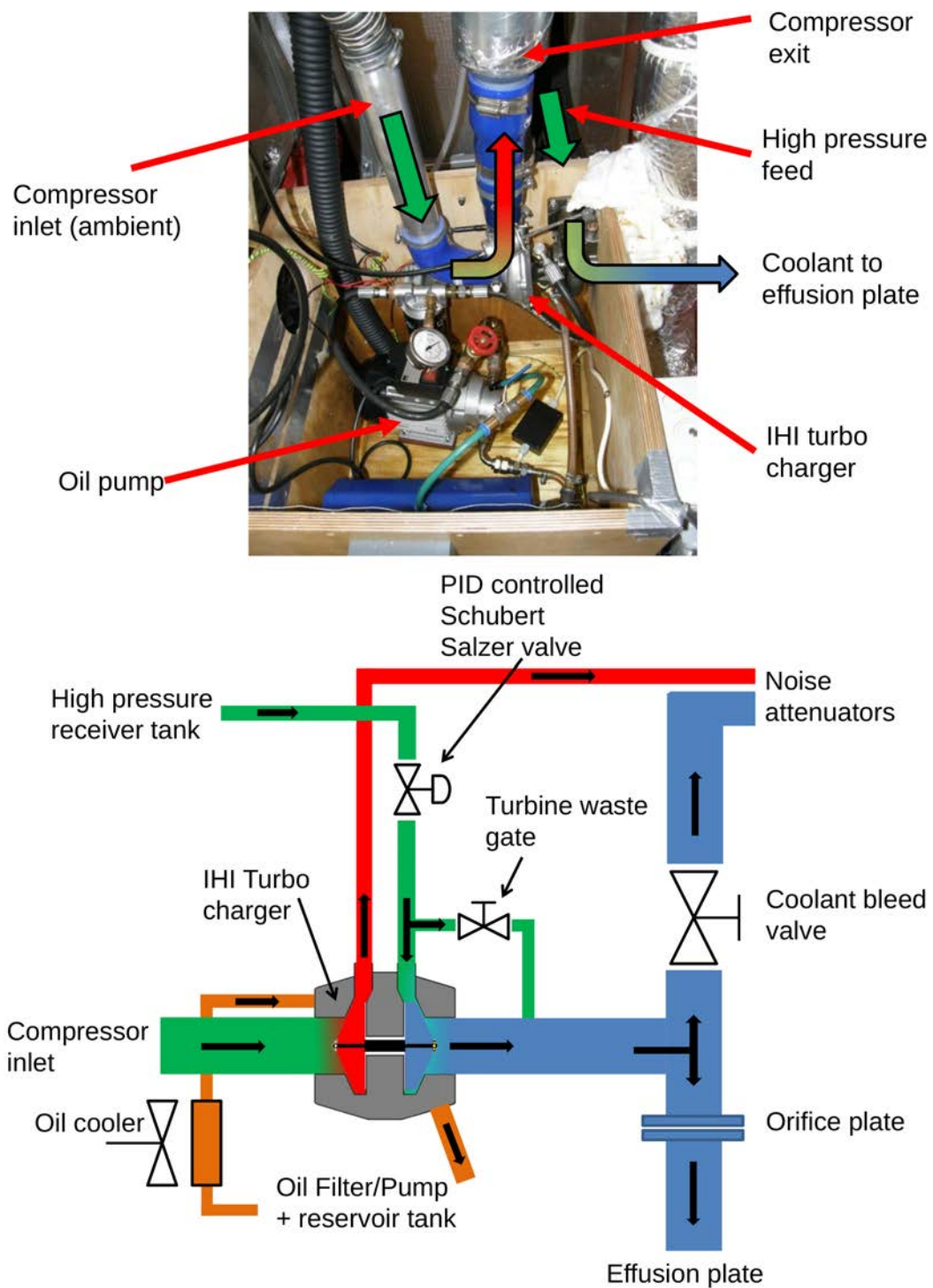


Figure 3.23: Photography and schematic of turbo expander system

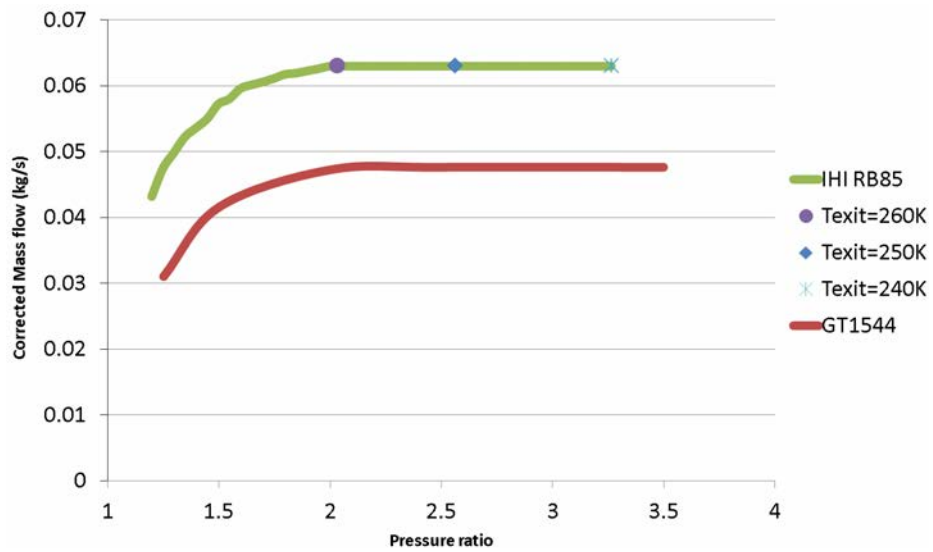


Figure 3.24: Turbine performance plot of IHI RB85 and similar sized Garret charger

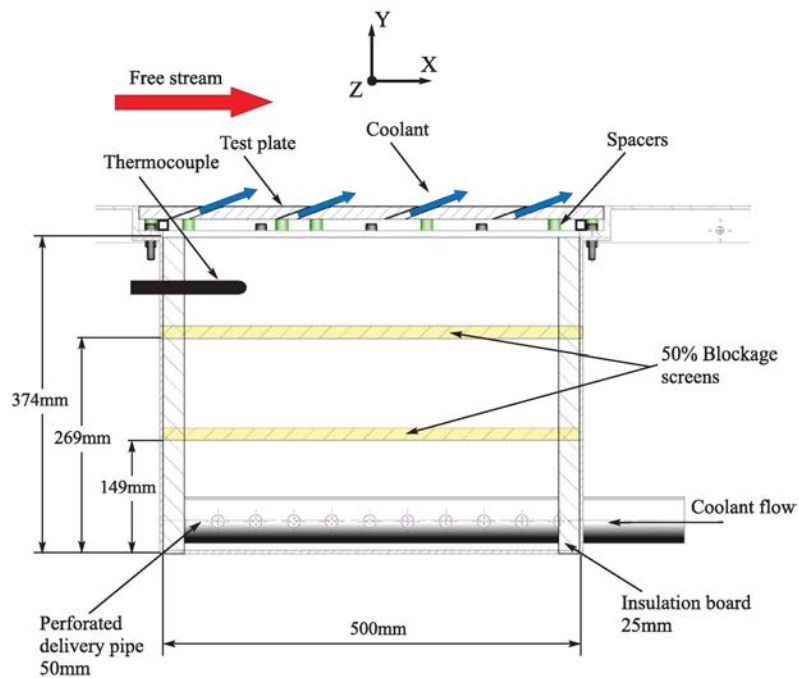


Figure 3.25: A diagram that illustrates the coolant feed plenum construction

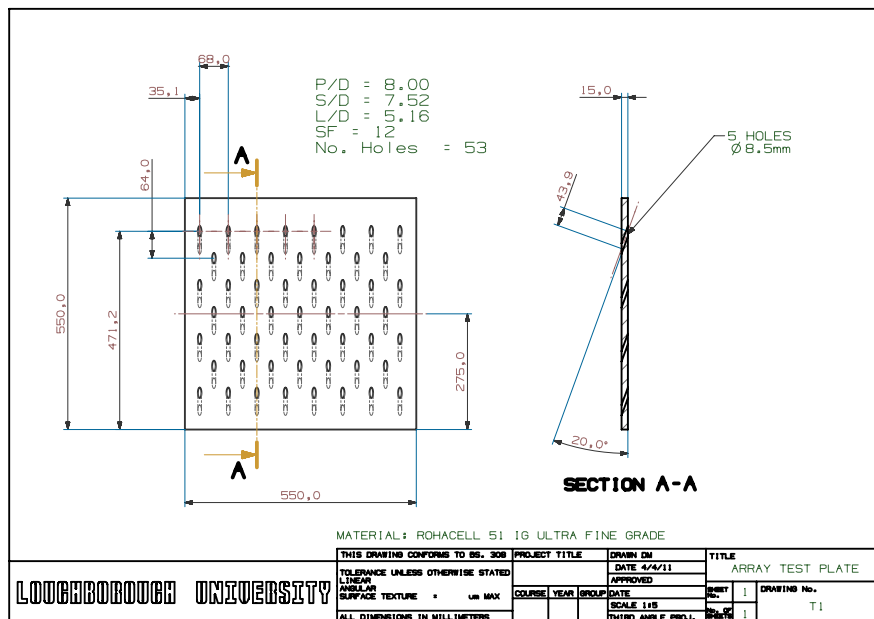


Figure 3.26: Plain hole effusion test plate 1

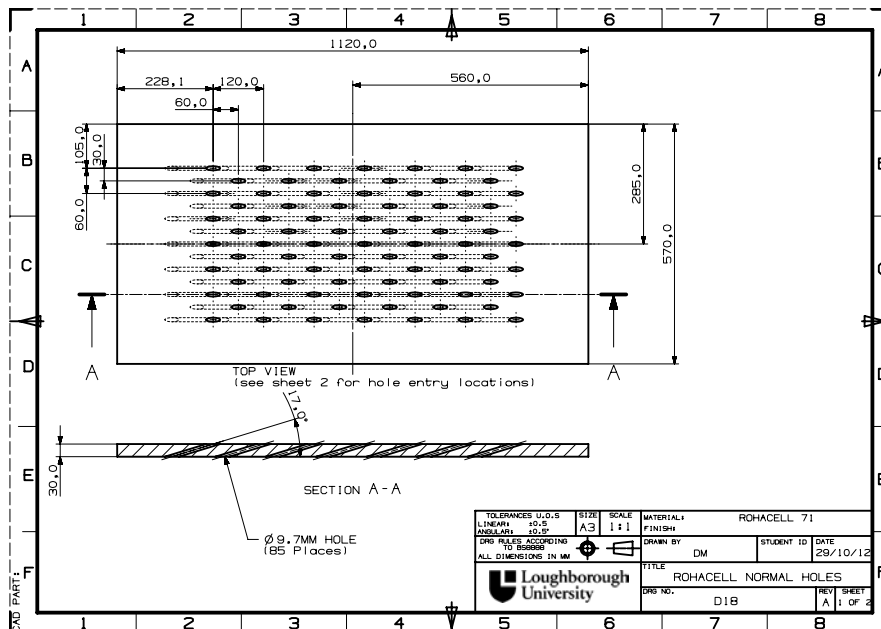


Figure 3.27: Effusion hole array pattern for fanned and plain effusion tests 2, 3 and 4

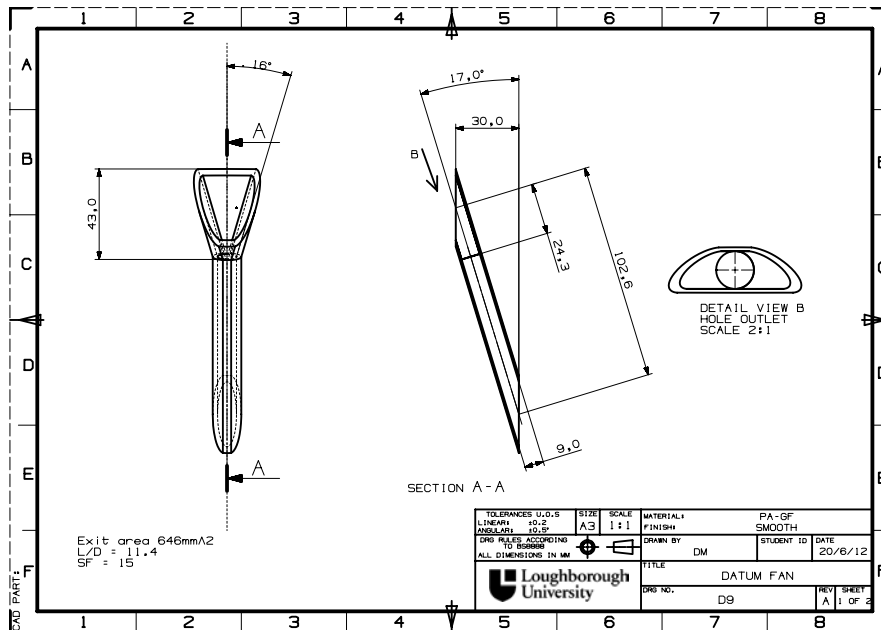


Figure 3.28: Datum fan definition

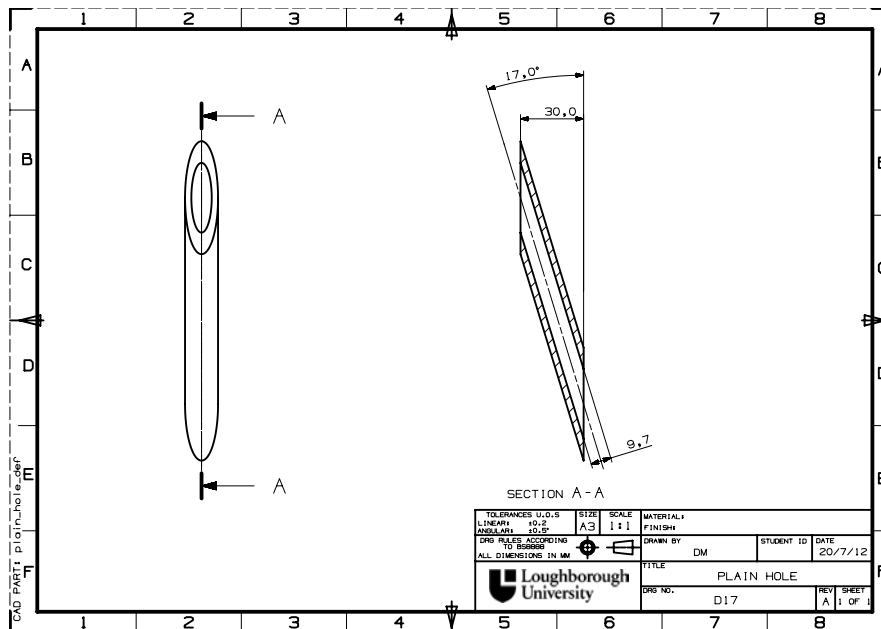


Figure 3.29: Plain hole definition

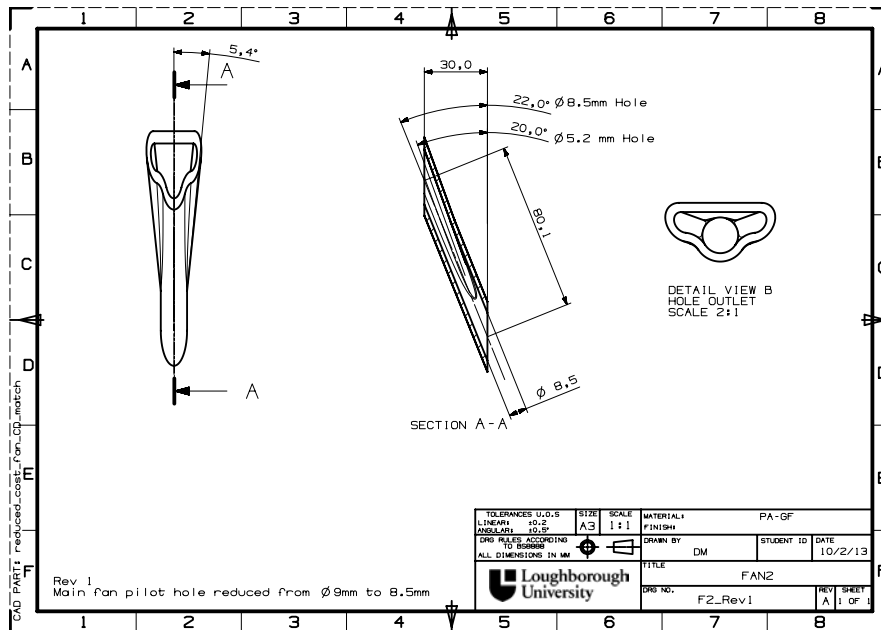


Figure 3.30: Modified fan definition

SPEY FAN

FAN ANGLE 15°
INCLINATION 17° (MAIN HOLE & FAN)
FAN AREA= 645mm^2

DESIGN 1

LASER CROSS AT HOLE INLET
FAN ANGLE 5.4°
INCLINATION 22° (MAIN HOLE), 20° (FAN)
FAN AREA= 389.3mm^2
EDGE BLEND

DESIGN 2

LASER CROSS AT HOLE INLET
FAN ANGLE 11.3°
INCLINATION 22° (MAIN HOLE), 20° (FAN)
FAN AREA= 624.2mm^2
EDGE BLEND

DESIGN 3

LASER CROSS AT HOLE CENTER
FAN ANGLE 15.4°
INCLINATION 22° (MAIN HOLE), 20° (FAN)
FAN AREA= 439.2mm^2
EDGE BLEND

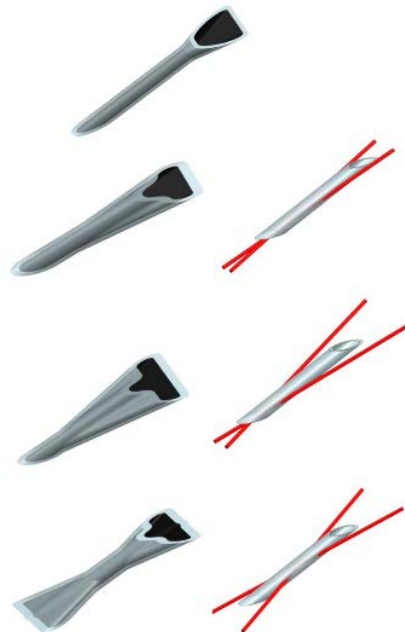


Figure 3.31: Laser drilled Designs

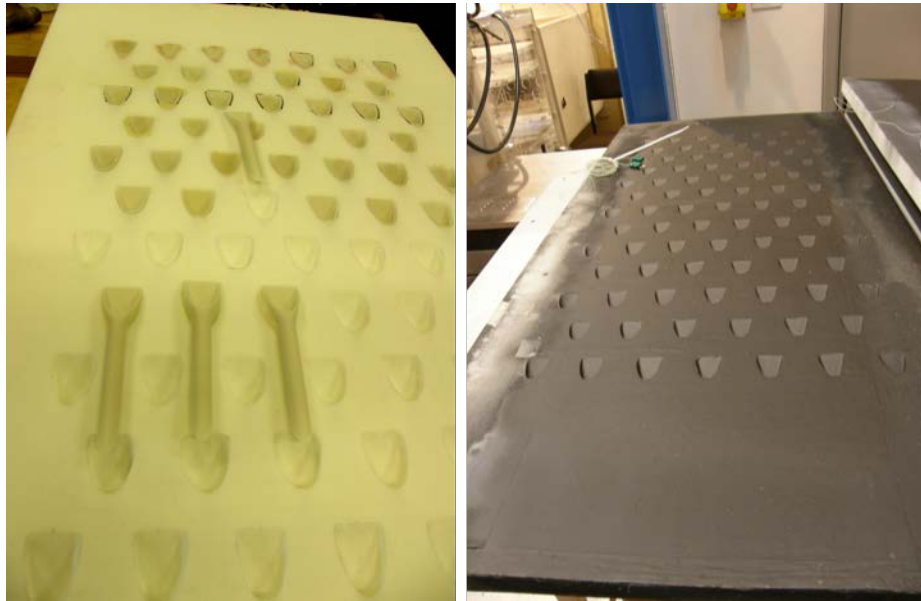


Figure 3.32: Photographs of the insert assembly and the finished foil bonded test plate



Figure 3.33: Test plate with bonded heating foil

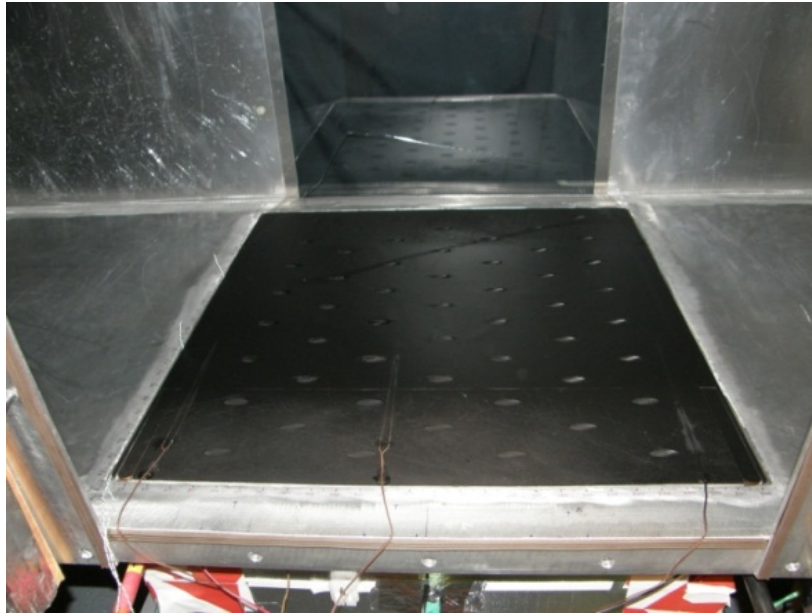


Figure 3.34: Effusion array mounted in test section with heater foil and reference thermocouples

Chapter 4

Measurement techniques and instrumentation

In this chapter, the experimental techniques used to acquire adiabatic film effectiveness and normalised heat transfer coefficient are described in detail and discussed. The testing campaigns for chapters 6 and 7 are also outlined, along with a description of the data acquisition system used to control and monitor the test facility.

4.1 Test Matrix

The experimental results are divided across chapters 6 and 7. Chapter 6 forms the main component of the experimental testing and is focused on a single test plate (test plate 1), operated across a broad range of flow conditions. Within the chapter two different ways of analysing the surface adiabatic effectiveness are presented. The first method is referred to as “direct adiabatic effectiveness measurement” and the second “liner superposition technique”. The latter of these techniques also generates normalised heat transfer data but with limitations placed upon the available density ratio range. Therefore, high density ratio tests have only been investigated using the direct adiabatic effectiveness technique.

A wide variety of parameters were varied in order to generalise the conclusions. A summary of the testing campaign for chapter 6 is shown in Fig. 4.1. A total of four aerodynamic parameters were varied which include bulk free-stream turbulence intensity, length scale, coolant density ratio and coolant blowing ratio. The coolant blowing ratio was incremented in 0.1 steps for the direct effectiveness method and was repeated at each free-stream turbulence and density ratio condition. The blowing ratio range investigated is consistent with that found in dual skin combustor tile arrangements. The turbulent length scale was also varied independently at the free-stream turbulence intensity of 16% by removing the span-wise flow control cylinder as shown earlier in Fig. 3.22.

The second test series labelled “linear superposition” was conducted with a fixed moderate density ratio to prevent foil bond failure. The blowing ratio increment was increased to 0.2 to reduce the number of tests, as the superposition technique required each test condition to be evaluated over a range of heater power settings.

Direct adiabatic measurements			
Dr	1.065 - 1.43	T_c	264 - 289K
Br	0.3 - 1.5	T_∞	308 - 378K
I	0.06 - 2.1	$Re_j \times 10^3$	0.7 - 4.7
Tu	10%, 16%, 25%	$Re_\infty \times 10^3$	2.2 - 3.2
ΛL	13D, 26D	No. Test	96

Linear superposition			
Dr	1.08	T_c	289 K
Br	0.3, 1.5	T_∞	315 K
I	0.082, 2.06	$Re_j \times 10^3$	0.89, 4.5
Tu	10%, 25%	$Re_\infty \times 10^3$	3
ΛL	13D, 26D	No. Test	156

Temperature traverse			
Row Pos	1 st , 3 rd , 5 th	T_c	289K
Dr	1.08	T_∞	315K
Br	0.4, 1.3	$Re_j \times 10^3$	1.2 - 3.9
Tu	10%, 25%	$Re_\infty \times 10^3$	2.2 - 3
ΛL	13D, 26D	No. Tests	12

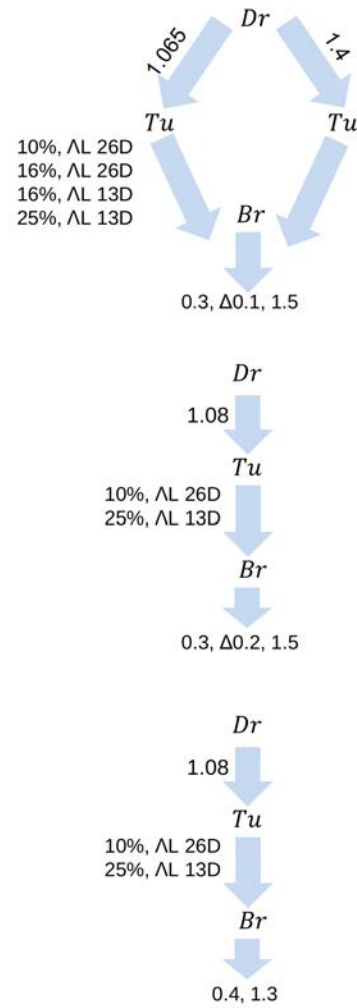


Figure 4.1: Testing campaign for chapter 6

In addition to the surface measurements outlined above, further tests were carried out to establish the coolant film mixing in the free-stream. Due to the extensive time required to perform this type of measurement (of the order 5 hours at each location), experiments were limited to two blowing ratios at the high and low free-stream turbulence conditions. Measurements were made at three span-wise locations and one single central stream-wise location.

Chapter 7 consists of the results obtained for the fanned effusion investigations. The number of flow variables was reduced, as these tests involved multiple test plates. The main focus of these experiments was to investigate the relative performance of fanned and plain hole cooling arrays. In order to take full advantage of the diffusing shape of the fan, higher blowing ratios are required. This is reflected in the blowing ratios tested (Br 2.5-5) and which are representative of a single skin combustor, where the entire pressure drop drives the coolant delivery. A summary of the test conditions is shown in Fig.4.2.

Linear superposition (Test plates 2,3,4)			
Dr	1.2	T_c	267K
Br	2.5 , 5	T_∞	314K
I	5.3 , 21.2	$Re_j \times 10^3$	6 – 11.7
Tu	10%, 25%	$Re_\infty \times 10^3$	2.81
ΛL	13D, 26D	No. Test	156
Temperature traverse (Test plates 2 and 3)			
Row Pos.	1 st , 6 th , 12 th	No. Tests	24

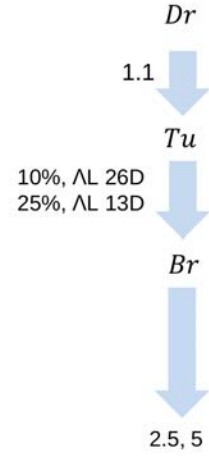


Figure 4.2: Testing campaign for chapter 7

A combination of the surface and free-stream temperature measurements was used to establish both surface cooling performance and coolant mixing with the free-stream. Details of each measurement technique, along with its operational procedure, are described in the following section.

4.2 IR camera measurements

Surface temperature measurements are acquired by using an infrared based imaging system. Every body emits radiation with a spectral distribution $W_{\lambda,0}$ described by Planck's law.

$$W_{\lambda,b} = \frac{2\pi hc^3}{\lambda^5 (e^{\frac{hc}{\lambda kT}} - 1)} \times 10^{-6} \{Watt/m^2 \mu m\} \quad (4.1)$$

Planck's formula, when plotted graphically for various temperatures, produces a family of curves. According to Planck's law, the emitted radiation is dependent upon the object's total temperature and its spectral emissivity

$\epsilon\lambda$. The spectral emissivity is influenced by the material properties and surface quality, and is expressed as a ratio to that of a black body. The latter is an idealised body which emits and absorbs all incident radiation at all wavelengths. In contrast, incident radiation may be reflected or transmitted by real objects. Therefore knowledge of the spectral emissivity is vital when calculating temperature from spectral radiation.

Infrared thermography makes use of the energy emitted at infrared wavelengths. From the target surface to the measuring system, ambient air is present, which has wavelength dependent transmissivity. For infrared thermography two frequency bands are prevalent; the mean infrared from 2 to $5\mu\text{m}$ and the far infrared from 8 to $12\mu\text{m}$. For this study temperatures were expected to fall within the 270-373K range. Since a medium range of surface temperatures is to be detected, an infrared camera (Flir A40M) with a focal plane array (FPA) and an uncooled microbolometer detector with a spectral range of 7.5-13 μm was used. The camera was mounted above a traversable Zinc Selenide window with a 12 μm anti-reflection coating, this was selected because of its high IR transmittance over the appropriate wave length range ($3.5\mu\text{m} - > 12\mu\text{m}$).

As indicated earlier, real physical bodies can reflect and absorb fractions of the incident radiation. Within the test area this can become problematic without careful calibration. Fig. 4.3 shows the main sources of error present in the test section, which can corrupt the reported surface temperature. The incident radiation detected by the camera is comprised of the body surface

component (I_{obj}), attenuated by the atmosphere transmittance (τ) and the surrounding ambient radiation (I_{amb}) from the test section side walls. Furthermore, the atmosphere itself may also emit radiation to be detected by the camera. Other sources of error include optical (i.e. window) effects such as reflections which can be seen as a central halo in the recorded image. In order to reduce the impact of optical reflections, incident radiation and window transmission, an in-situ calibration procedure was developed.

Camera calibration

Before each camera calibration, the tunnel was operated at its intended test condition until thermal equilibrium was achieved. This ensured that the surrounding wall temperatures during calibration were consistent with those present during the experiment. The effusion test plate was then replaced with a 10mm thick aluminium plate, mounted in a 2 inch thick RohacellTM foam with an embedded silicone heater pad. The exposed aluminium surface was coated with high emissivity paint consistent with the test plate itself. The aluminium plate was instrumented with embedded thermocouples and thin film surface thermocouples to monitor both internal and surface temperatures. Details of the calibration plate setup are shown in Fig. 4.4. The high thermal conductivity and thickness of the plate presents a near isothermal surface to the camera optics. With the wind tunnel operating at a stable aerodynamic and thermal condition, the temperature of the plate was gradually increased using the silicone heater pad. During this process, and at

set plate temperature intervals, measurement frames were acquired with the IR camera along with simultaneous measurements of thermocouple temperatures. For each camera pixel the raw IR intensity data was then compared with the corresponding plate thermocouple measurements. A unique polynomial calibration curve was then generated for each camera pixel, describing the relationship between intensity and temperature. The calibration data was stored in a matrix for converting raw IR measurements into temperature maps. This pixel-by-pixel calibration process resulted in surface temperature measurements within $\pm 0.25\text{K}$ of the surface reference thermocouple data. Calibration data of this form was acquired each time the camera location and/or test condition was changed. This approach is much more robust than applying a global calibration to all pixels as window reflections and edge effects can be removed.

A typical calibration curve of a pixel is presented in Fig. 4.5. Each pixel maps to a geometric area of 0.7 mm^2 square on the effusion plate under test. As a result, two separate camera locations were required to capture the full length of the effusion plate. For the high density ratio tests the calibration plate was pre-chilled using cold air from the turbo expander system to ensure the calibration captured the full temperature range expected during effusion plate test runs.

4.3 Coolant film mixing

In addition to the wall surface temperature measurements, coolant film mixing was investigated by traversing a fine-wire exposed bead thermocouple (wire diameter of 0.025 mm) in both span-wise and stream-wise directions through the coolant layer. The exposed bead was located 5mm from the ceramic tube mount to minimise thermal conduction errors to the probe stem. Fig. 4.6 shows the assembled fine wire thermocouple bonded to the ceramic tube. The time-averaged gas temperature was recorded at each location (based on 8 seconds of data), with measurements taken in either 2 or 4mm spatial increments, depending on the test requirements. This traverse data was then compiled to create a spatially resolved thermal profile of the near-wall flow at various free-stream and coolant flow conditions.

4.3.1 Data reduction

Direct adiabatic effectiveness measurements

For the direct adiabatic measurements, IR data was gathered by capturing images directly from the RohacellTM test plate surface without the heater foil. Fig. 4.7 shows a typical surface temperature map generated by the IR camera system after temperature conversion using an appropriate calibration matrix. The image is calculated from 60 individual images taken over a 60 second period, to create a time average wall surface temperature. The low thermal conductivity of the test plate material minimises the heat flux into the surface (see chapter 5), therefore the measured surface temperature represents a

near adiabatic wall temperature. The adiabatic wall temperature is then normalised using the coolant and free-stream delivery temperatures to give the familiar adiabatic effectiveness equation:

$$\eta = \frac{T_{\infty} - T_{aw}}{T_{\infty} - T_c} \quad (4.2)$$

This definition was used to normalise all of the surface temperature data and compare relative cooling performance of the effusion array under various operating conditions.

Superposition technique

The superposition technique requires the ability to adjust the surface temperature independently during the effusion test. This was achieved by varying the power supplied to an ohmic heating foil which was bonded directly onto the surface of the RohacellTM test plate as described in chapter 3. This process generated a set of wall temperatures for a fixed cooling condition. By recording the corresponding wall temperatures the superposition approach which was first described by [72] can be used. The approach takes advantage of the linear relationship between heat transfer coefficient (h_{mw}) and a non-dimensional temperature (ϕ). These parameters are defined by the following equations:

$$h_{mw} = \frac{\dot{q}_{avg}}{T_w - T_{\infty}} \quad (4.3)$$

$$\phi = \frac{T_{\infty} - T_c}{T_{\infty} - T_w} \quad (4.4)$$

A typical test run would require 13 heater power settings to generate wall temperatures T_w over a sufficient range across the foil surface. The method requires a much larger data set with a total of 2340 measurement images for each test condition. Data is then plotted in the form of h_{mw} vs ϕ . A typical set of data points for a single IR camera pixel is shown in Fig. 4.8, with a least-squares straight line fit. The axes intercepts produce the data of interest; adiabatic heat transfer coefficient at $\phi = 0$ and $\frac{1}{\eta}$ at $h_{mw} = 0$. The effectiveness data generated using this method is equivalent to the direct method described earlier. Fig. 4.9 compares two adiabatic effectiveness maps of the same test area using both measurement methods. This type of analysis broadly follows the method outlined by [73].

This process is also repeated for each free-stream turbulence condition with the coolant turned off, providing the equivalent un-cooled heat transfer coefficient. The additional test runs without cooling provides data which can then be used to normalise the film cooled HTC results. This is a necessary step since the presence of the holes in the Ohmic heater foil will impose a non-uniform heat flux at the surface. This prevents direct calculation of the local heat transfer coefficient without the added complexity of performing a thermal-electric simulation of the entire foil as performed by [46]. However, the intention here is to evaluate the heat flux reduction (HFR) parameter which requires only the ratio of $\frac{h_f}{h_o}$.

Heat Flux Reduction

The heat transfer in a film cooled environment can be described by:

$$h = \frac{\dot{q}}{T_{aw} - T_w} \quad (4.5)$$

Where T_w is the surface wall temperature and T_{aw} is the temperature of an assumed adiabatic wall that is driving the heat transfer. In film cooling investigations, h and η are the two quantities of interest. The heat transfer coefficient is sensitive to the flow field which changes considerably with the addition of film cooling. In fact, the introduction of film cooling actually augments the heat transfer coefficient due to the disturbance in the boundary layer. Therefore, a more comprehensive way of describing the film cooling performance is to combine these two quantities. This is captured by the HFR. The HFR was first identified by [7].

$$HFR = 1 - \frac{h_f}{h_o} \left(1 - \frac{\eta_{aw}}{\phi}\right) \quad (4.6)$$

$$\phi = \frac{T_\infty - T_w}{T_\infty - T_c} \quad (4.7)$$

Where ϕ is the non-dimensional metal temperature of the cooling system. Note that ϕ is not measured in this experiment. Therefore, a value for ϕ must be assumed in order to estimate the heat flux reduction. Typical values for an operational film cooled turbine air foil range from 0.5-0.8. The (HFR) data presented in this thesis is evaluated for a constant $\phi = 0.8$.

Flow field profile

The free-stream fluid temperature above the effusion array can be defined by the coolant/free-stream mixture fraction:

$$\eta_{aw} = \frac{T_{\infty} - T_{xy}}{T_{\infty} - T_c} \quad (4.8)$$

Where T_{xy} represents the time averaged local gas temperature measured by the fine wire thermocouple. This allows direct comparison of surface effectiveness and the thermal flow field. Data acquisition was performed by a National Instruments system with cold junction compensation. The time-mean gas temperature was calculated from 8 seconds of data at each measurement location. Typical test runs took around 5 hours to complete in order to capture the full height of the cooling film.

Rig monitor

The relevant physical parameters of the wind tunnel have to be monitored in real time to ensure flow conditions have stabilised at the target test condition. This was achieved by extensive instrumentation in combination with an on-line monitoring system. The system includes both instrumentation of the test rig and data acquisition and processing. A total of 16 parameters are measured to accurately control and describe the test conditions. The parameters are acquired via a National InstrumentsTM SCXI 1600 data acquisition system which monitors the raw data from the various pressure transducers and thermocouples located throughout the rig (see Fig. 4.10). This data is then digitized and passed to a PC running LabViewTM software. A custom

virtual instrument (VI) was created which allows real time data to be displayed during tunnel operation. Fig. 4.11 shows the layout of the VI front panel used to set conditions prior to a test run. This VI also displays the relevant derivatives, namely the main flow velocity U_∞ , the blowing ratio Br, momentum flux ratio M and density ratio Dr. All of the measured parameters are recorded along with relevant derivatives into data files which then undergo a more in depth post processing analysis using MatlabTM code.

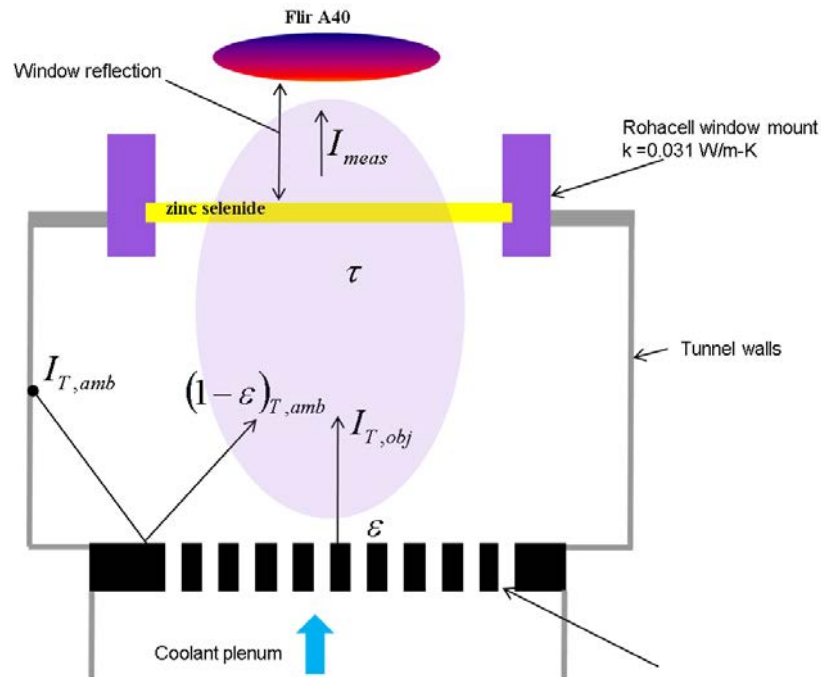


Figure 4.3: IR calibration set-up

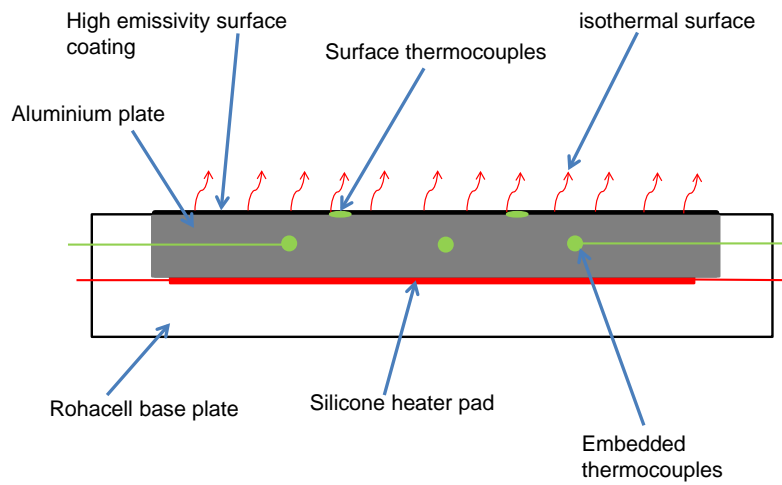


Figure 4.4: Isothermal calibration plate construction

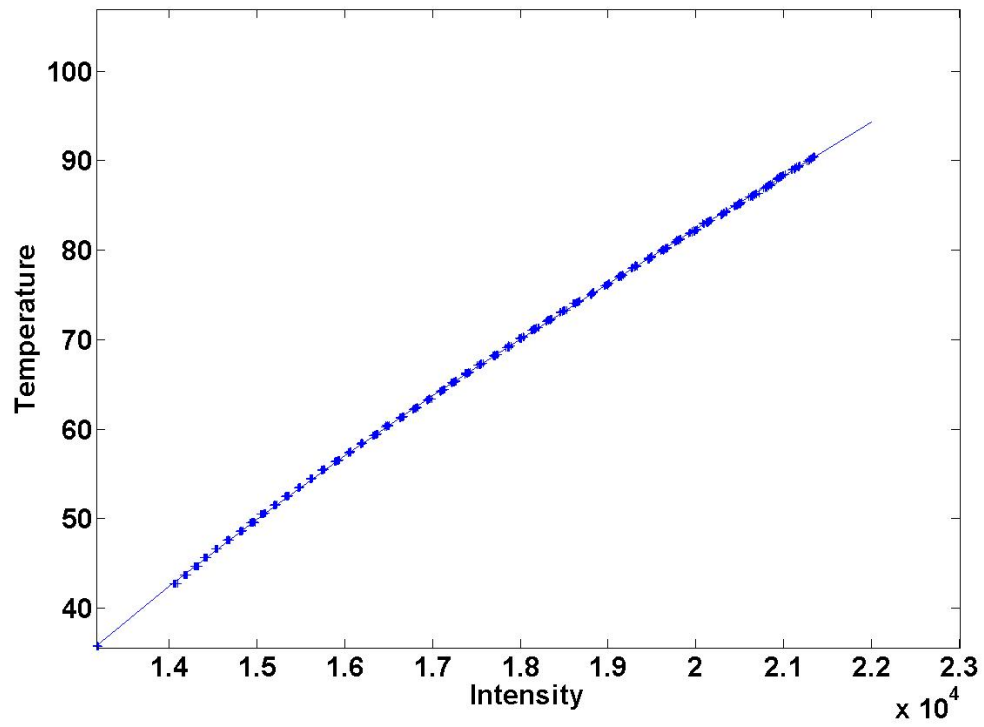


Figure 4.5: IR pixel calibration curve



Figure 4.6: Assembled fine wire thermocouple mounted to ceramic tube

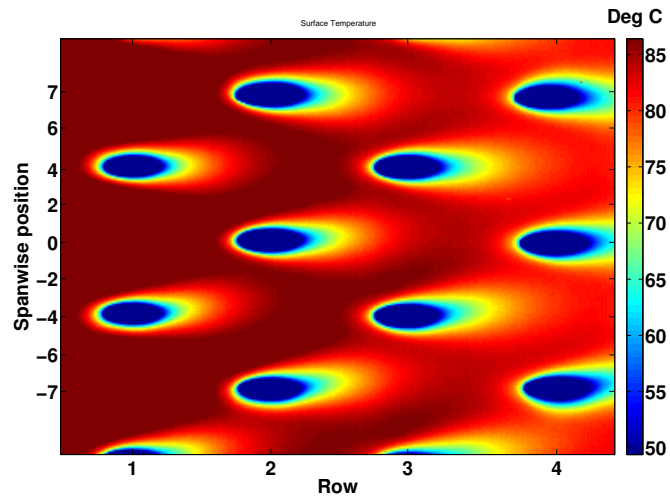


Figure 4.7: Typical surface temperature map from IR camera

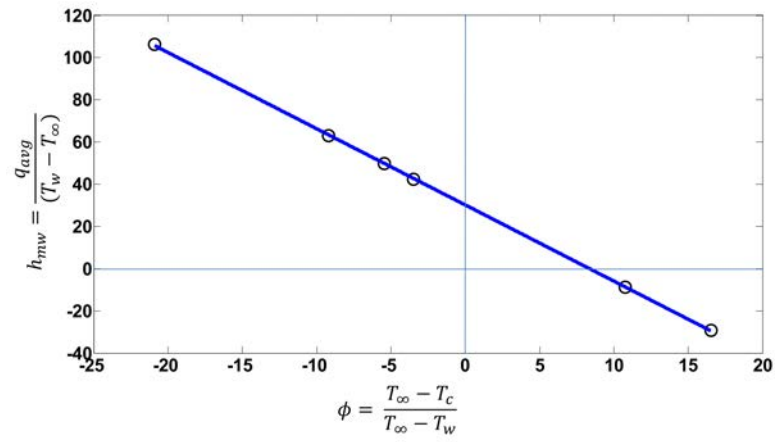


Figure 4.8: Typical data set and line fit used for adiabatic effectiveness and heat transfer coefficient

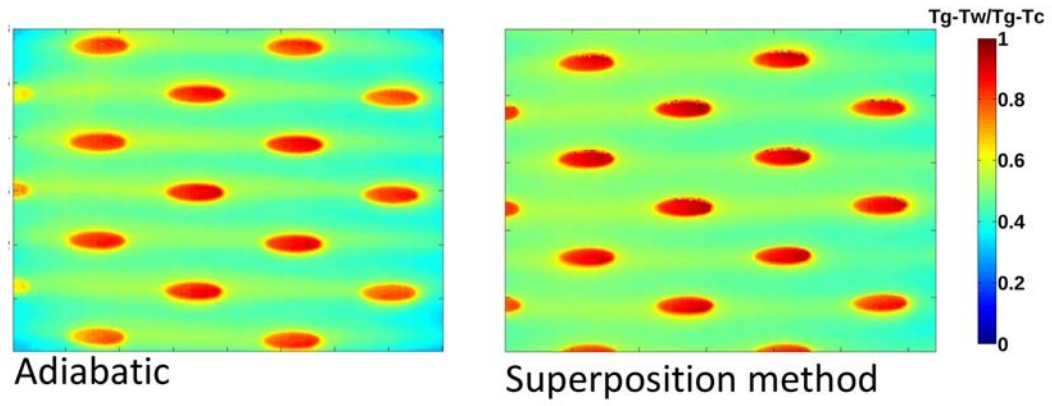


Figure 4.9: Comparison of measurement techniques at $Br\ 2.5\ Dr \approx 1.1$, $Tu\ 25\%$

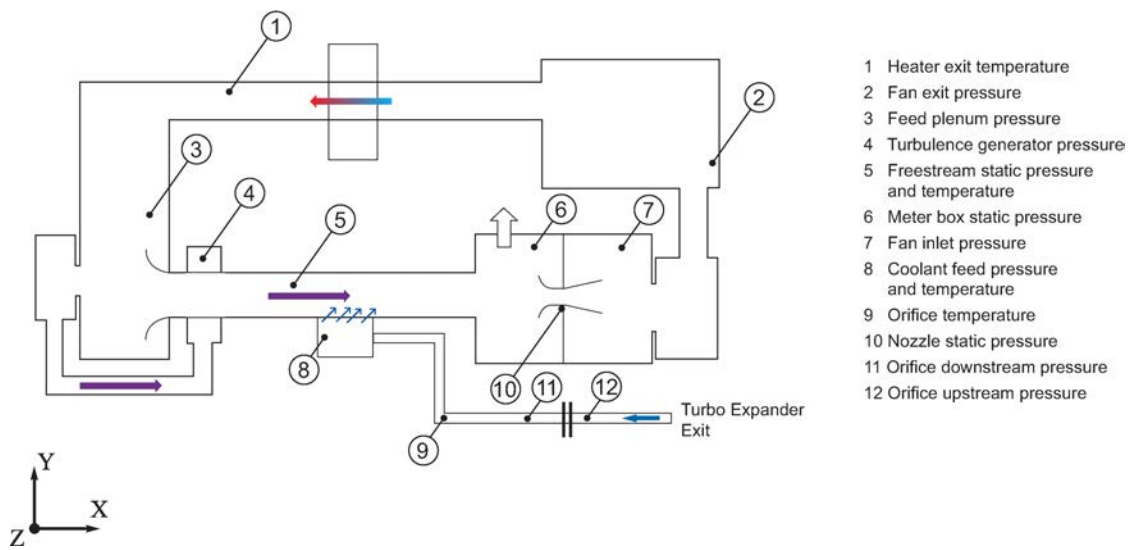


Figure 4.10: Schematic of test rig instrumentation locations

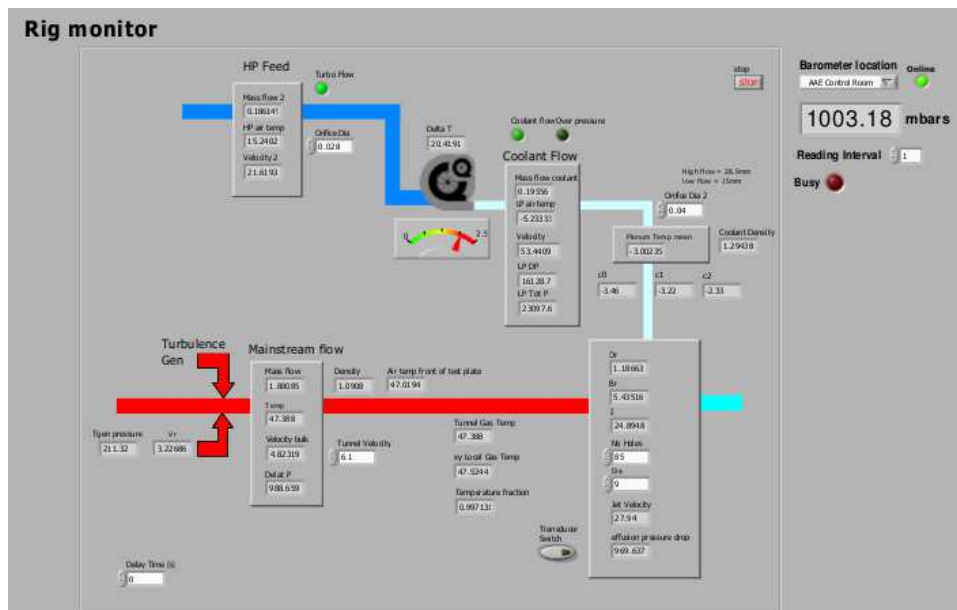


Figure 4.11: Labview™ virtual instrument

Chapter 5

Measurement uncertainty

In this chapter the experimental uncertainty is discussed. The uncertainty analysis is divided into two sections: surface measurements and cooling flow parameters. A conduction model of the Rohacell test plate was developed to calculate the bias error in the measured adiabatic effectiveness. A precision uncertainty analysis is performed which describes the uncertainty associated with data presented in this thesis.

5.1 Measurement uncertainty

The measurement uncertainty can be divided into two main categories, bias uncertainty and precision. A bias uncertainty refers to an error that is made consistently from measurement to measurement. This type of error is relevant to pressure transducers and data acquisition schemes. The precision uncertainty relates to the random errors which vary from measurement to measurement. The following sections detail the measurement uncertainty of the surface temperature measurements and the derived flow parameters.

5.1.1 Surface temperature measurements

Thermocouples form the basis of the surface temperature measurement and are used to calibrate the IR camera system using the in-situ calibration method described in chapter 4. The kinds of errors that make up the precision uncertainty of thermocouples are differing wire junctions, drifting cold junction and electrical noise. Any uncertainty in measurements of the calibration plate wall temperature directly impacts the uncertainty in the reported IR surface temperature. Consequently the T_w measurement has the same uncertainty as the other thermocouple measurements of T_∞, T_c .

The temperature measurements were made using K-type and N-type thermocouples and data acquisition was performed by an 8 channel National InstrumentsTM SCXI 1120 card with an additional SCXI 1328 cold junction module. All of the thermocouples were calibrated against a PRT temperature probe in a temperature controlled bath prior to use. This allowed tempera-

tures to be reported with an uncertainty of ± 0.5 °C.

For these experiments, the main source of bias uncertainty arises from conduction through the RohacellTM foam test plate. This can cause a bias in the surface temperature data. Since the experiment relies on the fact that the surface is adiabatic (zero heat flux), any conduction through the test plate will result in lower wall temperatures creating a bias in the measured adiabatic wall temperature. In order to quantify the effects of these fluxes on the measurement of the local adiabatic wall temperature, a conduction model of the effusion plate was developed similar to [19] using the commercial software Star-CCM+TM. In order to estimate the typical impact of wall conduction on effectiveness measurements, a case was considered with high blowing and density ratio, as these conditions would generally require the highest level of correction. An accurate three-dimensional model of the actual test plate was created and meshed using polyhedral volumes (approximately 185,000). The computational mesh was refined around the effusion holes in order to resolve the higher temperature gradients created in the near-hole regions.

The material properties of the modelled wall were set at the values quoted by the manufacturer and are listed in table 5.1.

Grade	51 IG-F
Density	0.0513 Kg/m ³
Thermal conductivity	0.029 W/m-k

Table 5.1: Rohacell material properties

The thermal boundary conditions on the surfaces of the test plate were defined by a combination of convective heat transfer correlations and measured surface temperature maps from the wind-tunnel experiment. The surface heat transfer coefficients were defined by a turbulent flat plate correlation [74]. The coolant side of the test plate was exposed to a uniform fluid temperature, and modelled as a uniform temperature boundary (this is considered a worst case approach). The effusion holes were defined as convective walls with ambient temperature set at the coolant delivery temperature and heat transfer coefficients defined by a fully-developed turbulent pipe flow correlation [74]. All other surfaces were modelled as adiabatic walls. The radiative heat transfer from the surrounding channel walls was approximated by a simple enclosed model:

$$q_{rad} = \sigma \varepsilon_w (T_a^4 - T_w^4) \quad (5.1)$$

substituting into equation 5.1 and re-arranging for adiabatic wall temperature yields:

$$T_{aw} = T_w + \frac{q_w - q_{rad}}{h_f} \quad (5.2)$$

After solving for the plate temperature distribution using Star-CCM+™, the local wall-surface heat flux was then divided by the assumed heat transfer coefficient on the hot-side of the plate to yield an estimate of the temperature difference between measured wall temperature and the modelled adiabatic wall temperature. Fig. 5.1 shows a contour plot of the temperature correction. As might be expected, the leading edge of the cooling hole shows the largest temperature correction, as at these locations the wall is thin with only a thin wedge of material between mainstream and coolant flows. Immediately downstream of the ejection hole a localized over prediction in surface temperature is observed, as the radiative heat flux dominates. Apart from some localised high temperature corrections, the majority of the measurement surface requires adjustment of less than two degrees. Therefore a surface temperature error estimate of 2°C has been applied to the data reduction process to account for plate conduction errors. A more sophisticated correction could be achieved by running additional simulations at different flow conditions. While this would be of negligible benefit in this low conduction case, it would provide a useful tool for correcting more conductive materials.

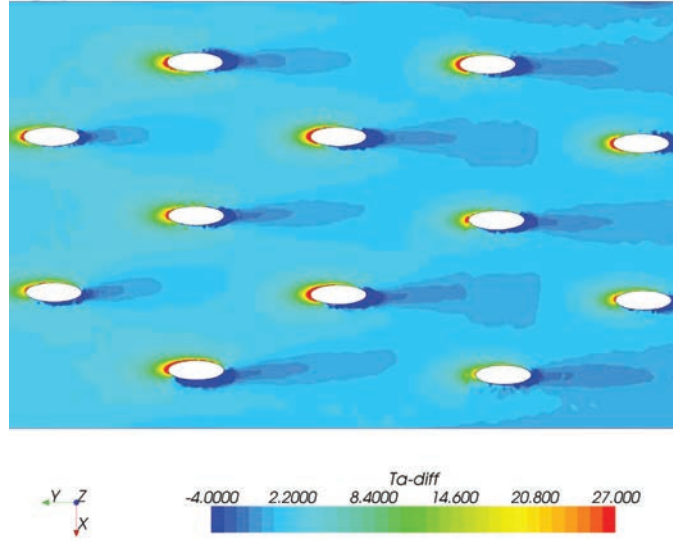


Figure 5.1: A contour plot of the difference between measured wall surface temperature and modelled adiabatic wall temperature.

Direct film effectiveness

With uncertainty values established for the individual temperature measurements the overall uncertainty in the effectiveness measurements was determined based on the well established method described by Kline-McClintock [57]:

$$\eta_{aw} = \frac{T_g - T_{aw}}{T_g - T_c} \quad (5.3)$$

$$\pm \eta_{aw} = \left[\left(\frac{\partial \eta}{\partial T_g} \right)^2 (\varepsilon T_g)^2 + \left(\frac{\partial \eta}{\partial T_c} \right)^2 (\varepsilon T_c)^2 + \left(\frac{\partial \eta}{\partial T_{aw}} \right)^2 (\varepsilon T_{aw})^2 \right]^{1/2} \quad (5.4)$$

and therefore

$$= \left[\left(\frac{T_c - T_{aw}}{(-T_g + T_c)^2} \right)^2 (0.5)^2 + \left(\frac{T_g - T_w}{(-T_g + T_c)^2} \right)^2 (0.5)^2 + \left(\frac{-1}{(T_g - T_c)^2} \right)^2 (2)^2 \right]^{1/2} \quad (5.5)$$

For the high density ratio tests (Dr=1.4), gas temperatures were typically around Tg= 363K and Tc=265.5K for the mainstream and coolant flow circuits respectively. Substituting these values into equation 5.5 for an area where the wall temperature Taw = 343k (near effusion exit), yields an effectiveness value of $0.2 \pm 10\%$. The percentage uncertainty decreases for higher values of η_{aw} , from as high as 27% at $\eta_{aw} = 0.04$ to as low as 4.7% at $\eta_{aw} = 0.44$

Superposition measurements

The linear superposition principle used to determine η , h_f and h_o from the heater foil based experiments is calculated by a least-squares straight line fit through experimental data points. The error of the slope and axis intercept associated with a straight line fit from data points with equal error are calculated using the following equations [75]:

$$Slope \ Error = S \times \sqrt{\frac{n}{(n \sum x_i^2) - (\sum x_i)^2}} \quad (5.6)$$

$$Intercept \ Error = S \times \sqrt{\frac{\sum x_i^2}{(n \sum x_i^2) - (\sum x_i)^2}} \quad (5.7)$$

$$S = \sqrt{\frac{\sum (y_i - ax_i - b)^2}{n - 2}} \quad (5.8)$$

The uncertainty values quoted below are representative of the measurement area:

$$h_o = \pm 3\% \quad h_f = \pm 2.5\% \quad \frac{h_f}{h_o} = \pm 5.5\% \quad \phi = 5\% \quad \eta_{aw} = \pm 2\%$$

A summary of typical surface measurement error is shown in table 5.2

Parameter	Uncertainty [\pm %]	Method
η_{aw}	4.7	Direct
η_{aw}	2	Superposition
h_o	3	Superposition
h_f	2.5	Superposition
$\frac{h_o}{h_f}$	5.5	Superposition

Table 5.2: Summary of surface measurement error

5.2 Flow parameters

The flow parameters are calculated from the free-stream and coolant mass flow rates. The free-stream mass flow rate was measured across a nozzle and diffuser arrangement (see appendix A.1). The coolant flow rate was measured downstream of the turbo expander and is shown in Fig. 5.3. The pressure drop across each system was measured using differential transducers. The voltage output from each transducer is monitored by a National Instruments[™] 8 channel lowpass butterworth filter module SCXI-1143. An in-situ calibration of each transducer was performed using a PACE[™] 5000

series pressure controller with a precision of up to 0.005% reading $\pm 0.005\%$ full scale.

A typical pressure transducer calibration plot is shown in Fig. 5.2. Two different types of pressure transducers are used in these experiments: The main tunnel circuit pressures were all recorded using Furness™ differential pressure traducers with an accuracy of $\pm 0.5\%$ of reading. The differential pressure across the orifice plate was measured using a Sensor Technics™ differential transducer with a $\pm 0.25\%$ of full scale output.

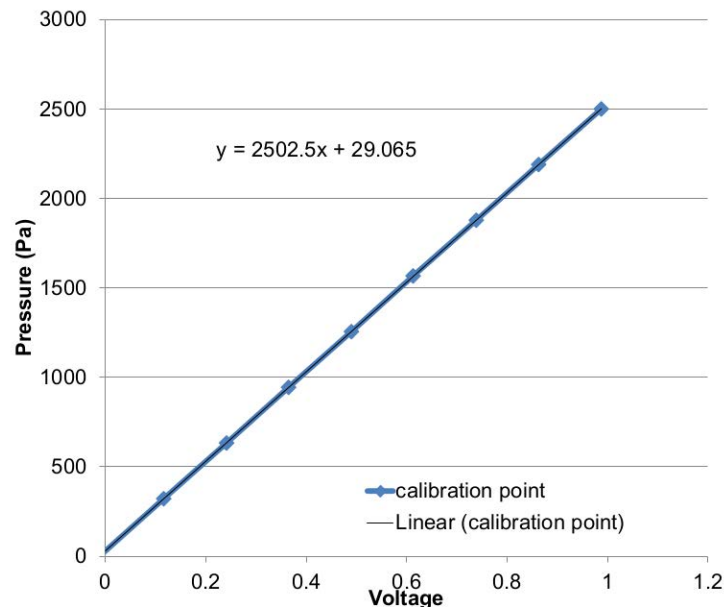


Figure 5.2: Typical pressure transducer calibration plot

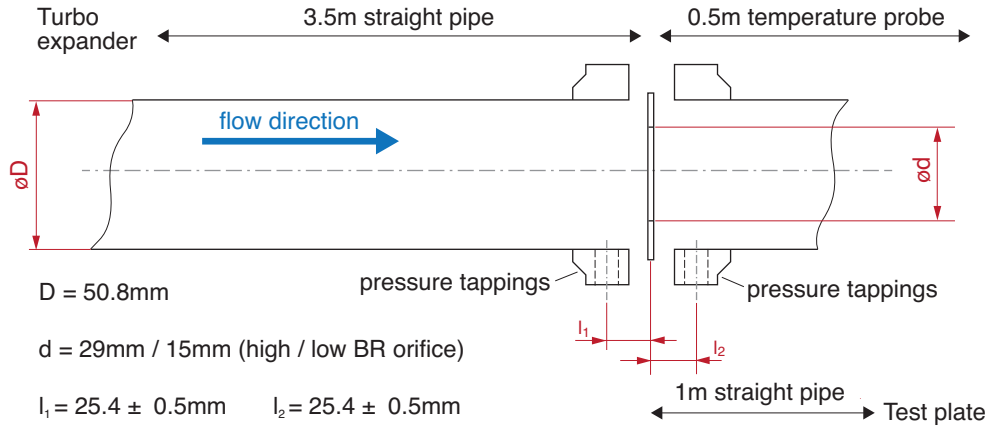


Figure 5.3: Schematic of orifice plate configuration for coolant mass flow measurement

The detailed calculation of the uncertainty of the mass flow measurements are presented in appendix A.6. A summary of the uncertainty of the mass flow and derived flow parameters are presented in table 5.3.

Parameter	Uncertainty [\pm %]
$M_{coolant}$	1.7
$M_{freestream}$	1.36
ρ_c	0.56
ρ_∞	0.4
BR	4
DR	1.1

Table 5.3: Flow parameter uncertainties

Hot wire measurements

The main sources of uncertainty which affect the measurement of velocity using hot-wire measurements result from: Calibration, A/D conversion resolution and linearisation (curve fitting). The uncertainty analysis detailed below broadly follows the method outlined in [76].

Calibration equipment

$$U(U_{cal}) = \frac{1}{100} \sigma_{U_{cal}\%} \quad (5.9)$$

Where: $\sigma_{U_{cal}\%}$ is the standard deviation of the calibration velocity. The calibration of the hot-wire probe was performed using a dedicated Dantec™ calibration unit. The calibration nozzle was operated across a flow rate range of 1-10m/s. It is suggested that the value of the standard deviation is therefore given as 1.02% [76].

A/D board resolution

The uncertainty resulting from the resolution of the A/D conversion may be found using the following formula:

$$U(U_{res}) = \frac{1}{\sqrt{3}} \cdot \frac{1}{U} \cdot \frac{E_{AD}}{2^n} \cdot \frac{\partial U}{\partial E} \quad (5.10)$$

Where E_{AD} is the voltage range of A/D converter (National Instruments PCI6052e), which in this case is a maximum of 10V, and n is the resolution in bits which is 16. The partial derivative may be found from the calibration curve equation and is given by:

$$\frac{\partial U}{\partial E} = \frac{2E}{Bn} \left(\frac{E^2 - A}{B} \right)^{\frac{1-n}{n}} \quad (5.11)$$

The wire voltage, E may be found from a linearisation approach using Kings Law [77]

$$E = \sqrt{BU^n + A} \quad (5.12)$$

The value of uncertainty is a function of the measured velocity and is a maximum at the lowest velocity (1m/s). Therefore the uncertainty value is evaluated at 1m/s.

Linearisation

The uncertainty associated with the curve fitting of data points during calibration may be estimated as follows:

$$U(U_{lin}) = \frac{1}{100} \sigma_{\Delta ulin\%} \quad (5.13)$$

Where $\Delta ulin\%$ is the standard deviation of the error between data points recorded and derived calibration curve. This quantity is calculated directly from Dantec[™] Streamware[™] calibration software, a typical calibration produces a value of 0.097%. The components of the measurement uncertainty are summarised in table 5.4.

Error Source	Value ε_i
Calibration	0.0102
Linearisation	0.0010
A/D Conversion Resolution	0.0007

Table 5.4: Hot-wire measurement uncertainties

The total measurement uncertainty may be calculated from:

$$\varepsilon_{tot} = 2\sqrt{\sum_{i=1}^n \varepsilon_i^2} \quad (5.14)$$

Using the values in Table 5.4, gives an velocity uncertainty of ± 0.0205 , or approximately $\pm 2\%$.

Chapter 6

Investigation of plain hole effusion subjected to highly turbulent free-stream conditions

An extensive experimental study has been conducted to investigate the performance of a film cooling array at engine representative conditions. The tests were conducted in two phases: The first phase examined a purely adiabatic test case at a range of blowing ratios, density ratios and free-stream turbulence conditions. For the second phase, a heater film was attached to the test plate to allow non dimensional HTC to be evaluated at unity density ratio. Both sets of data are presented and explained in the following chapter.

6.1 Adiabatic effectiveness

The results of adiabatic tests are presented in this section and are divided into three specific areas. Firstly, the effects of varying free-stream turbulence on span-wise averaged and spatially averaged adiabatic film-cooling effectiveness; secondly, the impact of free-stream conditions on the mixing of coolant and free-stream flows; thirdly, the effects of density ratio on cooling effectiveness. Together, the results capture the effects of free-stream turbulence on the film-cooling behaviour of an angled effusion geometry. Full surface effectiveness contour maps were measured based on the method described in chapter 4. Fig 6.1 shows the installed effusion test plate. The dashed line shows the measurement area used for IR data processing. The location of the embedded surface reference thermocouples are also shown.

6.1.1 Free-stream turbulence effects

One of the main objectives of this work was to investigate effusion film-cooling effectiveness under highly turbulent free-stream conditions. Fig 6.2 shows the measured impact of free-stream turbulence on span-wise average adiabatic effectiveness for three blowing ratios at a constant density ratio of 1.4. The effusion holes have been removed from the analysis, as measurements in this area were inaccurate due to the orientation relative to the IR camera sensor array. At the lowest BR considered (0.3), it can be seen that increasing the free-stream turbulence level from 10% to 16% causes a small reduction in the film-cooling effectiveness in the more downstream area, while there is no further change when increasing the turbulence intensity to

25%. At the highest BR (1.5), the impact of free-stream turbulence level is markedly different. In this case the effect of the elevated turbulence is now seen to lead to a marked increase in the measured adiabatic effectiveness, particularly in the downstream region. This suggests that there is increased turbulent transport of coolant fluid back towards the wall surface. This result seems counter intuitive at first, as elevated free-stream turbulence is generally seen as detrimental to film cooling performance. However, the relatively few single row studies which have included free-stream turbulence augmentation (for example, [31] and [34]) have demonstrated a similar potential for improved film coverage at elevated free-stream turbulence conditions. This coolant transport mechanism, is an inefficient way of augmenting effectiveness since it relies upon a strong interaction with the hot mainstream flow.

The mechanisms which produce this result can be seen in more detail from adiabatic surface maps presented in Figs. 6.3 to 6.5. Fig. 6.3 shows the variation in film effectiveness with both blowing ratio and free-stream turbulence intensity at the lower blowing rate range (0.3 - 0.7). The lefthand set of images shows the variation of effectiveness with BR at 10% free-stream turbulence intensity, while the right hand set of images shows the equivalent data for 25%. For the lowest BR condition (0.3), the data clearly shows an increase in lateral spreading of the coolant immediately downstream of the ejection points which is caused by the increase in bulk turbulence levels. The lateral spreading is also accompanied by a reduction in streamwise coolant coverage as the cooling layer mixes out more quickly with the free-stream. At the low blowing rates (<0.7), the benefits gained from increased lateral

spreading are outweighed by the reduction in streamwise coverage. As the coolant blowing rate approaches 0.7 the coolant jet begins to change mode from an attached cooling jet, which produces a coolant film on the surface of the plate, to a detached cooling jet which penetrates into the free-stream. In this transitional phase the lateral spreading and streamwise reduction in coolant imposed by the free-stream conditions are approximately equal, which produces a collapse in the span-wise average data (Fig. 6.2) at BR 0.6. The change in coolant delivery mode also signals a shift in the response to increased free-stream turbulence. Above the point at which the coolant detaches from the surface $BR > 0.7$ (see Fig. 6.4 and 6.5) the centerline effectiveness is already very poor, so any further reduction due to increased free-stream turbulence is marginal. However, the turbulent transport of coolant induced by the high free-stream turbulence improves the lateral spreading of coolant which ultimately benefits the film-cooling effectiveness.

At the highest blowing ratio tested here ($BR=1.5$), an increase in spatially averaged effectiveness of 74% is observed at $Tu=25\%$, relative to the 10% turbulence case. A summary of the spatially averaged results for high and low turbulence levels is given in Table 6.1. These results are in stark contrast to a similar study using normal angled effusion [42], which reported a consistent decrease in spatially averaged effectiveness with increasing free-stream turbulence. This indicates that when jet lift-off is pronounced, as in the case of normal jets, the free-stream turbulence mixes the coolant jet so extensively that any transport of coolant back towards the surface is of negligible benefit. In the angled effusion case jet lift-off is reduced, thereby

allowing free-stream turbulence to transport the coolant into the near-wall area without completely mixing out with the free-stream. The relatively modest gains demonstrated in earlier angled single row studies are merely enhanced by the additional rows found in arrays. The successive rows increase the coolant concentration above the surface which increases the amount of coolant present in the near wall mixing region. Although all of the data shown in this section is at the higher density ratio of 1.4, the same trends were also found at the lower density ratio of 1.06. The only difference was a shift in the transition from an attached to a detached jet occurring at a slightly higher blowing rate, as the increase in coolant density produced a jet with a lower momentum for a given blowing ratio.

BR	Tu=10%	Tu=25%	$\Delta\%$
0.3	0.104	0.094	-9.2
0.4	0.113	0.108	-4.4
0.5	0.111	0.115	3.2
0.6	0.111	0.121	9.0
0.7	0.096	0.123	27.9
0.8	0.089	0.120	35.0
0.9	0.079	0.117	47.0
1.0	0.072	0.115	58.7
1.1	0.067	0.112	67.6
1.2	0.065	0.110	69.9
1.3	0.064	0.109	69.8
1.4	0.061	0.114	84.9
1.5	0.063	0.110	74.9

Table 6.1: Spatially averaged adiabatic effectiveness at high and low turbulence intensity (masked effusion holes).

6.1.2 Free-stream turbulence length scale

The capabilities of the wind-tunnel turbulence generator have allowed a unique investigation of the impact bulk turbulent integral length scale has on film cooling effectiveness. For a free-stream turbulence intensity of 16%, normalised integral length scales of $\Lambda L/D = 13$ and 26 have been investigated; note that the other free-stream flow parameters, such as the mean velocity and spatial profile, were otherwise unaffected by this change. The

larger length scale of $\Lambda L/D = 26$ was shown to be representative of the scale generated by fuel injectors in engine-standard combustors. The results associated with this part of the study are presented in Figs. 6.6 and 6.7. Fig. 6.6 shows the surface effectiveness for three blowing ratios; 0.3, 0.7 and 1.5. For the two length scale cases considered, it can be seen that the impact of length scale is relatively low, although some increase in effectiveness is evident in the more downstream regions at a BR of 0.3 at $L/D = 26$. Fig. 6.7 shows this difference more clearly in a span-wise averaged adiabatic effectiveness plot for BRs of 0.3 and 1.3. This result differs from a similar study by [31] which reported significant increases in film effectiveness with increases in length scale for a single row of cooling holes. However, this previous study considered a very low length scale range of $\Lambda L/D = 0.12$ to 0.33 . This improvement in effectiveness is thought to be brought about by the disruption of the counter rotating vortex pair (CRVP) which entrain hot gas towards the effusion surface. These localised structures are likely to be quickly disrupted by the large scale turbulent structures in the free-stream, even at the smaller scale of $\Lambda L/D = 13$ tested here. Therefore, increasing the length scale further has only a marginal effect on film-cooling effectiveness, as the turbulent structures are already much larger than any localised flow features. Another potential reason for this insensitivity to length scale is due to the relatively low turbulence intensity levels. The variation in length scale was only possible at a free-stream turbulence intensity of 16 %, which is relatively low in combustor terms. At these intensity levels the structures may have insufficient energy to impose any major disruption to the film coverage.

6.1.3 Flow field temperature measurements

The data presented so far has focused on the surface cooling performance. To understand in more detail how the surface coolant film develops, fluid temperature field measurements have been obtained at three traverse locations positioned downstream of the 1st, 3rd and 5th row of the cooling holes.

Fig. 6.8 - 6.11 show the span-wise gas temperature traverse data along with the corresponding adiabatic effectiveness data. The effectiveness contours become saturated in the jet exit/core region ($\eta \approx 1$) as the scale is limited to 0.5 for clarity. The reduced scale enabled the gas temperature data to be plotted using the same scale as the surface effectiveness data which is typically in the lower range. The gas temperature measurements were obtained at relatively coarse spacial increments of 4mm. Note that the traverse measurements do not include a 2mm region near the test surface to avoid damage to the fine wire thermocouple. The span-wise traverse temperature data can be used to reveal three of the main effects imposed by variations in the free-stream turbulence: 1) the mixing rate of the jets with the free-stream coolant, 2) the penetration of the jets into the free-stream, 3) the lateral spreading of the cooling jets.

The temperature traverse data shows quite clearly the difference between an attached and detached cooling jet. At the blowing ratio of 1.3 a well defined coolant jet is located above the test plate. The gas temperature measurements in Figs. 6.8 and 6.9 show that the increased level of free-stream

turbulence causes a significant reduction in the coolant concentration within the cores of the attached jets. The reduction of the core coolant concentration produces a consequent reduction in centre-line cooling effectiveness as seen in the associated surface effectiveness plots. The temperature traverse measurements also reveal the level of lateral coolant spreading; it is clear that the elevated free-stream turbulence leads to an increase in spreading in the jets emerging from each row. The surface effectiveness data presented in the previous section showed that free-stream turbulence has more impact on the cooling performance once the jet becomes detached from the surface. Fig. 6.10 and 6.11 show how the gas temperature field differs when the detached cooling jet is subject to 10% and 25% free-stream turbulence. In the low turbulence case the remnants of the two neighbouring cooling jets from the 2nd row are clearly visible. As the free-stream turbulence increases, these jets mix out completely reducing the streamwise distance of the coolant core. The reduction in core coolant is shown in more detail in Fig. 6.12 and 6.13, where the streamwise gas temperature at these conditions is mapped through rows 2-4. There is also clear evidence in this data that coolant mixing produces lower near wall temperatures. The process of mixing is also evident at low blowing conditions but is augmented once the jets lift off the surface. This mixing process becomes even more dominant as successive rows augment the thickness of the coolant layer. This results in a more rapid build up of the coolant film. For the detached jets in low free-stream turbulence case, the lack of mixing allows the coolant to remain in coherent jet structures above the test surface producing poor film cooling performance.

6.1.4 Density ratio

Typically experimental measurements of film cooling effectiveness are conducted at density ratios which are much lower than those encountered in the real engine environment. This is primarily due to the additional cost of the infrastructure required to enable representative density ratios to be simulated. To assess the impact of density ratio on cooling performance, the cooling effectiveness has been investigated at DRs of 1.065 and 1.4 for two free-stream turbulence levels. Fig. 6.14 to 6.16 shows the area-averaged adiabatic effectiveness data gathered. These are plotted against the three main coolant flow parameters; momentum flux ratio (I), velocity ratio (VR) and blowing ratio (BR). It is apparent that for high coolant injection levels ($VR > 0.8$) the elevated free-stream turbulence condition leads to a near doubling of the area-averaged effectiveness due to the increased spreading of coolant identified earlier. However, at these conditions the impact of density ratio as an independent parameter is relatively weak. Apart from some divergence at the very low VR conditions (when the cooling flows are attached to the wall) the effectiveness data appears to be reasonably well correlated by I, VR and BR. When these data are plotted as a function of BR (Fig. 6.15) the peak effectiveness is shifted to a higher blowing ratio case when the density ratio is increased: however, the behaviour is different for the two turbulence intensity cases presented. Similar effects have been observed in single row studies ([21] and [20]). In these studies the shift in the effectiveness peak was attributed to the fact that high density coolant has a lower momentum flux for a prescribed blowing ratio, thus delaying onset of jet separation which

signals a mode change of the coolant jet. The two density ratios scale well with momentum flux, confirming jet separation is primarily a function of momentum flux. The velocity ratio scaling falls somewhere between momentum flux and blowing ratio. Once jet separation has occurred, effectiveness scales reasonably well with velocity ratio. For the blowing ratio range considered here, of BR 0.3 - 1.5 which is typical of dual skin cooling arrangements, momentum flux is the appropriate parameter to scale for different density ratios. The area-averaged plots also show how increased free-stream turbulence widens the coolant flux range over which efficient cooling is possible. This provides a very powerful conclusion for experimental test facilities. By using momentum flux as the scaling parameter, significant costs in infrastructure can be avoided as data collected at low DR's can still be applied to engine representative DR's by scaling with momentum flux.

6.2 Normalised Heat Transfer Coefficient

The results presented in the previous sections have detailed the film cooling performance in terms of an adiabatic effectiveness and while this parameter indicates where the coolant is present, it gives no information about the surface heat transfer coefficient. To remedy this, the test plate was modified to enable the measurement of the surface heat transfer coefficient (HTC). For the second phase of testing an ohmic heating foil was bonded to the test surface to provide a means to vary surface wall temperatures independently of the cooling condition. Full details of this modification and the data reduction technique used to calculate the film effectiveness, normalised HTC and

a combined parameter of heat flux reduction (HFR) are described in chapter 4. Fig. 6.17 - 6.19 show a sample of a typical data set used to derive the normalised HTC. Fig. 6.17 is a measure of the average surface heat flux with the coolant turned on, while Fig. 6.18 shows the same test plate area, with the coolant turned off, under the same free-stream conditions. By combining these two data sets as a ratio of coolant injection relative to the comparable un-blown case (h/h_o), the effect of introducing the coolant in terms of HTC augmentation can be established (Fig. 6.19).

The spatially-resolved normalised HTC measurements for various blowing ratios as well as high and low free-stream turbulence intensities are presented in Fig 6.20. At low coolant blowing ratios the main feature of the data is a small region of reduced HTC located immediately downstream of the injection point. This feature is present at both high and low free-stream turbulence conditions. At low blowing conditions the well behaved nature of the cooling jet (attached to the surface) has only a small effect on the HTC. As the blowing ratio increases and the jets begin to detach from the surface, the cooling jets create a much larger disturbance in the near wall flow. This disturbance produces a marked increase in HTC, at the highest blowing ratio tested here (BR 1.5) an increase of 14% is observed. This increase in HTC is considered to be caused by the higher levels of shear at the jet boundary. The higher levels of shear increases the turbulence levels in the near wall region, augmenting the heat transfer. The spacing between each successive row does not allow the near wall flow to recover from the disruption caused by coolant injection. Therefore, the augmentation in HTC

becomes more pronounced as the coolant film develops with each successive row. The measurement technique used to gather the normalised HTC data also allows the adiabatic effectiveness to be calculated from the same data set, as outlined in chapter 3. The corresponding surface effectiveness data is presented in Fig 6.21.

The span-wise average measurements of the normalised heat transfer coefficient (h/h_o) and adiabatic effectiveness for high and low free-stream turbulence are presented in Fig. 6.22 and 6.23. The normalised heat transfer data emphasises the impact of blowing ratio on the wall HTC, with low blowing conditions having a small effect on HTC, while an increasingly pronounced increases in HTC was observed once the jet detaches from the surface. The introduction of the coolant for the lower free-stream turbulence case causes a greater increase in normalised HTC. This is because the baseline HTC level is lower, so the introduction of coolant film has a more pronounced effect. The span average data also shows that the normalised HTC quickly becomes asymptotic with downstream distance and finally repeating after the fourth row of effusion holes. The film effectiveness on the other hand is much slower and would require more rows than the 7 tested here in order to become asymptotic. The explanation for this difference is that the cooling film build up is much slower due to mixing with the free-stream, whereas the normalised HTC is only dependent on the near wall flow disturbance which occurs rapidly as the jet exits into the free-stream.

As mentioned at the start of this section, film effectiveness data only gives an indication of the coolant coverage. The normalised HTC data shows that the introduction of coolant also has a negative impact on the surface cooling, in the form of HTC augmentation. In order to assess these opposing factors a parameter known as the heat flux reduction (HFR) is used to indicate the effect on the wall heat flux (see chapter 3). The span-wise average HFR for low and high free-stream turbulence conditions is presented in Fig. 6.24. The distribution is similar to the normalised HTC data shown in Fig. 6.22, with a loose grouping dependent upon coolant blowing ratio. The differences between each blowing ratio correspond to the differences in the span average effectiveness measurements. The combination of a high blowing ratio (BR 1.5) and low free-stream turbulence produces the lowest HFR, resulting from poor surface effectiveness and augmentation of HTC.

6.3 Summary

An angled effusion cooling geometry with a combustor relevant design has been evaluated in terms of adiabatic effectiveness and normalised HTC over a range of free-stream turbulence conditions; 10, 16 and 25% intensity, integral length scale-to-coolant hole diameter ratios of 13 and 26; coolant to free-stream density ratios of 1.1 and 1.4.

- The detailed adiabatic surface effectiveness measurements on the effusion array, measured using the IR camera system, showed increased free-stream turbulence can both improve and reduce the film effectiveness depending upon the coolant jet blowing ratio.

- The mode change of the coolant jet signals a change in the response of the cooling film to free-stream turbulence intensity. Once the coolant detaches from the surface the elevated turbulence increases the mixing between the film and the free-stream. This then transports some of the detached coolant back towards the surface.
- At the highest blowing ratio ($BR = 1.5$) an increase in spatially averaged effectiveness of 74% is observed at $Tu=25\%$ relative to the 10% turbulence case.
- Increasing free-stream turbulence improves lateral spreading and also reduces the streamwise coverage as the film mixes with the free-stream.
- At a turbulence intensity of 16% a doubling of the turbulent length scale from $\Lambda L/D = 13$ to 26 had only a minor impact on the surface effectiveness.
- An interrogation of the gas temperature field was performed, which revealed some of the important fluid behaviour that drives the changes in measured surface effectiveness.
- Coherent jet structures were revealed by the free-stream temperature traverse measurements, and the core coolant concentration within the detached effusion jets was found to be reduced as the free-stream turbulence was increased.
- The streamwise temperature traverse data shows lateral spreading reduces the coolant core length, and gives rise to the lower centerline effectiveness values shown in the film effectiveness data.

- The impact of density ratio as an independent parameter is relatively weak. The area averaged plots show momentum flux as the appropriate scaling parameter for variable density ratio tests. This provides strong evidence that data collected at low DR's can be scaled to engine representative DR's.
- The introduction of the coolant film augments the surface heat transfer coefficient. The augmentation in HTC is a strong function of the coolant blowing ratio. The combination of a high blowing ratio and low free-stream turbulence produces the lowest HFR due to the poor surface film coverage and the significant disruption to the near wall flow.

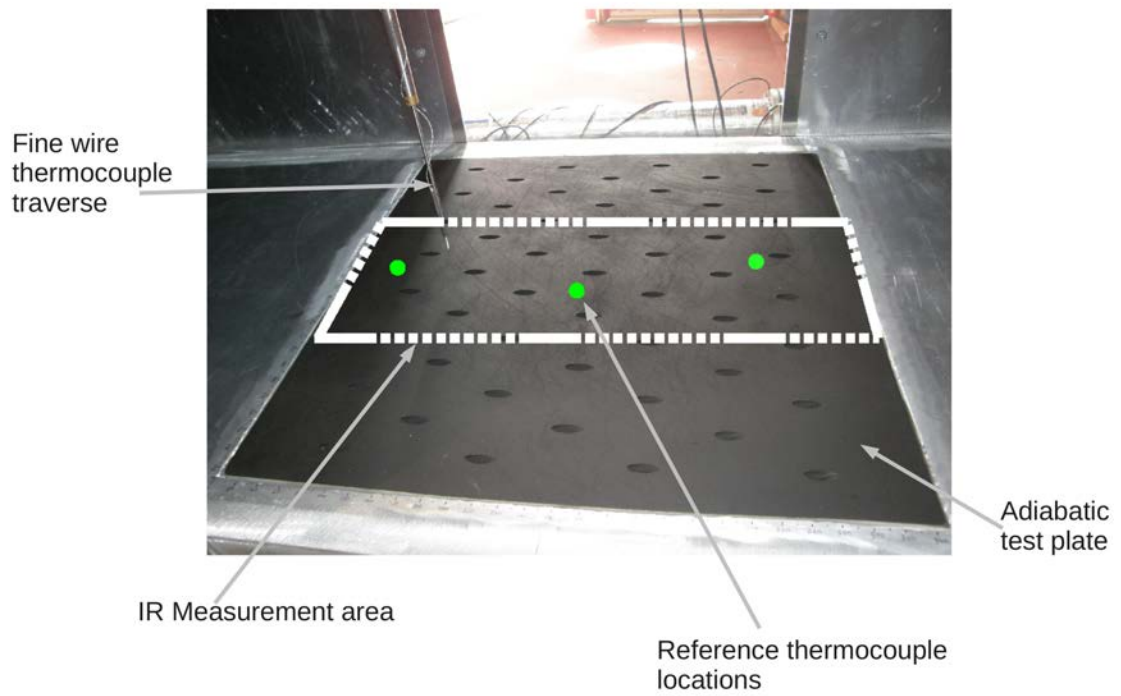
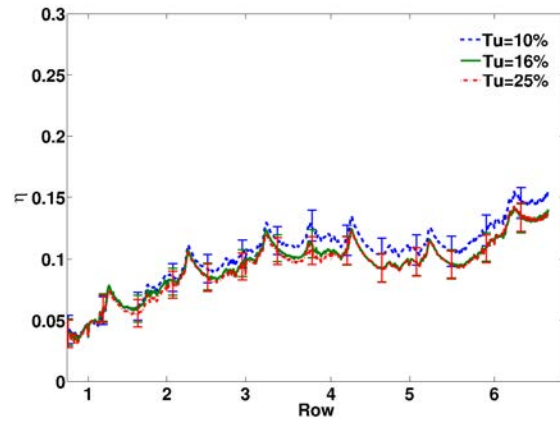
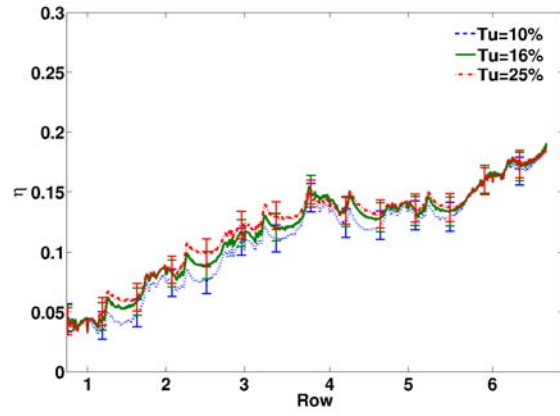


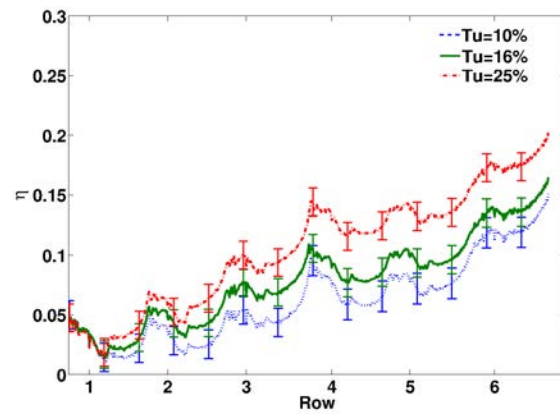
Figure 6.1: Measurement area of adiabatic test plate and surface mounted reference thermocouple locations



(a)



(b)



(c)

Figure 6.2: Spanwise averaged adiabatic effectiveness for Dr 1.4 (a) BR 0.3; (b) BR 0.6; (c) BR 1.5

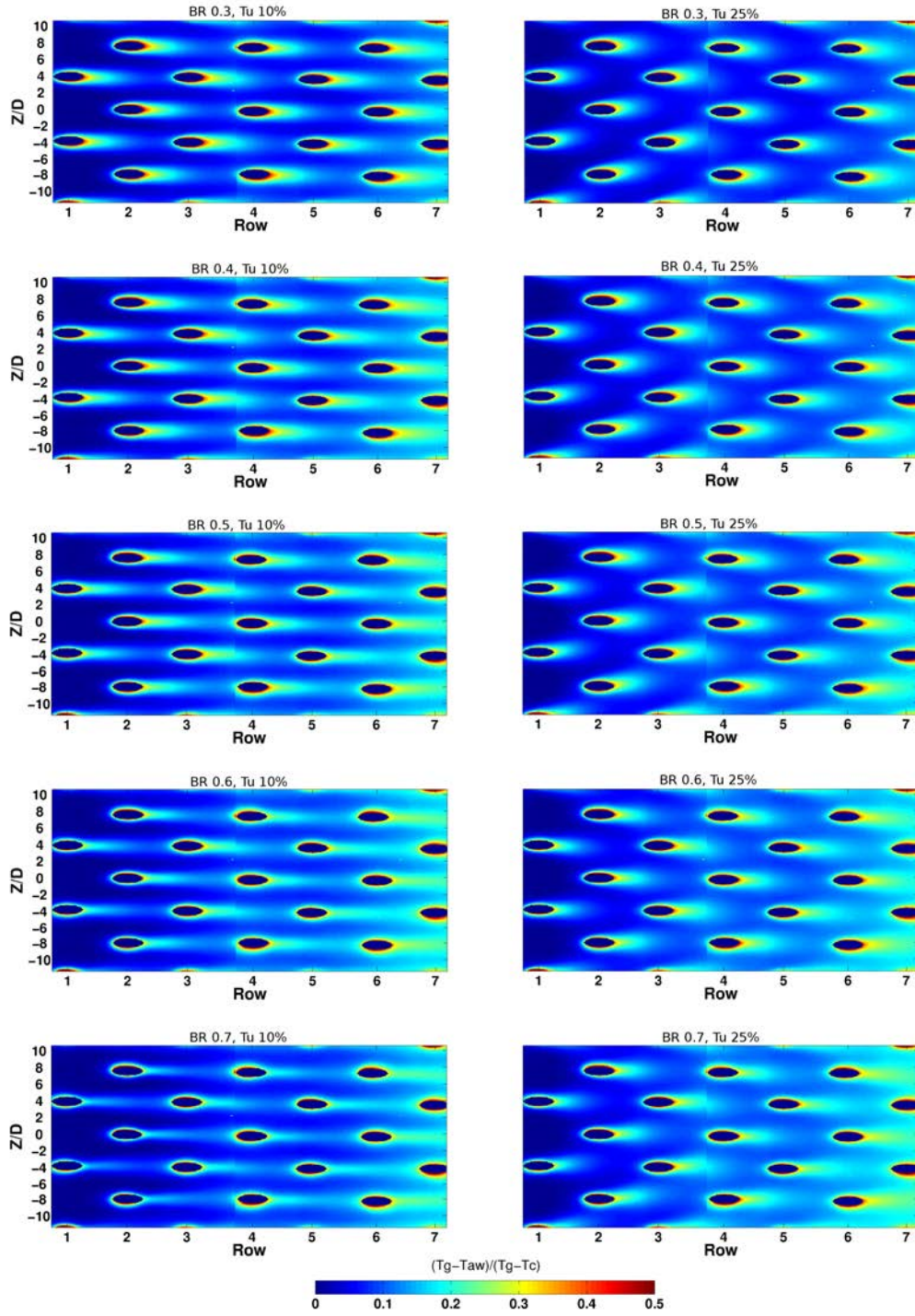


Figure 6.3: Surface adiabatic effectiveness, DR 1.4, BR 0.3 - 0.7, Tu 10 -25%

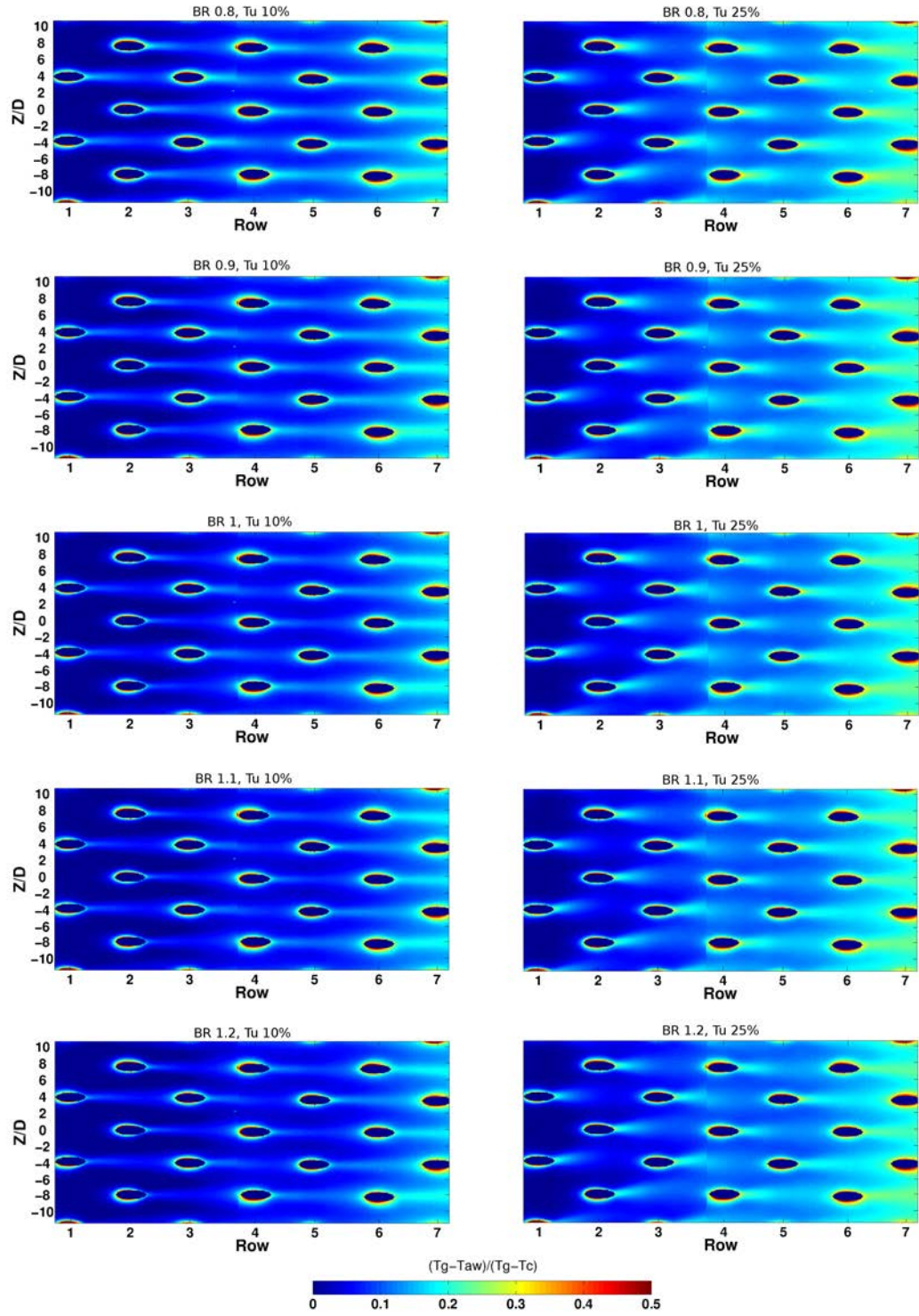


Figure 6.4: Surface adiabatic effectiveness, DR 1.4, BR 0.8 - 1.2, Tu 10 -25%

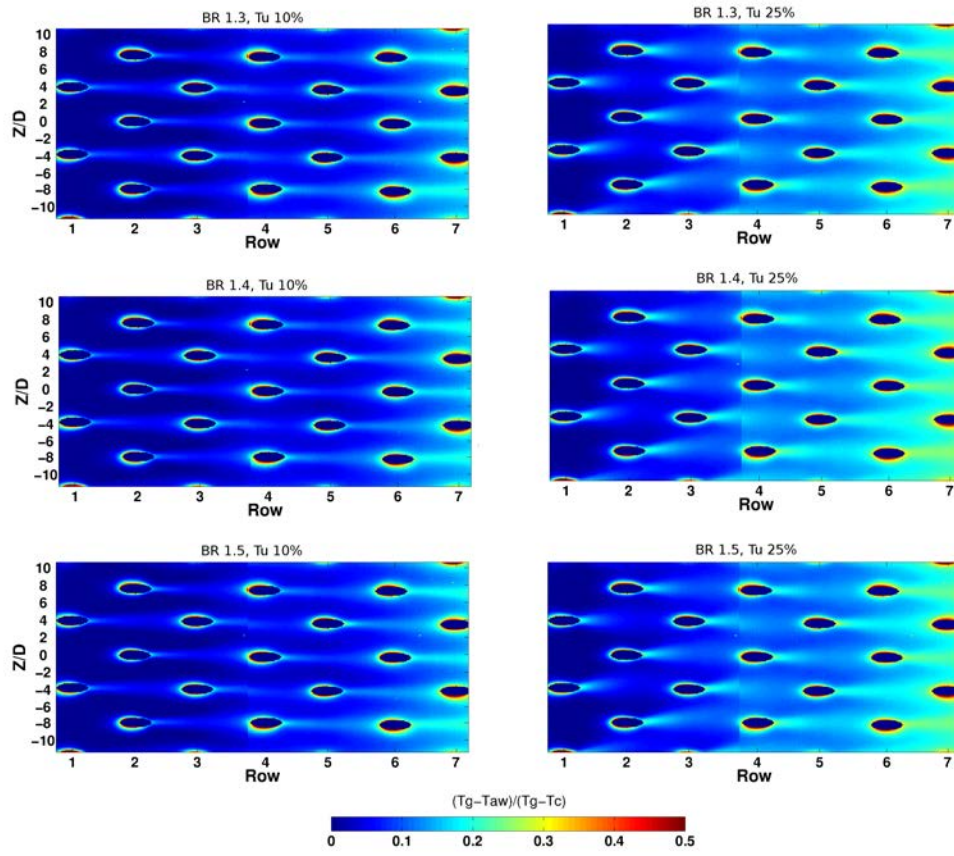


Figure 6.5: Surface adiabatic effectiveness, DR 1.4, BR 1.3 - 1.5, Tu 10 -25%

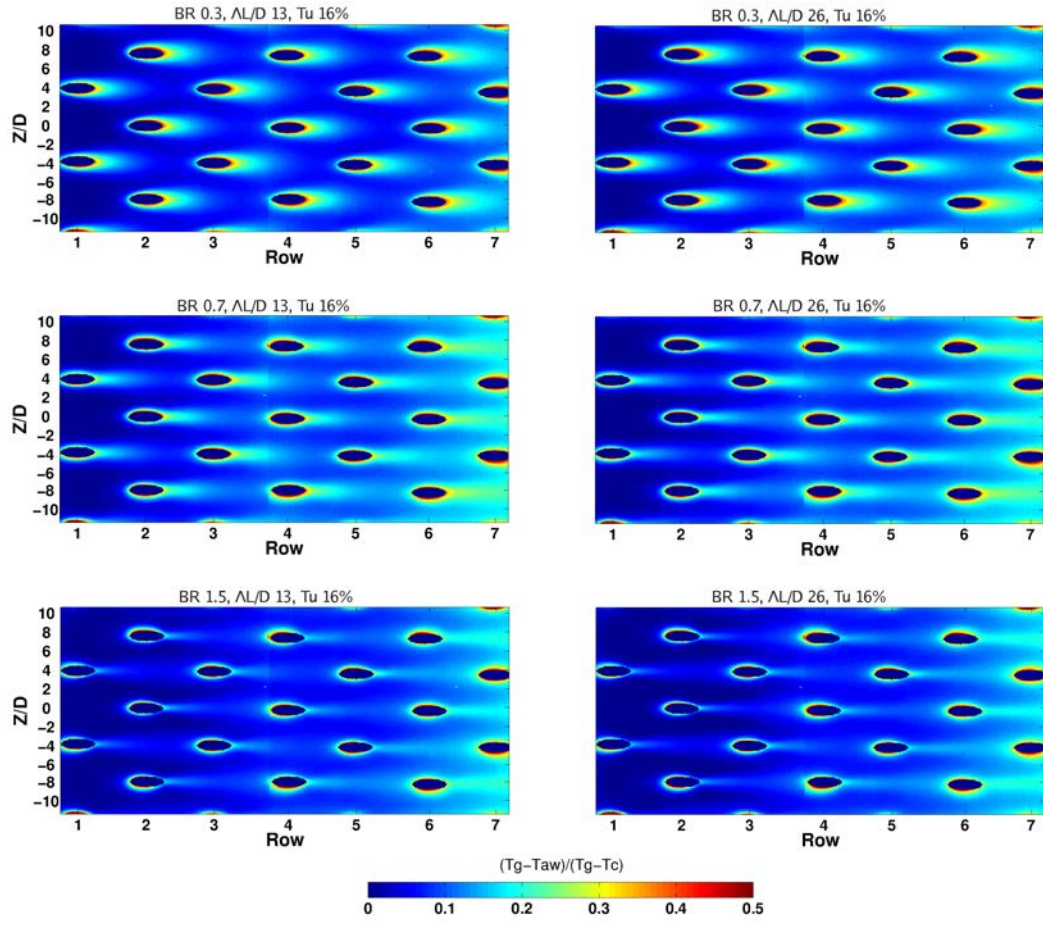
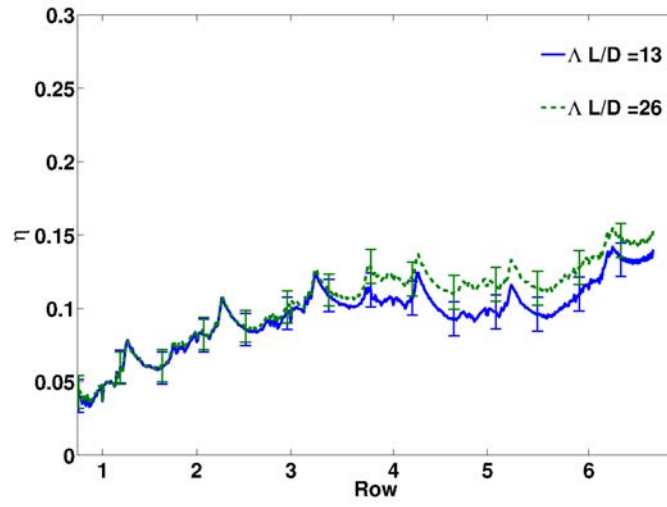
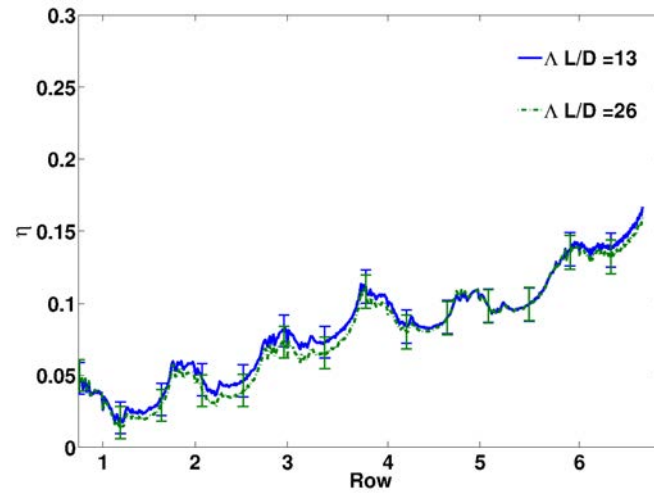


Figure 6.6: Surface adiabatic effectiveness at DR 1.4 and a fixed free-stream turbulence Tu16%



(a)



(b)

Figure 6.7: Spanwise average adiabatic effectiveness at DR 1.4 (a) BR 0.3;
(b) BR 1.3

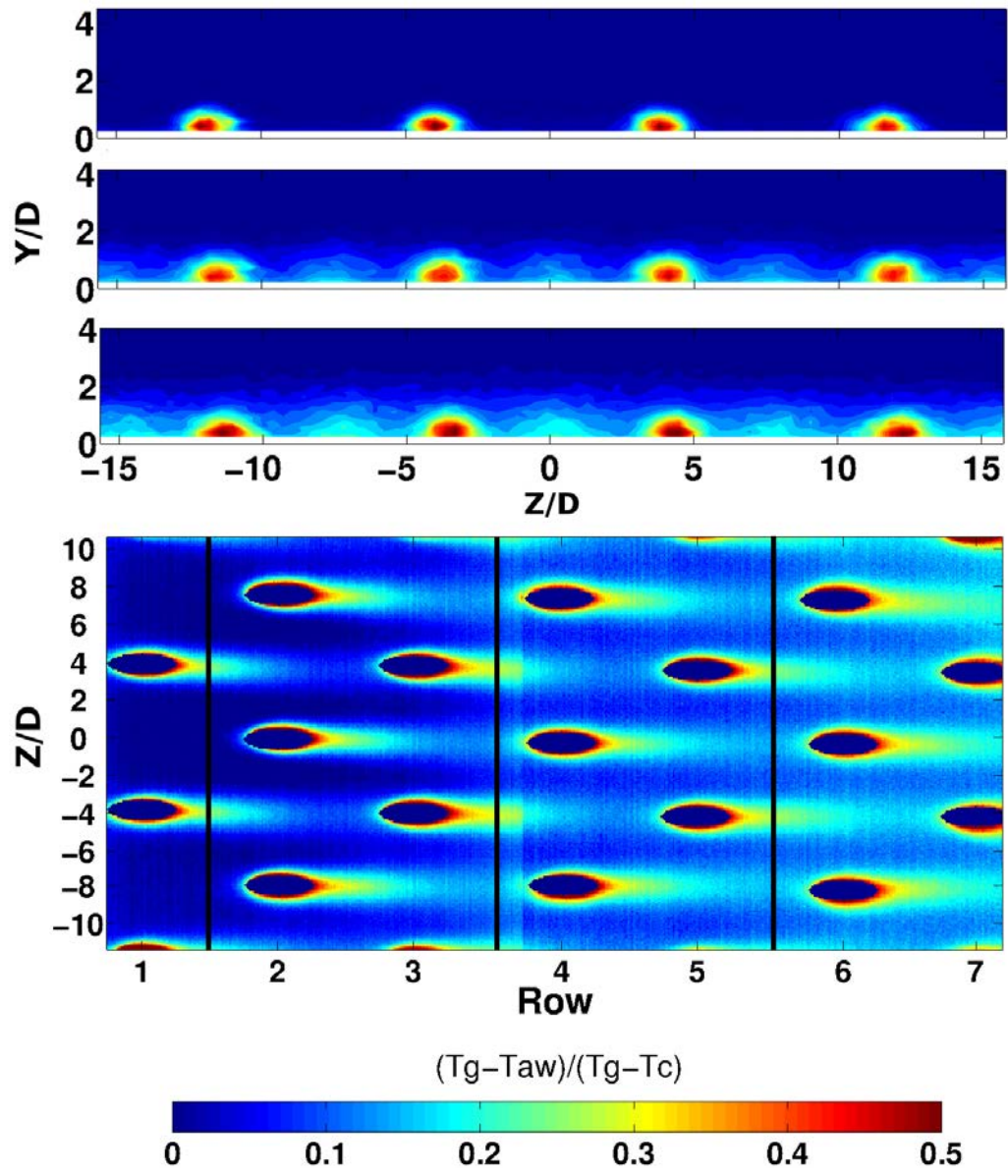


Figure 6.8: Measured span-wise gas temperature and surface effectiveness, DR 1.065, BR 0.4, T_u 10%

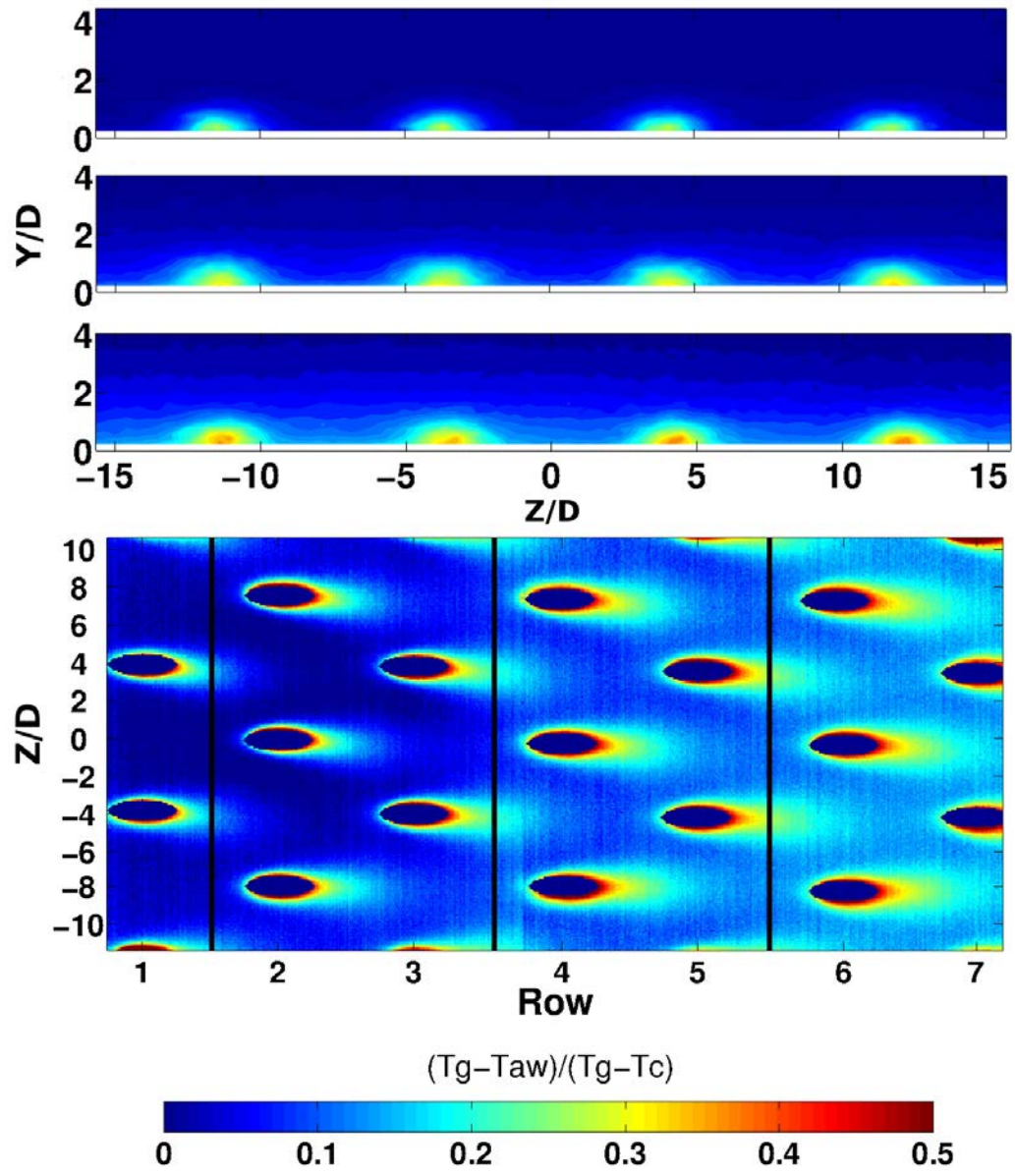


Figure 6.9: Measured span-wise gas temperature and surface effectiveness, DR 1.065, BR 0.4, T_u 25%

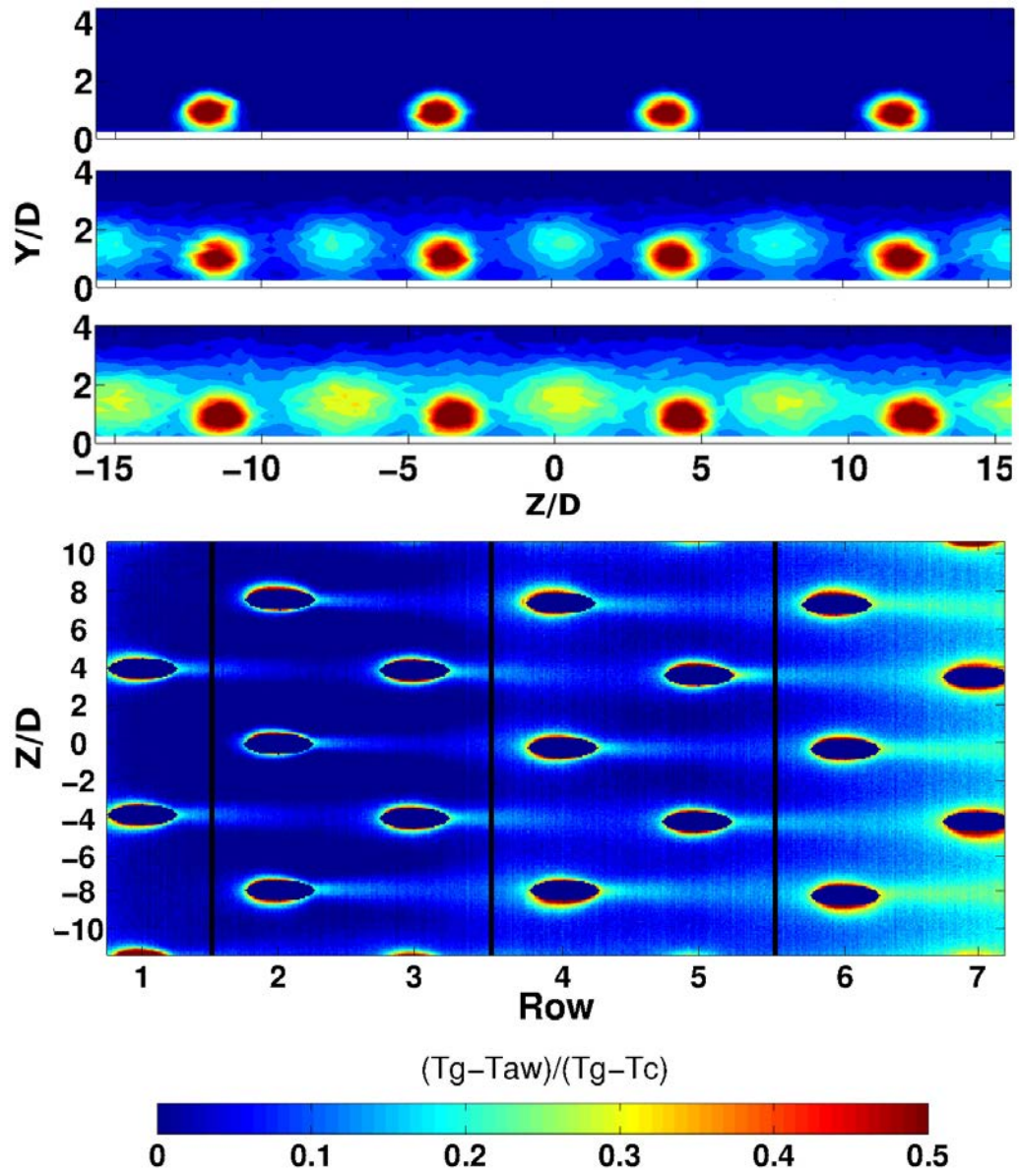


Figure 6.10: Measured span-wise gas temperature and surface effectiveness, DR 1.065, BR 1.3, T_u 10%

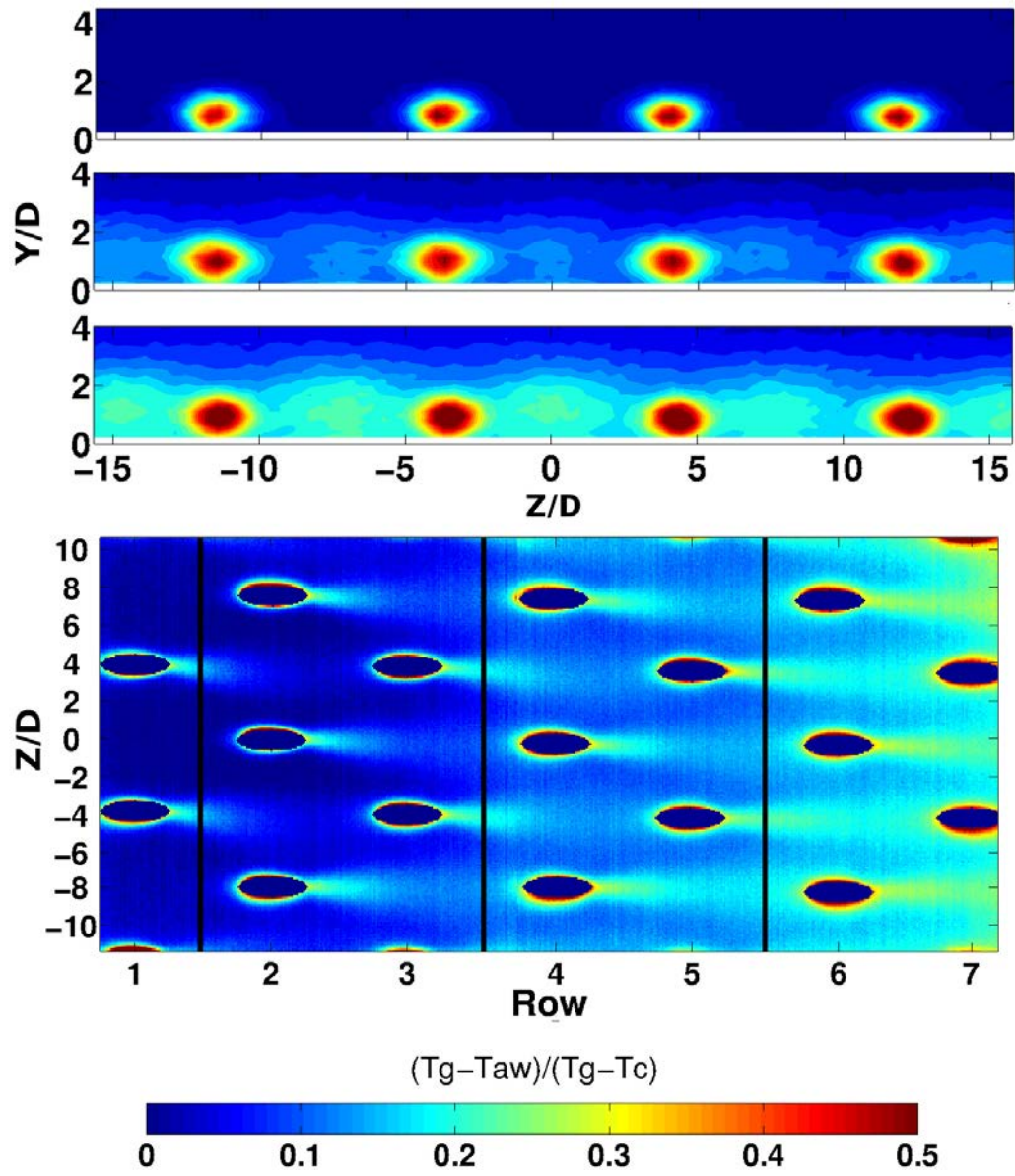


Figure 6.11: Measured span-wise gas temperature and surface effectiveness, DR 1.065, BR 1.3, Tu 25%

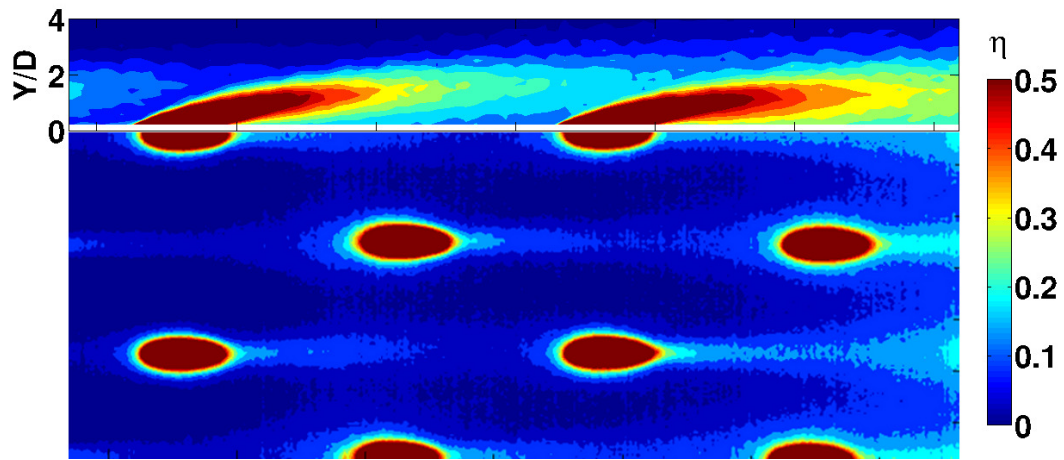


Figure 6.12: Streamwise temperature traverse (rows 2-4), DR 1.065, BR 1.3, $T_u=10\%$

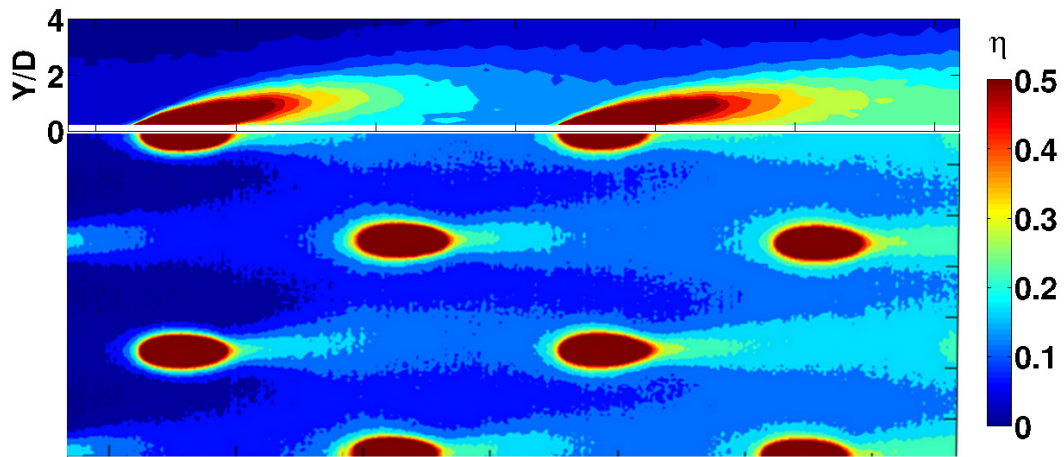


Figure 6.13: Streamwise temperature traverse (rows 2-4), DR 1.065, BR 1.3, $T_u=25\%$

,

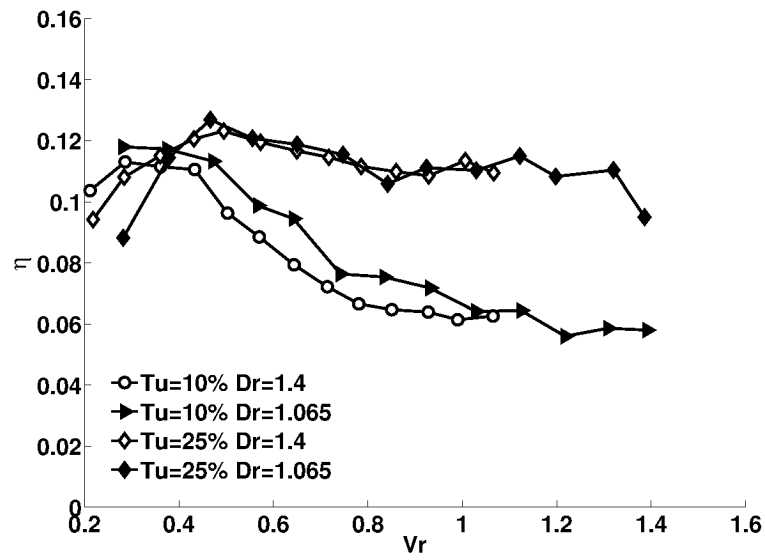


Figure 6.14: Average Surface effectiveness against velocity ratio, V_r

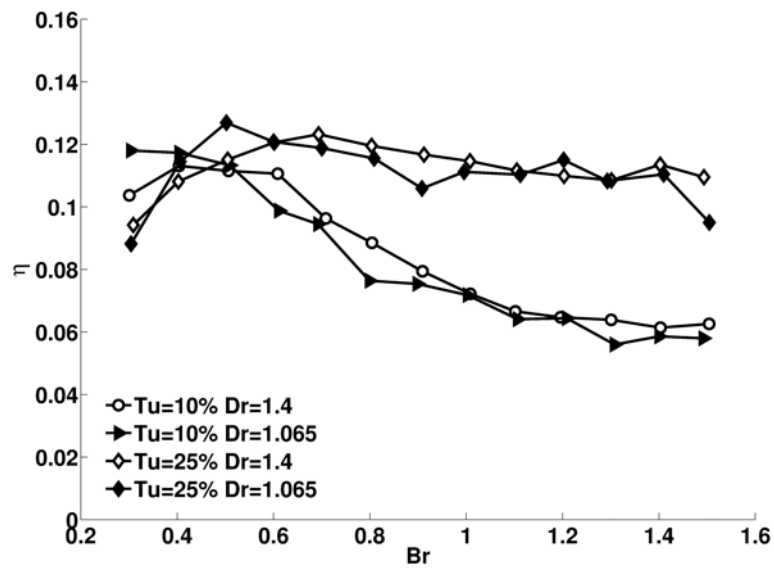


Figure 6.15: Average Surface effectiveness against blowing ratio, Br

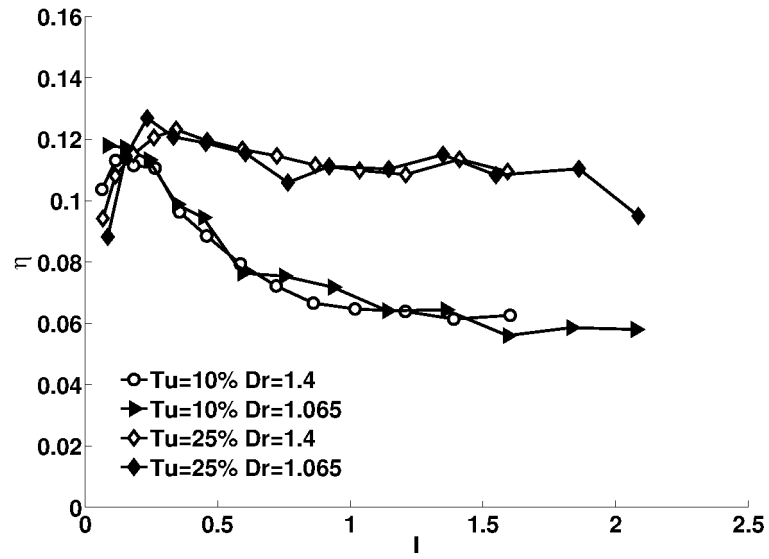


Figure 6.16: Average Surface effectiveness against momentum flux ratio, I

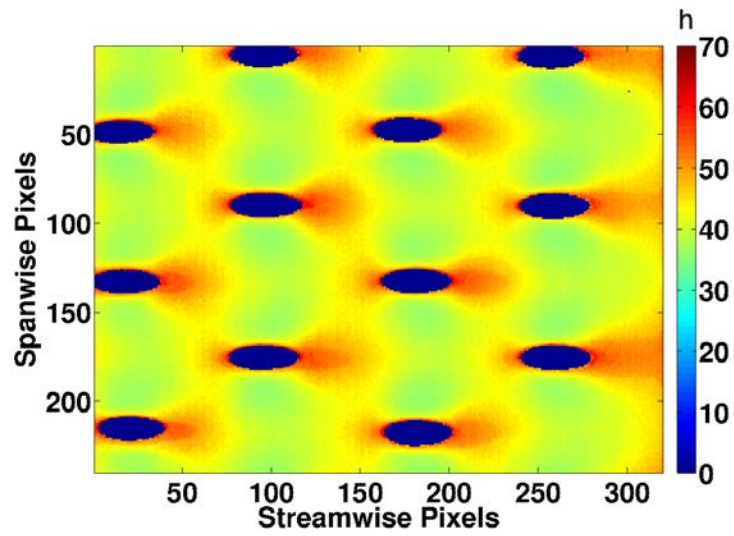


Figure 6.17: Average heat transfer, DR 1.1, BR 1.5, Tu 25%

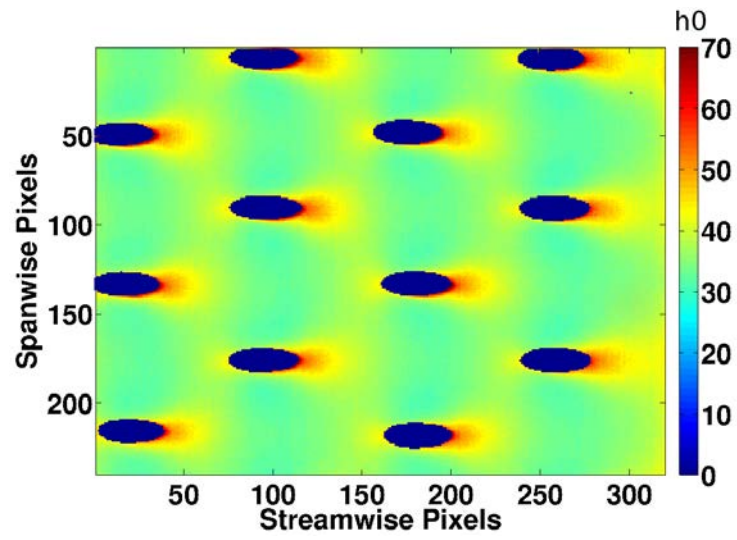


Figure 6.18: Average heat transfer with coolant off at free-stream Tu 25%

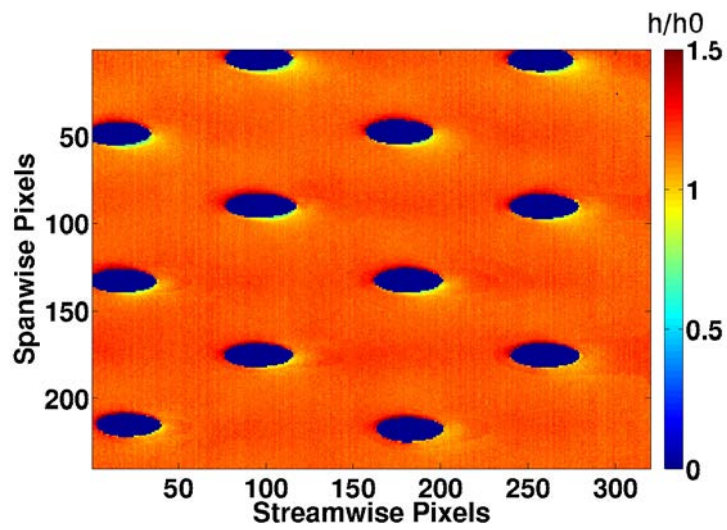


Figure 6.19: Normalised h/h_0 plot at DR 1.1, BR 1.5, Tu 25%

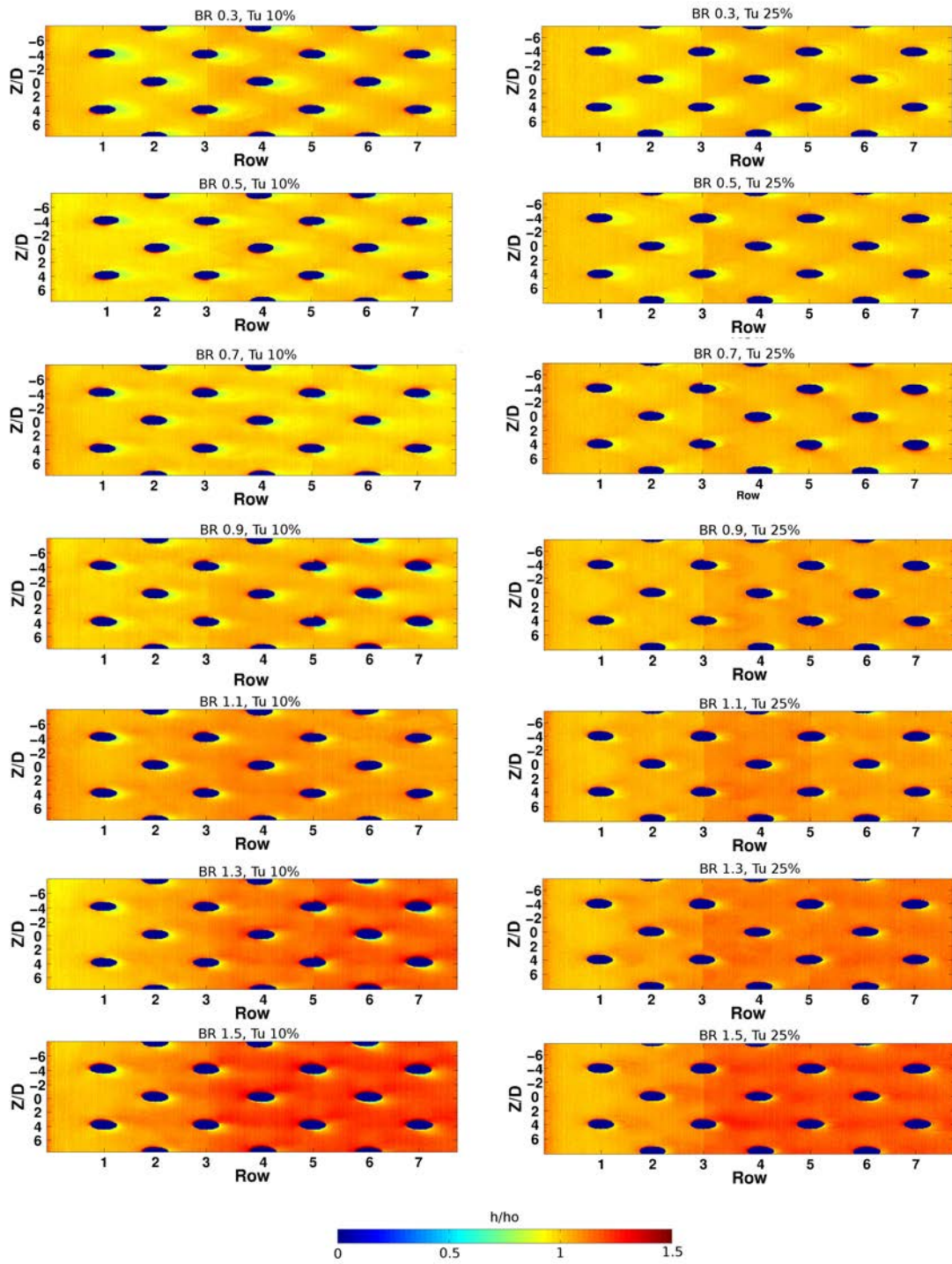


Figure 6.20: Normalised heat transfer coefficient, DR 1.1, BR 0.3 - 1.5, Tu 10 - 25%

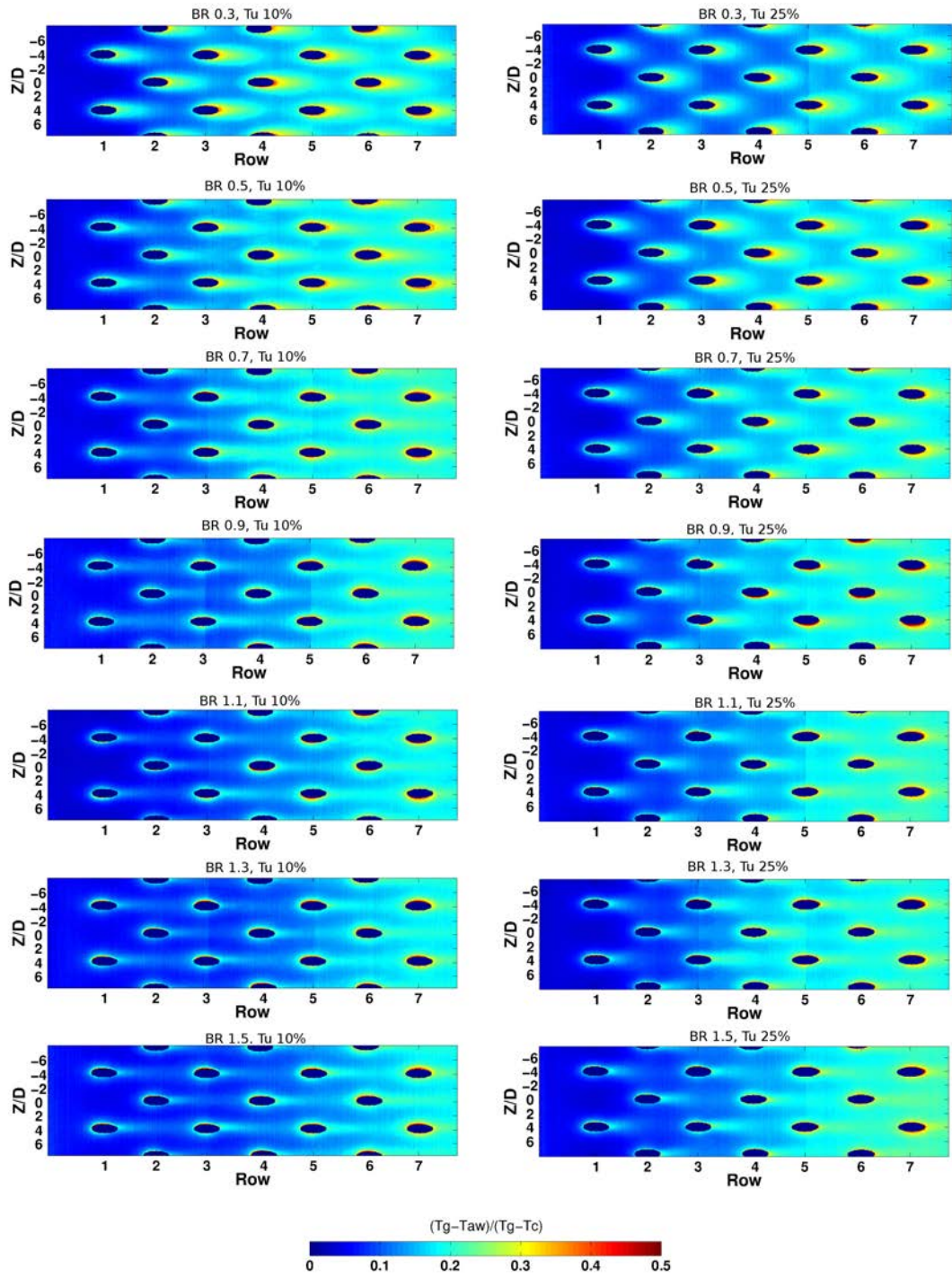


Figure 6.21: Surface adiabatic effectiveness, DR 1.1, BR 0.3 - 1.5, Tu 10 - 25%

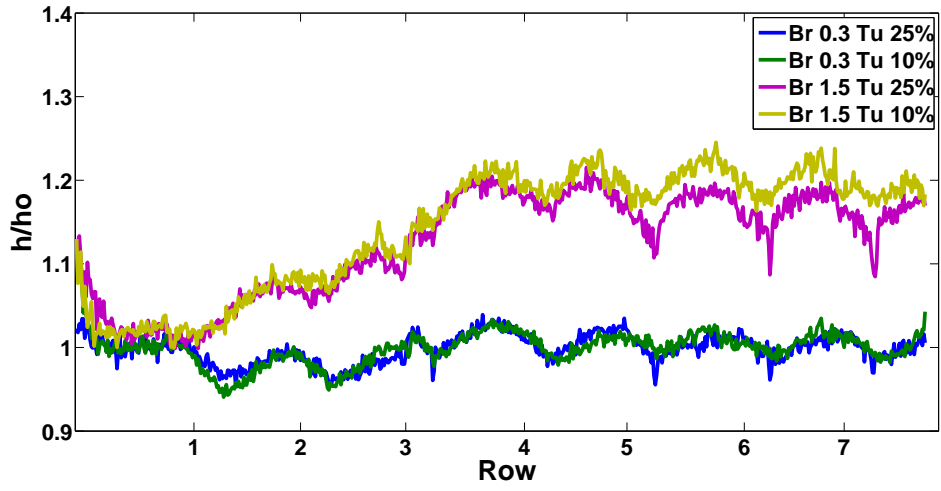


Figure 6.22: Span average h/h_o , DR 1.065, BR 0.3 and 1.5 at Tu 10 - 25%

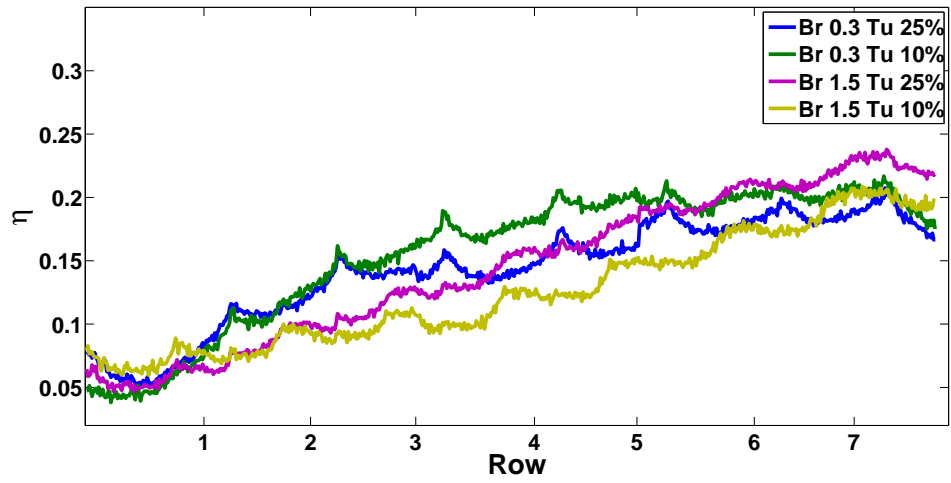


Figure 6.23: Span-average effectiveness, DR 1.065, BR 0.3 and 1.5 at Tu 10 - 25%

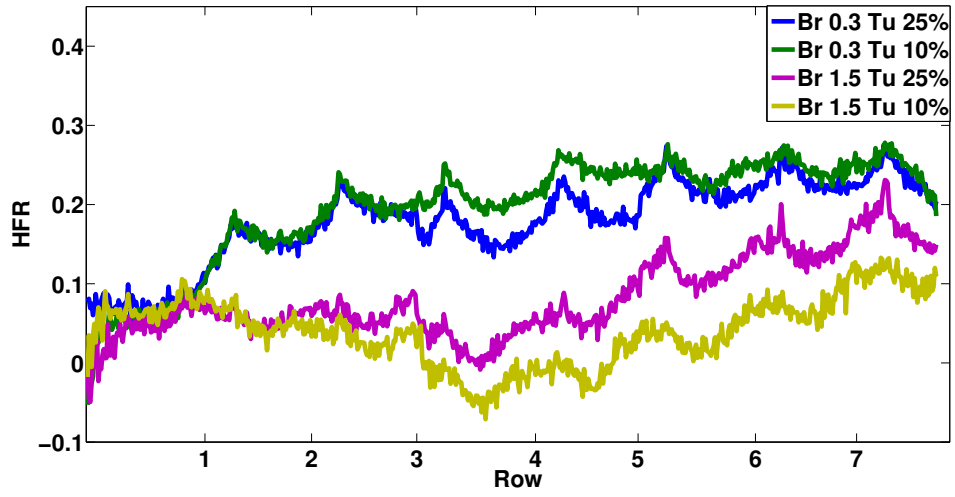


Figure 6.24: Span-average heat flux reduction, $\phi = 0.8$, DR 1.065, BR 0.3 and 1.5 at Tu 10 - 25%

Chapter 7

Investigation of shaped film cooling effusion arrays

The work reported in this chapter characterises the performance of a fan shaped effusion array. The fan shape was defined from an existing fanned effusion design and is typical of those found on high-pressure turbine blades. The detailed film effectiveness and normalised heat transfer data for fanned effusion and a porosity matched plain hole case confirmed that fanned effusion offers significant gains in film cooling performance. Based on these findings, a new diffusing hole was defined. This hole shape was developed with a focus on manufacturability, enabling conventional laser drilling techniques to be used. This new design produces similar coolant coverage to the base line fan definition.

7.1 Fanned shaped cooling

The previous chapter has shown that for plain angled effusion hole arrangements, a significant proportion of the coolant becomes detached from the surface at moderate blowing ratios. Moreover, cooling schemes of this type are typical of those found on the hot skin of dual skin architecture. The detachment of the coolant represents a significant loss in the cooling potential of the fluid. As discussed in chapter 2, shaping the hole exit to introduce a level of diffusion can dramatically improve film effectiveness by reducing the extent of coolant penetration into the free-stream, particularly at higher blowing ratios (>2.5). Indeed, single row studies by [28] and [29] have demonstrated spatially averaged film effectiveness improvements of 75% when using fan shaped cooling holes instead of plain cylindrical alternative.

While this provides compelling evidence that a fanned effusion array would produce improved film coverage, there are some drawbacks. The main difficulty in applying fanned effusion to large arrays stems from the expensive manufacturing techniques required. Using current manufacturing methods, the fan shapes can only be created by laser ablation or electro-discharge machining (EDM). There are other technologies in development, such as direct laser deposition (DLD), which will eventually remove this manufacturing limitation. However, this technology is still some way off the maturity required for application to engine production.

So, with current manufacturing capabilities the cost of producing a fan shaped hole is of the order of four to eight times more expensive to manufacture [27] than a plain cylindrical hole. This would have a significant impact on combustor liner cost which requires large numbers of cooling holes (20K+) to thermally manage liner temperatures. Therefore the direct application of a fanned geometry, using current manufacturing techniques, is not attractive and as a consequence, there are few studies in the literature which have investigated effusion arrays with diffusion. Therefore the work presented in this chapter is divided into two main sections. Firstly, the film-cooling performance of a fanned and porosity matched plain hole effusion array are evaluated. Secondly, the relative film cooling performance of a new fanned effusion design, which can be created using conventional laser drilling, is presented. Together the results quantify the relative performance of the three effusion designs in terms of film effectiveness, normalised HTC and HFR.

Fanned and plain hole effusion arrays

Using the same superposition technique described in chapter 4 the film performance of a fanned and porosity matched plain cylinder array was investigated. The hot side cooling performance has been evaluated in terms of cooling effectiveness, normalised heat transfer coefficient, free-stream temperature distribution and heat flux reduction. This has been performed at two coolant blowing rates and two free-stream turbulence conditions. Full details of the testing campaign can be found in chapter 4.

Fig. 7.7 shows the span averaged adiabatic effectiveness for each test condition. The data shows a consistent improvement in film effectiveness when using fanned effusion. The cylindrical hole data shows the surface effectiveness is insensitive to both blowing ratio and free-stream turbulence intensity, with a collapse of the span-averaged data for all test conditions onto a single line. The data also shows that the film created by the fanned effusion array develops rapidly, with the film effectiveness becoming asymptotic by the 9th cooling row. The situation is less clear for the plain hole effusion case, as the cooling layer builds up very slowly, indeed the cooling film only starts to develop after the 3rd successive row of effusion holes.

The flow fields driving the surface effectiveness distribution are visualised using the same gas temperature traverse technique discussed in chapter 4. The flow field and surface effectiveness results for each of the test conditions are presented in Figs. 7.1 - 7.4. This data shows the combined plots of free-stream gas temperatures at three span-wise traverse positions along with the film effectiveness measurements, for the fanned and plain cylindrical effusion plate. The gas temperature traverse data clearly demonstrates the benefits of diffusing the coolant flow by fanning the hole exit. The diffusion of the jet decelerates the coolant sufficiently to ensure that the coolant remains attached across the blowing ratio range of 2.5 - 5. This produces greater injectant concentrations near the surface. At the highest blowing ratio ($BR=5$) an increase in spatially averaged effectiveness of 89% for the fanned effusion plate is observed at a free-stream turbulence level of $Tu=10\%$, relative to

plain hole effusion. Similar levels of improvement are measured at lower free-stream turbulence and coolant blowing conditions. A summary of the spatially averaged effectiveness values are given in Table 7.1.

BR	Tu %	Plain hole	Fanned	$\Delta\%$
2.5	10	0.373	0.670	79.4
2.5	25	0.365	0.630	72.1
5	10	0.369	0.699	89.3
5	25	0.368	0.672	82.8

Table 7.1: Spatially averaged effectiveness at high and low turbulence (masked effusion holes).

The significant improvement in film effectiveness is not solely due to the attachment of the coolant jet. The diffusion direction also plays an important role in the film development. The diffusion of the flow in the lateral direction created by the 16° fan has the added benefit of promoting the spread of coolant between neighbouring effusion holes. The temperature traverse plots shown in Figs. 7.1(a), 7.2(a), 7.3(a) and 7.4(a) all show coolant merging between effusion holes which creates a continuous film by the 9th row. In contrast the plain cylindrical case produced detached jets at both blowing conditions. Without the diffusion and lateral spreading created by a fan, the coolant jets remain completely detached from surface in coherent structures across the first four cooling rows. After the sixth row of cooling holes there is noticeable build up of a coolant film, which continues until the 12th row. This shows that even in the case of complete penetration into the free-stream,

cooling benefits, in terms of adiabatic effectiveness, occur due to the mixing of the coolant within the main flow temperature. This process, however, is very slow and inefficient with similar span-averaged values at 12th row produced by the fanned geometry after only three rows of cooling holes.

Effects of free-stream turbulence

In terms of surface effectiveness both cooling schemes demonstrated low sensitivity to free-stream turbulence. The well behaved nature of the fanned holes (coolant jets remain attached) and the high blowing ratios makes the film insensitive to bulk free-stream turbulence changes. Figs. 7.1(a) and 7.2(a) show only a slight thinning of the film layer resulting in a 5.9% reduction in the spatially averaged effectiveness, when the free-stream turbulence was increased from $Tu=10\%$ to 25% . This result is consistent with the findings of [30] who reported 6% reduction in film effectiveness for a single row of fanned shaped holes, when free-stream turbulence was increased from 1.2% to 8.9% .

At the highest blowing ratio tested ($BR=5$) the free-stream gas temperature and surface effectiveness distributions for the fanned geometry are almost identical for both turbulence conditions (Figs. 7.3(a) and 7.4(a)). In the case of the cylindrical hole, elevated bulk free-stream turbulence does have a noticeable impact on the coolant mixing with the free-stream. Fig. 7.1(b) and 7.2(b) illustrate this by a reduction of the coolant in the core of the jets as the free-stream turbulence is increased from 10% to 25% . However, as

this mixing occurs well above the surface, the resulting surface effectiveness remains largely unchanged. Following a similar trend to the fanned effusion geometry, the impact of free-stream turbulence is reduced further as the coolant blowing rate is increased.

Normalised HTC and HFR

As in Chapter 6 heat transfer coefficients are presented in the normalised form (h/h_o). The spatially resolved normalised HTC measurements for BR 2.5 are presented in Fig. 7.5. The data shows little difference in HTC augmentation between the plain and fanned hole geometries under the low blowing conditions. The main characteristic of the data is the local increase in heat transfer coefficient at the hole exit. This feature is a direct result of the increased levels of flow shear at the jet boundaries. For the fanned geometry the distribution of the localised increase is consistent with the 9mm metering hole of the fan (see Fig. 3.28 in Chapter 3), indicating the coolant flow cores along the fan centerline. This provides evidence of flow separation within the fanned section of the hole which creates a centre-biased flow profile. This feature becomes more dominant as the blowing ratio is increased to BR=5 as shown in Fig. 7.6. At BR=5 the normalised area averaged HTC increases by 51% and 47% for the fanned and plain hole case respectively. The level of augmentation created by the fan is higher because the coolant is attached to the effusion surface and therefore the disturbance to the near wall flow is greater.

The impact of the increased heat transfer on the overall hotside film cooling performance is captured in the span-averaged heat flux reduction, which is shown in Fig. 7.8. As discussed earlier, for the plain cylindrical case, an increase in coolant blowing rate has little impact on the surface effectiveness since the cooling jet remains in its detached mode. However, increasing the coolant blowing rate augments the HTC by 47%. This produces a grouping of the span averaged HFR based on the coolant blowing rate. For the fanned effusion case, the HTC augmentation is at a similar level, but has a negligible effect on the HFR as the cooling effectiveness remains consistently high. This widens the performance deficit of the cylindrical effusion geometry. A summary of the spatially averaged normalised HTC and HFR is given in Table 7.2.

Conditions		Plain hole		Fanned	
BR	Tu %	h/ho	HFR	h/ho	HFR
2.5	10	1.28	0.317	1.43	0.768
2.5	25	1.35	0.266	1.36	0.711
5	10	1.88	-0.013	2.17	0.726
5	25	1.87	-0.01	2.07	0.669

Table 7.2: Spatially average normalised HTC and HFR at high and low turbulence intensity (masked effusion holes).

7.1.1 Modified fan design

Following the significant improvements in the hot side cooling performance demonstrated by the fanned effusion, it was clear that diffusing the flow

sufficiently to maintain an attached cooling jet was crucial for both film development and surface coverage. For this reason, an approximation of the fanned design was created, which can be manufactured using relatively inexpensive manufacturing methods such as simple laser/percussion drilling. Creating a fan design whilst adhering to these conventional manufacturing methods ensures the effusion design remains relevant to combustor liner applications.

An approximation of the fan design can be created by laser drilling at angles in a similar plane to the inclined metering hole. The break out area of the fan is set by the laser crossover point and drilling angle. Fig. 3.31 shows a range of hole definitions that can be created by varying these parameters. Fan design 2 was selected as the test case, as this design contained a well-defined metering length and a more gradual diffusion of the central hole. The main metering hole angle was inclined at 22° and the fan shape was then created by two further drilled holes at the minimum laser drilling angle of 20° with a 5.4° fan angle. This created a slightly laid back fan with an uniform break out onto the test surface.

Modified fan performance

The adiabatic surface effectiveness for all three test cases is shown in Fig. 7.9. The surface effectiveness distributions show that the coolant jets of the modified fan remain attached at the highest blowing ratio tested (BR 5), indicating that the reduced diffusion in the modified fan is still sufficient to prevent jet

detachment. However, while the cooling jets remain attached between the two fan designs, the lateral spread of coolant is not maintained. The reduction of the fan angle in the modified case, prevents neighbouring jets from merging together to produce a uniform continuous film. As a consequence of the reduced lateral spread in coolant, the spatially averaged effectiveness at $BR=5$, $Tu=10\%$ is 11% less than the baseline fan at the same flow conditions. However, this still represents a 67% increase in film effectiveness over the plain cylindrical hole case.

In terms of film development, the adiabatic surface effectiveness data shown in Fig. 7.9 shows a similar rate of film development in comparison to the fan design. The film appears to be fully developed after the 8th row of cooling holes as the surface effectiveness distributions repeat after each successive row. The development of the cooling films can be seen more clearly in the span-averaged effectiveness plot presented in Fig. 7.11. The data shows that the fan produces a superior film at all locations for the two blowing ratios tested ($BR=2.5, 5$). In terms of adiabatic effectiveness, the modified fan demonstrated a similar insensitivity to free-stream turbulence with a reduction in the spatially averaged effectiveness of 5.6%, when the free-stream turbulence was increased from $Tu=10\%$ to 25%.

The measurement of the normalised heat transfer coefficients for the three test cases are presented in Fig. 7.10. The data shows a marked decrease in the HTC augmentation of the modified fan in comparison to the baseline fan geometry, with a spatially averaged reduction of 17%. This is due to the

improved diffusion of the modified fan created by the reduced fan angle and the increased diffuser length. However, when this data is combined with the effectiveness results in the HFR parameter (see Fig. 7.11). The superior film effectiveness produced by the fan produces the best film cooling performance in terms of HFR. A summary of the spatial averaged values are presented in table 7.3.

Conditions		Plain hole			Modified Fan		
BR	Tu %	η	h/ho	HFR	η	h/ho	HFR
2.5	10	0.373	1.28	0.317	0.600	1.18	0.705
2.5	25	0.365	1.35	0.266	0.583	1.23	0.666
5	10	0.369	1.88	-0.013	0.618	1.68	0.618
5	25	0.368	1.87	-0.01	0.594	1.72	0.557

Table 7.3: Spatially average effectiveness, normalised HTC and HFR at high and low turbulence not including holes.

In terms of hot side film performance, the modified fan geometry demonstrates significant gains over the plain cylindrical array case. While these improvements are not as great as the baseline fan, the modified fan can be created using relatively inexpensive laser/percussion drilling techniques.

7.2 Summary

A fan shaped and porosity matched plain hole effusion array has been evaluated in terms of adiabatic effectiveness, normalised HTC and HFR over two free-stream turbulence conditions; 10 and 25%. A new diffusing fanned hole design has been developed, which can be manufactured using existing laser drilling techniques. The performance of the modified fan design has been compared with the that of two other existing cooling schemes in order to establish the relative hot side cooling performance.

Investigation of fanned and cylindrical hole effusion arrays

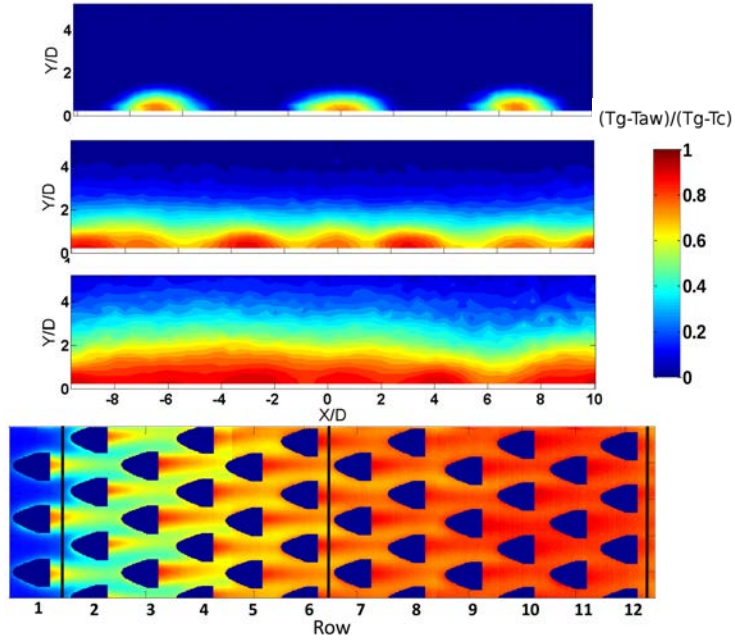
- The adiabatic surface effectiveness measurements of fanned and cylindrical hole effusion revealed a substantial improvement in film effectiveness when fanned effusion was employed. At the highest blowing ratio (BR=5) an increase in spatially average effectiveness of 89% is observed at a free-stream turbulence level of $Tu=10\%$, relative to cylindrical hole effusion.
- The diffusion created by fanning the hole exit produced an array of attached cooling jets across the blowing ratio range of 2.5 - 5. In contrast the coolant delivered by the cylindrical effusion array remains detached due to the increase in coolant momentum normal to the surface.
- The cylindrical effusion data showed that detached cooling jets still offer benefits in terms of film effectiveness due to the reduction in near

wall gas temperature caused by the mixing of the coolant with the mainstream flow.

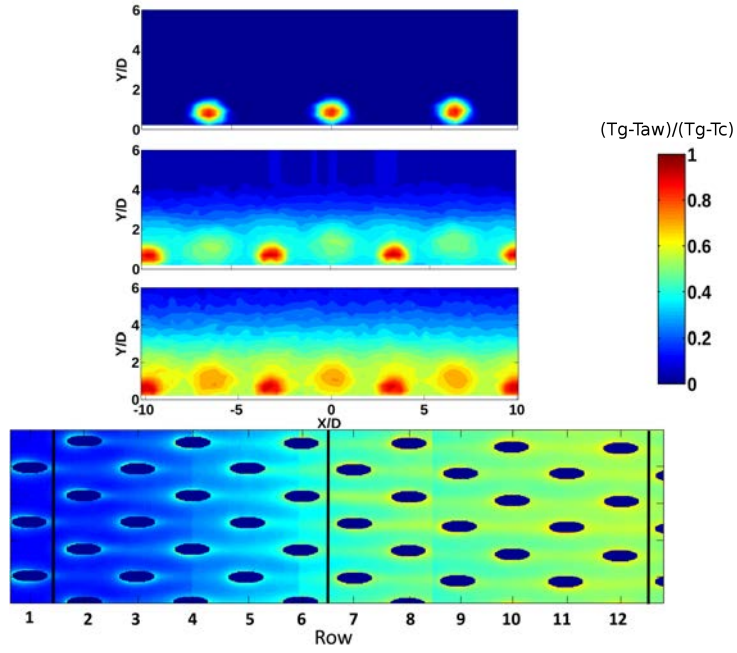
- The data shows the film created by the fanned effusion array develops rapidly, with the film effectiveness becoming asymptotic by the 9th row of cooling holes. In the case of the cylindrical array the film build up is much slower, with similar span-averaged values at the 12th row produced by the fanned geometry after only three rows of cooling holes.
- Flow field temperature measurements revealed the 16° fan angle to spread coolant laterally between neighbouring holes. This leads to the development of a uniform, continuous film by the 9th row of cooling holes.
- In terms of surface effectiveness both cooling schemes demonstrated low sensitivity to free-stream turbulence. For the fanned geometry, an increase in free-stream turbulence intensity from $Tu=10\%$ to 25% resulted in a 5.9% reduction in spatially averaged effectiveness.
- At $BR=2.5$ the introduction of the coolant film produced similar levels of HTC augmentation for fanned and cylindrical hole effusion. At $BR=5$, the level of augmentation increases by 51% and 47% for the fanned and cylindrical hole case respectively.

Modified fan design

- A new diffusing hole design has been defined which can be created using conventional manufacturing techniques such as laser/percussion drilling.
- The adiabatic film effectiveness measurements showed the reduced fan angle of 5.4° and increased inclination angle of 22° was sufficient to prevent coolant detachment. However, the reduced fan angle did not maintain the same level of lateral coolant spreading.
- The spatially averaged adiabatic film effectiveness data showed similar improvements over cylindrical effusion, with an increase in spatially averaged effectiveness of 67% at $BR=5$, $Tu=10\%$.
- The data showed a marked decrease in the HTC augmentation of the modified fan in comparison to the baseline fan geometry, with a spatially averaged reduction of 17%. However, the superior film performance of the baseline fan produced the best overall film performance (HFR).

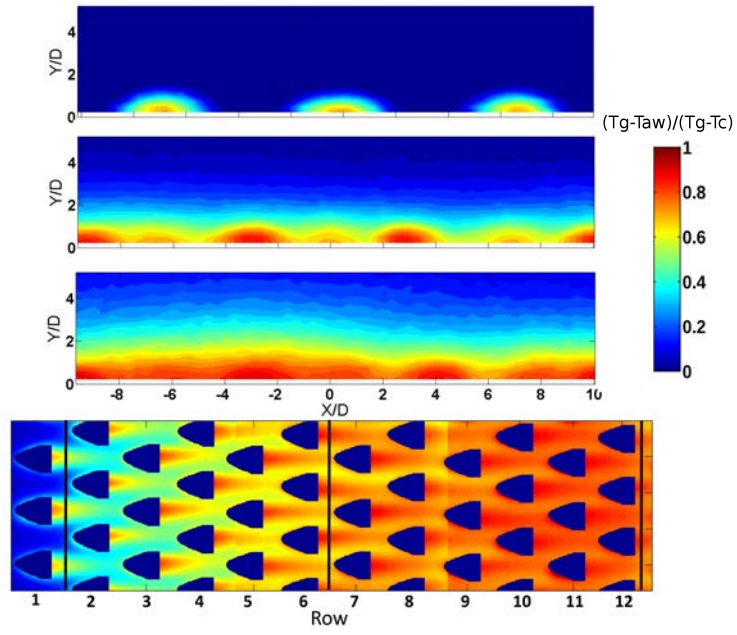


(a)

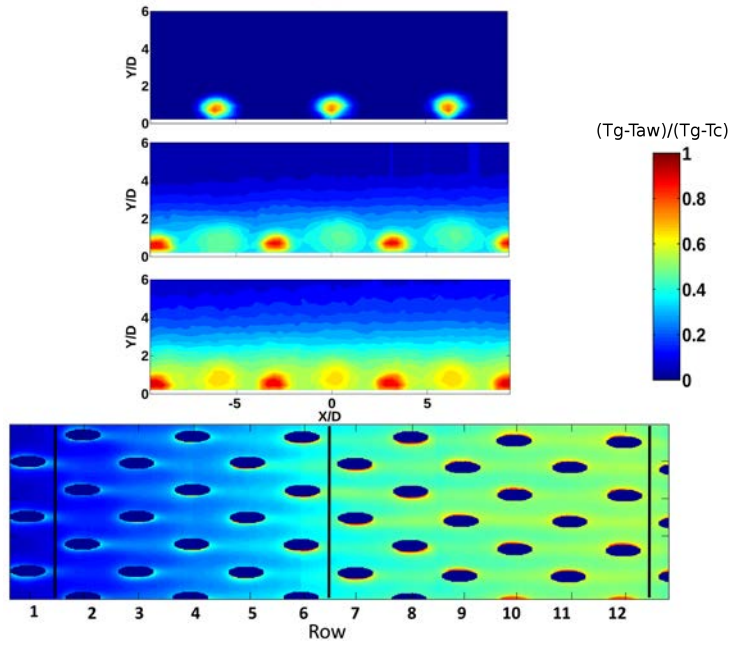


(b)

Figure 7.1: Measured spanwise gas temperature and surface effectiveness, Dr 1.065, Br 2.5, Tu 10% (a) Fanned hole; (b) Plain hole

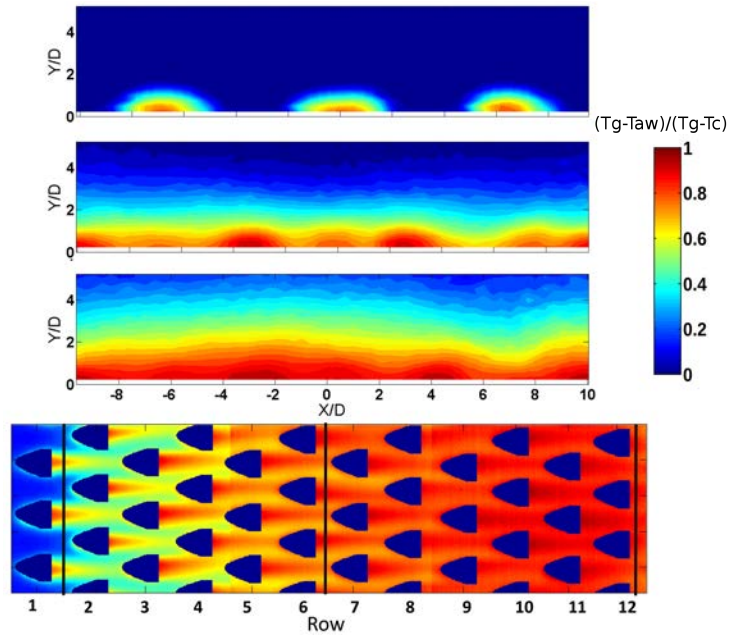


(a)

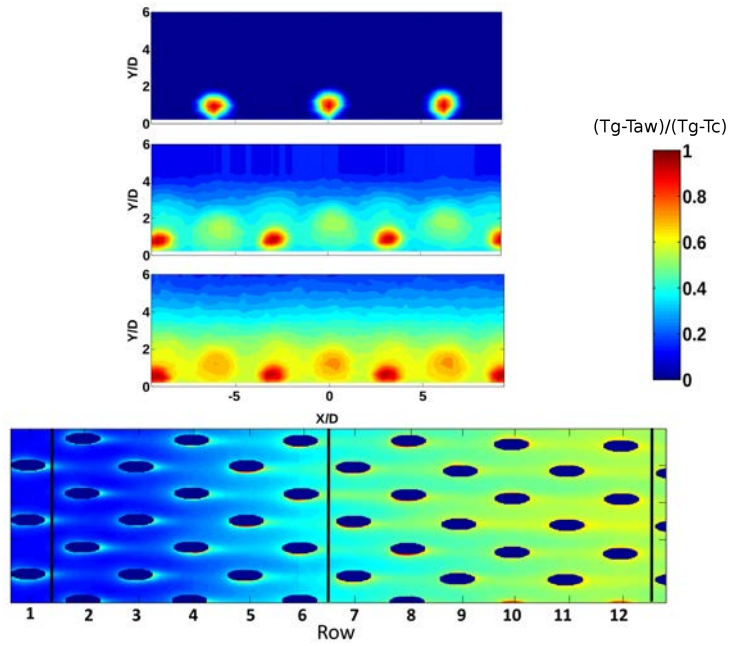


(b)

Figure 7.2: Measured spanwise gas temperature and surface effectiveness, Dr 1.065, Br 2.5, Tu 25% (a) Fanned hole; (b) Plain hole

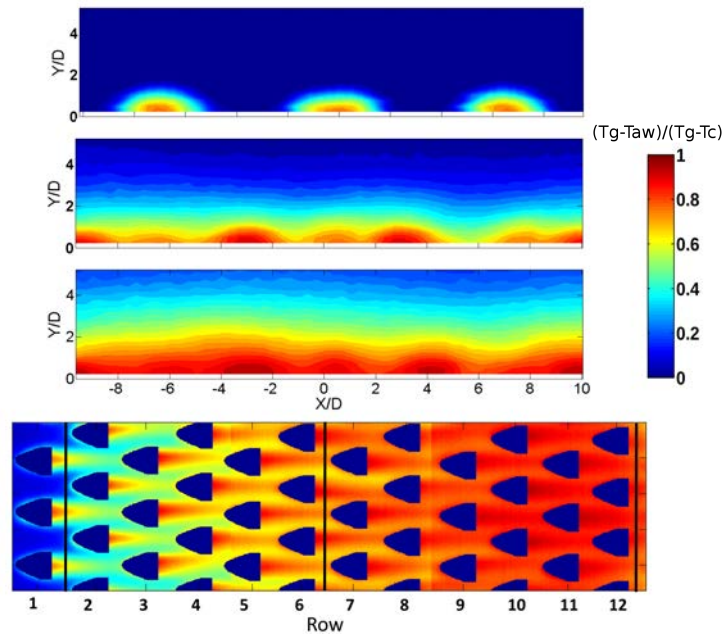


(a)

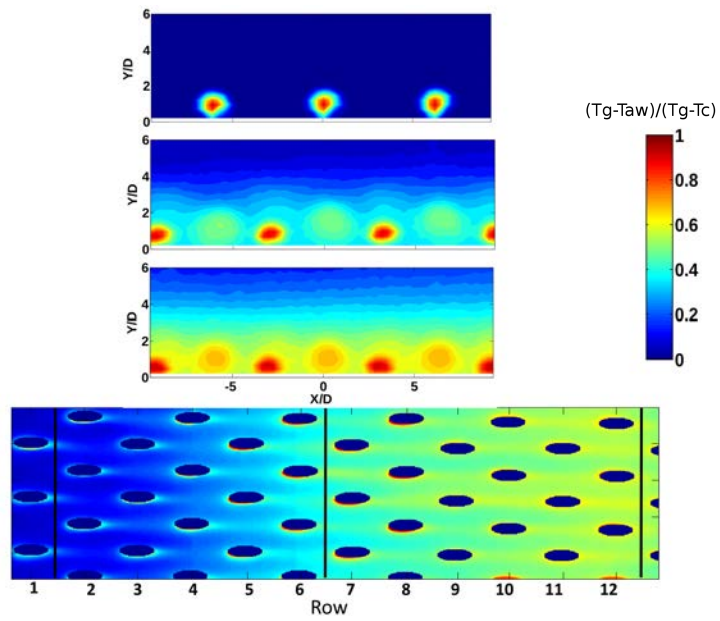


(b)

Figure 7.3: Measured spanwise gas temperature and surface effectiveness, Dr 1.065, Br 5, Tu 10% (a) Fanned hole; (b) Plain hole



(a)



(b)

Figure 7.4: Measured spanwise gas temperature and surface effectiveness, Dr 1.065, Br 5, Tu 25% (a) Fanned hole; (b) Plain hole

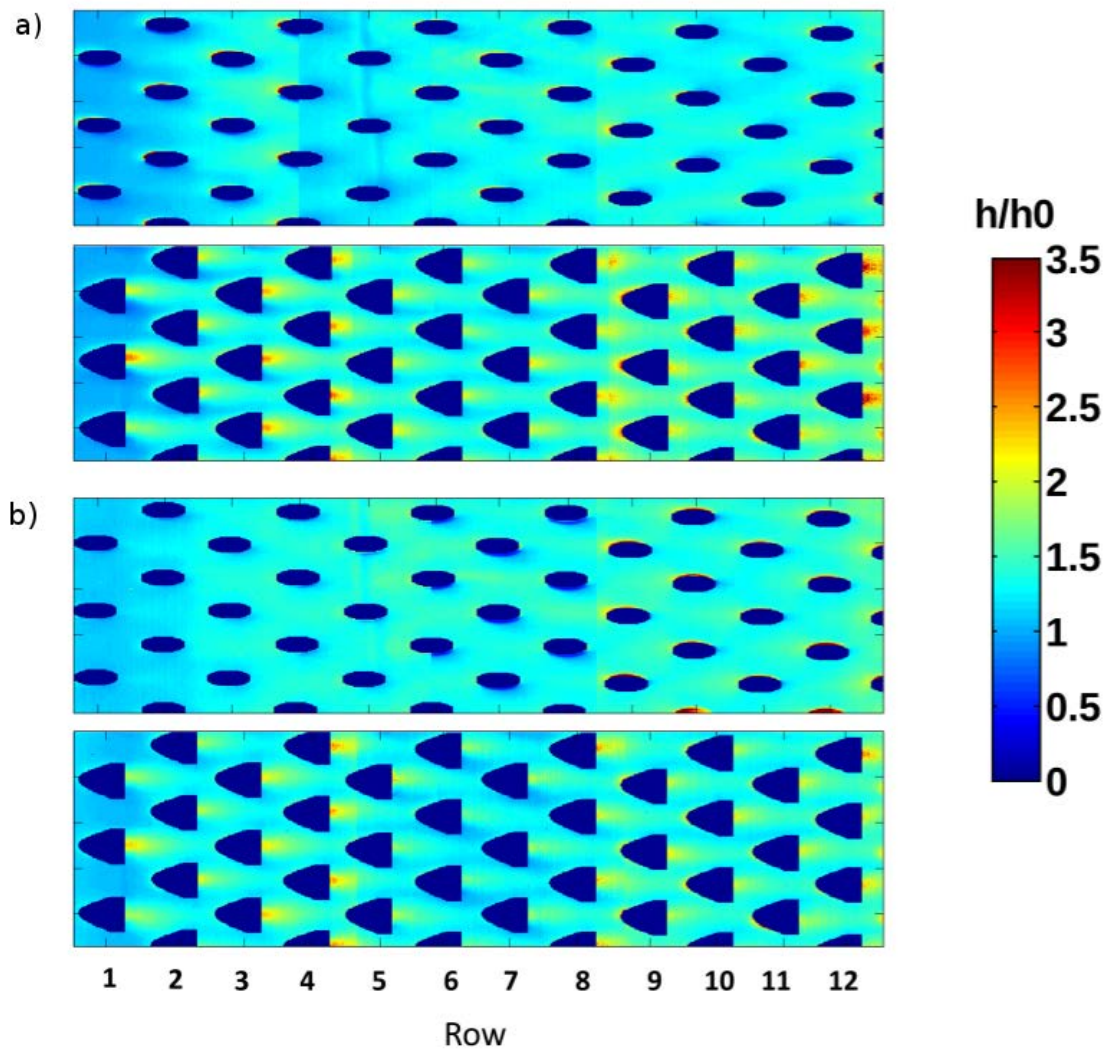


Figure 7.5: Normalised HTC, $Dr = 1.065$, $Br = 2.5$ a) $Tu = 10\%$; b) $Tu = 25\%$

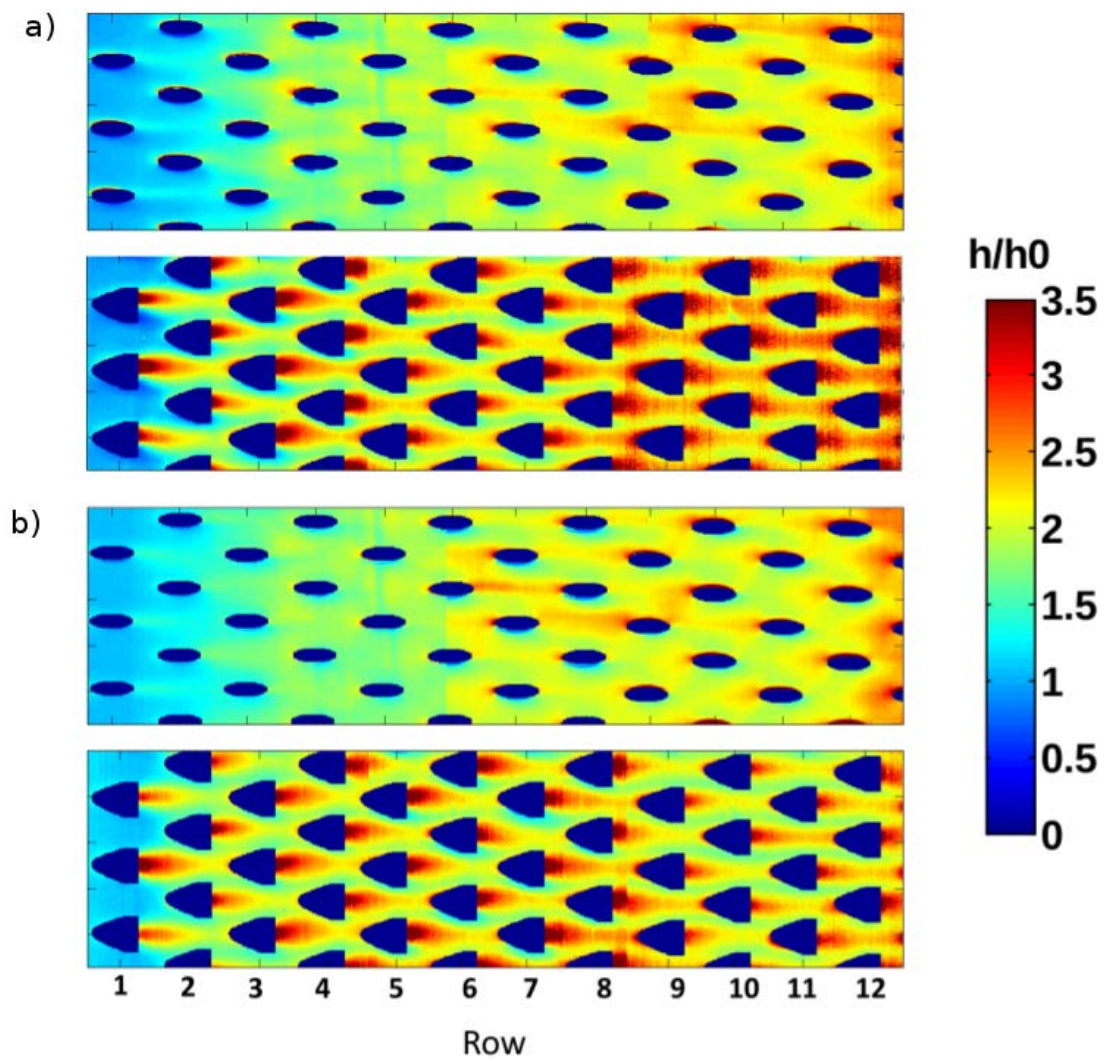


Figure 7.6: Normalised HTC, $Dr = 1.065$, $Br = 5$ a) $Tu = 10\%$; b) $Tu = 25\%$

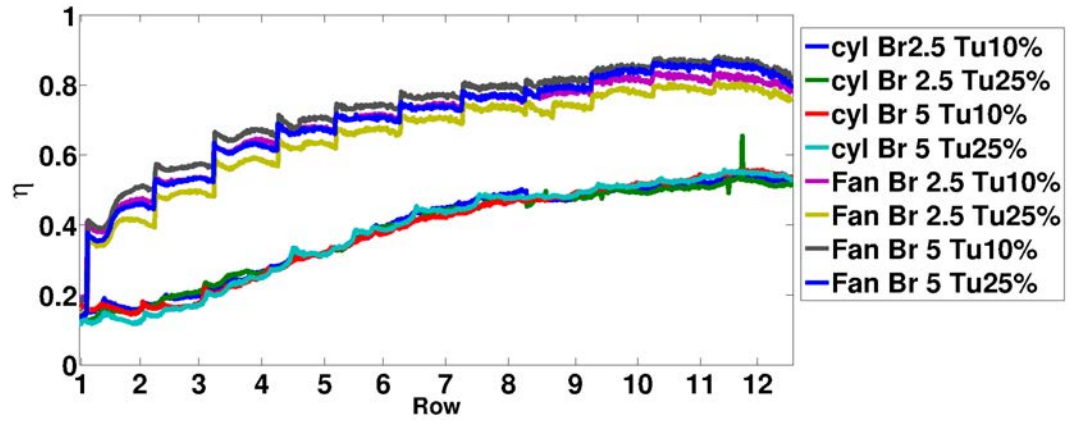


Figure 7.7: Span averaged effectiveness of fanned and plain hole effusion

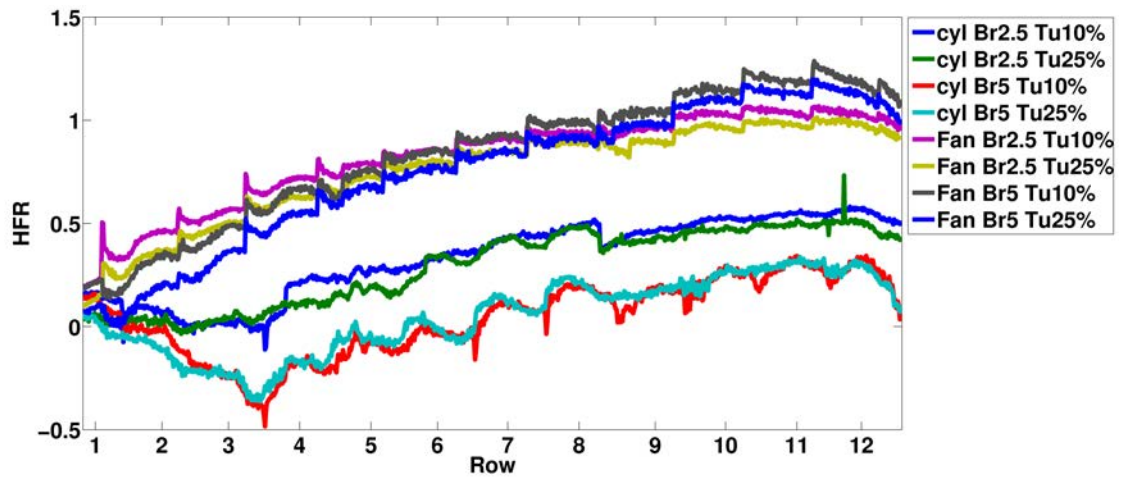


Figure 7.8: Span-averaged HFR of fanned and plain hole effusion, $\phi = 0.8$

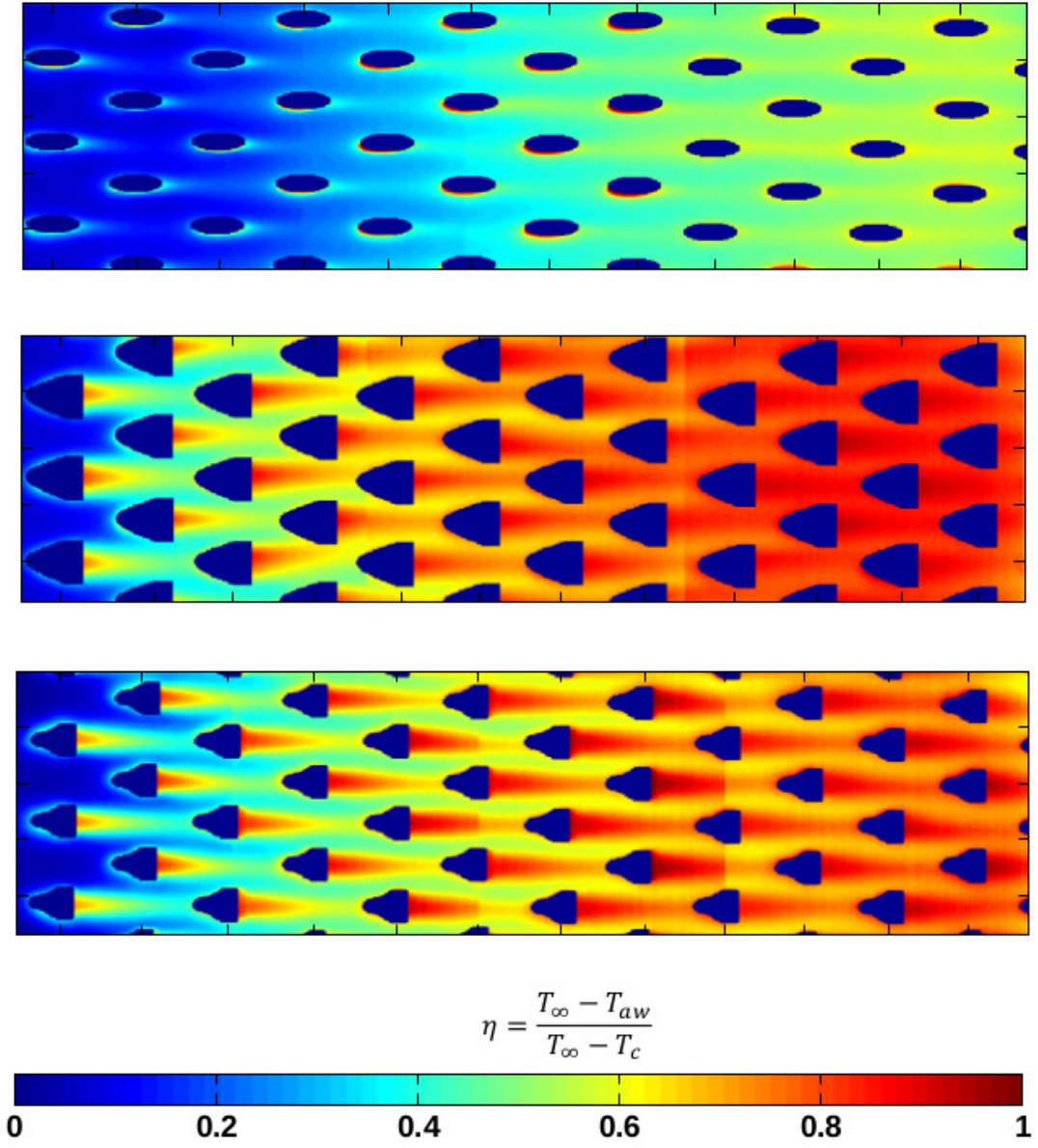


Figure 7.9: Film effectiveness of datum plain cylinder, datum fan and modified fan, Br 5, Tu 25%

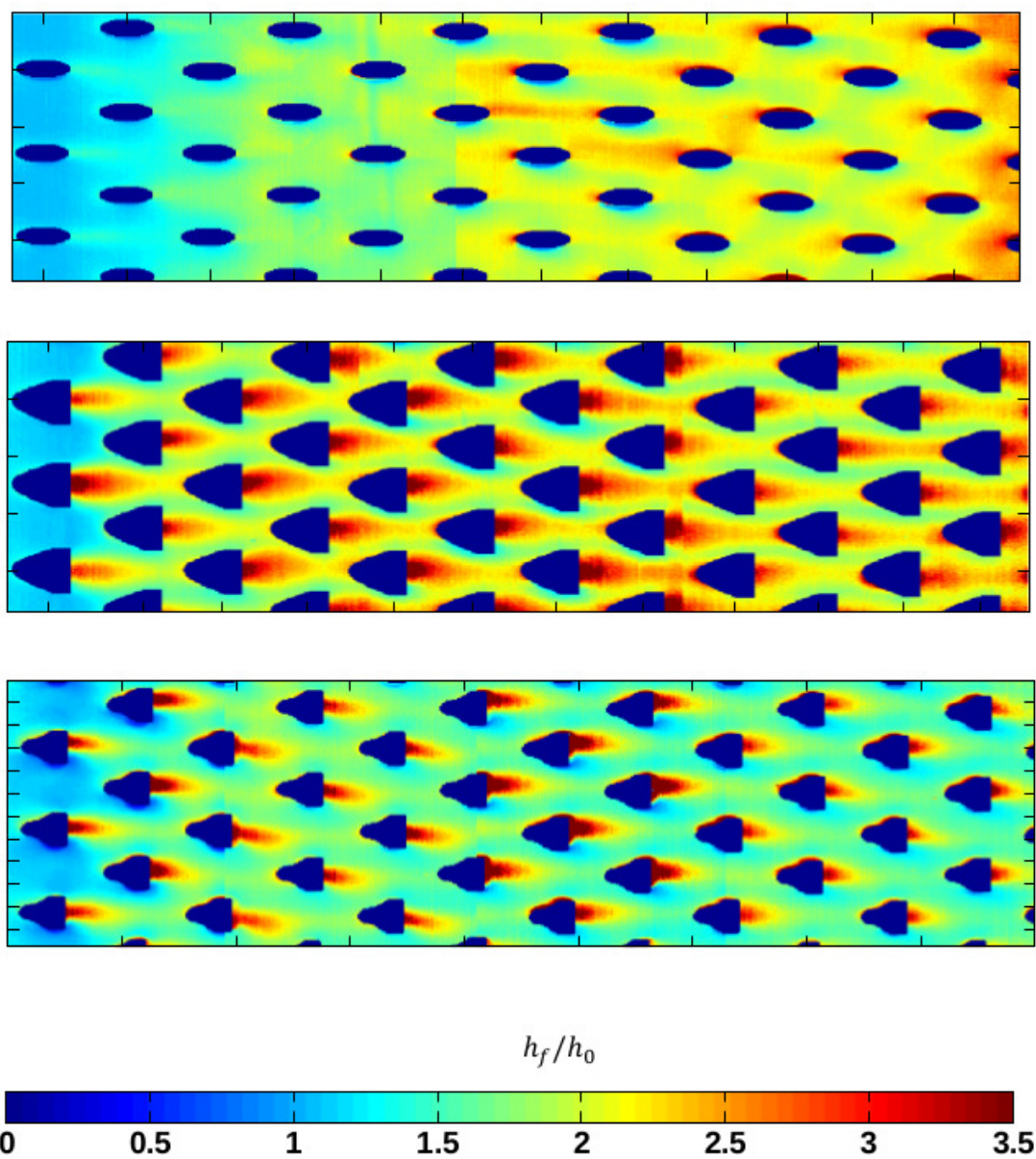


Figure 7.10: Normalised htc of datum plain cylinder, datum fan and modified fan, Br 5, Tu 25%

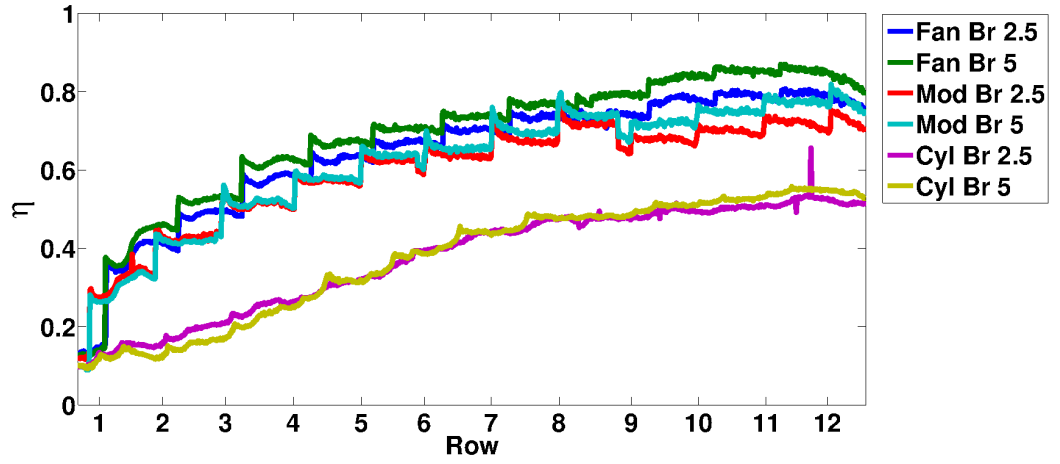


Figure 7.11: Span-averaged effectiveness of datum fan, modified fanned and plain hole effusion, Tu 25%

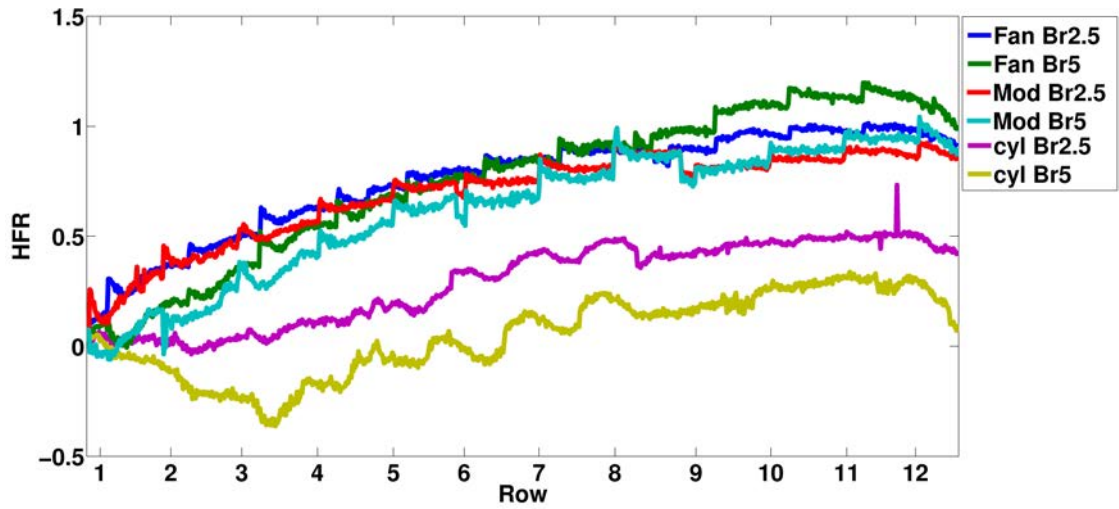


Figure 7.12: Span-averaged HFR of datum fan, modified fanned and plain hole effusion, $\phi = 0.8$, Tu 25%

Chapter 8

Conclusions

The goal of this research was to develop an understanding of the interaction between the cooling film generated by an effusion array and the main combustor flow. An area of particular interest was the impact of combustor generated turbulence and flow structures on film effectiveness. To achieve this, a new wind tunnel test facility was created which incorporates a novel jets in cross flow turbulence generator and turbo expander system.

A test matrix was developed to evaluate film effectiveness, free-stream mixing and normalised HTC of an angled hole effusion array at various bulk turbulence conditions, density, blowing and momentum flux ratios. Gas temperature measurements of the film were combined with surface effectiveness data to reveal some of the important fluid behaviour, which drives surface effectiveness distributions. Within this testing campaign the impact of density ratio as an independent parameter was investigated.

The use of shaped effusion holes was investigated in the context of single skin effusion cooling (i.e. $BR > 3$). The relative hot side film performance of a fanned and porosity matched cylindrical hole effusion plate was evaluated. Based on these results, a new shaped hole design was specified, which could be created using conventional laser drilling procedures. The film performance of the new shaped hole was compared to the existing fan and cylindrical hole design, and evaluated in terms of film effectiveness and normalised HTC.

Section 8.1 provides a summary of the wind tunnel development. Section 8.2 recounts the findings of the measurements of the angled plain hole effusion array. Section 8.3 contains a summary of the fanned effusion results. Finally, section 8.5 offers suggestions for further investigations of this topic.

8.1 Experimental test facility

A large scale, low speed wind tunnel has been designed, built and commissioned for investigating hot side film cooling performance of combustor liners. Preliminary hot-wire measurements of a fully featured lean burn combustor were used to establish representative flow conditions inside the combustion chamber under isothermal conditions. The measurements from these tests indicated that turbulence intensities were $>25\%$ with integral length scales of the order $\Lambda_x \approx 37D$. A jets in cross flow turbulence generator was constructed with the specific aim of producing similar turbulence conditions within a large scale test section. Hot-wire traverse measurements were used to establish the turbulent flow properties at the test plate location. It was

found that the amount of air required to create high free-stream turbulence levels resulted in significant peaks in the velocity and turbulence profile at the test plate location. To overcome this issue, injection plates containing an array of holes of different diameter were specified resulting in a more uniform flux distribution at the turbulence generator location. The combination of the multi diameter injection plate and a full span cylinder produced sufficiently uniform turbulence profiles at the test section location. A total of three different turbulence intensity profiles (Tu 10, 16 and 25%) were created by varying the velocity ratio of the cross flow jets. Independent length scale control at a Tu=16% was made possible by removing the span-wise cylinder.

For the simulation of engine density ratios, a novel turbo expander system was designed and built to deliver stable coolant flows across a range of temperatures. The system is capable of producing temperatures of $-20^{\circ}\text{C}\pm$ for extended periods of time.

8.2 Cylindrical hole effusion subjected to highly turbulent free-stream conditions

An angled effusion cooling geometry with a combustor relevant design has been evaluated in terms of adiabatic effectiveness and normalised HTC over a range of free-stream turbulence conditions; 10, 16 and 25% intensity, integral length scale-to-coolant hole diameter ratios of 13 and 26; coolant to free-stream density ratios of 1.1 and 1.4.

- The detailed adiabatic surface effectiveness measurements on the effusion array, measured using the IR camera system, showed increased free-stream turbulence can both improve and reduce the film effectiveness depending on the coolant jet blowing ratio.
- The mode change (i.e. attached or detached jet flow) of the coolant jet signals a change in the response of the cooling film to free-stream turbulence intensity. Once the coolant detaches from the surface the elevated turbulence increases the mixing between the film and the free-stream. This then transports some of the detached coolant back towards the surface.
- At the highest blowing ratio ($BR=1.5$), an increase in spatially averaged effectiveness of 74% is observed at $Tu=25\%$ relative to the 10% turbulence case.
- Increasing free-stream turbulence improves lateral spreading and also reduces the streamwise coverage, as the film mixes with the free-stream.
- A doubling of turbulent length scale from $\Lambda L/D = 13$ to 26 had only a minor impact on the surface effectiveness.
- An interrogation of the gas temperature field was performed, which revealed some of the important fluid behaviour which drives the changes in measured surface effectiveness.
- Coherent jet structures revealed by temperature traverse measurements showed that, the core coolant concentration in the detached effusion jets was reduced as the free-stream turbulence was increased.

- The streamwise temperature traverse shows that the lateral spreading reduces the coolant core length, producing the lower centerline effectiveness values shown in the film effectiveness data.
- The impact of density ratio as an independent parameter was found to be relatively weak. The area averaged plots show momentum flux as the appropriate scaling parameter for variable density ratio tests. This provides strong evidence that data collected at low DR's can be scaled to engine representative DR's.
- The introduction of the coolant film augments the surface heat transfer coefficient. The augmentation in HTC is a strong function of the coolant blowing ratio. The combination of a high blowing ratio and low free-stream turbulence produces the lowest HFR due to the poor surface film coverage and the significant disruption to the near wall flow.

8.3 Fanned hole effusion

8.4 Summary

A fan shaped and porosity matched plain hole effusion array has been evaluated in terms of adiabatic effectiveness, normalised HTC and HFR over two free-stream turbulence conditions; 10 and 25%. A new diffusing fanned hole design has been developed, which may be manufactured using existing laser drilling techniques. The performance of the modified fan design has been

compared with the that of two other existing cooling schemes (i.e. plain cylindrical and conventional fanned effusion designs) in order to establish the relative hot side cooling performance.

Investigation of fanned and cylindrical hole effusion arrays

- The adiabatic surface effectiveness measurements of fanned and cylindrical hole effusion revealed a substantial improvement in film effectiveness when fanned effusion was employed. At the highest blowing ratio (BR=5) an increase in spatially average effectiveness of 89% is observed at a free-stream turbulence level of $Tu=10\%$, relative to cylindrical hole effusion.
- The diffusion created by fanning the hole exit produced an array of attached cooling jets across the blowing ratio range of 2.5 - 5. In contrast, over the same range, the coolant delivered by the cylindrical effusion array remains detached due to the increase in coolant momentum normal to the hot side surface.
- The cylindrical effusion data showed that detached cooling jets still offer benefits in terms of film effectiveness due to the reduction in near wall gas temperature caused by the mixing of the coolant with the mainstream flow.
- The data shows the film created by the fanned effusion array develops rapidly, with the film effectiveness becoming asymptotic by the 9th

row of cooling holes. In the case of the cylindrical array the film build up is much slower, with similar span-averaged values at the 12th row produced by the fanned geometry after only three rows of cooling holes.

- Flow field temperature measurements revealed the 16° fan angle to spread coolant laterally between neighbouring holes. This leads to the development of a uniform, continuous film by the 9th row of cooling holes.
- In terms of surface effectiveness both cooling schemes demonstrated low sensitivity to free-stream turbulence. For the fanned geometry, an increase in free-stream turbulence intensity from $Tu=10\%$ to 25% resulted in a 5.9% reduction in spatially averaged effectiveness.
- At $BR=2.5$ the introduction of the coolant film produced similar levels of HTC augmentation for fanned and cylindrical hole effusion. At $BR=5$, the level of augmentation increased by 51% and 47% for the fanned and cylindrical hole case respectively.

Modified fan design

- A new diffusing hole design has been defined which can be created using conventional manufacturing techniques such as laser/percussion drilling.
- The adiabatic film effectiveness measurements showed the reduced fan angle of 5.4° and increased inclination angle of 22° was sufficient to

prevent coolant detachment. However, the reduced fan angle did not maintain the same level of lateral coolant spreading.

- The spatially averaged adiabatic film effectiveness data showed similar improvements over cylindrical effusion, with an increase in spatially averaged effectiveness of 67% at $BR=5$, $Tu=10\%$.
- The data showed a marked decrease in the HTC augmentation of the modified fan in comparison to the baseline fan geometry, with a spatially averaged reduction of 17%. However, the superior film performance of the baseline fan produced the best overall film performance (HFR).

8.5 Outlook and future work

The present investigation evaluated the hot side film performance of effusion cooling at combustor representative turbulence conditions. An extensive range of flow conditions were tested on a limited range of geometries. The current work could be continued by investigating a wider range of geometric configurations. In addition, an optimization study could also be performed to determine optimal hole shape, number, spacing, injection and compound angle. This would provide a valuable database of the relative performance of different cooling configurations.

The detailed film effectiveness data and flow field gas temperature measurements could be used to evaluate computational codes and analytical models. An additional single row study would provide the data required to evaluate the Sellers superposition model [41]. The heat transfer coefficient data presented in this thesis was normalised by the un-blown HTC; further work could be carried out to evaluate the local heat transfer coefficient by performing a thermal-electric simulation of the entire foil similar to [46].

Other work beyond the scope of the present apparatus includes the time resolved mixing processes between the coolant jet and the free-stream. This could be visualised using qualitative techniques such as Shadowgraph and Schleieren photography. Quantitative methods such as particle image velocimetry (PIV) could also be performed.

Looking towards the future of effusion cooling research, the growing maturity of manufacturing techniques such as Direct Laser Deposition (DLD) are set to revolutionise effusion cooling technology. The use of DLD opens up the design space significantly by removing almost all of the manufacturing limitations of current laser/percussion drilling methods, allowing intricate heat removal features to be created both internally and externally on effusion cooling schemes. To take full advantage of this emerging technology, fully coupled heat transfer (Biot scaled) experiments will be required in addition to the film experiments reported in this work.

It is hoped that, the preceding suggestions for research activity will, in conjunction with results of the current work, help to establish design methods of greater accuracy that enhance the confidence in initial designs of film cooled effusion arrays of combustor liners.

Bibliography

- [1] J. D. Mattingly, *Elements of Gas Turbine Propulsion*. McGraw-Hill, 2000.
- [2] Z. S. Spakovszky, “Unified: Thermodynamics and propulsion,” *Massachusetts Institute of Technology*, no. 16.Unified.
- [3] K. M. B. Gustafsson and T. G. Johansson, “An experimental study of surface temperature distribution on effusion-cooled plates,” *Journal of Engineering for Gas Turbines and Power*, vol. 123, no. 2, pp. 308–316, 2001.
- [4] A. H. Lefebvre, *Gas turbine combustion*. Taylor & Francis, 2 ed., 1999.
- [5] Y. A. engel, *Heat transfer : a practical approach*. McGraw-Hill, 2 ed., 2003.
- [6] R. J. Goldstein, *Film cooling, Advances in Heat Transfer*, vol. 8. Academic, New York, 1971.
- [7] B. Sen, D. L. Schmidt, and D. G. Bogard, “Film cooling with compound angle holes: heat transfer,” *Journal of Turbomachinery*, vol. 118, pp. 800–806, Oct 1996.

- [8] D. Martin and S. J. Thorpe, “Experiments on combustor effusion cooling under conditions of very high free-stream turbulence,” in *Proceedings of the 2012 Turbine Technical Conference & Exposition, June 11 - 15*, (Copenhagen, Denmark), pp. GT2012–68863, ASME, June 2012.
- [9] D. Martin, “Effusion wall cooling studies (part 1),” *Loughborough UTC*, p. TT12R17, December 2012.
- [10] D. Martin, “Effusion wall cooling studies (part 2),” *Loughborough UTC*, p. TT13R05, March 2013.
- [11] T. F. Fric and A. Roshko, “Vortical structure in the wake of a transverse jet,” *Journal of Fluid Mechanics*, vol. 279, pp. 1–47, 1994.
- [12] Z. M. Moussa, J. W. Trischka, and S. Eskinazi, “Near field in the mixing of a round jet with a cross-stream,” *Journal of Fluid Mechanics*, vol. 80, pp. 49–80, 1977.
- [13] D. K. Walters and J. H. Leylek, “Detailed analysis of film-cooling physics. part i: Streamwise injection with cylindrical holes,” *Journal of Turbomachinery*, vol. 122, pp. 102–112, January 2000.
- [14] D. G. Bogard and K. A. Thole, “Gas turbine film cooling,” *Journal of Propulsion and Power*, vol. 22, no. 2, pp. 249–270, 2006.
- [15] A. B. H.-J. Wurm, B.; Schulz, “A new test facility for investigating the interaction between swirl flow and wall cooling films in combustors,” in *ASME TURBO EXPO 2009: Power for land sea and air, June 8 - 12*, (Orlando, FL, USA), pp. GT2009–59961, ASME, June 2009.

- [16] S. Baldauf, M. Scheurlen, A. Schulz, and S. Wittig, “Correlation of film cooling effectiveness from thermographic measurements at engine like conditions,” *Journal of Turbomachinery*, vol. 124, pp. 686 – 698, June 2002.
- [17] R. Goldstein, E. Eckert, and F. Burggraf, “Effects of hole geometry and density on three-dimensional film cooling,” *International Journal of Heat and Mass Transfer*, vol. 17, no. 5, pp. 595 – 607, 1974.
- [18] J. P. Bons, C. D. MacArthur, and R. B. Rivir, “The effect of high free-stream turbulence on film cooling effectiveness,” *Journal of Turbomachinery*, vol. 118, no. 4, pp. 814–825, 1996.
- [19] S. Baldauf, A. Schulz, and S. Wittig, “High-resolution measurements of local effectiveness from discrete hole film cooling,” *Journal of Turbomachinery*, vol. 123, no. 4, pp. 758–765, 2001.
- [20] D. R. Pedersen, E. R. G. Eckert, and R. J. Goldstein, “Film cooling with large density differences between the mainstream and the secondary fluid measured by the heat-mass transfer analogy,” *Journal of Heat Transfer*, vol. 99 Ser C, no. 4, pp. 620–627, 1977.
- [21] A. K. Sinha, D. G. Bogard, and M. E. Crawford, “Film-cooling effectiveness downstream of a single row of holes with variable density ratio,” *Journal of Turbomachinery*, vol. 113, no. 3, pp. 442–449, 1991.
- [22] J. M. Cutbirth and D. G. Bogard, “Effects of coolant density ratio on film cooling performance on a vane,” in *ASME TURBO EXPO 2003*:

International joint power generation, June 16 - 19, vol. 5, (Atlanta, Georgia, USA), pp. GT2003-38582, ASME, 2003.

- [23] A. Kohli and D. G. Bogard, “Adiabatic effectiveness, thermal fields, and velocity fields for film cooling with large angle injection,” *Journal of Turbomachinery*, vol. 119, pp. 352 – 358, 1997.
- [24] N. Foster and D. Lampard, “Flow and film cooling effectiveness following injection through a row of holes,” *Journal for Engineering for Power*, vol. 102, pp. 584 – 588, 1980.
- [25] V. Aga, M. Rose, and R. S. Abhari, “Experimental flow structure investigation of compound angled film cooling,” *Journal of Turbomachinery*, vol. 130, no. 3, pp. 031005-2 – 031005-8, 2008.
- [26] M. Gritsch, A. Schulz, and S. Wittig, “Effect of crossflows on the discharge coefficient of film cooling holes with varying angles of inclination and orientation,” *Journal of Turbomachinery*, vol. 123, no. 4, pp. 781–787, 2001.
- [27] R. S. Bunker, “A review of shaped hole turbine film-cooling technology,” *Journal of Heat Transfer*, vol. 127, no. 4, pp. 441–453, 2005.
- [28] M. E. Taslim and A. Khanicheh, “Film effectiveness downstream of a row of compound angle film holes,” *Journal of Heat Transfer*, vol. 127, no. 4, pp. 434–440, 2005.
- [29] J. Dittmar, A. Schulz, and S. Wittig, “Assessment of various film-cooling configurations including shaped and compound angle holes based on

- large-scale experiments,” *Journal of Turbomachinery*, vol. 125, no. 1, pp. 57–64, 2003.
- [30] W. Colban, K. A. Thole, and M. Haendler, “A comparison of cylindrical and fan-shaped film-cooling holes on a vane endwall at low and high freestream turbulence levels,” *Journal of Turbomachinery*, vol. 130, pp. 031007–1 – 031007–9, May 2006.
- [31] K. Kadotani and R. J. Goldstein, “On the nature of jets entering a turbulent flow - a. jet-mainstream interaction,” *Journal of engineering for power*, vol. 101, no. 3, pp. 459–465, 1979.
- [32] K. Kadotani and R. J. Goldstein, “On the nature of jets entering a turbulent flow - b. film cooling performance,” *Journal of engineering for power*, vol. 101, no. 3, pp. 466–470, 1979.
- [33] B. Bangert, A. Kohli, J. Sauer, and K. Thole, “High freestream turbulence simulation in a scaled-up turbine vane passage,” in *Proceedings of the 1997 International Gas Turbine & Aeroengine Congress & Exposition, June 2 - 5*, (Orlando, FL, USA), pp. 97–GT–51, American Society of Mechanical Engineers, June 1997.
- [34] J. E. Mayhew, J. W. Baughn, and A. R. Byerley, “The effect of freestream turbulence on film cooling adiabatic effectiveness,” *International Journal of Heat and Fluid Flow*, vol. 24, pp. 669–679, October 2003.

- [35] A. Kohli and D. G. Bogard, “Effects of very high free-stream turbulence on the jet-mainstream interaction in a film cooling flow,” *Journal of Turbomachinery*, vol. 120, no. 4, pp. 785–790, 1998.
- [36] G. B. Kelly and D. G. Bogard, “An investigation of the heat transfer for full coverage film cooling,” in *ASME TURBO EXPO 2003: International joint power generation, June 16 - 19*, vol. 5 A, (Atlanta, GA, United states), pp. GT2003–38716, ASME, June 2003.
- [37] F. Ames, C. Wang, and P. Barbot, “Measurement and prediction of the influence of catalytic and dry low nox combustor turbulence on vane surface heat transfer,” *Journal of Turbomachinery*, vol. 125, pp. 221–231, 2003.
- [38] F. Ames, M. Argenziano, and C. Wang, “Measurement and prediction of heat transfer distributions on an aft-loaded vane subjected to the influence of catalytic and dry low nox combustor turbulence,” *Journal of Turbomachinery*, vol. 126, pp. 139–149, 2004.
- [39] C. Saumweber, A. Schulz, and S. Wittig, “Free-stream turbulence effects on film cooling with shaped holes,” *Journal of Turbomachinery*, vol. 125, no. 1, pp. 65–73, 2003.
- [40] M. Sasaki, K. Takahara, T. Kumagai, and M. Hamano, “Film cooling effectiveness for injection from multirow holes,” *Journal of Engineering for Power, Transactions ASME*, vol. 101, no. 1, pp. 101 – 108, 1979.
- [41] J. P. Sellers, “Gaseous film cooling with multiple injection stations,” *AIAA*, vol. 1, no. 9, pp. 2154 – 2156, 1963.

- [42] M. K. Harrington, M. A. McWaters, D. G. Bogard, C. A. Lemmon, and K. A. Thole, “Full-coverage film cooling with short normal injection holes,” *Journal of Turbomachinery*, vol. 123, no. 4, pp. 798–805, 2001.
- [43] M. Martiny, A. Schulz, and S. Wittig, “Full-coverage film cooling investigations: adiabatic wall temperatures and flow visualization,” in *International Mechanical Engineering Congress and Exposition November 12 - 17*, (San Francisco, CA, USA), pp. 95–WA/HT–4, 1995.
- [44] J. J. Scritture, K. A. Thole, and S. W. Burd, “Investigation of velocity profiles for effusion cooling of a combustor liner,” *Journal of Turbomachinery*, vol. 129, pp. 518–526, August 2006.
- [45] A. Ceccherini, B. Facchini, L. Tarchi, L. Toni, and D. Coutandin, “Combined effect of slot injection, effusion array and dilution hole on the cooling performance of a real combustor liner,” in *Proceedings of the ASME Turbo Expo 2009: Power for Land, Sea and Air, June 8 - 12*, (Orlando, FL, United states), pp. GT2009–60047, June 2009.
- [46] B. Facchini, F. Maiuolo, L. Tarchi, and D. Coutandin, “Combined effect of slot injection, effusion array and dilution hole on the heat transfer coefficient of a real combustor liner: Part 1—experimental analysis,” *ASME Conference Proceedings*, pp. GT2010–22937, June 2010.
- [47] P. E. Roach, “The generation of nearly isotropic turbulence by means of grids,” *International Journal of Heat and Fluid Flow*, vol. 8, pp. 82–92, 6 1987.

- [48] W. D. Baines and E. G. Peterson, “An investigation of flow through screens,” *Trans ASME*, pp. 467–480, 1951.
- [49] J. M. Cecil and R. T. Robert, “Effect of free-stream turbulence on film cooling,” *NASA Lewis Research Center Cleveland*, no. NASA/TN-D-7958, 1975.
- [50] S. Nasir, J. S. Carullo, W. F. Ng, K. A. Thole, H. Wu, L. J. Zhang, and H. K. Moon, “Effects of large scale high freestream turbulence, and exit reynolds number on turbine vane heat transfer in a transonic cascade,” *Journal of Turbomachinery*, vol. 131, pp. 021021–1–021021–11, April 2009.
- [51] M. G. el hak and S. Corrsin, “Measurements of the nearly isotropic turbulence behind a uniform jet grid,” *Journal of Fluid Mechanics*, vol. 62, pp. 115–143, 1974.
- [52] S. Jenkins, K. Varadarajan, and D. G. Bogard, “The effects of high mainstream turbulence and turbine vane film cooling on the dispersion of a simulated hot streak,” *Journal of Turbomachinery*, vol. 126, no. 1, pp. 203–211, 2004.
- [53] D. G. Bogard, K. A. Thole, and M. E. Crawford, “Hydrodynamic effects of heat transfer for film-cooled turbine blades,” *Wright laboratory*, pp. AFB OH 45433–6563, 1992.
- [54] K. A. Thole, D. G. Bogard, and J. L. Whan-Ton, “Generating high freestream turbulence levels,” *Experiments in fluids*, vol. 17, no. 6, pp. 375–380, 1994.

- [55] J.-C. Han, S. Dutta, and S. Ekkad, *Gas turbine heat transfer and cooling technology*. Washington, D.C. ; London: Taylor & Francis, 2000.
- [56] F. E. Ames, C. Wang, and P. A. Barbot, “Measurement and prediction of the influence of catalytic and dry low nox combustor turbulence on vane surface heat transfer,” *Journal of Turbomachinery*, vol. 125, no. 2, pp. 221–231, 2003.
- [57] S. J. Kline and F. A. McClintock, “Describing uncertainties in single-sample experiments,” vol. 75, pp. 3 – 8, 1953.
- [58] H. D. Ammari, N. Hay, and D. Lampard, “The effect of density ratio on the heat transfer coefficient from a film-cooled flat plate,” *Journal of Turbomachinery*, vol. 112, no. 3, pp. 444–450, 1990.
- [59] B. Facchini, L. Tarchi, L. Toni, G. Cinque, and S. Colantuoni, “Investigation of circular and shaped effusion cooling arrays for combustor liner application—part 1: Experimental analysis,” in *ASME TURBO EXPO 2009: Power for land sea and air, June 8 - 12*, (Orlando, FL, USA), pp. GT2009–60037, ASME, 2009.
- [60] L. T. D. C. o. A. P. S. T. A. Andreini. G. Cacioli, B. Facchini, “Density ratio effects on the cooling performances of a combustor liner cooled by a combined slot/effusion system,” in *Proceedings of the 2012 Turbine Technical Conference & Exposition, June 11 - 15*, (Copenhagen, Denmark), pp. GT2012–68263, ASME, 2012.
- [61] Y. Lin, B. Song, B. Li, G. Liu, and Z. Wu, “Investigation of film cooling effectiveness of full-coverage inclined multihole walls with different hole

- arrangements,” *ASME Conference Proceedings*, vol. 2003, no. 36886, pp. 651–660, 2003.
- [62] P. Bradshaw, “The design of low-speed wind tunnels,” *Progress in Aerospace Sciences*, vol. 5, pp. 1–69, 1964.
- [63] J. B. Barlow, W. H. Rae, and A. Pope, *Low-speed wind tunnel testing*. New York ; Chichester: Wiley, 3 ed., 1999.
- [64] R. D. Mehta and P. Bradshaw, “Design rules for small low speed wind tunnels,” *Aeronautical Journal*, vol. 83, no. 827, pp. 443–449, 1979.
- [65] A. T. McDonald and R. W. Fox, “Experimental investigation of incompressible flow in conical diffusers,” *International Journal of Mechanical Sciences*, vol. 8, no. 2, pp. 125–139, 1966.
- [66] H. H. Bruun, *Hot-wire anemometry : principles and signal analysis*. Oxford: Oxford University Press, 1995.
- [67] P. Koutmos and J. McGuirk, “Isothermal flow in a gas turbine combustor a benchmark experimental study,” *Experiments in Fluids*, vol. 7, pp. 344–354, 1989.
- [68] R. MacMullin, W. Elrod, and R. Rivir, “Free-stream turbulence from a circular wall jet on a flat plate heat transfer and boundary layer flow,” *Journal of Turbomachinery*, vol. 111, no. 1, pp. 78–86, 1989.
- [69] F. Ames and R. Moffat, “Effects of simulated combustor turbulence on boundary layer heat transfer,” vol. 138, pp. 11 – 17, 1990.

- [70] B. Prette and D. Baines, “Profiles of the round turbulent jet in a cross flow,” 1967.
- [71] C. Johnston, D. Bogard, and M. McWaters, “Highly turbulent mainstream effects on film cooling of a simulated airfoil leading edge,” in *International Gas Turbine and Aeroengine Congress and Exhibition*, June 7 - 9, pp. 99–GT–261, June 1999.
- [72] M. DE and F. DD, “Evaluation of heat transfer for film-cooled turbine components,” *Journal of Aircraft*, vol. 8, no. 1, pp. 33 – 38, 1971.
- [73] J. Sargison, S. Guo, M. Oldfield, and A. Rawlinson, “The variation of heat transfer coefficient, adiabatic effectiveness and aerodynamic loss with film cooling hole shape,” *Annals of the New York Academy of Sciences*, vol. 934, no. 1, pp. 361–368, 2001.
- [74] W. Kays and M. Crawford, *Convective Heat and Mass Transfer*. New York, MA: McGraw-Hill, 1993.
- [75] J. L. Devore, *Probability and Statistics for Engineering and the Sciences*. Monterey ; CA: Brooks/Cole Publishing Company, 2 ed., 1987.
- [76] F. E. Jørgensen, *How to measure turbulence with hot-wire anemometers - a practical guide*. Dantec Dynamics, 2002.
- [77] L. S. King, “On the convection heat transfer from small cylinders in a stream of fluids, determination of convection constants of small platinum wires with application to hot-wire anemometry,” *Phil. Trans. Roy. Soc. London*,, vol. 214A, pp. 373–432, 1914.

Appendix A

Appendix

A.1 Flow Nozzle

Operating range of bulk main flow through test section.

$$U_{\infty} = 5 - 7 \text{ m/s}$$

For $A_{test} = 0.3575 \text{ m}^2$, $\rho_{\infty} = 0.948 \text{ kg/m}^3$,

$$\dot{M} = 1.7 - 2.4 \text{ kg/s}$$

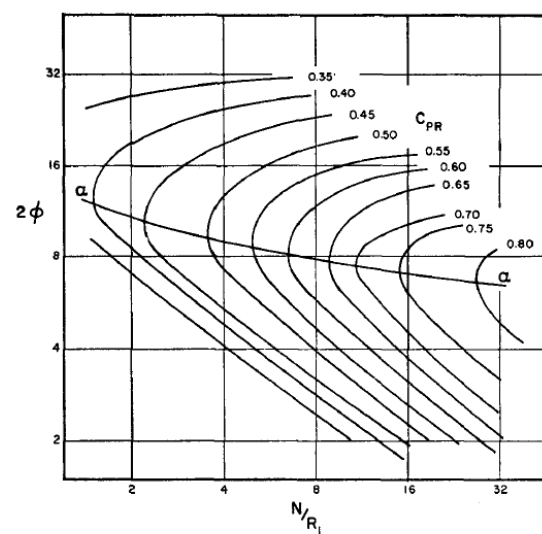
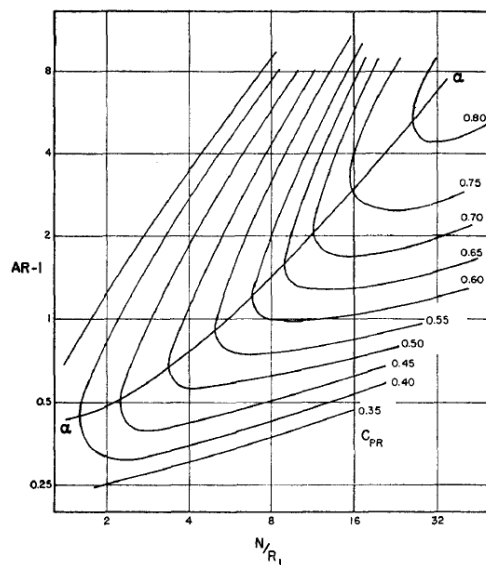
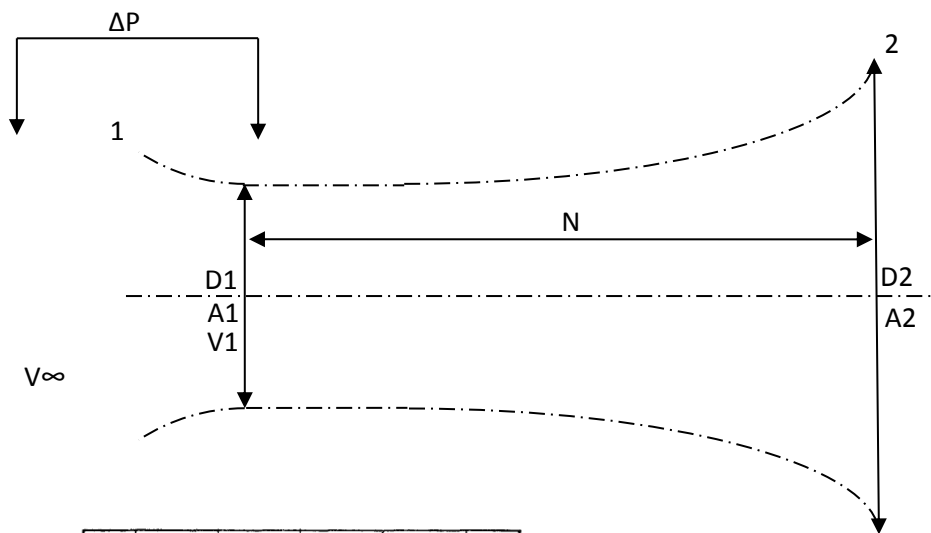
Metering box dimensions:

Dims: 1390x1350x1200

Area: 1.877 m^2

This translates to a meter box velocity range:

$$U_{\infty} = 0.95 - 1.33 \text{ m/s}$$



Pressure recovery contours cross-plotted from conical diffuser data

Config	V_{∞}	D1(m)	A1(m ²)	V1(m/s)	N/Ri	CPR	AR-1	N	D2(m)	A2(m ²)	ΔP	Loss
1	1.33	0.282	0.0624	40	4	0.525	0.75	0.564	0.373	0.109	757.56	359.84
2	0.95	0.282	0.0624	28.57	4	0.525	0.75	0.564	0.373	0.109	386.47	183.57
3	1.33	0.230	0.0416	60	4	0.525	0.75	0.460	0.305	0.073	1705.6	810
4	0.95	0.230	0.0416	42.85	4	0.525	0.75	0.460	0.305	0.073	870.1	413.3

N= length along diffuser centre line

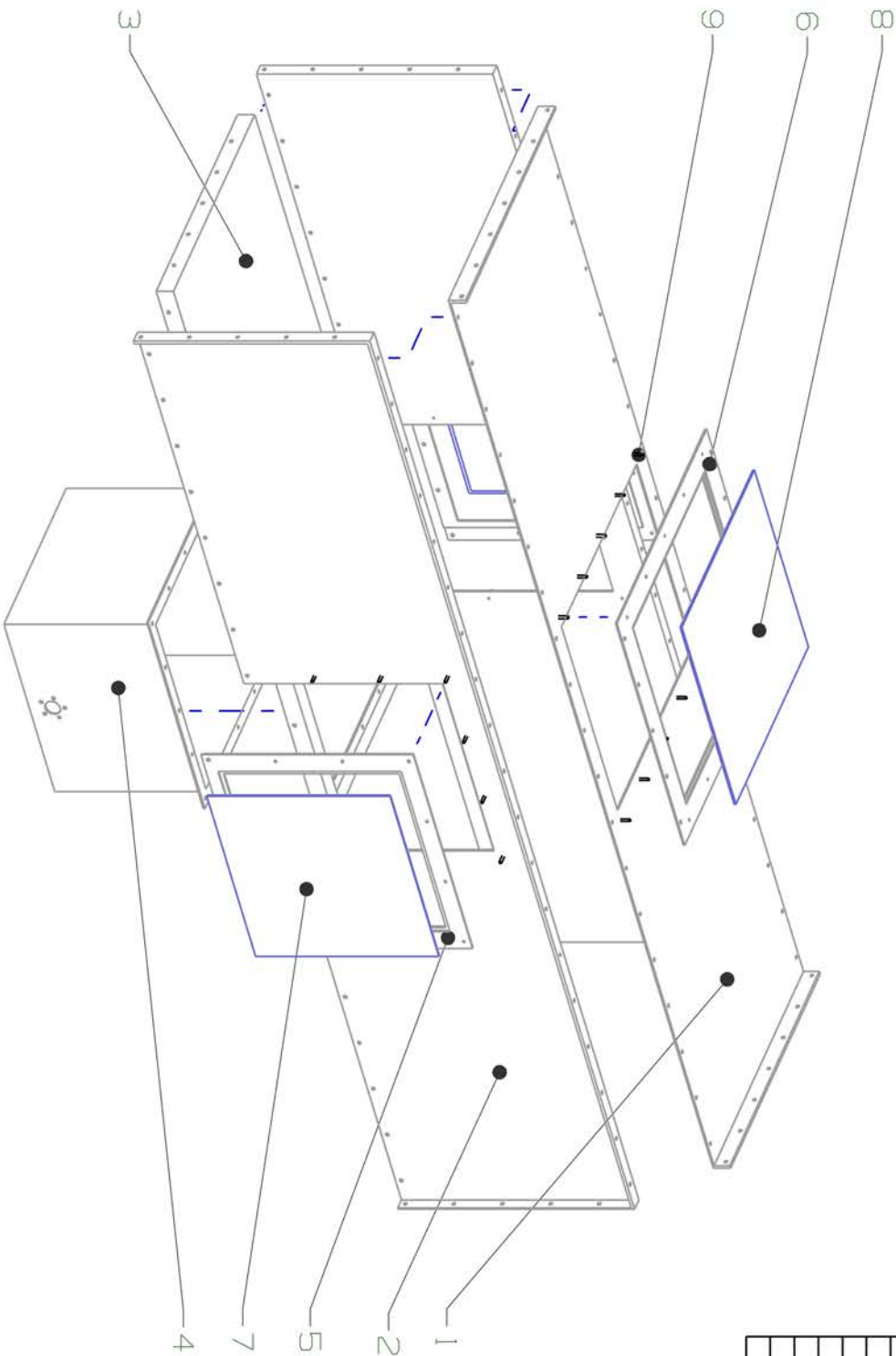
Ri= Local radius of conical diffuser

AR = Area Ratio

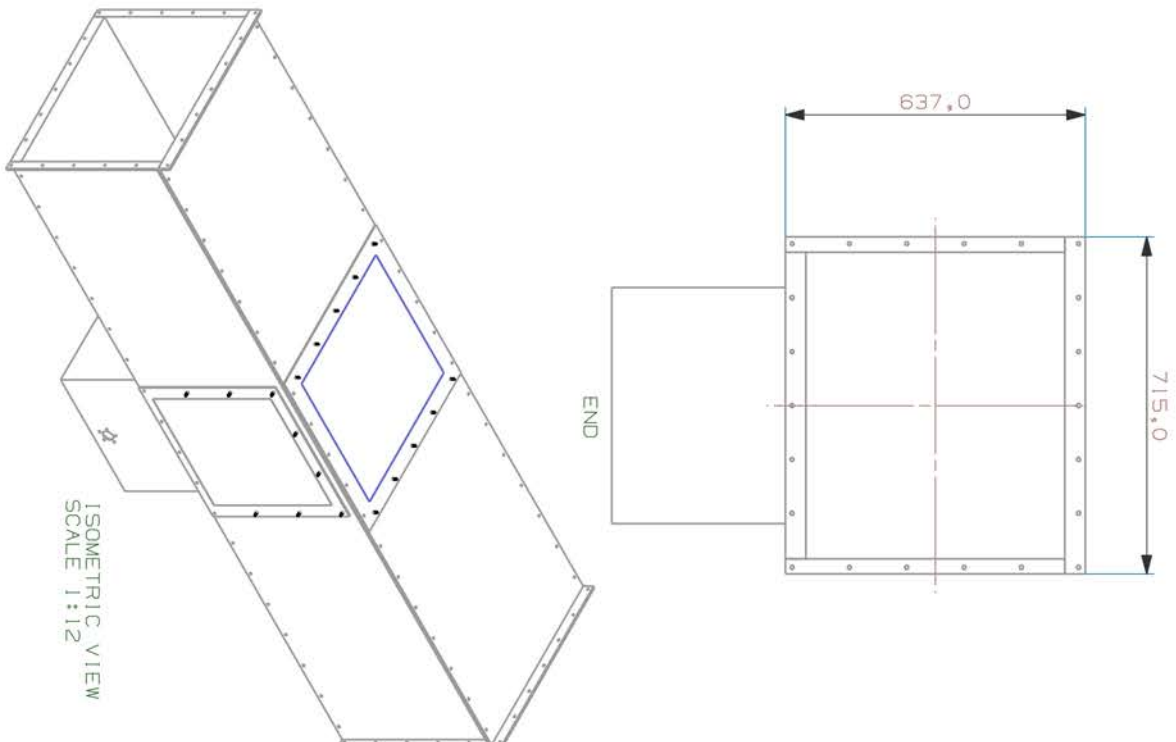
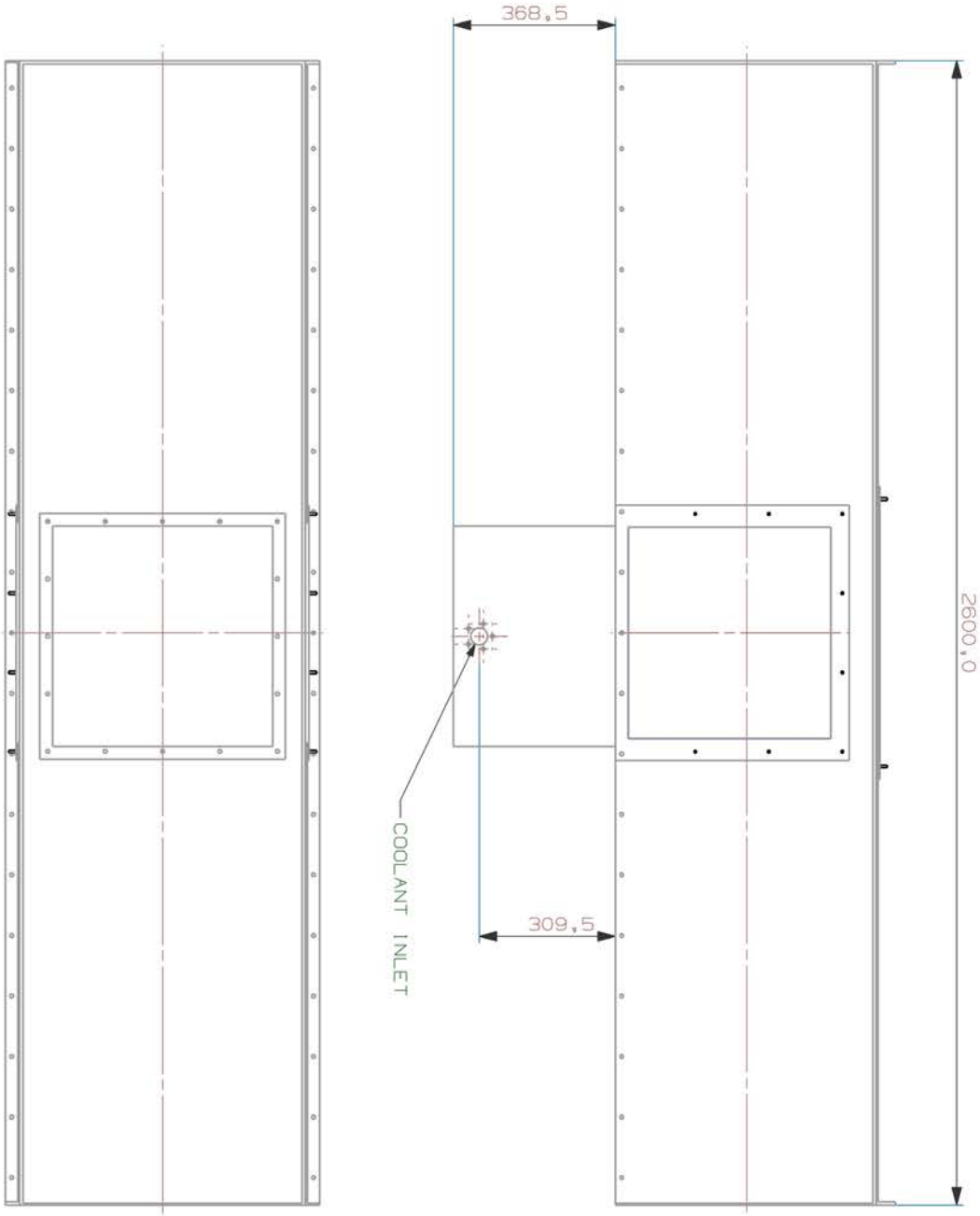
Configuration 3 was selected to be used with a 2500pa differential transducer.

A.2 Rig drawings

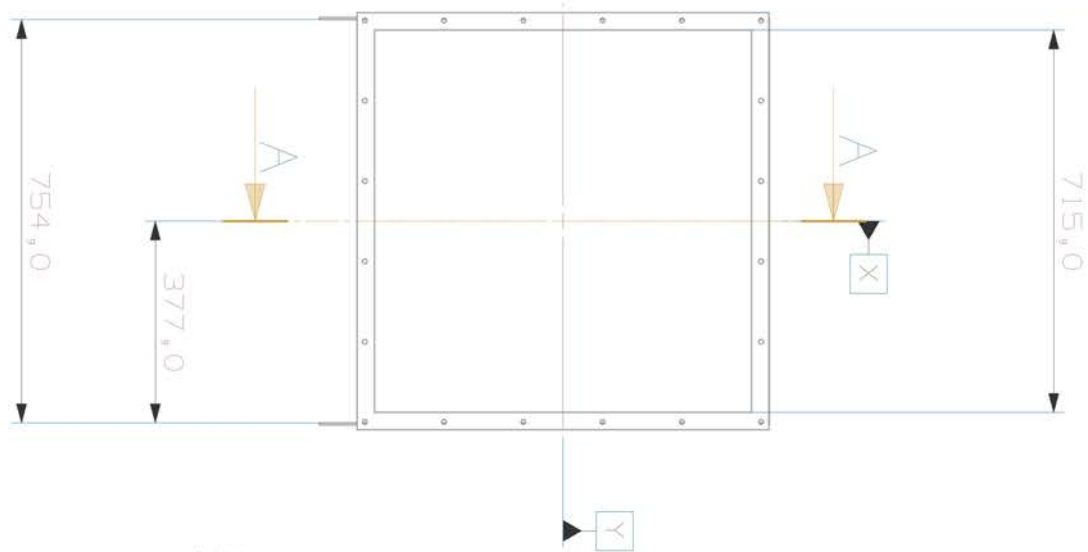
A Fully featured 3D model of the wind tunnel facility is presented. Detail drawings of the main tunnel components and sub assemblies are also shown in isometric and 2D arrangements.



NO.	COMPONENT	QTY
1	TEST SECTION TOP PANEL	1
2	TEST SECTION SIDE PANEL	2
3	TEST SECTION BASE PLATE	3
4	COOLANT PLENUM	1
5	WINDOW MOUNT	2
6	WINDOW MOUNT TOP	1
7	GLASS SIDE	2
8	GLASS TOP	1
9	M6 STUD	26

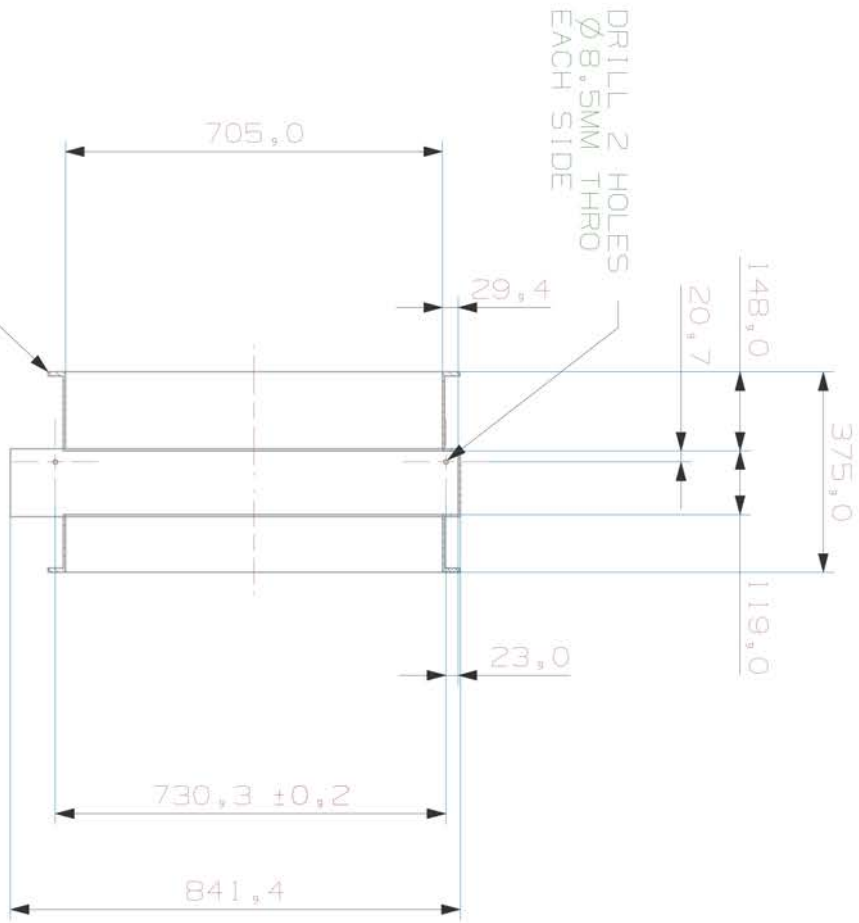


ISOMETRIC VIEW
SCALE 1:12



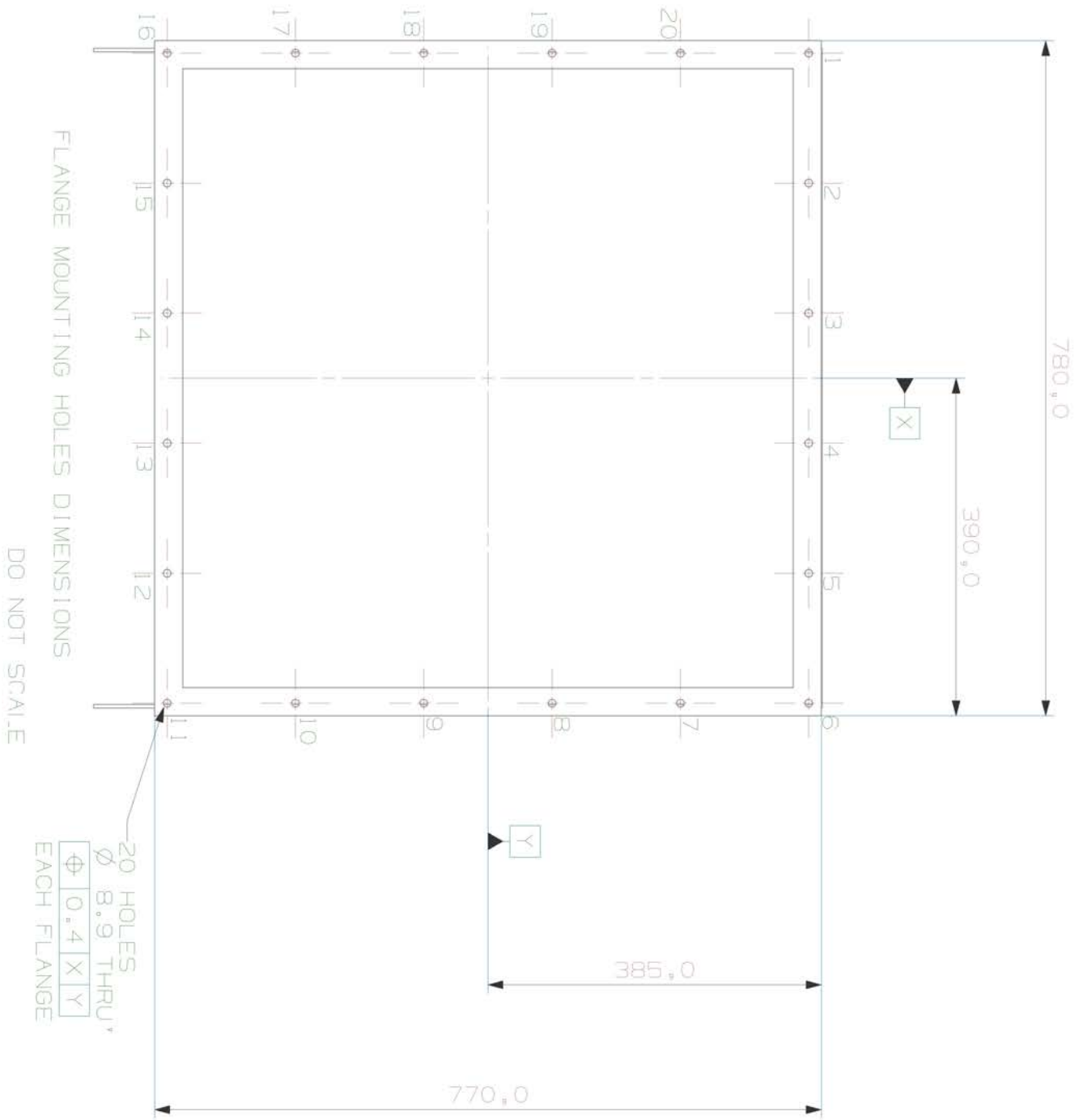
32,5MM FLANGE 8MM THK
2 PLACES
(SEE SHEET 2 FOR HOLE SPACING)

SECTION A - A



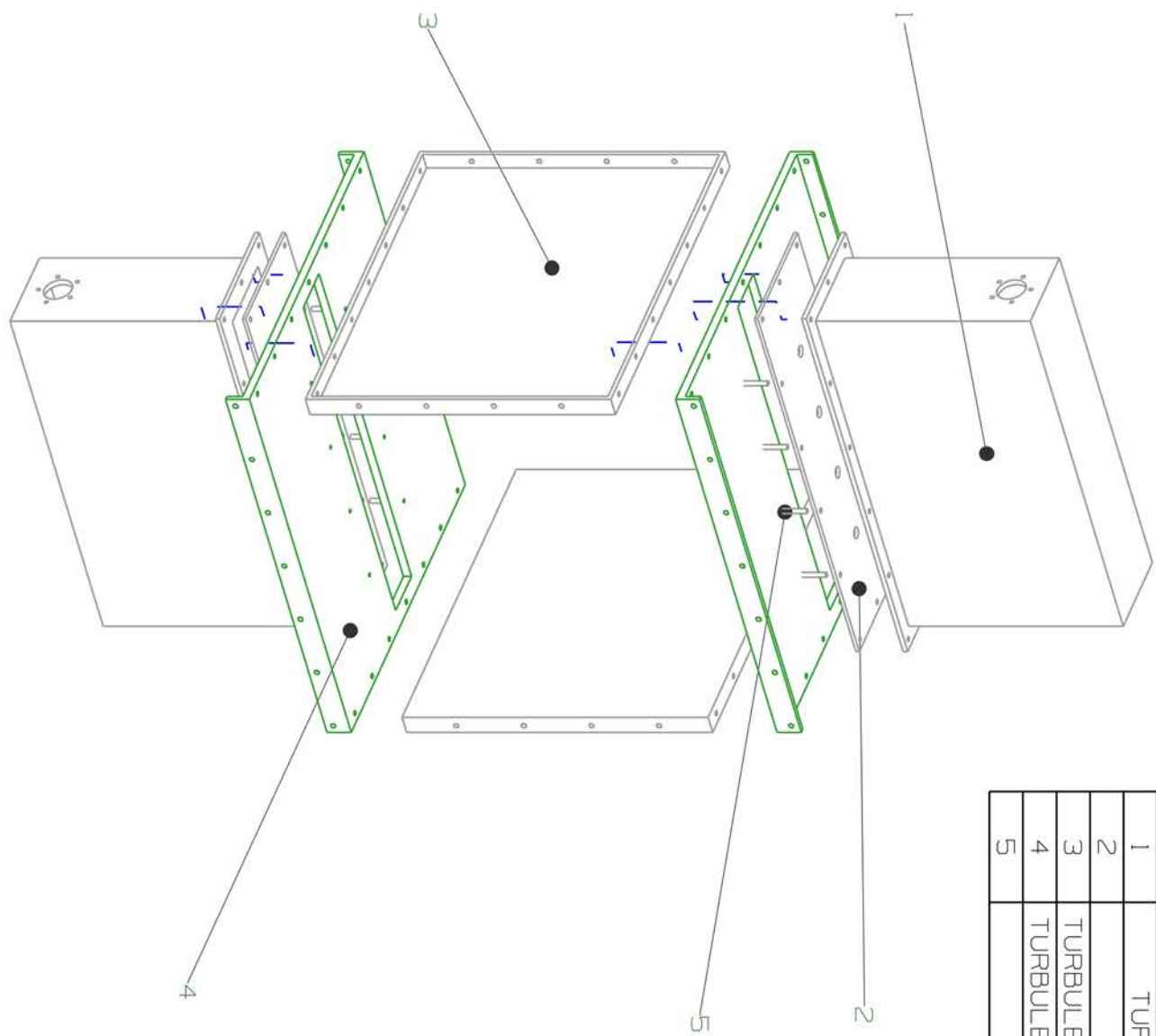
DO NOT SCALE

NOTE:
FABRICATED FROM 4MM
ALUMINIUM ALLOY

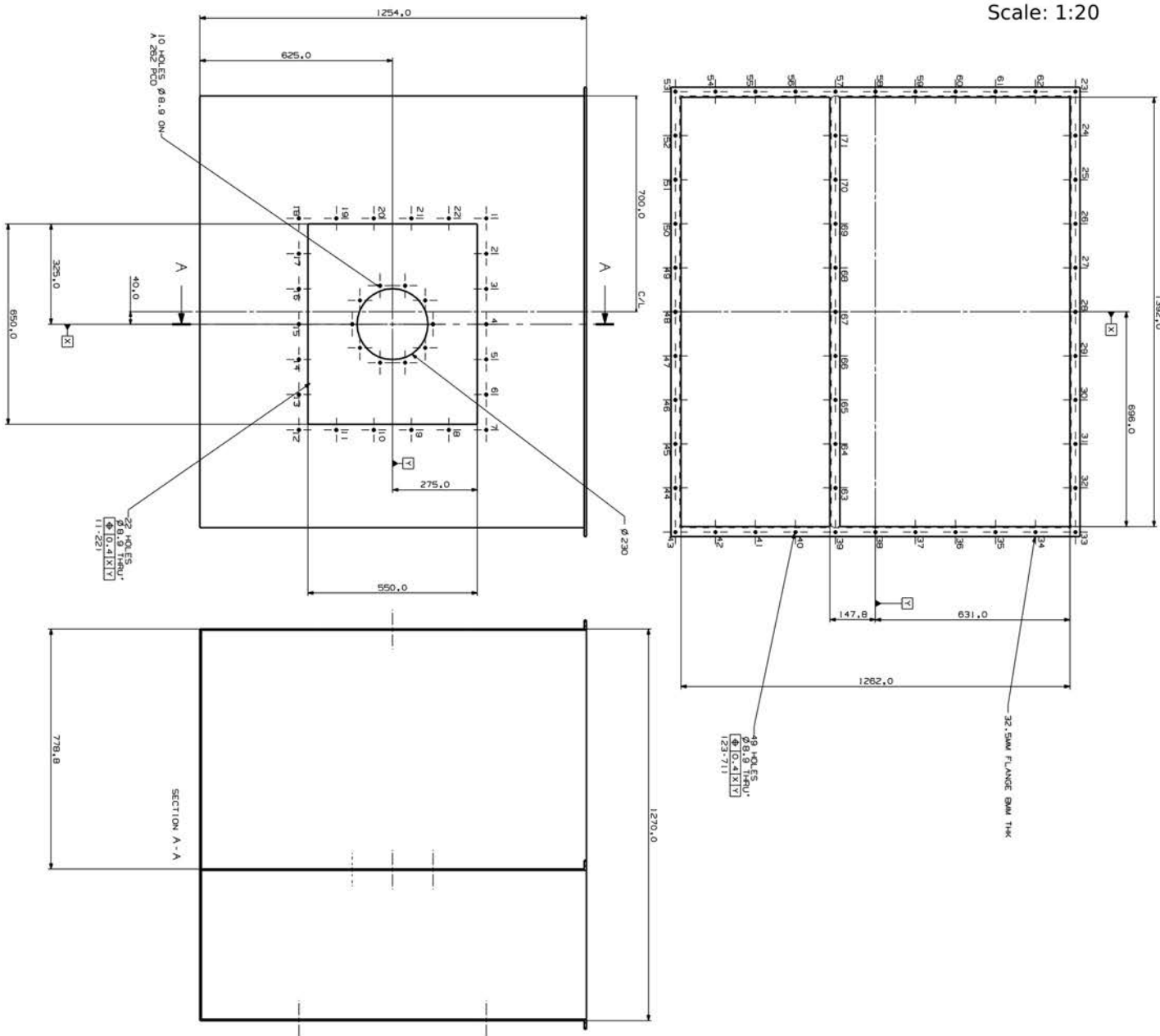


HOLE LOCATIONS		
HOLE NO.	X	Y
1	-375.5	370.5
2	-225.3	370.5
3	-75.1	370.5
4	75.1	370.5
5	225.3	370.5
6	375.5	370.5
7	375.5	222.3
8	375.5	74.1
9	375.5	-74.1
10	375.5	-222.3
11	375.5	-370.5
12	225.3	-370.5
13	75.1	-370.5
14	-75.1	-370.5
15	-225.3	-370.5
16	-375.5	-370.5
17	-375.5	-222.3
18	-375.5	-74.1
19	-375.5	74.1
20	-375.5	222.3

Title: Turbulence generator assembly



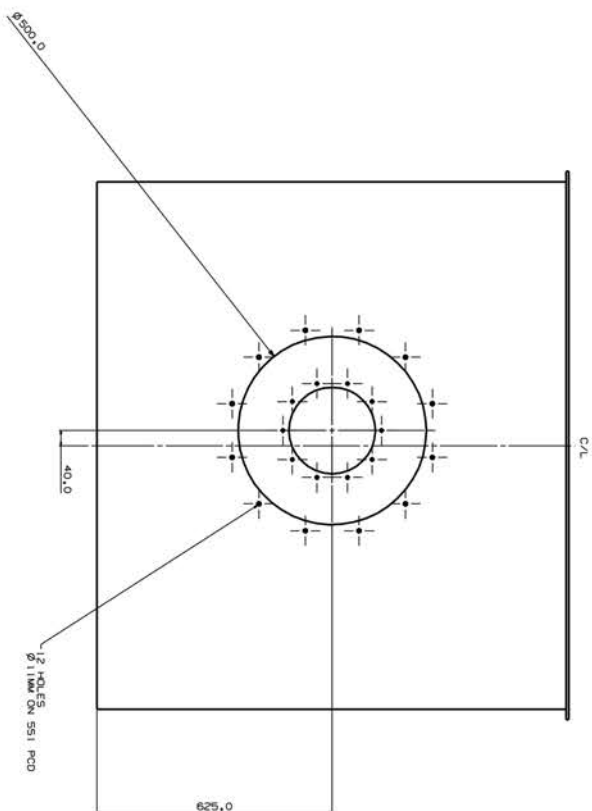
NO.	COMPONENT	QTY
1	TURBULENCE PLENUM	2
2	JET PLATE	2
3	TURBULENCE GEN SIDE PANEL	2
4	TURBULENCE GEN BASE PLATE	2
5	M8 STUD	16



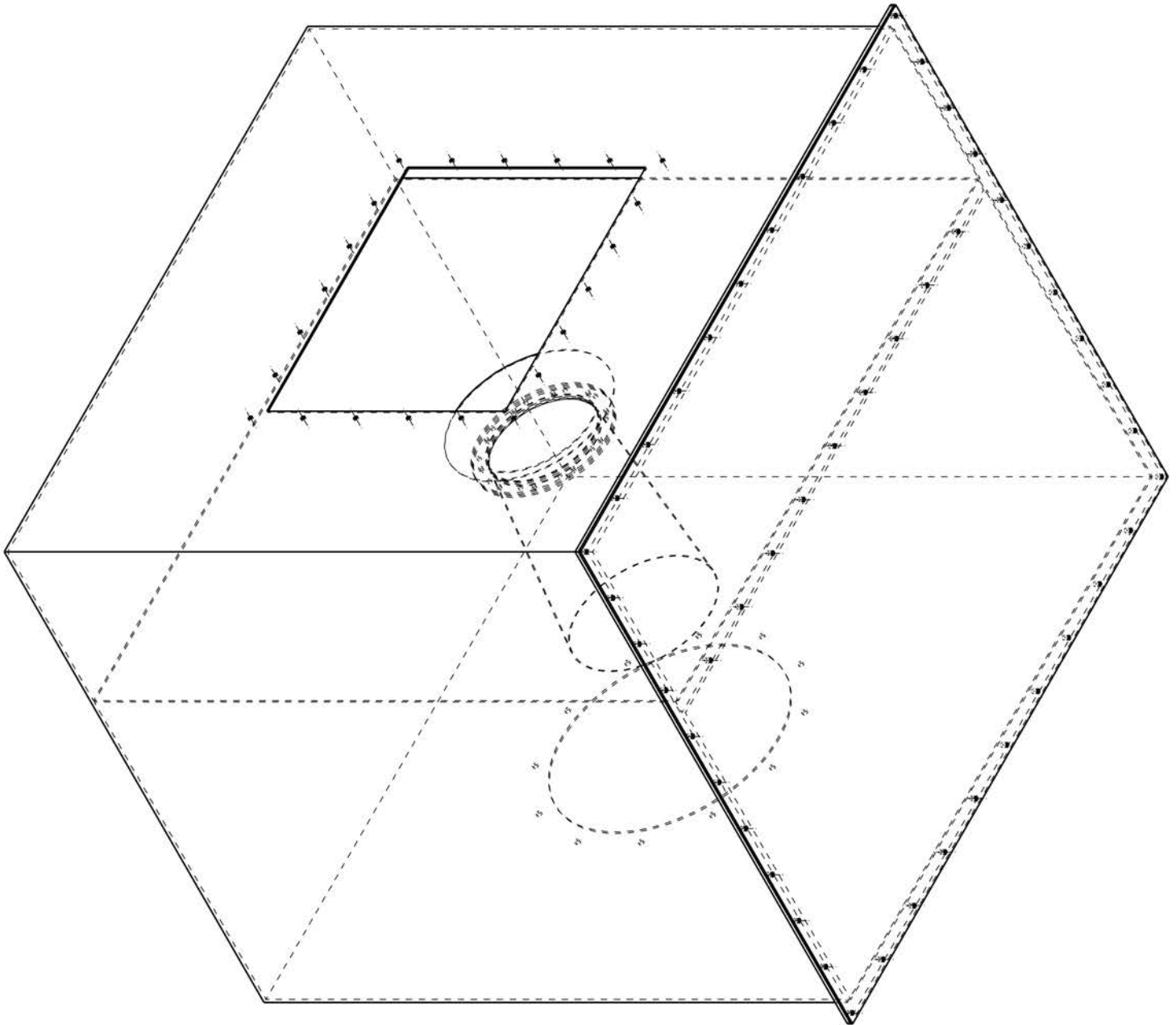
68	-142.8	-129.6
69	-265.6	-129.6
70	-429.4	-129.6
71	-571.2	-129.6

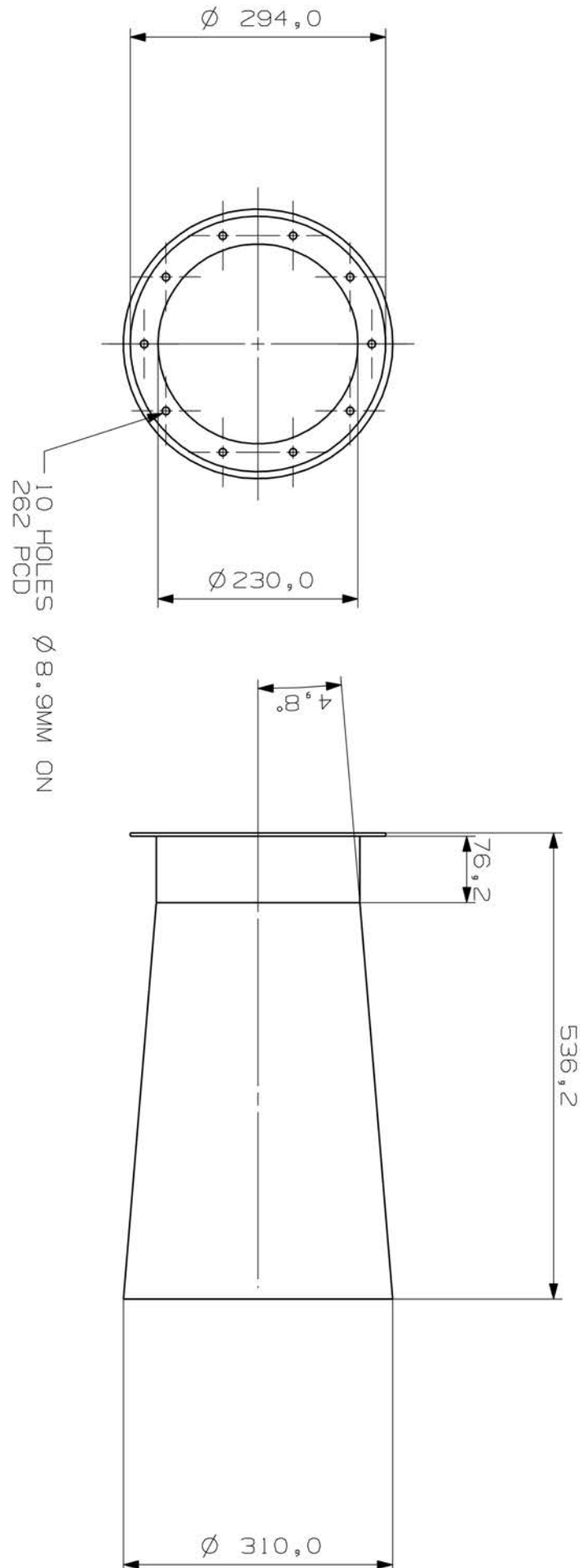
53	71.4	6.8	519.2	0
54	71.4	6.8	519.2	0
55	71.4	6.8	519.2	0
56	71.4	6.8	519.2	0
57	71.4	6.8	519.2	0
58	71.4	6.8	519.2	0
59	71.4	6.8	519.2	0
60	71.4	6.8	519.2	0
61	71.4	6.8	519.2	0
62	71.4	6.8	519.2	0
63	71.4	6.8	519.2	0
64	71.4	6.8	519.2	0
65	71.4	6.8	519.2	0
66	71.4	6.8	519.2	0
67	71.4	6.8	519.2	0
68	71.4	6.8	519.2	0
69	71.4	6.8	519.2	0
70	71.4	6.8	519.2	0
71	71.4	6.8	519.2	0
72	71.4	6.8	519.2	0
73	71.4	6.8	519.2	0
74	71.4	6.8	519.2	0
75	71.4	6.8	519.2	0
76	71.4	6.8	519.2	0
77	71.4	6.8	519.2	0
78	71.4	6.8	519.2	0
79	71.4	6.8	519.2	0
80	71.4	6.8	519.2	0
81	71.4	6.8	519.2	0
82	71.4	6.8	519.2	0
83	71.4	6.8	519.2	0
84	71.4	6.8	519.2	0
85	71.4	6.8	519.2	0
86	71.4	6.8	519.2	0
87	71.4	6.8	519.2	0
88	71.4	6.8	519.2	0
89	71.4	6.8	519.2	0
90	71.4	6.8	519.2	0
91	71.4	6.8	519.2	0
92	71.4	6.8	519.2	0
93	71.4	6.8	519.2	0
94	71.4	6.8	519.2	0
95	71.4	6.8	519.2	0
96	71.4	6.8	519.2	0
97	71.4	6.8	519.2	0
98	71.4	6.8	519.2	0
99	71.4	6.8	519.2	0
100	71.4	6.8	519.2	0

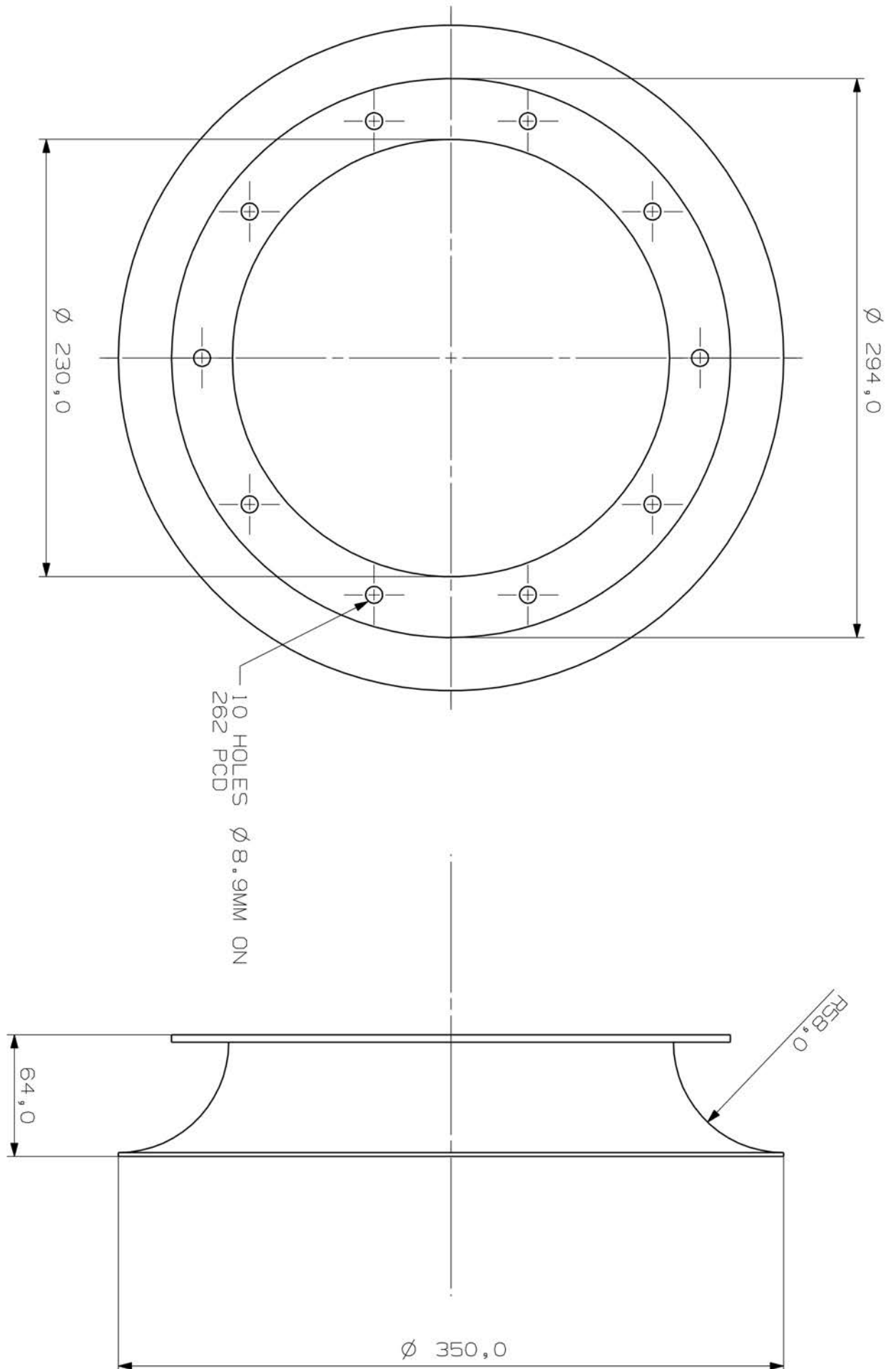
HOE NO.	HOE LOCATION	X
1	-28.3	304
2	-28.7	304
3	-14.3	304
4	0	304
5	14.3	304
6	28.7	304
7	43.0	304
8	57.3	182.4
9	34.3	80.8
10	34.3	-80.8
11	34.3	-182.4
12	34.3	-304
13	28.7	-304
14	14.3	-304
15	0	-304
16	-14.3	-304
17	-28.7	-304
18	-34.3	-304
19	-34.3	-182.4
20	-34.3	-80.8
21	-34.3	80.8
22	-34.3	182.4
FLANGE HOE LOCATIONS		
23	-71.4	649
24	-57.2	649
25	-42.8	649
26	-28.4	649
27	-14.2	649
28	0	649
29	14.2	649
30	28.5	649
31	42.8	649
32	57.2	649

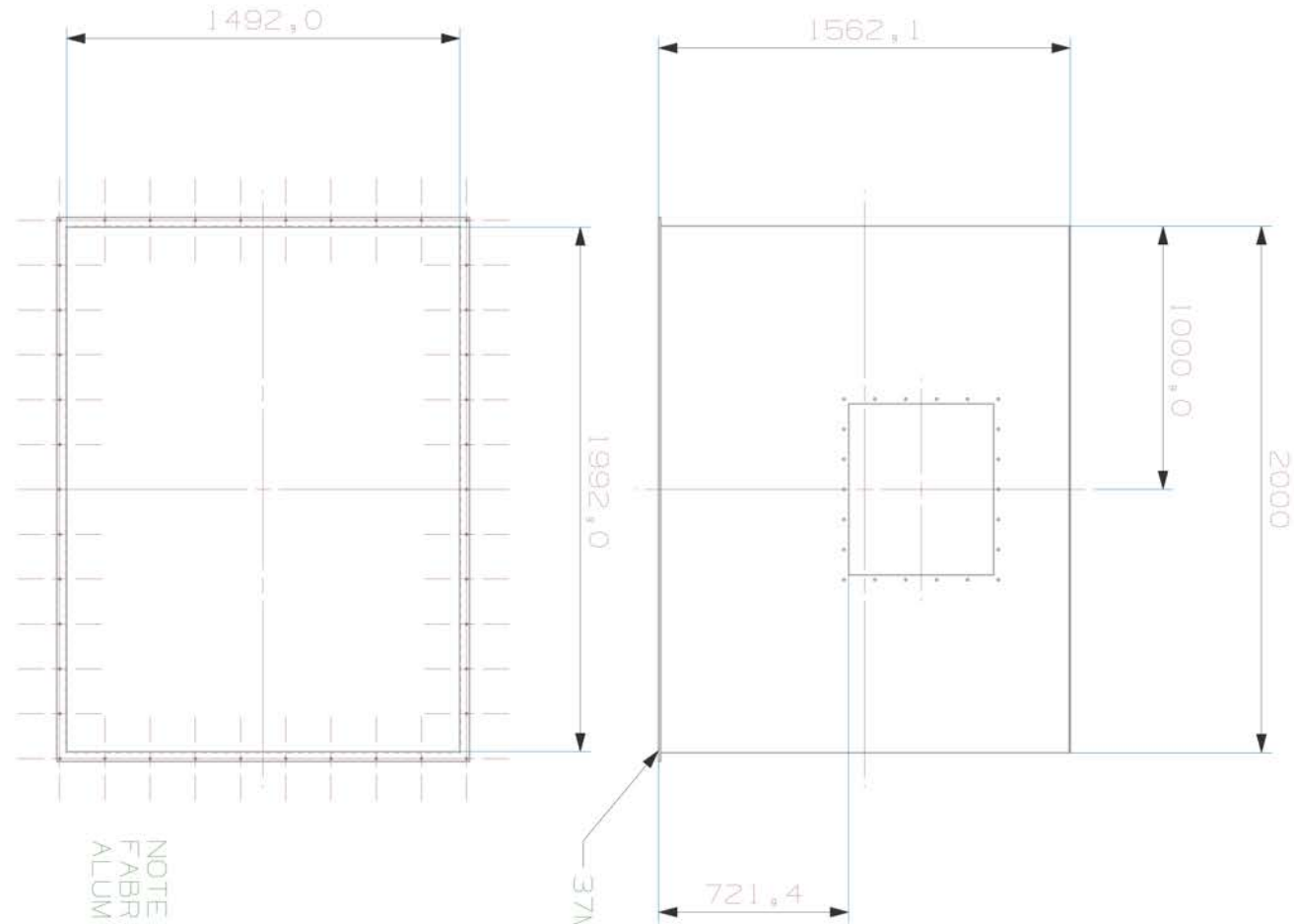


Title: Meter Box
assembly





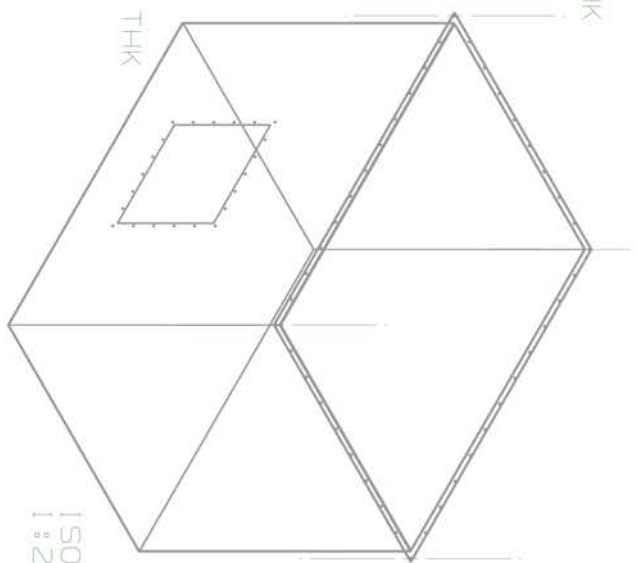




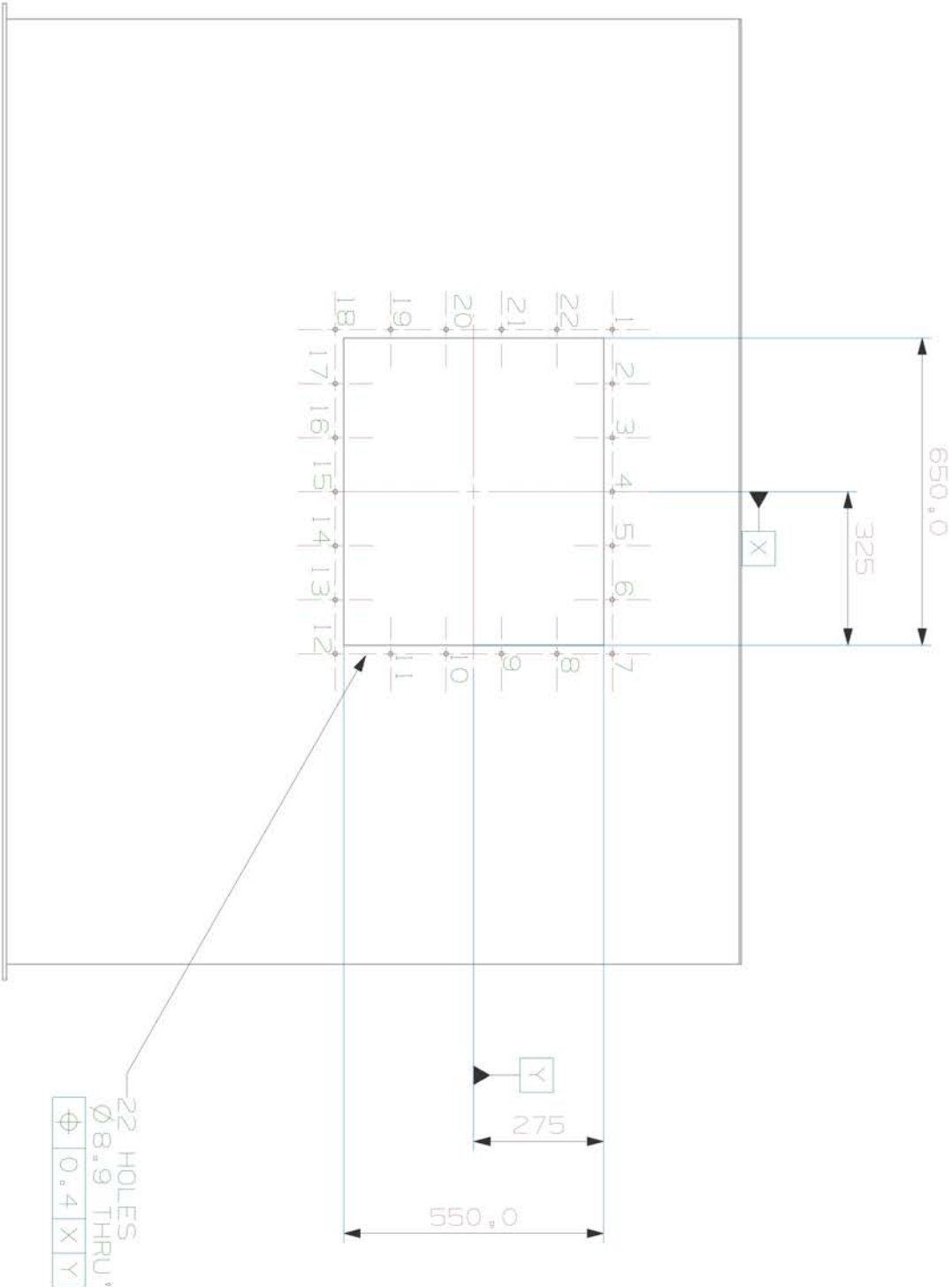
37MM FLANGE 8MM THK

NOTE:
FABRICATED FROM 4MM THK
ALUMINIUM

DO NOT SCALE



ISOMETRIC VIEW
1:25



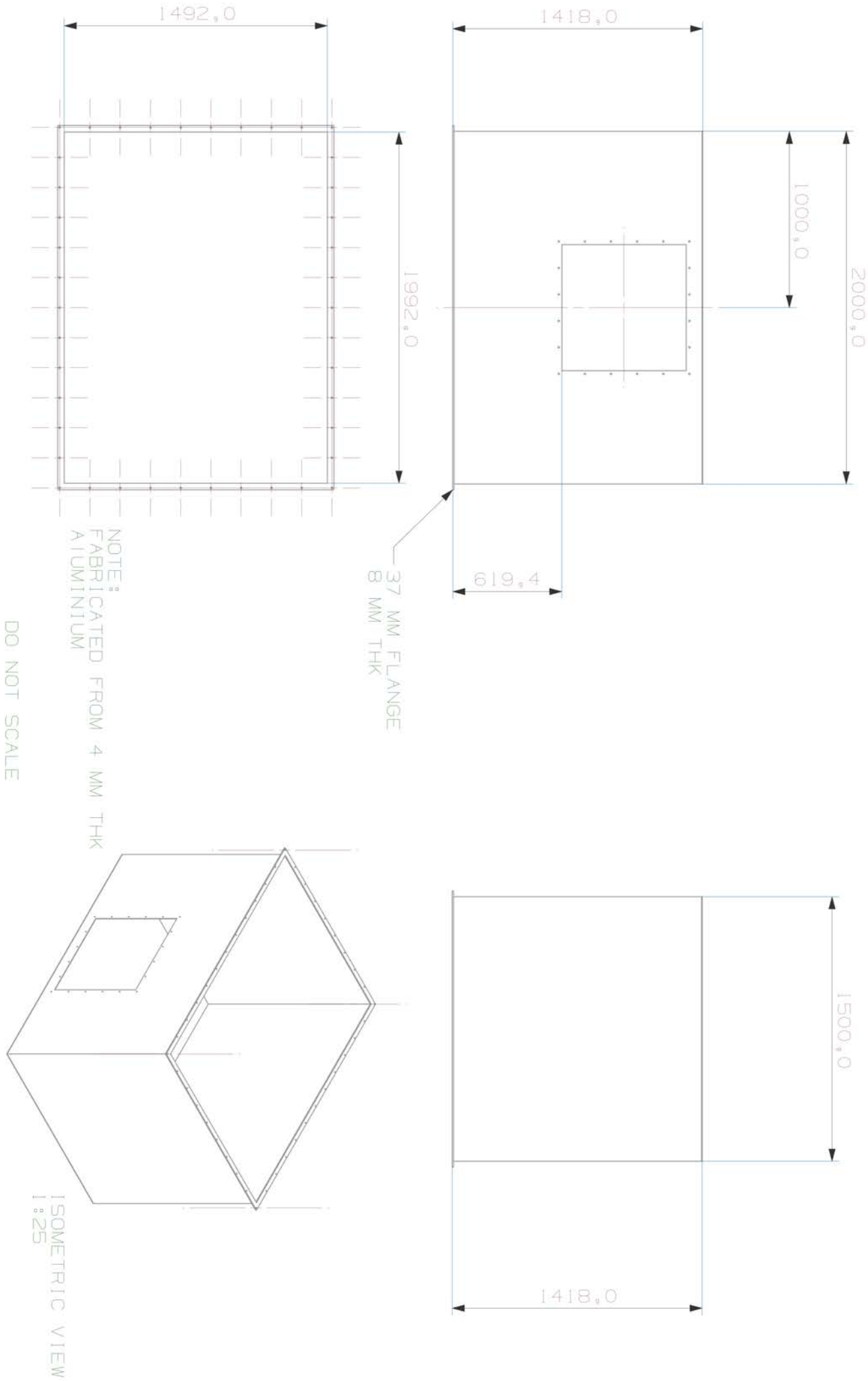
HOLE LOCATIONS		
HOLE NO.	X	Y
1	-343	293
2	-228.7	293
3	-114.3	293
4	0	293
5	114.3	293
6	228.7	293
7	343	293
8	343	175.8
9	343	58.6
10	343	-58.6
11	343	-175.8
12	343	-293
13	228.7	-293
14	114.3	-293
15	0	-293
16	-114.3	-293
17	-228.7	-293
18	-343	-293
19	-343	-175.8
20	-343	-58.6
21	-343	58.6
22	-343	175.8

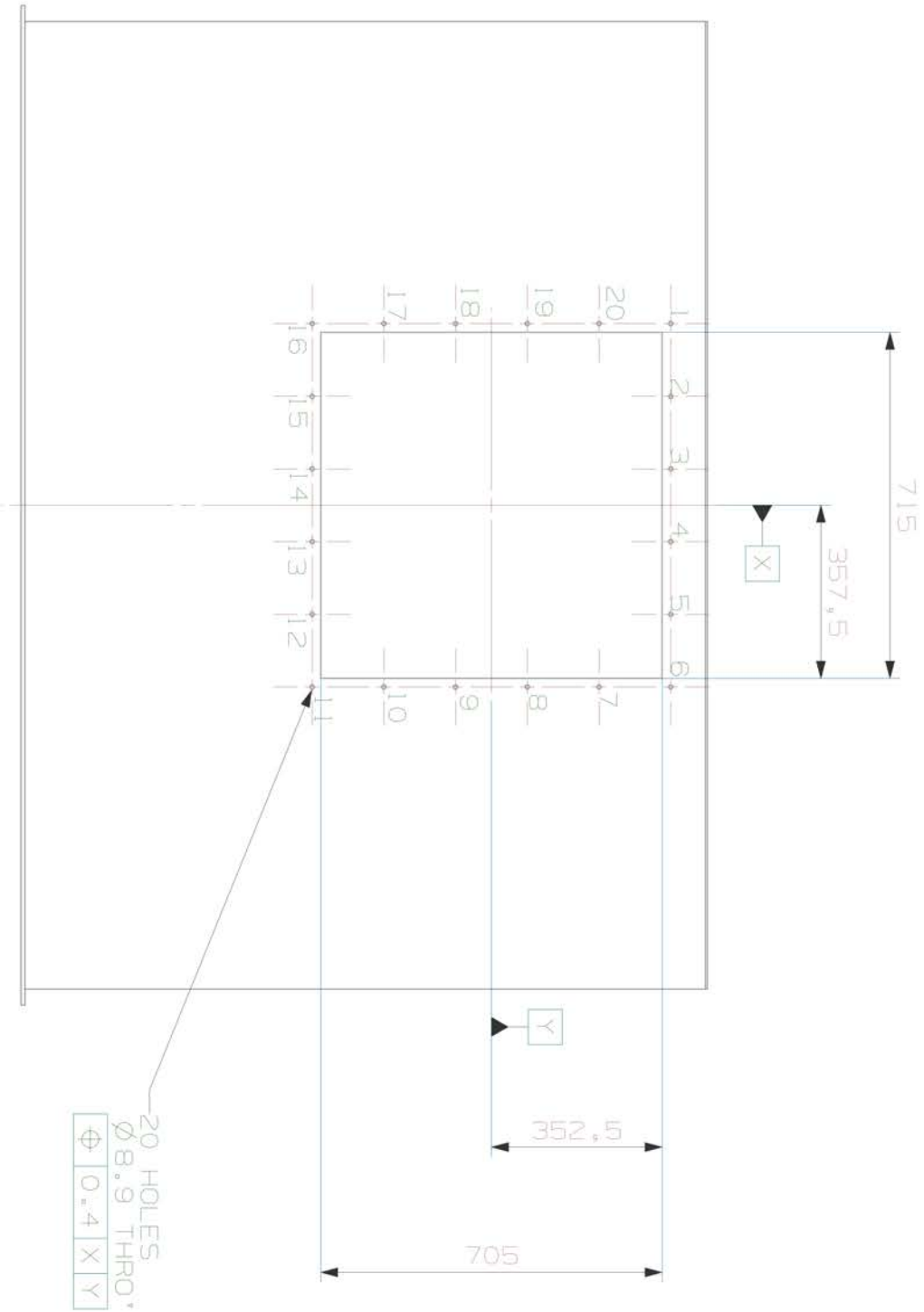
DO NOT SCALE



27	170.5	-772
28	0	-772
29	-170.5	-772
30	-340.8	-772
31	-511.1	-772
32	-681.4	-772
33	-851.7	-772
34	-1022	-772
35	-1022	-600.4
36	-1022	-428.8
37	-1022	-257.2
38	-1022	-85.6
39	-1022	85.6
40	-1022	257.2
41	-1022	428.8
42	-1022	600.4

HOLE LOCATIONS		
HOLE NO.	X	Y
1	-1022	772
2	-851.7	772
3	-681.4	772
4	-511.1	772
5	-340.8	772
6	-170.5	772
7	0	772
8	170.5	772
9	340.8	772
10	511.1	772
11	681.4	772
12	851.7	772
13	1022	772
14	1022	600.4
15	1022	428.8
16	1022	257.2
17	1022	85.6
18	1022	-85.6
19	1022	-257.2
20	1022	-428.8
21	1022	-600.4
22	1022	-772
23	851.7	-772
24	681.4	-772
25	511.1	-772
26	340.8	-772

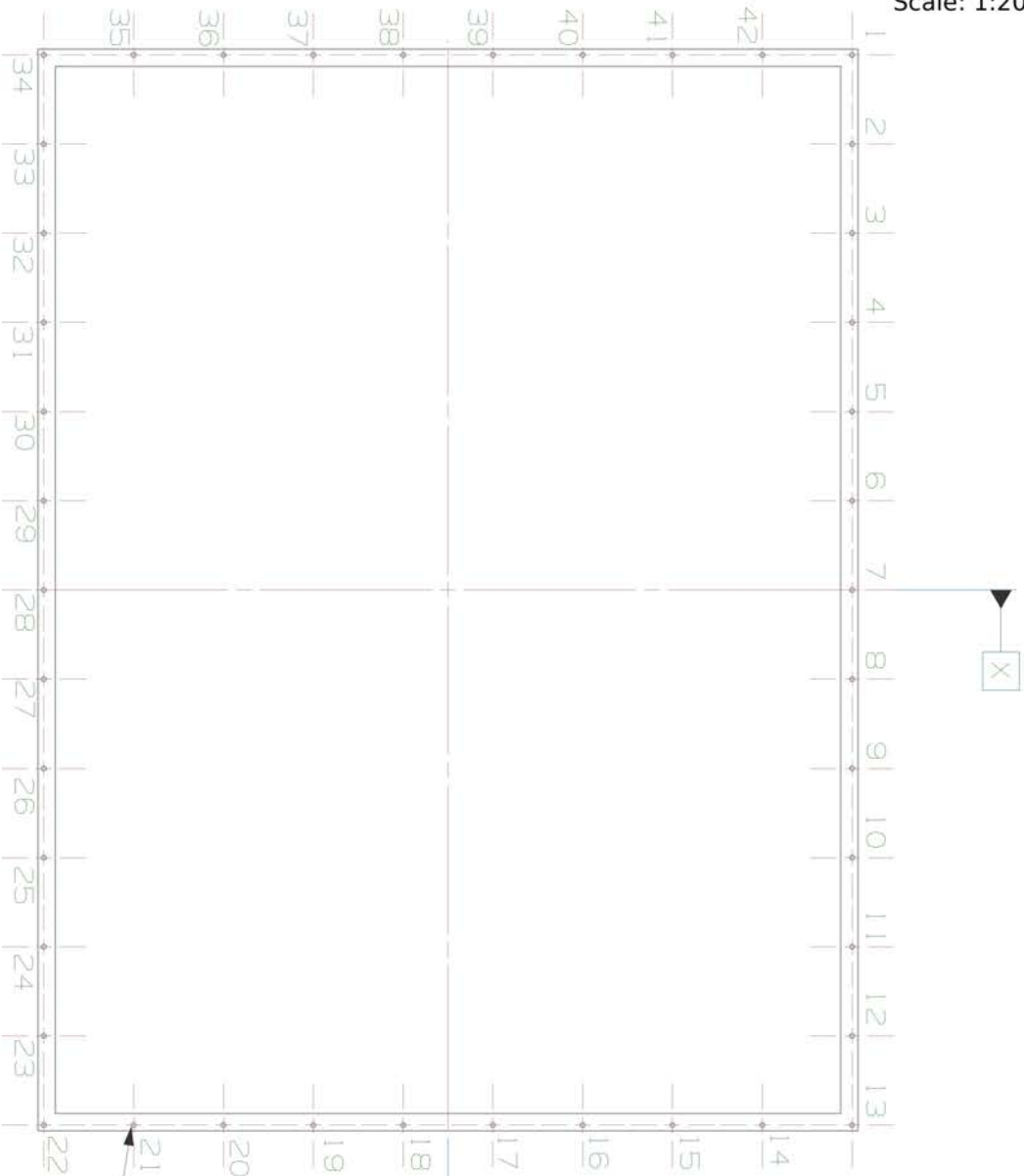




CHANNEL MOUNTING HOLE DIMENSIONS

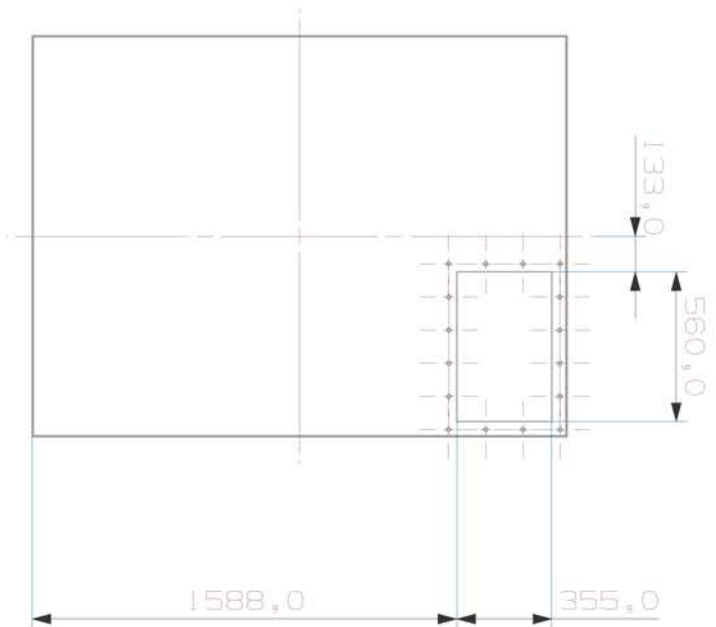
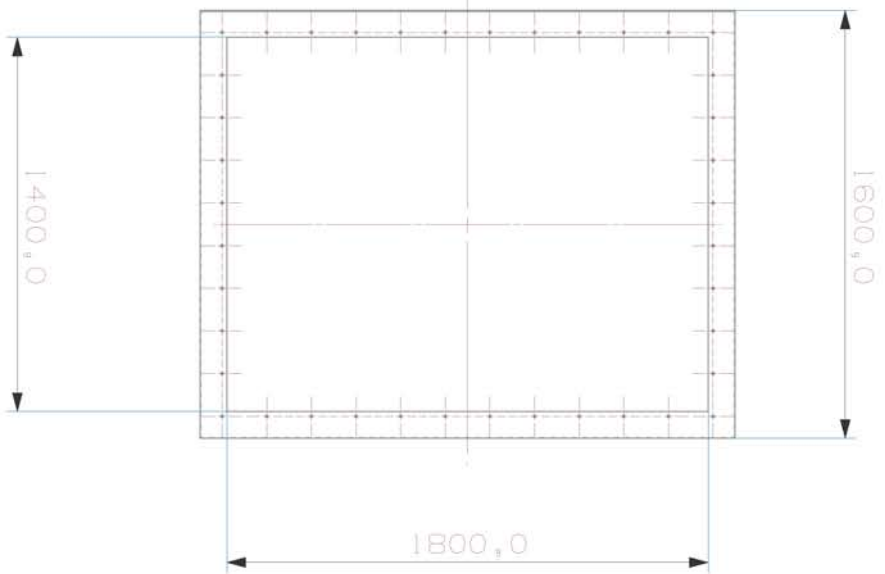
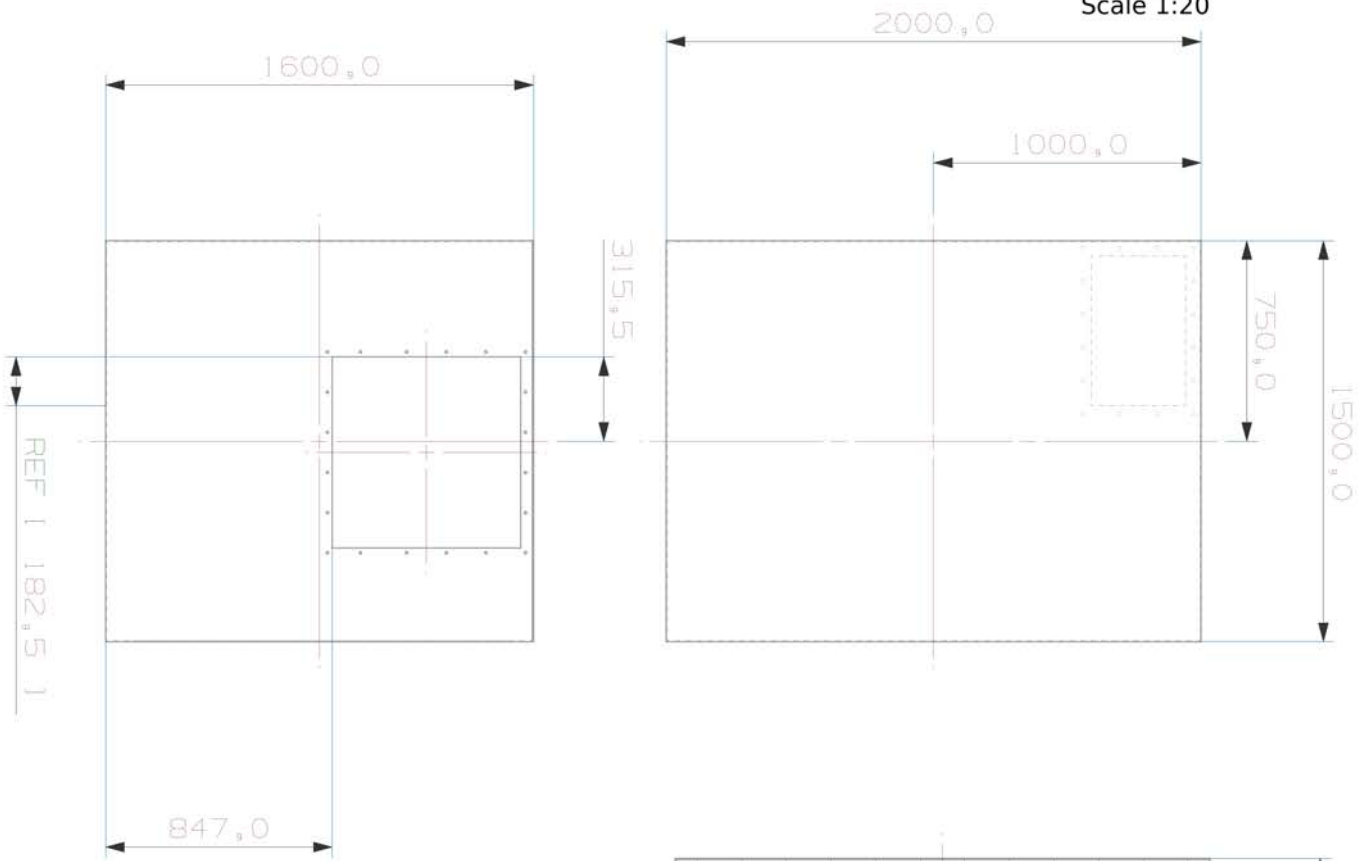
DO NOT SCALE

HOLE LOCATIONS		
HOLE NO.	X	Y
1	-375.5	370.5
2	-225.3	370.5
3	-75.1	370.5
4	75.1	370.5
5	225.3	370.5
6	375.5	370.5
7	375.5	222.3
8	375.5	74.1
9	375.5	-74.1
10	375.5	-222.3
11	375.5	-370.5
12	225.3	-370.5
13	75.1	-370.5
14	-75.1	-370.5
15	-225.3	-370.5
16	-375.5	-370.5
17	-375.5	-222.3
18	-375.5	-74.1
19	-375.5	74.1
20	-375.5	222.3



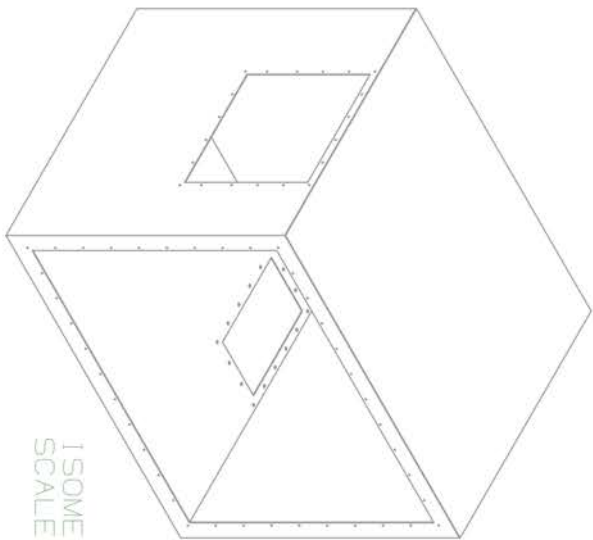
		HOLE LOCATIONS	
	HOLE NO.	X	Y
27	170.5	-772	
28	0	-772	
29	-170.5	-772	1
30	-340.8	-772	2
31	-511.1	-772	3
32	-681.4	-772	4
33	-851.7	-772	5
34	-1022	-772	6
35	-1022	-600.4	7
36	-1022	-428.8	8
37	-1022	-257.2	9
38	-1022	-85.6	10
39	-1022	85.6	11
40	-1022	257.2	12
41	-1022	428.8	13
42	-1022	600.4	14

15	1022	428.8	
16	1022	257.2	
17	1022	85.6	
18	1022	-85.6	
19	1022	-257.2	
20	1022	-428.8	
21	1022	-600.4	
22	1022	-772	
23	851.7	-772	
24	681.4	-772	
25	511.1	-772	
26	340.8	-772	

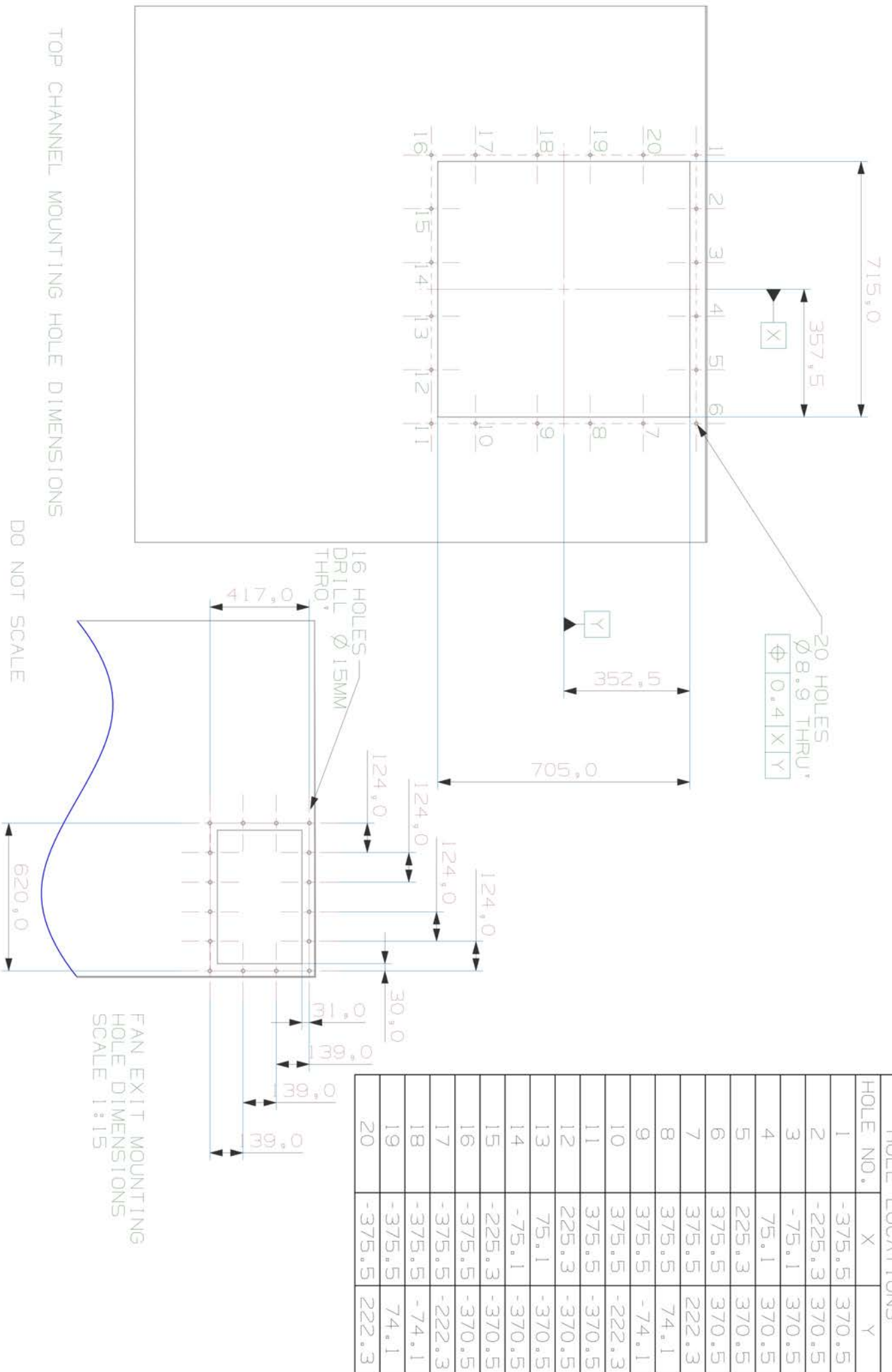


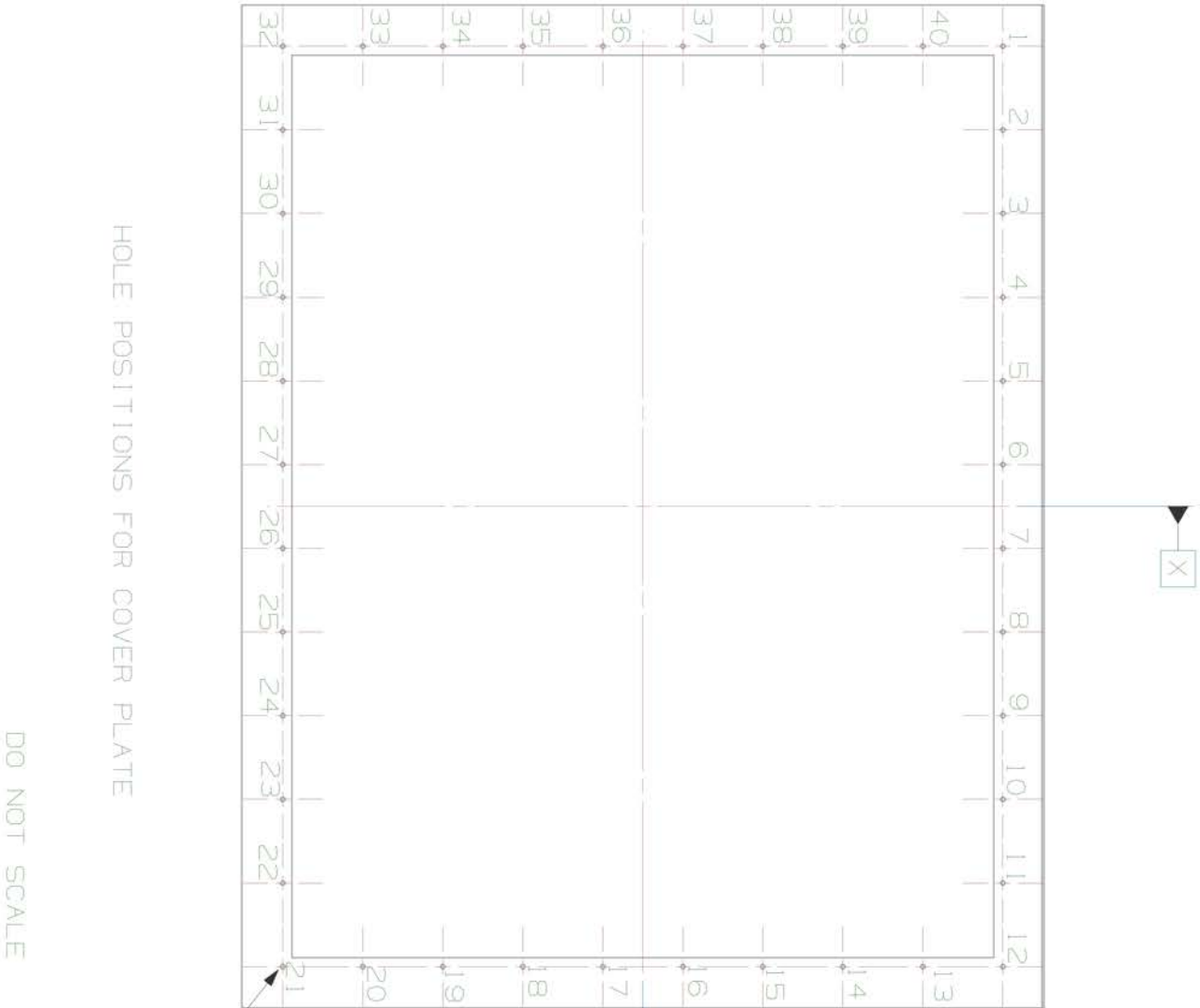
NOTE:
FABRICATED FROM 4MM THICK
ALUMINIUM ALLOY

DO NOT SCALE



ISOMETRIC VIEW
SCALE 1:25





40 HOLES
Ø8.9 THRU"
Ø 0.4 X Y

HOLE LOCATIONS		HOLE NO.	
X	Y		
-83.5	-718	27	1
-250.4	-718	28	2
-417.3	-718	29	3
-584.2	-718	30	4
-751.1	-718	31	5
-918	-718	32	6
-918	-558.5	33	7
-918	-398.9	34	8
-918	-239.3	35	9
-918	-79.8	36	10
-918	79.8	37	11
-918	239.3	38	12
-918	398.9	39	13
-918	558.5	40	14
83.5	718	26	15
918	718	25	16
918	79.8	24	17
918	-79.8	23	18
918	-239.3	22	19
918	-398.9	21	20
918	-558.5	20	21
918	-718	19	22
751.1	-718	18	23
584.2	-718	17	24
417.3	-718	16	25
250.4	-718	15	26

A.3 Conduction Loss

Conduction losses

This simple heat loss calculation assumes the film cooling flow is completely removed from the main stream (Thus the system is assumed closed). Mixing of the cooling film and bulk flow are also assumed negligible.

External Surface area & Volume	M ²	M ³
• First Plenum		
Base/top (1.386x1.928)x2	5.344	3.55
Side (1.601x1.928)x2	6.174	
Side_2(1.601x1.386)x2	4.438	
• Plenum Feed		
Side (0.666x0.304)x2	0.405	0.0604
End (0.355x0.304)x2	0.216	
• Top Channel (Short)		
Side (0.690x0.892)x2	1.231	0.417
Side_2(0.678x0.892)x2	1.210	
• Top Channel (Long)		
Side(0.690x1.985)x2	2.739	0.929
Side_2(0.678x1.985)x2	2.692	
• Feed Plenum Top		
Base (1.996x1.496)	2.986	4.5
Side(1.496x1.507)x2	4.509	
Side_2(1.996x1.496)x2	5.972	
• Feed Plenum Bottom		
Base(1.996x1.496)	2.986	4.66
Side(1.496x1.500)x2	4.488	
Side_2(1.996x1.500)x2	5.988	
• Heater Mount		
Side(0.690x0.116)x2	0.160	0.054
Side_2(0.678x0.116)x2	0.157	
• Test section		
Sides(0.6x1.593)x4	3.823	0.504
• Baffle box		
Side (1.2x1.4)x2	3.36	2.285
Side_2(1.36x1.4)x2	3.808	

Total estimated area = 62.69M²

Total volume =17.03M³

$$Q = \frac{(A \times \Delta T \times K)}{\Delta x}$$

$A = \text{External Surface Area (M}^2\text{)}$

$\Delta T = \text{Temperature Difference (K)}$

$K = \text{Thermal conductivity (W/mK)}$

$\Delta x = \text{Insulation thickness (M)}$

Heat loss from conduction

Where

$\Delta T = 80K$ (assume $T_{amb} = 20^\circ C$)

$K = 0.031 W/mK$ (Rohacell 31)

$\Delta x = 0.0254M$

$$Q = \frac{62.69 \times 80 \times 0.031}{0.0254} = 6.12Kw$$

To approximate further losses due to support structure and fan casing conduction this loss is increased by 25%.

$$Q_{+25\%} = 7.65Kw$$

Time to reach steady state calculation

$$Q = \dot{Q} \Delta t$$

$$\dot{Q} = \dot{m} C_p \Delta T \text{ (Open system)}$$

$$Q = m C_v \Delta T \text{ (Closed system)}$$

$t = \text{time interval (sec)}$

$m = \text{Weight of air (Kg)}$

$C_v = \text{Specific heat capacity (J Kg}^{-1}\text{K}^{-1}\text{)}$

$Q = \text{Net heat addtion (W)}$

Initial Air flow properties:

$$T = 293K$$

$$C_p = 1005.2 J Kg^{-1}K^{-1}$$

$$C_v = 718 J Kg^{-1}K^{-1}$$

$$\gamma = 1.4$$

$$\rho = 1.21 kg/m^3$$

$$m = 17.03 \times 1.21 = 20.61 kg$$

$$Q = 20.61 \times 718 \times 80 = 1183.63Kw$$

Net rate of power addition

$$\dot{Q} = 50 - 7.65 = 42 \text{ Kw}$$

$$\therefore 1183.63 = 42\Delta t \quad \Delta t = 28.18 \text{ seconds}$$

A.4 Pressure Loss

Pressure loss approximation

Frictional head loss using the Darcy-Weisbach equation with friction coefficient calculated using the Colebrook equation.

Assumed conditions:

$$\begin{aligned}\dot{Q} &= 5.4 \text{ m}^3/\text{s} \\ \mu &= 1.786 \times 10^{-5} \text{ Kg/ms} \\ \rho &= 1.21 \text{ Kg/m}^3 \\ T &= 293\text{K}\end{aligned}$$

Frictional pressure loss calculations of each tunnel component. In all cases the material is assumed to be smooth stainless steel.

First Plenum

$$D_h = \frac{4 \times 1.386 \times 1.928}{2(1.386 + 1.928)} = 1.613$$

$$V = \frac{5.4}{(1.386 \times 1.928)} = 2.02 \text{ m/s}$$

$$R_{Dh} = \frac{1.21 \times 2.02 \times 1.613}{1.786 \times 10^{-5}} = 220744$$

$$e = 4.5 \times 10^{-5} \text{ m}$$

$$\therefore f = 0.0156$$

$$h_l = 0.0156 \times \frac{1.6}{1.613} \frac{2.02^2}{2} = 0.0316 \text{ Pa}$$

Top Channel sections (long & short)

$$D_h = \frac{4 \times 0.690 \times 0.678}{2(0.690 + 0.678)} = 0.684$$

$$V = \frac{5.4}{(0.690 \times 0.678)} = 11.54 \text{ m/s}$$

$$R_{Dh} = \frac{1.21 \times 11.54 \times 0.684}{1.786 \times 10^{-5}} = 534769$$

$$e = 4.5 \times 10^{-5} \text{ m}$$

$$\therefore f = 0.01391$$

$$h_l = 0.01391 \times \frac{3}{0.684} \frac{11.54^2}{2} = 4.0623 \text{ Pa}$$

Feed Plenums (top & Bottom)

$$D_h = \frac{4 \times 1.496 \times 1.996}{2(1.496 + 1.996)} = 1.71$$

$$V = \frac{5.4}{(1.496 \times 1.996)} = 1.8 \text{ m/s}$$

$$R_{Dh} = \frac{1.21 \times 1.8 \times 1.71}{1.786 \times 10^{-5}} = 208532$$

$$e = 4.5 \times 10^{-5} \text{ m}$$

$$\therefore f = 0.01573$$

$$h_l = 0.01573 \times \frac{3}{1.71} \frac{1.8^2}{2} = 0.045 \text{ Pa}$$

Test section

$$D_h = 0.6$$

$$V = \frac{5.4}{(0.6 \times 0.6)} = 15 \text{ m/s}$$

$$R_{Dh} = \frac{1.21 \times 15 \times 0.6}{1.786 \times 10^{-5}} = 609742$$

$$e = 4.5 \times 10^{-5} \text{ m}$$

$$\therefore f = 0.01379$$

$$h_l = 0.01379 \times \frac{1.593}{0.6} \frac{15^2}{2} = 4.12 \text{ Pa}$$

Baffle Box

$$D_h = \frac{4 \times 1.2 \times 1.36}{2(1.2 + 1.36)} = 1.275$$

$$V = \frac{5.4}{(1.2 \times 1.36)} = 3.3 \text{ m/s}$$

$$R_{Dh} = \frac{1.21 \times 3.3 \times 1.275}{1.786 \times 10^{-5}} = 285055$$

$$e = 4.5 \times 10^{-5} m$$

$$\therefore f = 0.014955$$

$$h_l = 0.014955 \times \frac{1.4}{1.275} \frac{3.3^2}{2} = 0.089 Pa$$

A summary of the pressure loss due to friction is presented in the following table.

Summary of friction losses					
Section	R_{dh}	D_h	f	e	h_l (pa)
First plenum	220744	1.613	0.015587	4.50E-05	0.0316
Top channels	534769	0.684	0.013907	4.50E-05	4.062
Feed plenums	208532	1.71	0.015729	4.50E-05	0.045
Test section	609742	0.6	0.013794	4.50E-05	4.12
Baffle box	285055	1.275	0.014955	4.50E-05	0.089
$\sum h_l$					8.35

Dump losses

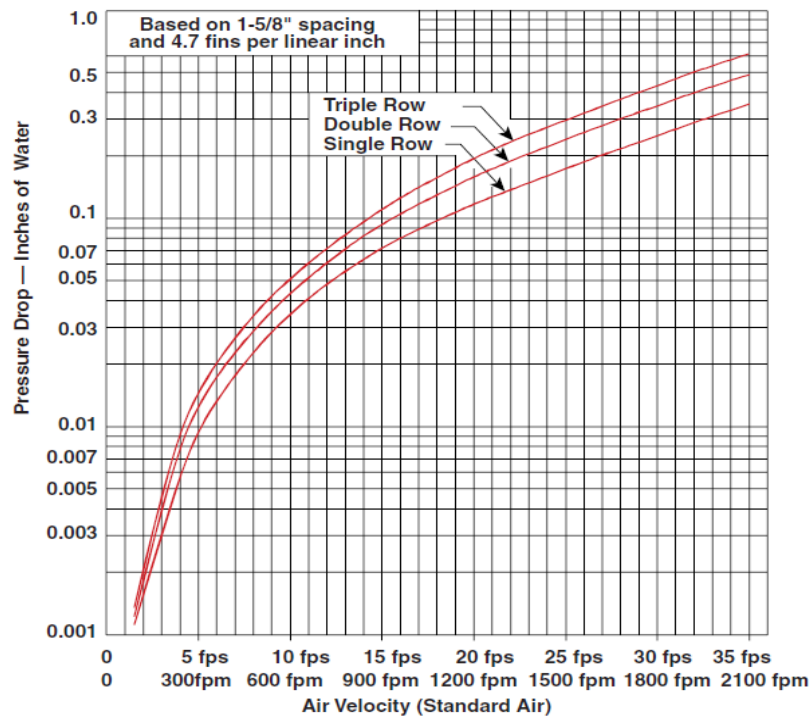
In order to produce a compact tunnel design, the diffusion is performed by dumping flow into two large plenum assemblies. This approach incurs a higher pressure loss but enables a smaller tunnel design. The pressure loss at each of these locations is assumed equal to the dynamic pressure.

$$P = \frac{1}{2} \rho V^2$$

Summary dump losses		
Section	$V(m/s)$	h_l (pa)
Fan exit	27.2	447.6
Top channel exit	11.54	80.57
Test section exit	15	136.13
Baffle plate (50% Area reduction)	6.6	26.35
Orifice meter plate*	40	968
$\sum h_l$		1658.7

*Some diffusion will be applied to the orifice plate in order to recovery some of the pressure loss

Heater pressure loss



$$V = 11.54 \text{ m/s} \approx 37.9 \text{ ft/s}$$

$$\approx 15.24 \text{ mm (water)}$$

$$\therefore h_l = 9.81 \times 15.24 = 149.5 \text{ pa}$$

A.5 Misalignment

Misalignment considerations

Top channel expansion joint

The channel expansion joint forms the connection between the two plenums. The maximum misalignment will occur when machine tolerances act in opposite signs.

Feed Plenum

Cut out $\pm 1\text{mm}$

Flange hole location $\pm 0.2\text{mm}$

Top Channel long

Duct $\pm 1\text{mm}$ x2

Hole location $\pm 0.2\text{mm}$ x2

Heater Mount

Duct $\pm 1\text{mm}$ x2

Hole location $\pm 0.2\text{mm}$ x2

Top Channel

Duct $\pm 1\text{mm}$ x2

Hole location $\pm 0.2\text{mm}$ x2

First Plenum

Duct $\pm 1\text{mm}$ x2

Hole location $\pm 0.2\text{mm}$ x2

Misalignment total

Total=10.8mm

To aid the assembly this offset is increased by a factor of three to increase the amount of free play when connecting the tunnel sections.

Misalignment requirement = 33mm

Thermal expansion check

As this rig will be operated at elevated temperatures the thermal expansion of the large panels which form the box sections must be considered.

$$\frac{\Delta L}{L_o} = \alpha \Delta T$$

$$\text{Steel} = 11 - 13 \times 10^{-6} \mu\text{m/m} - ^\circ\text{C at } 20^\circ\text{C}$$

$$\text{Rohacell} = 33 \times 10^{-6} \mu\text{m/m} - ^\circ\text{C at } 20^\circ\text{C}$$

Longest length $\approx 2\text{m}$, $\Delta T \approx 100^\circ\text{C}$

$$\Delta L = 2 \times 33 \times 10^{-6} \times 100 = 6.6\text{mm} \quad (\text{Rohacell})$$

$$\Delta L = 2 \times 13 \times 10^{-6} \times 100 = 2.6\text{mm} \quad (\text{Steel})$$

This calculation shows the thermal expansion of the steel sections remains acceptable. The Rohacell expands further which require space to be left between flanges and Flexlink support structure to prevent buckling as temperatures increases.

A.6 Uncertainty Calculations

Coolant flow rate

The coolant mass flow rate uncertainty of the orifice plate was calculated from the equation given in ISO 5167-1:2003 and is reproduced below:

$$\frac{\delta qm}{qm} = \left[\left(\frac{\delta C}{C} \right)^2 + \left(\frac{\delta \varepsilon}{\varepsilon} \right)^2 + \left(\frac{2\beta^4}{1-\beta^4} \right)^2 \left(\frac{\delta D}{D} \right)^2 + \left(\frac{2}{1-\beta^4} \right)^2 \left(\frac{\delta d}{d} \right)^2 + \frac{1}{4} \left(\frac{\delta \Delta p}{\Delta p} \right)^2 + \frac{1}{4} \left(\frac{\delta \rho 1}{\rho 1} \right)^2 \right]^{1/2} \quad (\text{A.1})$$

The equation accounts for various elements which taint the calculated mass flow rate. The uncertainty of the individual components is detailed as follows:

Uncertainty of discharge coefficient C for the $\phi 15\text{mm}$ orifice plate set in the $\phi 50.8\text{mm}$ coolant feed pipe.

$$\beta = 0.278$$

$$C = 0.5 + 0.9(0.75 - 0.278)(2.8 - \frac{D}{25.4})\% \quad C = 0.795\%$$

Uncertainty of expansibility factor ε

$$Br0.4, \Delta P = 2304\text{pa}, P1 = 9.9618 \times 10^4$$

$$Br1.5, \Delta P = 30000\text{pa}, P1 = 9.9618 \times 10^4$$

$$3.5 \times \frac{\Delta P}{KP1}$$

$$3.5 \times \frac{2304}{1.404 \times 9.9618 \times 10^4} = 0.057\%$$

$$3.5 \times \frac{30000}{1.404 \times 9.9618 \times 10^4} = 0.751\%$$

Uncertainty of D (pipe diameter) and d (orifice diameter) From ISO 5167
the maximum uncertainty $\frac{\delta D}{D} = 0.4\%$, $\frac{\delta d}{d} = 0.1\%$

Uncertainty of pressure measurement

$$\text{Br } 0.4, \Delta P = 2304 \text{ pa}, \delta P = 50 \text{ pa}, \frac{50}{2304} = 2.1\% \text{ (worst case)}$$

$$\text{Br } 1.5, \Delta P = 30000 \text{ pa}, \delta P = 50 \text{ pa}, \frac{50}{30000} = 0.16\% \text{ (worst case)}$$

Uncertainty of density measurement

High density case

$$T_c = -6 \text{ }^\circ\text{C}, P1 = 9.962 \times 10^4, \rho_c = 1.3$$

Low density

$$T_c = 12 \text{ }^\circ\text{C}, P1 = 9.344 \times 10^4, \rho_c = 1.14$$

$$\rho = \frac{P}{RT}$$

$$\pm \rho = \left[\left(\frac{\partial \rho}{\partial P} \right)^2 (\varepsilon P)^2 + \left(\frac{\partial \rho}{\partial T} \right)^2 (\varepsilon T)^2 + \left(\frac{\partial \rho}{\partial R} \right)^2 (\varepsilon R)^2 \right]^{1/2} \quad (\text{A.2})$$

$$\pm \rho = \left[\left(\frac{1}{RT} \right)^2 (\varepsilon P)^2 + \left(\frac{-P}{RT^2} \right)^2 (\varepsilon T)^2 \right]^{1/2} \quad (\text{A.3})$$

$$\pm \rho = \left[\left(\frac{1}{287 \times 267} \right)^2 (50)^2 + \left(\frac{-9.9618 \times 10^4}{287 \times 267^2} \right)^2 (1.5)^2 \right]^{1/2} \quad (\text{A.4})$$

$$= \pm 0.0073, 0.006 \quad (\text{A.5})$$

$$\rho = 1.3 \pm 0.56\%, \rho = 1.14 \pm 0.5\% \quad (\text{A.6})$$

Using equation A.1 and considering the worst case conditions the following uncertainty is placed on the measured coolant mass flow rate derived parameters:

$$\therefore M_{coolant} = 0.0311 \pm 1.7\% kg/s \quad (\text{A.7})$$

Main stream flow rate

The mainstream mass flow rate was measured using the nozzle diffuser arrangement detailed in appendix A.1. The metering nozzle may be used to calculate the mass flow using the known throat diameter, along with calculations of density and velocity obtained by taking pressure and temperature measurements within the plenum and nozzle. The inlet to the nozzle was radiused to improve the discharge coefficient, for mass flow calculations it is

assumed $CD=1$.

$$m = CD \times A \times \rho \times U \quad (A.8)$$

The velocity inside the nozzle (U) is calculated from the following equation:

$$U = \sqrt{\frac{\Delta P}{0.5 \times \rho}} \quad (A.9)$$

Where ΔP is the measured pressure drop across the nozzle. Typical tests were run with a mainstream mass flow of approximately 1.8kg/s. At this flow condition pressure drop across the nozzle is approximately 1700pa. The uncertainty of nozzle velocity is calculated using the following equation:

$$\pm U = \left[\left(\frac{\partial U}{\partial P} \right)^2 (\varepsilon P)^2 + \left(\frac{\partial U}{\partial \rho} \right)^2 (\varepsilon \rho)^2 \right]^{1/2} \quad (A.10)$$

$$= \pm 0.46$$

$$U = 60 \pm 0.8\%$$

The uncertainty of mass flow measurement was calculated by combining the uncertainty of the density ($\approx 0.5\%$) and velocity measurement and is estimated as:

$$\therefore M_{mainstream} = 1.88 \pm 1.36\% kg/s$$

A.7 ASME GT2012-68863

GT2012-68863

EXPERIMENTS ON COMBUSTOR EFFUSION COOLING UNDER CONDITIONS OF VERY HIGH FREE-STREAM TURBULENCE

Damian Martin and Steven J. Thorpe

Department of Aeronautical and Automotive Engineering
Loughborough University
Loughborough
Leicestershire, LE11 3TU, UK
Email: d.martin@lboro.ac.uk

ABSTRACT

Full-coverage or effusion cooling is commonly used in the thermal management of gas turbine combustion systems. The combustor environment is characterised by highly turbulent freestream flow conditions and relatively large turbulent length scales (length scale-to-coolant hole diameter ratios in excess of 30) that are primarily created by the fuel injector and dilution jets; indeed, the available evidence suggests that large energetic eddies interact strongly with the coolant flows and may have a significant impact on the film-cooling performance. The desire to create compact low-emission combustion systems for aero gas turbine engines has also given rise to a desire to reduce the quantity of air used in wall cooling, and has led to the need for improved thermal design approaches, cooling correlations and validated computational methods. In order to establish a greater understanding of effusion cooling under conditions of very high freestream turbulence, a new laboratory-based test facility has been created that is capable of simulating representative combustor flow conditions, and that allows for a systematic investigation of film-cooling performance over a range of freestream turbulence conditions and coolant to mainstream density ratios. This paper describes the new test facility and its capabilities, including the method for generating combustor relevant flow conditions. Adiabatic film-cooling effectiveness data obtained at a range of blowing ratios are also presented for a typical combustor effusion cooling geometry that uses a twenty degree injection angle. The analysis of this data is supported by fluid temperature field measurements which are presented for low and high freestream

turbulence conditions. The interpretation of the data has established the impact of turbulence intensity and integral length scale on the mixing processes between freestream and coolant flows.

NOMENCLATURE

D	effusion hole diameter
\dot{m}	mass flow rate, kg/s
DR	coolant to free-stream density ratio
I	coolant to free-stream momentum ratio
BR	coolant to free-stream blowing ratio
VR	coolant to free-stream velocity ratio
L	integral length scale
P	spanwise effusion hole spacing, mm
Re_j	coolant Reynolds number
S	streamwise effusion hole spacing
T	temperature, K
Tu	turbulence intensity, %
ΔL	length scale, mm
U	velocity, m/s
X	streamwise coordinates, mm
Y	spanwise coordinate, mm
Z	lateral coordinates, mm
α	coolant hole angle, deg
ρ	density, kg/m^3
η	film cooling effectiveness

Subscripts

aw	adiabatic wall
w	wall
∞	freestream
c	coolant
xy	local position
j	coolant jet
f	flow field

INTRODUCTION

This article considers the performance and behaviour of a typical gas turbine combustor effusion cooling arrangement, and, in particular, the impact of the freestream flow conditions on adiabatic film-cooling effectiveness and coolant/freestream mixing. The historical trends in turbofan engine design have included increases in turbine entry temperature, overall pressure ratio and bypass ratio in order to improve both the thermal and propulsive efficiencies. In addition, the requirement to meet increasingly stringent emissions regulations has resulted in a desire to employ lean-burn combustion technology. The greater fraction of engine core air that is consumed by lean fuel-injectors has a consequent impact on the combustor liner thermal management, since less compressor delivery air is generally available for wall cooling. Given these trends it is apparent that improved wall cooling technologies and design methods are necessary for the implementation of compact low-emission aero-gas turbine combustors.

The thermal management of gas turbine combustion systems typically involves a combination of internal (convective) cooling, film-cooling and thermal barrier coatings. The combustion system designer must balance the performance of these cooling components such that the liner has an appropriate and predictable service life. Consequently, an efficient and cost-effective design strategy must be established; for example, cooling correlations, validated aero-thermal computational methods and life prediction. The behaviour of film cooling arrangements in the combustor environment is complicated by the particular freestream conditions that are usually present, namely, highly turbulent swirling flows, and the presence of relatively large diameter dilution jets. In general, for a particular wall geometry, the film-cooling situation can be characterised by the coolant and freestream flow conditions: velocity ratio, density ratio, Reynolds number and turbulence level. It has been known for some time that freestream turbulence levels have an impact on the adiabatic film-cooling effectiveness [1]. In general terms the increased level of turbulent mixing that such conditions promote, means that the coolant fluid is more rapidly dispersed into the free-stream, and that consequently the near-wall flow temperature is raised. Much of the available literature regarding the impact of free-stream turbulence on film-cooling performance is focused on typical high-pressure turbine nozzle guide vane cooling geometries (for ex-

ample, [2], [3]) these being predominantly single-rows of discrete angled holes. Many of these studies consider free-stream turbulence intensity levels of up to the mid-teens percent, which is considered typical of combustor exit / turbine inlet conditions. In addition, the characteristic length-scale of the free-stream turbulence has rarely been considered as an independent parameter, and in fact those cases that have addressed this ([1], [4], [5]) have generally considered relatively small turbulent scales. Other notable studies include those of [6] and [7] which have used a combination of laboratory-based combustor simulators and passive grids to generate a range of turbulence intensities and length scales. These studies considered the heat transfer characteristics of a nozzle guide vane in response to high freestream turbulence. In all of the test cases reported, elevated turbulence levels led to augmented heat transfer. The effect of turbulent length scale was observed with smaller scale grid generated turbulence ($Tu=7.6\%$, $\Delta L=20\text{mm}$) resulting in earlier transition to turbulent flow and increased heat transfer when compared against larger scale combustor turbulence ($Tu=8.8\%$ $\Delta L=90\text{mm}$) with slightly higher intensity.

EXPERIMENTAL FACILITY

A new test facility for the investigation of combustor film cooling arrangements has been created that allows for the systematic experimentation into the effects of free-stream turbulence conditions, coolant to free-stream blowing ratio and density ratio on film-cooling performance. The test-section of this facility is equipped with instrumentation that permits the measurement of: adiabatic film-cooling effectiveness, spatially resolved measurements of local flow temperature (coolant/free-stream mixture fraction) and flow velocity/turbulence parameters. Currently this facility is configured for the measurement of the adiabatic film-cooling effectiveness of effusion cooled combustor-type geometries. Typical effusion arrangements in aero-gas turbine combustors utilise staggered arrays of angled holes with a diameter of between 0.5 and 1.0 mm, and angled at approximately 20° to the cooled surface. The combustor flow conditions in a modern turbofan engine typically yield coolant to freestream density ratios in the range of 1.5 to 3. Because of the differences in the local near-wall freestream flow velocity at various locations within a combustion system, coolant to freestream velocity ratios typically span a wide range in any given system; for the purposes of this study a range between 0.2 and 1.5 has been considered.

In order to make detailed and accurate measurements of film-cooling performance, and in common with many previous film-cooling studies, the new wind-tunnel facility involves using geometrically and aerodynamically scaled model geometries, and air flow conditions at near-atmospheric pressure. The geometric scale factor that has been applied to the engine-scale cooling geometry is approximately 10, while flow velocities are se-

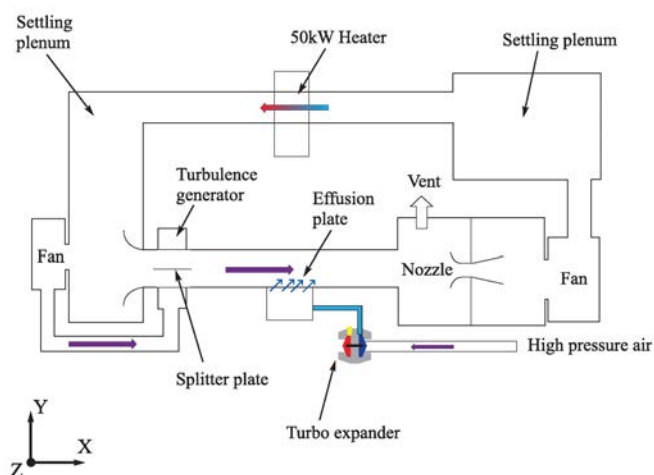


FIGURE 1. A schematic diagram of the effusion cooling wind-tunnel.

lected that yield an engine-relevant range of coolant jet Reynolds numbers. A schematic diagram of the wind-tunnel is shown in Fig.1. Essentially the facility is a recirculating wind-tunnel driven by a 37 kW radial fan; it also incorporates a 50 kW inline electrical flow heater that is used to raise the temperature of the recirculating air up to a maximum of 110°C. The flow condition in this main circuit is designed to be representative of the free-stream flow within a combustor, ie. it simulates the combustor hot-gas flow. Recirculating flow rates of up to 6.5 kg/s can be created with an average working section flow velocity of up to 15 m/s. The rectangular working section is shown in Figs. 1 and 2, and is 550 mm wide and 650 mm high. The effusion test plate is mounted above a thermally insulated plenum through which the low temperature coolant fluid is supplied. Various thermocouples were positioned throughout the wind-tunnel in order to establish the wind-tunnel operating condition.

Free-stream turbulence generation

The main wind-tunnel air flow enters the working section channel through a bell-mouthed inlet from a plenum as shown in Figs. 1 and 2. Flow blockage screens are incorporated in this region so as to improve the spatial uniformity of this flow as it enters the working section. In order to create prescribed turbulence properties in this freestream fluid as it approaches the test-section, a jets in cross-flow turbulence generation approach [8] has been investigated and adopted. As shown in the schematic diagram of Fig. 1 a secondary blower draws air from the working section feed-plenum and provides sufficient pressure rise to allow the injection of this fluid back into the working section upstream of the effusion plate at relatively high velocity; rows of normal jets on both the top and bottom walls of the channel are supplied

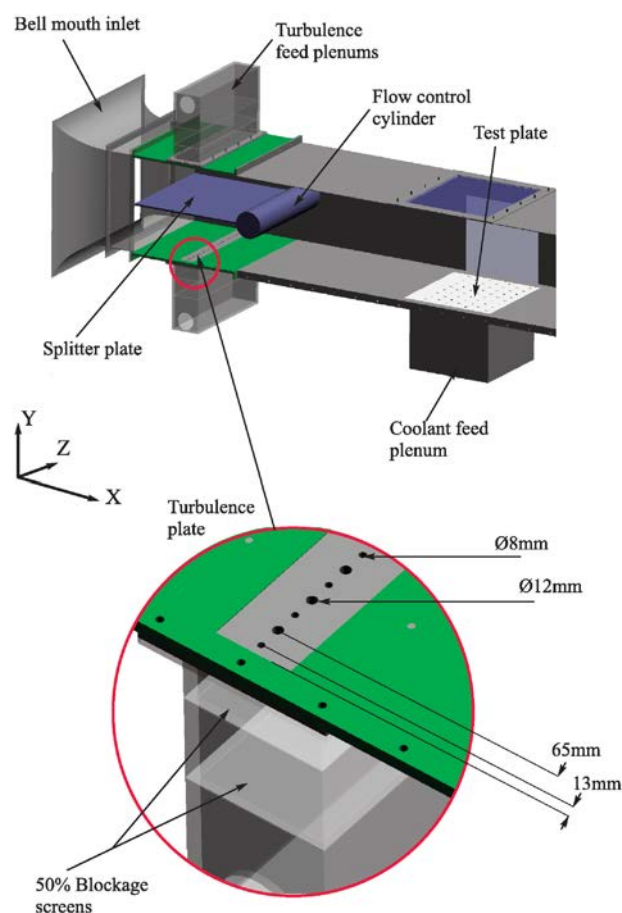


FIGURE 2. Schematic diagrams of the wind-tunnel working section and turbulence generator detail.

in this way. A splitter plate is placed horizontally between the normal jets in order to prevent the opposing jets directly interacting and causing poor spatial uniformity in the freestream flow profile. In addition, a full-span cylinder is also placed across the feed-channel at the downstream end of the splitter plate so as to improve uniformity in the freestream flow that approaches the cooling plate under test (such an approach was first reported by [9]).

Due in part to the relatively large size of the test section a single row of uniformly spaced turbulence generator injection holes proved incapable of producing free-stream conditions with adequate spatial uniformity; therefore a turbulence generator jet-hole pattern was adopted which combined a secondary set of smaller diameter holes (as shown in Fig. 2). The smaller diameter holes help to even out the mass flux distribution from the turbulence generator injector plate due to the differing jet trajectories. In this way a sufficiently uniform distribution of mean

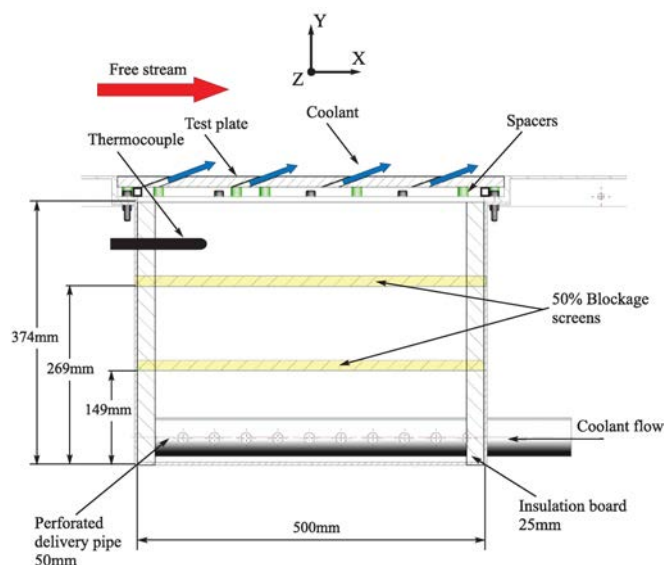


FIGURE 3. A diagram that illustrates the coolant feed plenum construction.

velocity, turbulence intensity and integral length scale has been created. The final turbulence generator design consists of two rows of holes: the first row consists of 8 mm diameter holes while the second row consists of 12 mm diameter holes (with spanwise pitch to diameter ratios of 6.5 and 4.3 respectively). A detailed view of these components is shown in Fig. 2.

Coolant fluid conditions

In order to investigate the effect of different coolant to freestream density ratios, the wind-tunnel can operate at elevated free-stream flow temperatures of up to 110 °C and sub-ambient coolant temperatures. The elevated free-stream temperatures are created by virtue of the recirculating heated design of the wind-tunnel, while the cold coolant is generated by a turbo-expander system that is based around an automotive turbo-charger (shown in Fig. 1). This system is capable of producing coolant air-flow temperatures of -20°C, yielding a maximum coolant to free-stream density ratio of 1.5. This value is at the low end of the expected density ratio range to be seen in combustor applications. However, the intention here is to diagnose the impact of density ratio as an independent parameter over a sensible range of values. Whilst it would clearly be attractive to conduct investigations over the typical combustor range of ratios, this would involve additional experimental difficulty and cost. Note that the use of a turbo-expander for film-cooling tests has previously been reported by [10]. Dry compressed air is delivered to the turbine of an IHI RB85 turbo-charger at pressures of up to 2.5 bar. The compressed air is then expanded through the turbine which re-

sults in a reduction of the air temperature as work is extracted. The air mass flow rate through the turbo-charger is measured by an orifice plate device and is controlled by an electrically operated control valve. As well as feed pressure control, the air temperature drop across the turbine can be fine-tuned via the turbine waste-gate which allows flow to bypass the turbine. The cold air issuing from the turbine then feeds into a T-section pipe which incorporates a bypass valve; excess coolant is bled to atmosphere before the required coolant flow rate is passed through a further orifice plate meter. The cold air is fed into the insulated coolant plenum located beneath the effusion plate, which contains flow control screens and an air filter to capture any oil that may have contaminated the air within the turbo-charger. The coolant air temperature is measured in the feed-plenum using sheathed K-type thermocouples. These details are shown in a sectional view of the coolant plenum in Fig. 3.

Wind-tunnel commissioning tests

The primary commissioning tests for the wind-tunnel were hot-wire based traverse measurements of the velocity field in the freestream flow; such data were acquired so as to develop and verify the characteristics of the turbulence generator system. The measurements were obtained within a span-wise plane that is aligned with the first row of effusion cooling holes. A Dantec constant temperature hot-wire anemometer was used to measure the time-mean flow velocity and turbulence statistics: integral length scales, turbulence intensity and energy spectra. The free-stream turbulence characteristics have been altered by changing the turbulence generator to free-stream velocity ratio and the spanwise cylinder diameter; in this way a range of freestream turbulence properties was produced that includes low, medium and high turbulence, and two integral length scales. The resulting spanwise averaged profiles are shown in Figs. 4, 5 and 6 as a function of position across the working section (expressed as y/D): Fig. 4 shows the integral length scale profiles; Fig. 5 shows the turbulence intensity profiles while Fig. 6 shows the measurements for three different turbulence generator blowing ratios. To summarise, three different turbulence intensity cases have been considered (nominal values of 10, 16 and 25%) and two length scales ($\Lambda/D=13$ and 26). Experimental results showed that the mean velocity at the start of the test area was uniform to within 5% of the area-averaged mean velocity, while the turbulence intensity and length scale were uniform to within 14%.

EXPERIMENTAL GEOMETRY AND TEST CONDITIONS

The effusion-cooled test plate consists of a staggered array of angled cylindrical holes with dimensions as given in Fig. 7. The spanwise pitch to diameter ratio is 8, while the stream-wise pitch to diameter ratio is 7.5 and the hole angle is 20°. The plate is manufactured from a closed-cell rigid foam (Rohacell) which

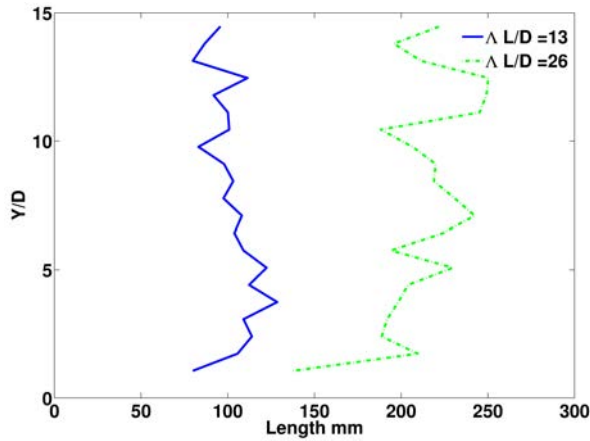


FIGURE 4. Measured integral length scale profiles at entrance to the working section (nominal free-stream turbulence intensity of 16%).

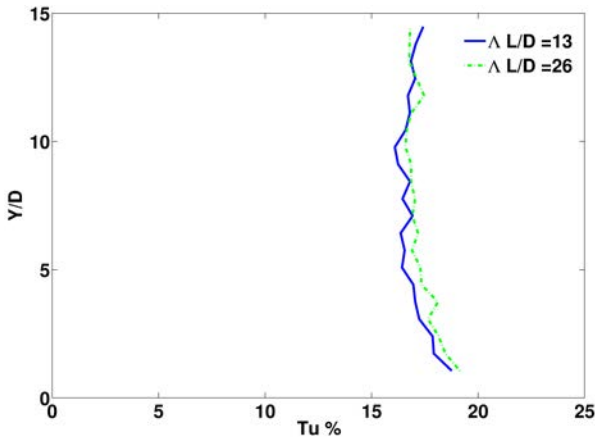


FIGURE 5. Measured turbulence intensity profiles at entrance to the working section (nominal free-stream turbulence intensity of 16%).

has a particularly low thermal conductivity (0.029 W/mK) and can be considered close to adiabatic. The surface of the plate is sprayed with a high emissivity black paint so as to aid infra-red based thermographic measurements of cooling effectiveness. The data presented here shows how the cooling layer develops from the first row of effusion holes up to row 7.

Adiabatic effectiveness measurement

The film-cooling effectiveness has been measured using an infra-red based imaging system that is based on a FLIR systems A40M thermal imaging device with 240 x 320 pixels. Each pixel maps to a geometric area of 0.7 mm square on the effusion test surface. The effusion surface is viewed through a 75 mm diam-

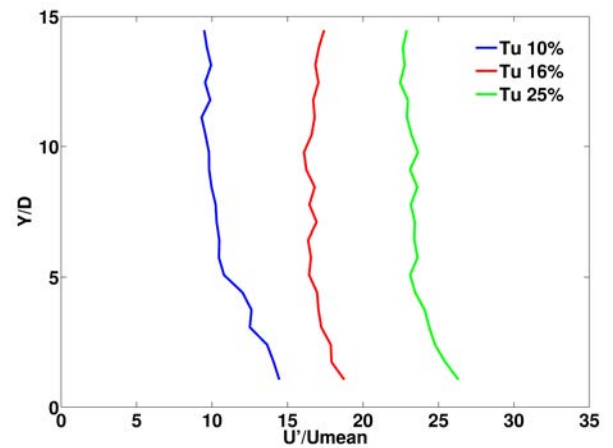


FIGURE 6. Measured turbulence intensity profiles at entrance to the working section for three turbulence conditions.

Dr	1.065-1.4	Tc	268-289K
Br	0.3-1.5	Tmain	308-378K
I	0.06-2.1	$Re_j(10^3)$	1.2-6
Tu	10%, 16%, 25%	$Re_\infty(10^3)$	2.2-3
AL	13D, 26D		

TABLE 1. Test conditions

eter zinc-selenide window that is incorporated into the top wall of the working section; note that the position of this window can be changed so as to allow measurement in different regions of the test plate. Three fine wire exposed-junction K-type thermocouples were embedded into the surface of the plate in order to provide a check of the calibration accuracy of the IR surface temperature measurement system.

IR thermography system calibration

In IR-based thermographic systems, the measured radiation intensity is influenced, and potentially corrupted, by a number of factors as has been described by [11]. In order to reduce the impact of optical reflections, incident radiation and window transmission, an in-situ calibration procedure was developed. A 10 mm thick aluminium plate with high emissivity surface coating and embedded K-type thermocouples was used to replace the Rohacell test plate, and to establish a near isothermal surface. With the wind-tunnel operating at a stable aerodynamic and thermal condition, the temperature of the plate gradually increased. During this process, and at set plate temperature intervals, measurement frames were acquired with the IR camera. For each pixel

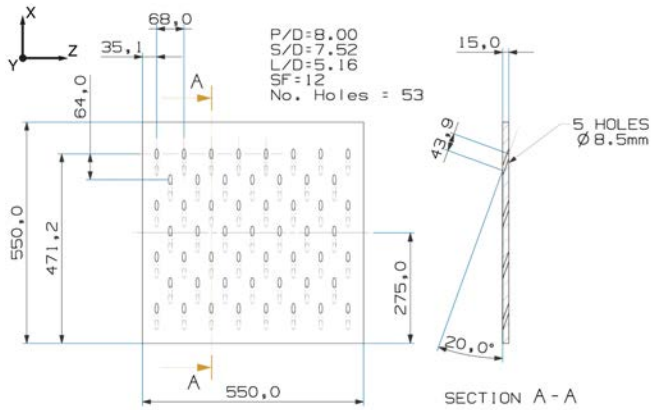


FIGURE 7. A drawing showing the effusion test-plate dimensions.

the raw IR intensity data was then compared with the corresponding plate thermocouple measurements. A unique polynomial calibration curve was then generated for each camera pixel, which describes the relationship between intensity and temperature. This pixel-by-pixel calibration resulted in surface temperature measurements within $\pm 0.25\text{K}$ of the surface reference thermocouple data. Such calibration data was acquired each time the camera location was changed.

Test procedure

During each test the coolant and mainstream flow parameters were set to their desired levels in terms of mass flow rate and temperature so as to establish particular blowing ratio and density ratio conditions. The wind-tunnel was typically left for approximately one hour at the start of testing so as to allow thermal equilibrium to be achieved throughout the facility. The surface temperature was then recorded by taking 60 measurement images with the IR camera; simultaneously, data was recorded from the effusion plate surface thermocouples so as to allow a check on the calibration of the IR system. The images were then averaged on a pixel-by-pixel basis to provide a time-mean surface temperature map for each experimental condition.

In addition to these wall surface temperature measurements the temperature distribution in the flow was investigated by traversing a fine-wire exposed bead thermocouple (wire diameter of 0.025 mm) in both spanwise and streamwise directions. The thermocouple was mounted on the end of a 2 mm diameter ceramic tube and a stepper-motor driven traverse that could cover the majority of the working section. The time-averaged gas temperature was recorded at each location (based on 8 seconds of data) with measurements taken in either 2 or 4 mm spatial increments, depending upon the test requirements. This traverse data was then compiled to create a spatially resolved thermal profile of the near-wall flow at various freestream conditions.

Test conditions

The effusion plate was tested with three different freestream turbulence intensities of 10, 16 and 25%. For each of these free-stream conditions, a total of thirteen different blowing ratios was investigated, along with two coolant to free-stream density ratios (1.065 and 1.4). The impact of varying the free-stream integral length scale was also investigated for the 16% turbulence intensity condition. The test conditions are summarized in Table 1. The primary measurements obtained in these experiments are the adiabatic film-cooling effectiveness and the coolant/free-stream mixture fraction; these are defined in equations 1 and 2, respectively.

$$\eta_{aw} = \frac{T_g - T_{aw}}{T_g - T_c} \quad (1)$$

$$\eta_f = \frac{T_g - T_{xy}}{T_g - T_c} \quad (2)$$

MEASUREMENT UNCERTAINTY

As mentioned earlier the test plate was manufactured from a very low thermal conductivity material so as to approximate an adiabatic wall. However, this material still has a finite thermal conductivity which will result in some level of thermal conduction through the wall. In order to quantify the effects of these fluxes on the measurement of the local adiabatic wall temperature, a conduction model of the effusion plate was developed similar to [12] using the commercial software Star-CCM+. In order to estimate the typical impact of wall conduction on effectiveness measurements a case was considered with high blowing and density ratio as these conditions would generally require the highest level of correction. An accurate three-dimensional model of the actual test plate was created and meshed using polyhedral volumes (approximately 185,000). The computational mesh was refined around the effusion holes in order to resolve the higher temperature gradients created in the near-hole regions. The material properties of the modelled wall were set at the values quoted by the manufacturer. The thermal boundary conditions on the surfaces of the test plate were defined by a combination of convective heat transfer correlations and measured surface temperature maps from the wind-tunnel experiment. Currently, there is no heat transfer coefficient data available. Therefore an estimation based on a turbulent flat plate correlation has been used [13]. The coolant side of the test plate is exposed to a uniform fluid temperature, and has been modelled as a uniform temperature boundary (this is considered a worst case approach). The effusion holes were defined as convective walls with ambient temperature set at coolant delivery temperature and heat transfer coefficient defined by a fully-developed turbulent pipe flow corre-

lation [13]. All other surfaces were modeled as adiabatic walls. The radiative heat transfer from the surrounding channel walls was approximated by a simple enclosed model.

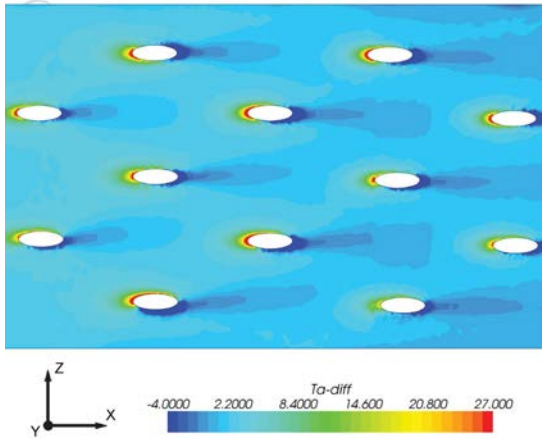


FIGURE 8. A contour plot of the difference between measured wall surface temperature and modelled adiabatic wall temperature.

After solving for the plate temperature distribution using Star-CCM+, the local wall-surface heat flux was then divided by the assumed heat transfer coefficient on the hot-side of the plate to yield an estimate of the temperature difference between measured wall temperature and the modelled adiabatic wall temperature. Fig. 8 shows a contour plot of the temperature correction. As might be expected the leading edge of the cooling hole shows the largest temperature correction as at these locations the wall is thin with only a thin wedge of material between mainstream and coolant flows. Immediately downstream of the ejection hole a localized over prediction in surface temperature is observed as the radiative heat flux dominates. Apart from some localised high temperature corrections, the majority of the measurement surface requires adjustment of a less than two degrees. Therefore a surface temperature error estimate of 2°C is applied to account for plate conduction.

With the relative accuracy of each measured term in the equation 1 quantified the film effectiveness uncertainty was calculated following the method of Kline and McClintock [14]. The estimated uncertainty intervals for the present experiment are $T_g = T_c \pm 0.2^{\circ}\text{C}$ and $T_{aw} = \pm 2^{\circ}\text{C}$. According to the uncertainty values above, the percent uncertainty decreases for higher values of η , from as high as 31% at $\eta=0.02$ to as low as 5% at $\eta=0.4$. The relative uncertainty in spanwise average adiabatic effectiveness is about 0.011. The uncertainty in mass flow rate was calculated based on the method described in ISO5167 and resulted

in $\dot{m} \pm 1.2\%$. This calculation included the density uncertainty of $\pm 0.5\%$. The mainstream velocity calculated from the hotwire data had an uncertainty of $\pm 3\%$.

RESULTS AND DISCUSSION

The data presented in this section are divided into three specific areas. Firstly, the effects of varying free-stream turbulence on spanwise averaged and spatially averaged adiabatic film-cooling effectiveness; secondly, the impact of free-stream conditions on the mixing of coolant and free-stream flows; thirdly, the effects of density ratio on cooling effectiveness. Each of these parts includes measurements at a variety of blowing ratios between 0.3 and 1.5. Together, the results capture the effects of free-stream turbulence on the film-cooling behaviour of an angled effusion geometry.

Free-stream turbulence intensity effects

One of the main objectives of this work was to investigate effusion film-cooling effectiveness under highly turbulent free-stream conditions. Figs. 9 to 11 show the measured impact of free-stream turbulence on the span-wise averaged adiabatic effectiveness for three blowing ratios and a density ratio of 1.4. At the lowest BR considered (0.3) it can be seen that increasing the free-stream turbulence level from 10 to 16% causes a small reduction in the film-cooling effectiveness (Fig. 9) in the more downstream area, while there is no further change when increasing the turbulence intensity to 25%. At the highest BR (1.5) the impact of free-stream turbulence level is markedly different. In this case the coolant jets detach from the wall and penetrate significantly into the free-stream; the effect of elevated turbulence is now seen to lead to a marked increase in the measured adiabatic effectiveness. This suggests that there is increased turbulent transport of the detached coolant fluid back towards the wall surface.

The impact of changing the free-stream turbulence level can also be appreciated from the adiabatic effectiveness maps presented in Figs. 12 and 13: Fig. 12 shows the variation of effectiveness with BR at 10% free-stream turbulence intensity, while Fig. 13 shows the equivalent data for 25%. For the low BR condition (0.3) the data clearly show the increase in lateral spreading of the coolant immediately downstream of the injection points that is caused by the increased turbulence level. There is also a reduction in coolant coverage in the streamwise direction as the cooling layer mixes out more quickly with the freestream. These phenomena have been well documented in single row film-cooling studies (for example, [1] and [15]). For low blowing cases this streamwise reduction outweighs any benefits gained from the increased spanwise spread, and therefore an overall decrease in the area-averaged surface effectiveness is observed. As the BR is increased the coolant jets detach from the surface and

penetrate into the free-stream, which results in poor jet centre-line effectiveness. However, the turbulent transport of coolant induced by the high free-stream turbulence ultimately benefits the film-cooling effectiveness. At the highest blowing ratio tested here ($BR=1.5$) an increase in spatially averaged effectiveness of 74% is observed at $Tu=25\%$, relative to the 10% turbulence case. A summary of the spatially averaged results for high and low turbulence levels are given in Table 2. These results are in stark contrast to a similar study using normal angled effusion [16], which reported a consistent decrease in spatially averaged effectiveness with increasing free-stream turbulence. This indicates that when jet-lift off is pronounced, as in the case of normal jets, the free-stream turbulence mixes the coolant jet so extensively that any transport of coolant back towards the surface is of negligible benefit. In the angled effusion case jet-lift off is reduced, thereby allowing free-stream turbulence to transport the coolant into the near-wall area.

Turbulence length scale effects

The capabilities of the wind-tunnel turbulence generator have allowed the impact of the integral length scale of turbulence to be considered independently of the turbulence intensity. For a free-stream turbulence intensity of 16%, normalised integral length scales of $\Lambda L/D = 13$ and 26 have been investigated; note that the other free-stream flow parameters, such as the mean

Br	Tu=10%	Tu=25%	$\Delta\%$
0.3	0.104	0.094	-9.2
0.4	0.113	0.108	-4.4
0.5	0.111	0.115	3.2
0.6	0.111	0.121	9.0
0.7	0.096	0.123	27.9
0.8	0.089	0.120	35.0
0.9	0.079	0.117	47.0
1.0	0.072	0.115	58.7
1.1	0.067	0.112	67.6
1.2	0.065	0.110	69.9
1.3	0.064	0.109	69.8
1.4	0.061	0.114	84.9
1.5	0.063	0.110	74.9

TABLE 2. Spatially averaged effectiveness at high and low turbulence not including holes.

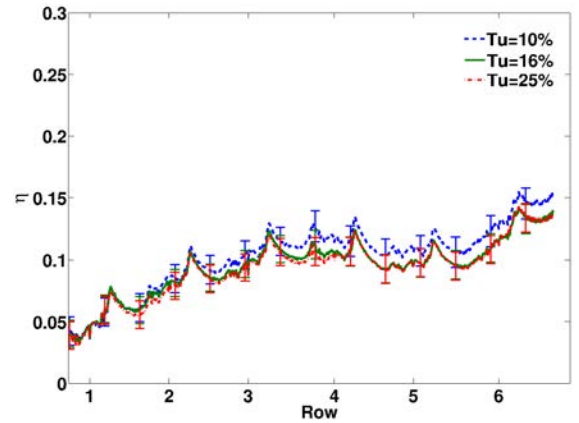


FIGURE 9. Spanwise averaged adiabatic effectiveness for $DR=1.4$, $BR=0.3$.

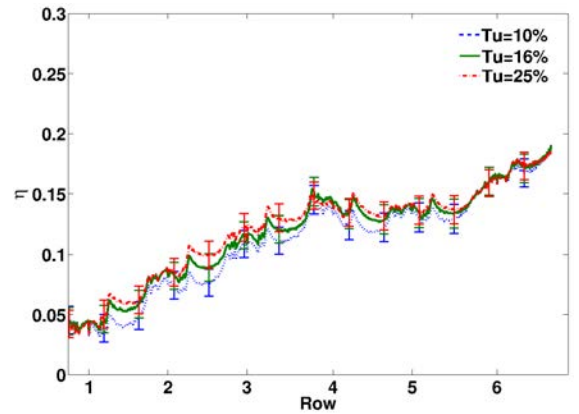


FIGURE 10. Spanwise averaged adiabatic effectiveness for $DR=1.4$, $BR=0.6$.

velocity and spatial profile, were otherwise unaffected by this change. The results associated with this part of the study are presented in Figs. 14 and 15 as span-wise averaged adiabatic effectiveness for BRs of 0.3 and 1.3. For the two length scale cases considered it can be seen that the impact of length scale is relatively low, although some increase in effectiveness is evident in the more downstream regions at a BR of 0.3. The study of [1] reported significant changes in effectiveness with changes in length scale for a single row of cooling holes. However this previous study considered very low length scales of $\Lambda L/D=0.12$ to 0.33. Therefore the data presented here suggests that above a certain length scale any further increases have marginal effects on film-cooling effectiveness.

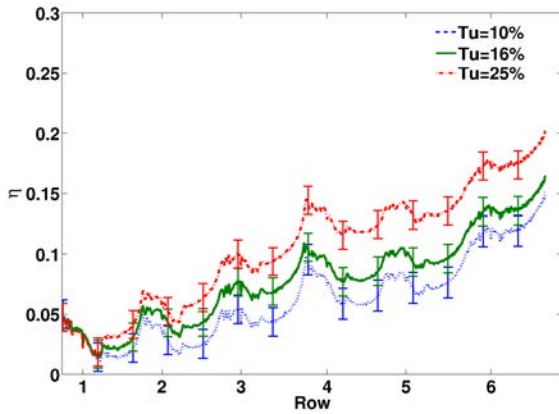


FIGURE 11. Spanwise averaged adiabatic effectiveness for DR=1.4, BR=1.5.

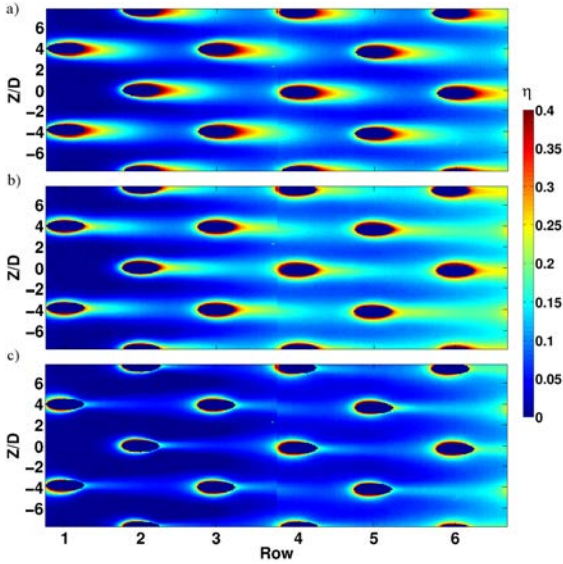


FIGURE 12. Measured adiabatic effectiveness for DR=1.4, Tu=10 %: a) BR=0.3; b) BR=0.6; c) BR=1.5.

Flow-field temperature measurements

Fluid temperature field measurements have been obtained for a traverse location positioned downstream of the 5th row of cooling holes. At this location, the trajectories of both the 4th and 5th rows of coolant jets are discernible, although these vary with the particular flow conditions. Figs.16 to 19 show the spanwise gas temperature traverse data along with the corresponding adiabatic effectiveness data. The gas temperature measurements were obtained at relatively coarse spacial increments of 4mm. Note that the traverse measurements do not include a 2mm region near the test surface. The spanwise traverse temperature

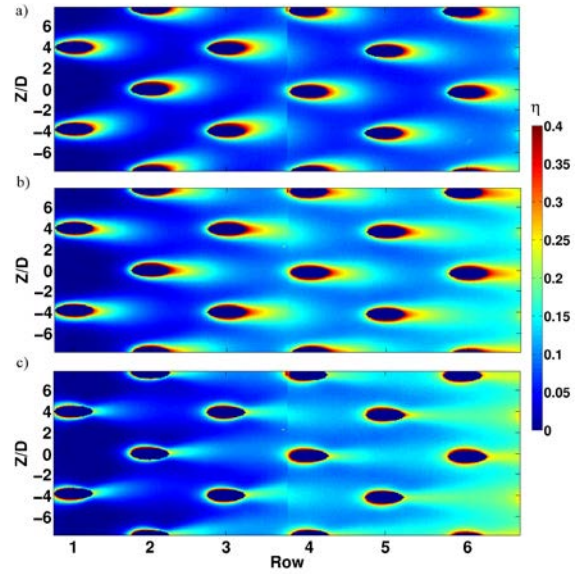


FIGURE 13. Measured adiabatic effectiveness for DR=1.4, Tu=25 %: a) BR=0.3; b) BR=0.6; c) BR=1.5

data can be used to reveal three of the main effects imposed by variations in the free-stream turbulence: 1) the mixing rate of the jets with the freestream coolant, 2) the penetration of the jets into the freestream, 3) the lateral spreading of the cooling jets.

Firstly considering the BR=0.4 measurements, the gas temperature measurements in Figs. 16 and 17 show that the increased level of free-stream turbulence causes a significant reduction in the coolant concentration within the cores of the attached jets. The reduction of the core coolant concentration pro-

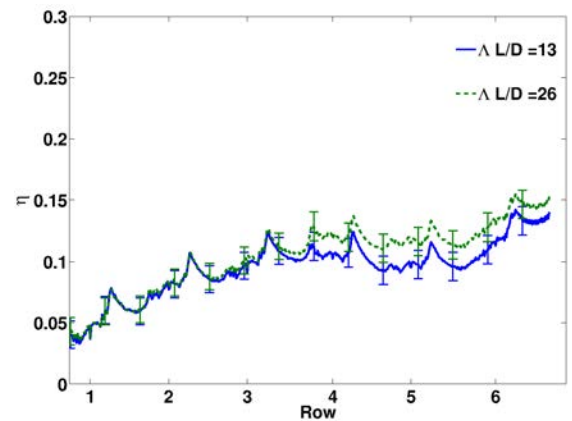


FIGURE 14. Measured spanwise averaged effectiveness at BR=0.3, Tu=16%, for two free-stream turbulence length scales.

duces a consequent reduction in centre-line cooling effectiveness as seen in the associated surface effectiveness plots. The temperature traverse measurements also reveal the level of coolant lateral spreading; it is clear that the elevated free-stream turbulence leads to an increase in spreading in the jets emerging from row 5 (at $X/D=\pm 4, \pm 12$), while the jets from row 4 are not evident in the higher turbulence case (at $X/D=0, \pm 8$). The coolant layer also appears to thin out as the turbulence level increases. In the low turbulence cases (Figs. 16 and 18 the remnants of the two neighbouring cooling jets from the 4th row are clearly visible. Fig 20 and 21 show the temperature field in the streamwise direction at a Br 1.3. The effectiveness contours become saturated in the jet exit/core region ($\eta = 1$) as the scale is limited to 0.5. This enables the temperature gradients around the cooling holes to be resolved. The streamwise traverse data correlated well with coolant delivery temperature measurements, with both measurements reporting the same coolant exit temperature to within a fraction of one degree. Upstream of the cooling hole the flow field effectiveness values are within 2% of the reported surface effectiveness. The streamwise traverse data reveals the full extent of the turbulent mixing in the mainstream. The coolant core length is significantly shorter for the high turbulence case. The low turbulence case shows a significant amount of coolant is completely detached from the surface, in this detached state very little coolant is transported back to the surface.

Density ratio effects

The impact of coolant to free-stream density ratio on cooling effectiveness has been investigated for two free-stream turbulence levels. Fig. 22 to 24 shows the area-averaged adiabatic effectiveness data gathered at free-stream turbulence levels of 10 and 25%, and at DRs of 1.065 and 1.4; these are plotted against momentum flux ratio (I), velocity ratio (VR) and blow-

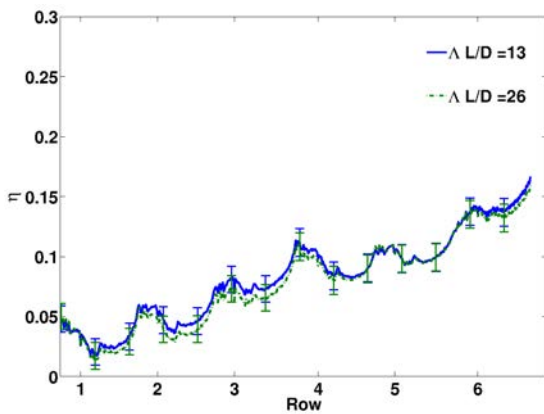


FIGURE 15. Measured spanwise averaged effectiveness at $BR=1.3$, $Tu=16\%$, for two free-stream turbulence length scales.

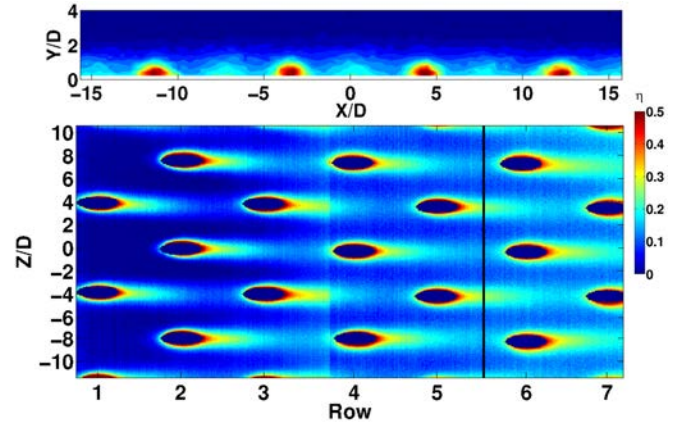


FIGURE 16. Measured spanwise gas temperature traverse at $X/D=37$ and surface effectiveness data, $DR=1.065$, $BR=0.4$, $Tu=10\%$.

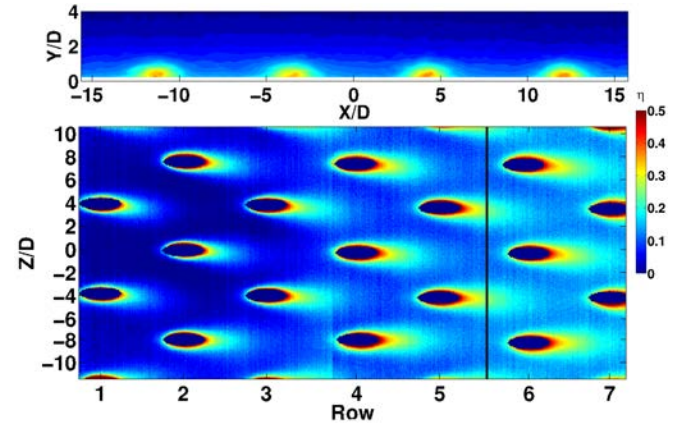


FIGURE 17. Measured spanwise gas temperature traverse at $X/D=37$ and surface effectiveness data, $DR=1.065$, $BR=0.4$, $Tu=25\%$.

ing ratio (BR). It is apparent that for high coolant injection levels ($VR>0.8$) the elevated free-stream turbulence condition leads to a near doubling of the area-averaged effectiveness. However, at these conditions the impact of density ratio as an independent parameter is relatively weak. Apart from some divergence at the very low VR conditions (when the cooling flows are attached to the wall) the effectiveness data appear to be reasonably well correlated by VR. When these data are plotted as a function of BR (Fig. 23) the peak effectiveness is shifted to a higher blowing ratio case when the density ratio is increased: however, the behaviour is different for the two turbulence intensity cases presented. Similar effects have been observed in several single row studies ([17] and [18]). With the shift in the effectiveness peak being attributed to the fact that high density coolant has a lower momentum flux for a prescribed blowing ratio, thus delaying on-

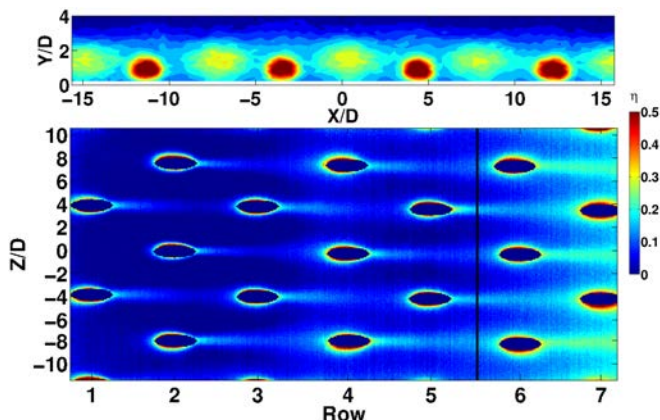


FIGURE 18. Measured spanwise gas temperature traverse at $X/D=37$ and surface effectiveness data, $DR\ 1.065$, $BR\ 1.3$, $Tu=10\%$.

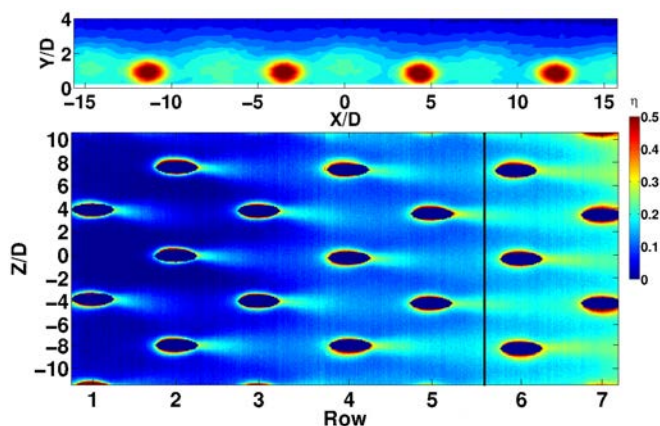


FIGURE 19. Measured spanwise gas temperature traverse at $X/D=37$ and surface effectiveness data, $DR=1.065$, $BR=1.3$, $Tu=25\%$

set of jet separation. The two density ratios scale well with momentum flux confirming jet separation is primarily a function of momentum flux. The velocity ratio scaling falls somewhere between momentum flux and blowing ratio. Once jet separation has occurred, effectiveness scales reasonably well with velocity ratio.

For the blowing ratio range considered here of $BR\ 0.3-1.5$ momentum flux is the appropriate parameter to scale for different density ratios. The area-averaged plots also show how increased freestream turbulence widens the coolant flux range over which efficient cooling is possible.

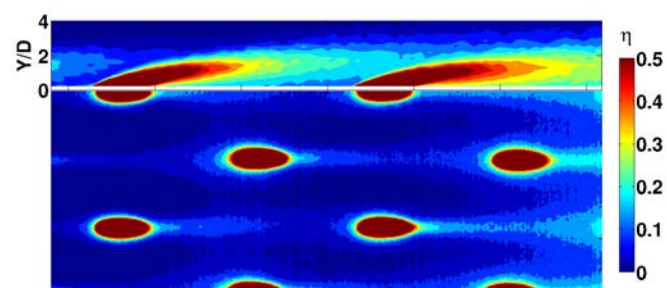


FIGURE 20. Streamwise temperature traverse (rows 2-4), $Dr\ 1.065$, $Br\ 1.3\ Tu=10\%$

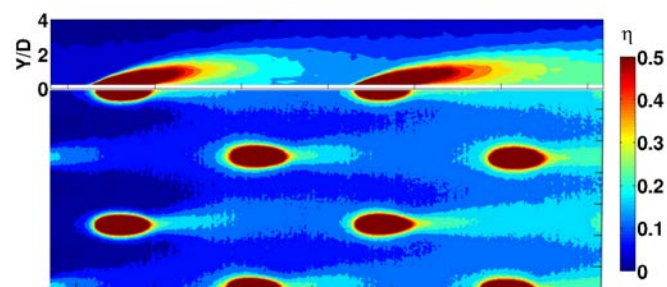


FIGURE 21. Streamwise temperature traverse (rows 2-4), $Dr\ 1.065$, $Br\ 1.3\ Tu=25\%$

CONCLUSIONS

A new test facility for the investigation of gas turbine combustor effusion cooling arrangements has been commissioned and its capabilities described. This wind-tunnel facility is capable of generating the relatively high free-stream turbulence conditions that are representative of a typical gas turbine combustor environment. The generation of a highly turbulent free-stream flow has been accomplished using a jets-in-cross-flow arrangement. The test facility is also capable of generating coolant to free-stream density ratios of between 1 and 1.5. Measurements of adiabatic effectiveness have been made using an infra-red based thermal imaging system, while flow temperature measurements that reveal the mixing of coolant and free-stream have also been acquired. An angled effusion plate with a staggered hole pattern has been tested. A combination of jets in cross-flow and a spanwise cylinder have been utilised to control turbulence length scale.

An angled effusion geometry with combustor relevant designs has been evaluated in terms of adiabatic effectiveness over a range of freestream turbulence conditions; 10, 16, 25% intensity, integral length scale-to-coolant hole diameter ratios of 13 and 26; and coolant to free-stream density ratios. An interrogation of the gas temperature field has also been performed, which

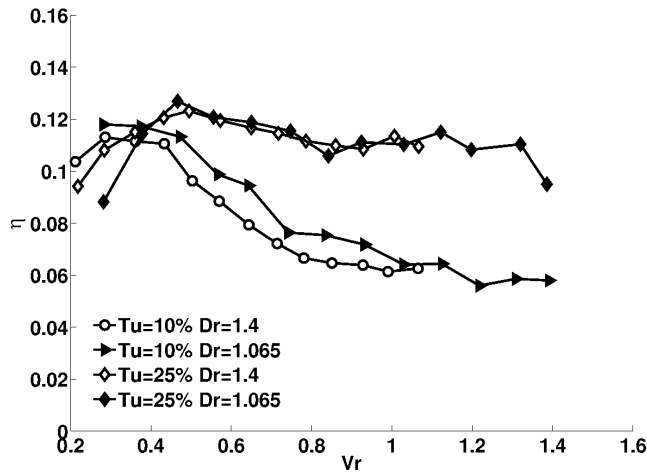


FIGURE 22. Area-averaged adiabatic effectiveness plotted against coolant to free-stream velocity ratio.

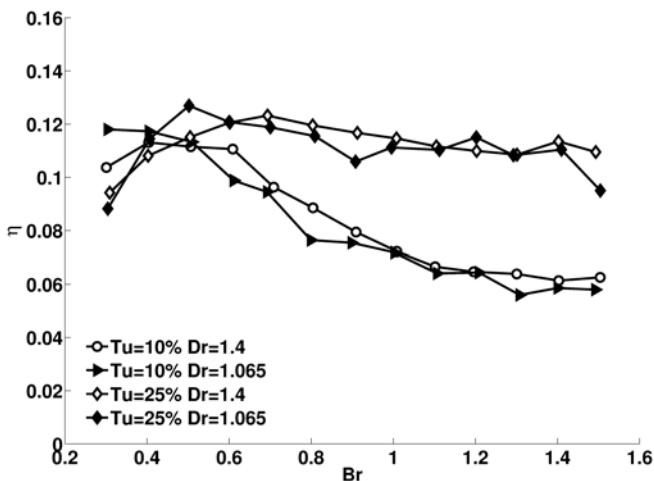


FIGURE 23. Area-averaged adiabatic effectiveness plotted against coolant to free-stream blowing ratio.

revealed some of the important fluid behaviour which drives the changes in measured surface effectiveness.

For angled effusion the spatially averaged effectiveness is reduced at low blowing ratios ($BR < 0.5$) when freestream turbulence is increased. For low blowing cases the additional spreading of coolant in the spanwise direction does not overcome the negative impact of reduced streamwise coverage. However, as blowing ratio increases the spatially averaged effectiveness can increase by as much as 85% at $BR=1.4$ with elevated freestream turbulence ($Tu=25\%$). This increase is attributed to the spanwise spreading of coolant and turbulent transport of coolant back to-

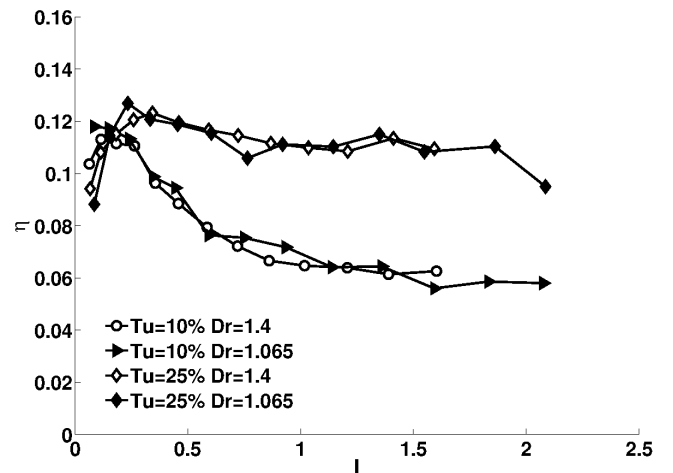


FIGURE 24. Area-averaged adiabatic effectiveness plotted against coolant to free-stream momentum ratio.

wards the surface. Once the coolant jet is detached, the centreline effectiveness is already very poor so the reduction in streamwise effectiveness becomes less dominant. This result differs considerably from normal angle effusion where a decrease in effectiveness is observed at all blowing ratios. This implies that if jet penetration is very high, extensive mixing with the freestream occurs such that any coolant transport back to the surface reduces film effectiveness. High freestream turbulence also widens the range of blowing ratios for efficient cooling due to the promotion of jet attachment.

The impact of turbulence length scale was investigated at a fixed turbulence intensity of $Tu=16\%$. A doubling of turbulent length scale from $\Lambda L/D=13$ to 26 had only a minor impact on the surface effectiveness measurements. The angled effusion array was tested at two coolant to free-stream density ratios (1.06 and 1.4). A reasonable collapse of the data over the full range of blowing conditions tested was observed when area averaged effectiveness was plotted as function of the coolant to free-stream momentum flux ratio. This implies that unity density ratio tests can be scaled to more engine specific density ratios using momentum flux.

ACKNOWLEDGMENT

This work was funded by the Engineering and Physical Sciences Research Council under grant number EP/E035078/1.

REFERENCES

- [1] Kadotani, K., and Goldstein, R., 1979. "On the nature of jets entering a turbulent flow: part b - film cooling performance". *ASME J. Eng. for Power*, **101**, pp. 466–470.
- [2] Bons, J., MacArthur, C., and Rivir, R., 1996. "The effect of high free-stream turbulence on film cooling effectiveness". *ASME J. Turbo.*, **118**(4), pp. 814–825.
- [3] Saumweber, C., Schulz, A., and Wittig, S., 2003. "Free-stream turbulence effects on film cooling with shaped holes". *ASME J. Turbo.*, **125**(1), pp. 65–73.
- [4] Bangert, B., Kohli, A., Sauer, J., and Thole, K. "High freestream turbulence simulation in a scaled-up turbine vane passage". *ASME Paper No. 97-GT-51*.
- [5] Kadotani, K., and Goldstein, R., 1979. "On the interaction of jets entering a turbulent flow: part a - jet-mainstream interaction". *ASME J. Eng. Gas Turbines & Power*, **101**(3), pp. 459–465.
- [6] Ames, F., Wang, C., and Barbot, P., 2003. "Measurement and prediction of the influence of catalytic and dry low nox combustor turbulence on vane surface heat transfer". *ASME J. Turbo.*, **125**, pp. 221–231.
- [7] Ames, F., Argenziano, M., and Wang, C., 2004. "Measurement and prediction of heat transfer distributions on an aft-loaded vane subjected to the influence of catalytic and dry low nox combustor turbulence". *ASME J. Turbo.*, **126**, pp. 139–149.
- [8] Thole, K., Bogard, D., and Whan-Ton, J., 1994. "Generating high freestream turbulence levels". *Exp. in Fluids*, **17**(6), pp. 375–380.
- [9] Johnston, C., Bogard, D., and McWaters, M., 1999. "Highly turbulent mainstream effects on film cooling of a simulated airfoil leading edge". *ASME Paper No. 99-GT-261*.
- [10] Wurm, B., Schulz, A., and Bauer, H., 2009. "A new test facility for investigating the interaction between swirl flow and wall cooling films in combustors". *ASME Paper No. GT2009-59961*.
- [11] Schulz, A., 2000. "Infrared thermography as applied to film cooling of gas turbine components". *Meas. Sci & Tech.*, **11**(7), pp. 948–956.
- [12] Baldauf, S., Schulz, A., and Wittig, S., 2001. "High-resolution measurements of local effectiveness from discrete hole film cooling". *ASME J. Turbo.*, **123**(4), pp. 758–765.
- [13] Kays, W., and Crawford, M., 1993. *Convective Heat and Mass Transfer*. McGraw-Hill, New York, MA.
- [14] Kline, S., and McClintock, F., 1953. "Describing uncertainties in single-sample experiments". *Mech. Eng.*, pp. 3–8.
- [15] Mayhew, J., Baughn, J., and Byerly, A., 2003. "The effect of freestream turbulence on film cooling adiabatic effectiveness". *Int. J. Heat & Fluid Flow*, **24**(5), pp. 669–679.
- [16] Harrington, M., McWaters, M., and Bogard, D., 2001. "Full-coverage film cooling with short normal injection holes". *ASME J. Turbo.*, **123**(4), pp. 798–805.
- [17] Pederson, D., Eckert, E., and Goldstein, R., 1977. "Film cooling with large density differences between the mainstream and the secondary fluid measured by the heat-mass transfer analogy". *ASME J. Heat Transfer*, **99**(4), pp. 620–627.
- [18] A.K. Sinha, D. B., and Crawford, M., 1991. "Film cooling effectiveness downstream of a single row of holes with variable density ratio". *Asme J. Turbo.*, **113**(4), pp. 442–449.